

Copyright
by
Amanda Flores
2025

The Dissertation Committee for Amanda Flores certifies that this is the approved version of the following dissertation:

**Heavy-Flavor Jet Fragmentation and Jet-Medium
Interactions in Pb–Pb Collisions**

Committee:

Deepa Thomas, Supervisor

Christina Markert

Peter Onyisi

Matthew Hersh

**Heavy-Flavor Jet Fragmentation and Jet-Medium Interactions in Pb–Pb
Collisions**

by

Amanda Flores

Dissertation

Presented to the Faculty of the Graduate School of
The University of Texas at Austin
in Partial Fulfillment
of the Requirements
for the degree of
Doctor of Philosophy

The University of Texas at Austin
December, 2025

For Adam “Joy”.

Acknowledgments

What a wonderful journey this has been. There are several people I'd like to thank for helping me reach this point. First, I'd like to thank my advisor Deepa Thomas for her steadfast guidance, her endless patience, and her encouragement to always challenge myself and think differently. I'll carry the wisdom you've shared with me along the way: If I can't explain something in simple terms, do I really understand it? It's been a pleasure working with you, and I'm honored to have been your first student. Thank you to Christina Markert, who as my first advisor saw something in me and provided crucial feedback on my work along the way. She has reminded me that progress in physics, or any field, flourishes from inclusivity. Thank you to my research group, starting with the senior graduate students: Erin, Ryan, and Justin. Thank you for your help when I felt like banging my head against the wall. Special shout out to Ryan who has been endlessly helpful when I've been stuck on something, or even just giving your time to listen to me and offer advice. That's meant a lot to me and I'm very grateful. Thank you to Josey, who started this journey at the same time as me and helped me make sure that I knew what I was talking about. I really admire how hard you work and your perseverance. Thank you to Ravi for our many physics conversations in the office and bringing up interesting questions I hadn't considered, and just for being a fun person to talk to. I'm excited to see where you go in your physics career. Shout out to the undergraduate students I've had the pleasure to spend time with: Daniel, Dev, Connie, Emilio. You guys will do amazing in everything that you do. Thank you also Lanny for your insight in our group meetings, and for getting us out of the office and in to happy hour at Posse. Thank you to Peter, for your extensive physics knowledge, your driest of humor, and for laughing at my jokes. I want to thank my parents, Norma Saucedo Bingaman and Gary Bingaman. Mom, thank you for always supporting me, listening to me, and for encouraging me to believe in myself. I couldn't have made it here without you, and this accomplishment of mine is your accomplishment as well. Dad, thank you for your support and for teaching me how to read. Thank you to my friends that I've met on this journey, and I would like to especially acknowledge my late friend Melanie "Rabbit" Boyle. Thank you for cheering me on. I'd like to acknowledge my high school teachers: Vinay Dulip, Kimberly Jackson, and Cheryl Flint. Mr. Dulip, I never would have dreamed big without your mentorship. Mr. Jackson, I fell in love

with physics because of you. I wouldn't be here without the two of you. Ms. Flint, thank you for teaching me about the power of my words. I have done my best to make the content of my dissertation grammatically correct. Finally, I'd like to thank my partner Adam. Adam, you've given so much to me, and meeting you changed the trajectory of my life. Without your love and support, I wouldn't have made it here. I love you and I look forward to spending the rest of my life with you.

Abstract

Heavy-Flavor Jet Fragmentation and Jet-Medium Interactions in Pb–Pb Collisions

by

Amanda Flores, Ph.D.

The University of Texas at Austin, 2025

SUPERVISOR: Deepa Thomas

The quark-gluon plasma (QGP) is an exotic state of matter generated in ultra-relativistic heavy-ion collisions. Properties of the QGP can be determined by the use of well-defined hard probes, such as heavy-flavor particles. Heavy-flavor (charm and beauty) quarks are generated through hard scattering early in the collision and experience the full lifetime of the QGP. In the hard-scattering process, the leading-order (LO) mechanism produces heavy-quark jets back-to-back in azimuth, which undergo fragmentation into constituent particles. The fragmentation of the heavy-flavor jet can be studied differentially in phase space by utilizing azimuthal correlation measurements between a heavy-flavor trigger particle and associated charged particles. The azimuthal correlation provides a measurement of the angular distribution and number of particles correlated with the trigger. The influence of the QGP medium on the fragmentation of the heavy-quark-initiated jet and potentially the influence of the jet on the medium can be studied by performing this measurement in heavy-ion collisions. In this thesis, the azimuthal correlation of electrons from the decays of heavy-flavor hadrons with associated charged particles in Pb–Pb collisions at $\sqrt{s_{\text{NN}}} = 5.02$ TeV is presented. This is the first jet-like correlation measurement in the heavy-flavor sector studied in heavy-ion collisions by the ALICE experiment. This measurement

is performed in the central and semicentral centrality classes of Pb–Pb collisions to determine how the size and temperature of the medium affect the fragmentation. The per-trigger nuclear modification factor (I_{AA}) is calculated to compare the correlation peak yields to those in pp collisions at $\sqrt{s} = 5.02$ TeV. The per-trigger nuclear modification factor for electron triggers from heavy-flavor hadron decays is compared with that for light-flavor and strange-particle triggers to investigate the dependence on different fragmentation processes and parton-medium dynamics.

Contents

List of Tables	12
List of Figures	14
Chapter One: Introduction	24
1.1 The Standard Model: A description of almost everything	25
1.2 Quantum Chromodynamics	27
1.3 Heavy-ion collisions: “Little” bangs	31
1.4 Hard probes of the QGP	38
1.5 Theoretical models and event generators	43
1.6 Experimental signatures of the QGP	51
1.7 Measuring heavy-flavor jet-fragmentation in heavy-ion collisions	63
Chapter Two: Experimental Apparatus	66
2.1 The LHC	66
2.2 The ALICE Detector	67
2.3 Data Acquisition and Processing	76
Chapter Three: Analysis Procedure	78
3.1 Analysis Overview	78
3.2 Dataset	80
3.3 Particle Tracking	82
3.4 Electron Identification	84

3.5 Mixed-event Correction	89
3.6 Non-HFe Background Subtraction	91
3.7 Associated particle corrections	99
3.8 Correlation Background Subtraction	100
Chapter Four: Systematic Uncertainties	115
4.1 Systematic Sources	116
4.2 Systematic Uncertainty Estimation	117
4.3 Systematic studies	119
4.4 Final Systematic Tables	144
Chapter Five: Measurement Results	154
5.1 Electron from HF hadron decay correlations in pp and p-Pb	154
5.2 $\Delta\varphi$ Correlation Distributions in Pb-Pb	159
5.3 $\Delta\varphi$ Correlation Distributions in Pb-Pb and pp	162
5.4 Per-Trigger Associated Width	164
5.5 Per-Trigger Associated Yield	166
5.6 Per-Trigger Nuclear Modification Factor (I_{AA})	168
5.7 Correlation $p_T^{\text{trig.e}}$ -dependence	172
5.8 I_{AA} Comparison to Light-Flavor	181
5.9 Comparison to Z-boson-triggered measurements	186
Chapter Six: Conclusion and Outlook	189
6.1 Analysis summary and conclusion	189

6.2 Future outlook	193
Bibliography	195

List of Tables

3.1	Track cuts used for electron candidate tracks.	84
3.2	Track selection cuts for associated particles.	84
3.3	Electron identification cuts	86
3.4	Additional track selection cuts used for associated electrons.	93
3.5	Values for v_2 used in baseline function in 0–10% centrality.	104
3.6	Values for v_2 used in baseline function in 30–50% centrality.	104
3.7	Values for v_3 used in baseline function in 0–10% centrality.	105
3.8	Values for v_3 used in baseline function in 30–50% centrality.	105
4.1	Electron tracking systematic uncertainties	120
4.2	Electron identification systematic uncertainties	123
4.3	Background electron systematic uncertainties	124
4.4	Associated particle tracking systematic uncertainties	127
4.5	$\Delta\varphi$ Systematic Relative Error for $4 < p_T^{\text{trig.e}} < 12$ in 0 - 10%	145
4.6	Near Side Yield Systematic Relative Error for $4 < p_T^{\text{trig.e}} < 12$ in 0 - 10%	145
4.7	Away Side Yield Systematic Relative Error for $4 < p_T^{\text{trig.e}} < 12$ in 0 - 10%	145
4.8	$\Delta\varphi$ Systematic Relative Error for $4 < p_T^{\text{trig.e}} < 12$ in 30 - 50%	146
4.9	Near Side Yield Systematic Relative Error for $4 < p_T^{\text{trig.e}} < 12$ in 30 - 50%	147
4.10	Away Side Yield Systematic Relative Error for $4 < p_T^{\text{trig.e}} < 12$ in 30 - 50%	147
4.11	$\Delta\varphi$ Systematic Relative Error for $4 < p_T^{\text{trig.e}} < 7$ in 0 - 10%	147
4.12	Near-Side Yield Systematic Relative Error for $4 < p_T^{\text{trig.e}} < 7$ in 0 - 10%	148
4.13	Away-Side Yield Systematic Relative Error for $4 < p_T^{\text{trig.e}} < 7$ in 0 - 10%	149
4.14	$\Delta\varphi$ Systematic Relative Error for $4 < p_T^{\text{trig.e}} < 7$ in 30 - 50%	149

4.15	Near-Side Yield Systematic Relative Error for $4 < p_T^{trig.e} < 7$ in 30 - 50%	149
4.16	Away-Side Yield Systematic Relative Error for $4 < p_T^{trig.e} < 7$ in 30 - 50%	150
4.17	$\Delta\varphi$ Systematic Relative Error for $7 < p_T^{trig.e} < 16$ in 0 - 10%	151
4.18	Near-Side Yield Systematic Relative Error for $7 < p_T^{trig.e} < 16$ in 0 - 10%	151
4.19	Away-Side Yield Systematic Relative Error for $7 < p_T^{trig.e} < 16$ in 0 - 10%	151
4.20	$\Delta\varphi$ Systematic Relative Error for $7 < p_T^{trig.e} < 16$ in 30 - 50%	152
4.21	Near-Side Yield Systematic Relative Error for $7 < p_T^{trig.e} < 16$ in 30 - 50%	153
4.22	Away-Side Yield Systematic Relative Error for $7 < p_T^{trig.e} < 16$ in 30 - 50%	153
5.1	σ values used for the yield integration. Associated yields are obtained by integrating $\pm 3\sigma$ from the mean peak values of 0 (near-side) and π (away-side)	166

List of Figures

1.1	Fundamental particles of the Standard model. Image from Symmetry magazine [6], a joint Fermilab/SLAC publication. Artwork by Sandbox Studio, Chicago.	26
1.2	Measurements of the QCD running coupling α_s performed by SLAC, DESY, CERN’s Large Electron–Positron (LEP) collider and Fermilab’s Tevatron experiments [11], [12].	28
1.3	Phase diagram of QCD matter in the plane of temperature vs baryon chemical potential [22].	30
1.4	Evolution of a heavy-ion collision at LHC energies [15].	33
1.5	Geometry of the hadronic collision.	35
1.6	Pseudorapidity (η) values at different θ angles. A larger absolute value of η is a more “forward” measurement.	36
1.7	The nuclear overlap of the colliding ions determines the average number of nucleon participants [46].	37
1.8	Cartoon showing the stages of jet fragmentation, where a shower of partons originate from the initiating parton which undergo hadronization. Image sourced from ericmetodiev.com [63].	40
1.9	The I_{AA} of a photon-triggered charged jet in Au–Au collisions at $\sqrt{s_{NN}} = 200$ GeV measured by STAR compared to the JETSCAPE prediction [96], [97].	47
1.10	Dihadron correlation distribution for pp collisions at $\sqrt{s_{NN}} = 200$ generated by AMPT [102].	49
1.11	Measurements of the strangeness enhancement factor for (multi-)strange particles in Cu–Cu and Au–Au collisions at $\sqrt{s_{NN}} = 200$ measured by STAR [114].	52
1.12	Measurements of v_2 and v_3 flow coefficients of inclusive D mesons [115], inclusive J/ψ [116], π^\pm , and protons [117] at $\sqrt{s_{NN}} = 5.02$ TeV measured by ALICE.	53

1.13	R_{AA} measurements of J/ψ in different centrality percentiles at $\sqrt{s_{NN}} = 5.02$ TeV measured by ALICE [120].	55
1.14	R_{AA} measurements of $\Upsilon(1S)$ and the bottomonium resonances at $\sqrt{s_{NN}} = 5.02$ TeV measured by CMS [121]. The measurement shows a hierarchy of suppression dependent on the quarkonium binding energy.	55
1.15	CMS measurement of the R_{AA} of different species [126]–[130] at $\sqrt{s_{NN}} = 5.02$ TeV for the full spectrum of Pb–Pb centrality classes.	57
1.16	Comparison of prompt vs non-prompt D^0 R_{AA} measured by ALICE [131].	58
1.17	Ratio of non-prompt [131] and prompt [76] D^0 R_{AA} at $\sqrt{s_{NN}} = 5.02$ TeV measured by ALICE compared to theoretical models.	59
1.18	(Left) 2D ($\Delta\varphi\Delta\eta$) azimuthal correlation distribution of charged particles in p–Pb collisions measured by ALICE at $\sqrt{s_{NN}} = 5.02$ TeV [133], [134]. (Right) 1D ($\Delta\varphi$) hadron-triggered correlation distribution in pp and Pb–Pb at $\sqrt{s_{NN}} = 5.02$ TeV measured by ALICE shown together [70]. In the right figure, there is a noticeable difference in the near- and away-side peaks between the two collision systems.	61
1.19	The π^0 correlation distribution in Pb–Pb collisions $\sqrt{s_{NN}} = 5.02$ TeV in the 0–10% central collisions measured by ALICE [71]. The depletion of the away-side peak observed in $4 < p_T^{\text{assoc.}} < 6$ GeV/ c is evidence of jet-quenching.	62
1.20	The near- (left) and away-side (right) π^0 I_{AA} at $\sqrt{s_{NN}} = 2.76$ TeV measured by ALICE [71] compared to the AMPT and JEWEL model predictions.	63
2.1	ALICE Detector during the Run 2 (2015 - 2018) data collection period. .	67
2.2	Layout of Inner Tracking System during Run 2 [144].	70
2.3	Impact parameter resolution performance of the ITS in the x-y plane as a function of p_T for pp, p-Pb, and Pb–Pb collisions provided publicly by ALICE [145].	70
2.4	3D Schematic of the TPC field cage provided by ALICE [147].	72
2.5	TPC performance plot for Pb–Pb collisions in 0–10% centrality class at $\sqrt{s_{NN}} = 5.02$ TeV provided by ALICE, illustrating the tracks for charged particle species.	72

2.6	Schematic of the electromagnetic calorimeter, which shows the components approximately opposite in azimuth provided by ALICE [151]. . . .	73
2.7	Schematic of the EMCal full-size super modules, which shows the strip structure composed of 24 strips, provided by ALICE [151].	74
2.8	Distribution of the sum of amplitudes from the VZERO arrays (black) in Pb–Pb collisions at $\sqrt{s_{NN}} = 2.76$, where the red line is the Glauber model fit, provided by ALICE [152].	75
3.1	σ_e^{TPC} distribution as a function of p_T for 0–10% collisions (left) and for 30–50% collisions (right) measured for this thesis. The electron TPC cut is shown with a black dotted line.	85
3.2	E/p distribution of electron candidates with $4 < p_T^e < 12$ GeV/ c , in the 0–10% centrality class. The black points are the distribution before hadron contamination subtraction. The red-point distribution is the E/p of particles selected with $-10 < \sigma_e^{\text{TPC}} < -4$ scaled to match the black distribution. Blue is after the contamination subtraction.	87
3.3	Correlation distributions for inclusive electrons before (black) and after (blue) subtraction of hadron contamination (red) for events in the 0–10% centrality class.	88
3.4	Two-dimensional $(\Delta\eta, \Delta\varphi)$ correlation distribution of electron candidates with charged particles, for $4 < p_T^e < 12$ GeV/ c in the most-central events. The triangular shape of the distribution in $\Delta\eta$ is due to the limited rapidity coverage of the detector. The distribution is also affected by detector inefficiencies and inhomogeneities.	89
3.5	Mixed event $(\Delta\eta, \Delta\varphi)$ distribution between inclusive electrons and charged particles normalized by β (yield from $(\Delta\eta, \Delta\varphi) = (0, 0)$) for $4 < p_T^e < 12$ GeV/ c and in different associated charged particle p_T intervals for 0–10% centrality class events.	90
3.6	Mixed-event-corrected 2D correlation distribution between inclusive electrons and charged particles for $4 < p_T^e < 12$ GeV/ c and in different associated charged particle p_T ranges for 0–10% centrality class events. . . .	91
3.7	Invariant mass distribution for the like-sign (red) and unlike-sign (blue) electron pairs for $4 < p_T^e < 12$ GeV/ c for 0–10% (left) and 30–50% (right) centrality collisions. The difference between the like-sign and unlike-sign distribution is more noticeable in the 0–10% centrality.	94

3.8	Invariant mass distribution for the like-sign (red) (after scaling) and unlike-sign (blue) electron pairs for $4 < p_T^e < 12$ GeV/ c for 0–10% and 30–50% collisions.	95
3.9	Spectra of π^0 and η from HIJING compared to the spectra of the artificially embedded spectra generated by PYTHIA.	96
3.10	Ratio of HIJING to PYTHIA spectra of π^0 and η fit with the Hagedorn function.	97
3.11	Monte Carlo p_T spectra of electrons from π^0 and η . (Left) shows the spectra of electrons when no weight is applied to the parent particles. (Right) shows the spectra of electrons after the weight is applied. Open circles for both figures represent electrons which pass the reconstruction procedure, and closed circles are all electrons identified as photonic. . . .	97
3.12	Tagging efficiency distribution for the photonic electron reconstruction for 0–10% events.	98
3.13	Tracking efficiency distribution for associated charged particles in the 0–10% centrality class.	99
3.14	Physical primary fraction distribution of charged particles in the 0–10% centrality class.	100
3.15	The p_T distribution of charged particle v_2 (left) and v_3 (right) shown for the 0–10% centrality percentile.	102
3.16	The p_T distribution of charged particle v_2 (left) and v_3 (right) shown for the 30–50% centrality percentiles. Notice the larger magnitude of v_2 for this centrality.	103
3.17	The flow coefficients v_2 (left) and the v_3 (right), calculated for the three trigger p_T^e ranges studied in this analysis using a statistically-weighted average in the 0–10% centrality class.	103
3.18	The flow coefficients v_2 (left) and the v_3 (right), calculated for the three trigger p_T^e ranges studied in this analysis using a statistically-weighted average in the 30–50% centrality class.	104
3.19	Gaussian distributions with different mean (μ) and standard deviation (σ) values [171].	107
3.20	Generalized Gaussian distribution with different β values.	108

3.21	von Mises distribution with different κ values.	110
3.22	Correlation distribution in the lowest $p_T^{\text{assoc.}}$ interval for the most-central collisions. The solid red line is only the near-side peak fitted with a von Mises PDF, and the dotted line is the corresponding baseline. The blue solid line is the characterization function using the von Mises PDF for both peaks. The blue dotted line represents the resulting baseline from the fit, which is unphysical.	112
3.23	Correlation distribution in the 0–10% centrality class. The left figure shows the distribution fitted with $B(\Delta\varphi)$ before subtraction. The right shows the distribution after $B(\Delta\varphi)$ subtraction.	114
4.1	$\Delta\varphi$ Correlation distribution of inclusive electrons with charged particles in the $p_T^{\text{assoc.}}$ interval of 2 - 3 GeV/c. The average of three values of the distribution around $-\frac{\pi}{2}$, $\frac{\pi}{2}$, and $\frac{3\pi}{2}$ are used to obtain the flat pedestal b , which is subtracted from the distribution. This is performed for the distributions the default and variation cuts before the systematic estimation.	118
4.2	Electron tracking systematic uncertainty estimation on the $\Delta\varphi$ correlation distribution, measured in the 0–10% centrality class (top) and the 30–50% centrality class (bottom).	121
4.3	Electron tracking systematic uncertainty estimation on the per-trigger yields, measured in the 0–10% centrality class (left) and the 30–50% centrality class (right).	121
4.4	Photonic electron systematic uncertainty estimation on the $\Delta\varphi$ correlation distribution, measured in the 0–10% centrality class (top) and 30–50% centrality class (bottom).	125
4.5	Photonic electron systematic uncertainty estimation on the near-side per-trigger yields, measured in the 0–10% centrality class (left) and 30–50% centrality class (right).	126
4.6	Six b parameter variations in the $4 < p_T^e < 12$ GeV/c trigger interval for the most-central collision events.	132
4.7	Six b parameter variations in the $4 < p_T^e < 12$ GeV/c trigger interval for the semicentral collision events.	133
4.8	$\Delta\varphi$ correlation distributions after subtracting the highest and lowest baseline in all $p_T^{\text{assoc.}}$ intervals. Shown for the most-central collision events. . .	134

4.9	$\Delta\varphi$ correlation distributions after subtracting the highest and lowest baseline in all $p_T^{\text{assoc.}}$ intervals. Shown for semicentral collision events	135
4.10	Ratios of the per-trigger yields of the b parameter variations to the nominal yields in the 0–10% centrality class.	136
4.11	Ratios of the per-trigger yields of the b parameter variations to the nominal yields in the 30–50% centrality class.	136
4.12	16 separate baseline variations made from the v_n variations in the $4 < p_T^e < 12$ GeV/ c trigger interval for the most-central collision events. . . .	139
4.13	16 separate baseline variations made from the v_n variations in the $4 < p_T^e < 12$ GeV/ c trigger interval for the semicentral collision events.	140
4.14	Ratios of the per-trigger yields of the baseline variations to the nominal yields in the 0–10% centrality class.	141
4.15	Ratios of the per-trigger yields of the baseline variations to the nominal yields in the 30–50% centrality class.	141
4.16	List of the 16 v_n variations and the 6 b parameter variations for the systematic baseline study.	142
4.17	Baseline uncertainty represented with a red band along $\Delta\varphi$, taken from the b variations. Shown is the correlation distribution for 0–10% centrality collisions in the $1 < p_T^{\text{assoc.}} < 2$ GeV/ c interval.	143
4.18	Baseline uncertainty represented with an open box, taken from the b variations. Shown is the correlation distribution for 0–10% centrality collisions.	144
5.1	Azimuthal-correlation distribution of heavy-flavor hadron decay electrons and charged particles measured pp (black) and p–Pb collisions (red) at $\sqrt{s_{\text{NN}}} = 5.02$ TeV by ALICE [135]. The distributions are shown in the trigger range of $4 < p_T^e < 12$ GeV/ c and three $p_T^{\text{assoc.}}$ intervals.	155
5.2	Per-trigger associated yields and peak widths measured from heavy-flavor hadron decay electron correlations in pp and p–Pb collisions at $\sqrt{s_{\text{NN}}} = 5.02$ TeV by ALICE [135]. The distributions are shown in the trigger range of $4 < p_T^e < 12$ GeV/ c and all $p_T^{\text{assoc.}}$ intervals.	156
5.3	Per-trigger associated yields and peak widths in pp compared to PYTHIA8 Monash and EPOS3 in $4 < p_T^e < 12$ GeV/ c and all $p_T^{\text{assoc.}}$ intervals at $\sqrt{s_{\text{NN}}} = 5.02$ TeV measured by ALICE [135].	157

5.4	Azimuthal-correlation distribution of heavy-flavor hadron decay electrons and charged particles measured in 0–10% central Pb–Pb collisions before background subtraction publicly available by ALICE [180]. The distributions are shown in the trigger range of $4 < p_T^e < 12$ GeV/ c and all p_T^{assoc} intervals. The near-side peak and transverse range of the $\Delta\varphi$ distribution is fit with a von Mises function (solid gray line), and the resulting baseline is shown with a solid black line. The statistical (uncorrelated systematic) uncertainties are shown as vertical lines (filled boxes). The uncertainties on the baseline are shown with the dotted lines.	159
5.5	Azimuthal-correlation distribution of heavy-flavor hadron decay electrons and charged particles measured in 30–50% central Pb–Pb collisions before background subtraction publicly available by ALICE [180]. The distributions are shown in the trigger range of $4 < p_T^e < 12$ GeV/ c and all p_T^{assoc} intervals. The near-side peak and transverse range of the $\Delta\varphi$ distribution is fit with a von Mises function (solid gray line), and the resulting baseline is shown with a solid black line. The statistical (uncorrelated systematic) uncertainties are shown as vertical lines (filled boxes). The uncertainties on the baseline are shown with the dotted lines.	160
5.6	Comparison of the azimuthal-correlation distribution of heavy flavor hadron decay electrons with charged particles measured in 0–10% central Pb–Pb collisions and in pp collisions publicly available by ALICE [180]. Uncorrelated background has been subtracted (both), as well as flow contribution (Pb–Pb), for $4 < p_T^e < 12$ GeV/ c and different associated p_T ranges. The statistical (uncorrelated systematic) uncertainties are shown as vertical lines (filled boxes). The uncertainties on the baseline estimation are shown as solid boxes at $\Delta\varphi \sim -2$ and 5 rad.	162
5.7	Comparison of the azimuthal-correlation distribution of heavy flavor hadron decay electrons with charged particles measured in 30–50% central Pb–Pb collisions and in pp collisions publicly available by ALICE [180]. Uncorrelated background has been subtracted (both), as well as flow contribution (Pb–Pb), for $4 < p_T^e < 12$ GeV/ c and different associated p_T ranges. The statistical (uncorrelated systematic) uncertainties are shown as vertical lines (filled boxes). The uncertainties on the baseline estimation are shown as solid boxes at $\Delta\varphi \sim -2$ and 5 rad.	163
5.8	Near-side widths from Pb–Pb collisions in the central and semicentral centrality classes compared to pp, for $4 < p_T^e < 12$ GeV/ c and all p_T^{assoc} intervals measured for this thesis. The systematic uncertainty was not determined for the Pb–Pb width, so the largest uncertainty on the width in p–Pb collisions was used (11%).	165

5.9	Per-trigger associated yields of the near- (left) and away-side (right) peaks for $4 < p_T^e < 12$ GeV/ c as a function of $p_T^{\text{assoc.}}$ in 0–10% and 30–50% central Pb–Pb collisions compared to those obtained from pp collisions publicly available by ALICE [180]. The statistical (systematic) uncertainties are shown as vertical lines (empty boxes). In some $p_T^{\text{assoc.}}$ intervals, the away-side yield is consistent with zero within one standard deviation of statistical and systematic uncertainties added in quadrature. For those intervals, upper limits on the yields for 68% (95%) confidence levels are evaluated, and are shown with arrows (boxes).	168
5.10	Per-trigger nuclear modification factor (I_{AA}) of near- (left) and away-side (right) associated yields, for $4 < p_T^e < 12$ GeV/ c as a function of $p_T^{\text{assoc.}}$ in 0–10% and 30–50% central Pb–Pb collisions publicly available by ALICE [180]. The statistical (systematic) uncertainties are shown as vertical lines (empty boxes). In some $p_T^{\text{assoc.}}$ intervals the away-side yield is consistent with zero within one standard deviation of total uncertainty. For those intervals, upper limits on the I_{AA} for 68% (95%) confidence levels are shown with arrows (boxes).	169
5.11	(Left) 3σ integration region of the $\Delta\varphi$ correlation. (Right) 2σ integration region of the $\Delta\varphi$ correlation.	171
5.12	Per-trigger nuclear modification factor (I_{AA}) of the near-side peak for $4 < p_T^e < 12$ GeV/ c as a function of $p_T^{\text{assoc.}}$. (Left) the near-side I_{AA} obtained from integrating within 3σ , publicly available by ALICE [180]. (Right) is the near-side I_{AA} obtained from integrating in 2σ measured for this thesis.	171
5.13	Per-trigger nuclear modification factor (I_{AA}) of the away-side peak for $4 < p_T^e < 12$ GeV/ c as a function of $p_T^{\text{assoc.}}$. The left is the near-side I_{AA} obtained from integrating within 3σ . The right is the near-side I_{AA} obtained from integrating in 2σ . The confidence intervals are not plotted in the left plot for ease of comparison.	172
5.14	Azimuthal-correlation distribution of heavy-flavor hadron decay electrons and charged particles measured in 0–10% central Pb–Pb collisions . The distributions are shown in the trigger range of $4 < p_T^e < 7$ GeV/ c and all $p_T^{\text{assoc.}}$ intervals.	174
5.15	Azimuthal-correlation distribution of heavy-flavor hadron decay electrons and charged particles measured in 0–10% central Pb–Pb collisions . The distributions are shown in the trigger range of $7 < p_T^e < 16$ GeV/ c and all $p_T^{\text{assoc.}}$ intervals.	175

5.16	Per-trigger associated near-side peak width in $4 < p_T^e < 7$ GeV/ c (red) and $7 < p_T^e < 16$ GeV/ c (blue) measured for this thesis.	176
5.17	Per-trigger associated yields and widths in pp collisions for $4 < p_T^e < 7$ GeV/ c and $7 < p_T^e < 16$ GeV/ c measured by ALICE compared to PYTHIA8 Monash and EPOS3 predictions [135].	177
5.18	Per-trigger associated yields and widths in pp collisions for $4 < p_T^e < 7$ GeV/ c and $7 < p_T^e < 16$ GeV/ c generated with PYTHIA8 Monash [135]. Associated peak widths are dependent on both the flavor of the electron's parent hadron and the trigger p_T	178
5.19	Per-trigger near- (left) and away-side (right) associated peak yields for $4 < p_T^{\text{trig.e}} < 7$ GeV/ c and $7 < p_T^{\text{trig.e}} < 16$ GeV/ c as a function of $p_T^{\text{assoc.}}$ in 0–10% central Pb–Pb collisions, compared to measurements in pp collisions publicly available by ALICE [180]. The statistical (systematic) uncertainties are shown as vertical lines (boxes). In some $p_T^{\text{assoc.}}$ intervals the away-side yield is consistent with zero within one standard deviation of total uncertainties. For those intervals, upper limits on the yields for 68% (95%) confidence levels are shown with arrows (boxes).	179
5.20	I_{AA} of the near- (left) and away-side (right) associated peak yields for $4 < p_T^{\text{trig.e}} < 7$ GeV/ c and $7 < p_T^{\text{trig.e}} < 16$ GeV/ c as a function of $p_T^{\text{assoc.}}$ in 0–10% central Pb–Pb collisions publicly available by ALICE [180]. The statistical (systematic) uncertainties are shown as vertical lines (boxes). In some $p_T^{\text{assoc.}}$ intervals the away-side yield is consistent with zero within one standard deviation of total uncertainty. For those intervals, upper limits on the I_{AA} for 68% (95%) confidence levels are shown with arrows (boxes).	180
5.21	I_{AA} of near- (top) and away-side (bottom) associated peak yield from correlation distribution of electron from heavy-flavor hadron decays as the trigger particle ($7 < p_T^e < 16$ GeV/ c) measured for this thesis compared with that of charged hadrons and K_s^0 as trigger particles ($8 < p_T^{\text{trig}} < 16$ GeV/ c) measured by ALICE [70]. The electron I_{AA} is calculated using the 2σ method.	182
5.22	Figure showing all I_{AA} measurements by ALICE [70]–[72].	184
5.23	Light-flavor I_{AA} measurements compared to AMPT and HIJING models [70].	185
5.24	Z-boson-triggered away-side I_{AA} in 0–10% Pb–Pb collisions in three different p_T^Z intervals measured by ATLAS [191].	186

5.25 Z-boson-triggered correlation distribution in Pb–Pb collisions measured by CMS [192]. (Top) The correlation measurement in pp is compared to Pb–Pb. (Bottom) The correlation measurement is compared to theoretical models.	187
--	-----

Chapter One: Introduction

The universe consists of matter and the forces by which this matter interacts. At the fundamental level, there are only four forces¹ which affect the behavior of matter. It is from these forces that all macroscopic behavior arises. These fundamental forces are: The electromagnetic, the gravitational, the weak, and the strong.

The effect of electromagnetic and gravitational forces are evident in everyday life. The pull between two cosmic bodies such as the Earth-moon system or the push between the north poles of two magnets are examples these forces at work. They also manifest in subtle and complicated ways, such as the rippling distortion of space-time in the form of gravitational waves from black hole mergers or coronal loops on the sun's surface generated from the magnetic fields of a solar dynamo. What may not be immediately evident are the effects of the strong and weak interactions.

The weak interaction is responsible for radioactive decay. This interaction occurs at length scales smaller than the size of a proton. Generally speaking, the weak-force interaction facilitates the transformation of one kind of matter spontaneously into another.

Protons and neutrons are not fundamental particles. They are both composed of even smaller constituents called quarks. These quarks are bound together by the strong interaction to form these composite particles. The residual strong force binds protons and neutrons into atomic nuclei, which overcomes the repulsive electromagnetic force between the protons.

Particle physics is the branch of physics which focuses on fundamental particles and forces. Two objectives of this field are to tie the building blocks of matter and the fundamental forces into a complete framework and to understand the interplay of these two. The analysis described in this text serves to contribute to the study of the strong force. However, to fully understand this contribution requires a primer involving the theoretical and experimental background of the physics involved this analysis.

¹Known as of November 2025.

1.1 The Standard Model: A description of almost everything

The confluence of theoretical breakthroughs in particle physics such as Dirac’s development of quantum electrodynamics (QED); the electroweak interaction developed by Weinberg, Glashow, and Salam; along with experimental discoveries of new particles led to a collective push to develop a unified model of all matter and forces.

The Standard Model of particle-physics is a theoretical framework which describes the fundamental forces and constituents of matter, with the exception of gravity. Developed in the mid-1970’s, the Standard Model is a quantum field theory which incorporates the $SU(3) \times SU(2) \times SU(1)$ gauge symmetries from the strong and electroweak interactions.

Fundamental particles are divided into two main groups: fermions, the matter particles; and gauge bosons, the force-carriers. Fermions consist of two families, the quarks and leptons. Both families contain three generations of fermions, with two particles in each generation. In terms of increasing mass, the quarks consist of the down, up, strange, charm, bottom (beauty), and the top. The up and down exist in the energy scales we are familiar with, and these form the composite particles protons and neutrons. The leptons include the electron, the muon, and tau particles, and each have their own corresponding neutrino. The bosons consist of: the photon, which mediates the electromagnetic interaction; the W^\pm and Z bosons, which are responsible for the weak force; and the gluon, which governs the strong force.

The Standard Model relies on several parameters which must be determined experimentally, with some examples being the gauge and Yukawa coupling constants, and the CKM matrix angles. These parameters in conjunction with the fundamental particles form the framework. In order for the framework to be complete, the Standard Model requires the existence of an additional boson dubbed the Higgs Boson, which bestows the fundamental particles with mass through the Higgs mechanism [1]–[3]. This particle was identified in 2012 by both the ATLAS [4] and CMS [5] experiments.

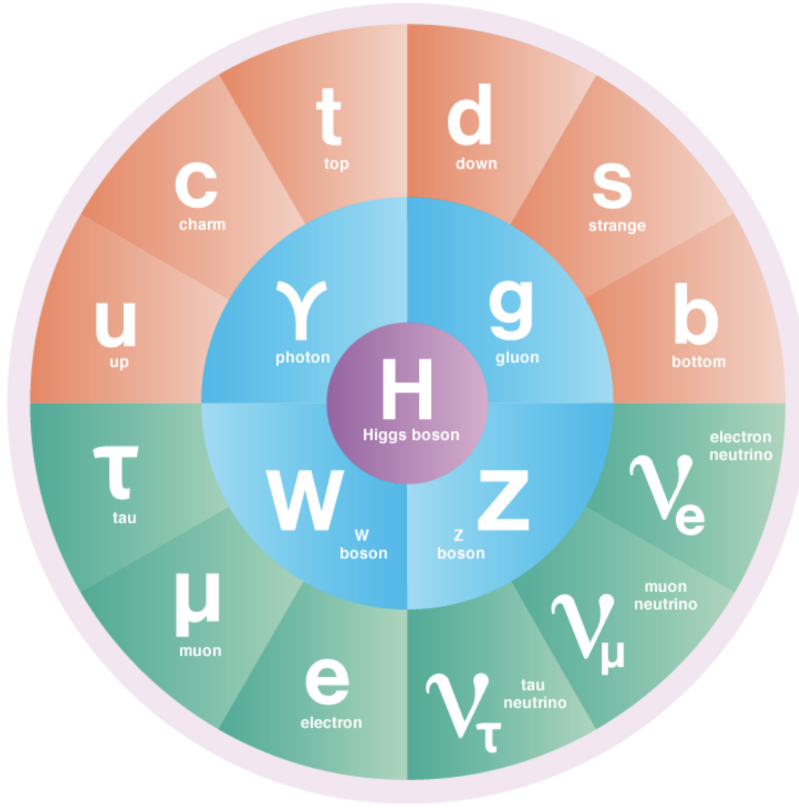


Figure 1.1: Fundamental particles of the Standard model. Image from Symmetry magazine [6], a joint Fermilab/SLAC publication. Artwork by Sandbox Studio, Chicago.

The Standard Model has withstood several high-precision tests such as the measurement of the muon anomalous magnetic moment [7] and the branching fraction measurement of the $B_s \rightarrow \mu^+ \mu^-$ decay [8]. However, the Standard Model fails to incorporate the equivalent building blocks for gravity. Additionally, the current iteration of the Standard Model fails to sufficiently describe observed phenomena such as the origin of neutrino mass, dark matter, or the extent of the matter-anti-matter asymmetry in the early universe [9]. These issues make this paradigm incomplete in its description of the universe. Therefore, the discovery a more comprehensive framework is an ongoing pursuit in particle physics.

1.2 Quantum Chromodynamics

Quantum chromodynamics (QCD) is the theoretical scheme of the Standard Model which describes the strong interaction between quarks and gluons (partons). While quarks have intrinsic properties such as spin, mass, and electric charge, similarly to leptons, they have an additional property inherent to QCD which is the color charge. In QCD, quarks can have one of three color charges, (dubbed red, blue, green). Anti-quarks can have one of three corresponding anti-color charges (anti-red, anti-blue, anti-green). A single color charge, therefore a single quark, cannot exist in isolation. This fact results in a defining characteristic of QCD called confinement, where quarks must form composite or bound states of color-neutral particles, called hadrons. A neutral-color state can be obtained via a quark and anti-quark pair, which is a meson; or a three-quark combination creates a color-neutral bound state called a baryon. There are other possible composite quark states, but for the purposes of this thesis, mesons and baryons will be primarily discussed.

QCD is based on the principle of local SU(3) gauge theory, meaning that the QCD Lagrangian is invariant under a continuous group of local SU(3) transformations. The QCD Lagrangian density (in its condensed form) is given in Eq. 1.1,

$$\mathcal{L}_{\text{QCD}} = \bar{\Psi}(i\gamma_{\mu}\mathcal{D}^{\mu} - m)\Psi - \frac{1}{4}F_{a,\mu\nu}F_a^{\mu\nu}. \quad (1.1)$$

The field strength tensor $F_a^{\mu\nu}$ is defined as,

$$F_a^{\mu\nu} = \partial^{\mu}A_a^{\nu} - \partial^{\nu}A_a^{\mu} - g_s f_{abc}A_b^{\mu}A_c^{\nu}. \quad (1.2)$$

Where in the $g_s f_{abc}A_b^{\mu}A_c^{\nu}$ component of the tensor, A_a^{μ} is the gluon vector field, g_s is the strong coupling constant, f_{abc} are the SU(3) structure constants, and a is the index of the eight gluon color labels. This non-Abelian component of the field strength tensor results in significant differences between QCD and QED: Gluons, unlike photons, can undergo self-interaction and they carry (color) charge. There are eight generators for the SU(3) group, which results in eight different “multicolored” states carried by the gluon. Since the gluon carries color, a quark can change color through gluon interactions; for example a gluon can carry a unit of “blueness” from the quark and replace that with a unit of “redness”. Due to these gluon color states, gluons experience confinement and cannot be isolated. However, they can participate

in the strong interaction independent of quarks, resulting in three- and four-gluon vertices and potentially form their own bound states dubbed “glueballs” [10].

1.2.1 Asymptotic freedom

The coupling constant g_s , or often written in the form $\alpha_s = \frac{g_s^2}{4\pi}$, is the only free parameter in the Lagrangian. Despite being referred to as a constant, α_s runs with the momentum transfer Q^2 . In contrast to the QED coupling, the strong coupling $\alpha_s(Q)$ decreases as the scale of the momentum transfer Q^2 increases or distances between colored partons decrease (see Fig. 1.2). At length scales starting around $\sim 10^{-15}$ m (1 fm), the strong force is ~ 137 times stronger than the electromagnetic interaction.

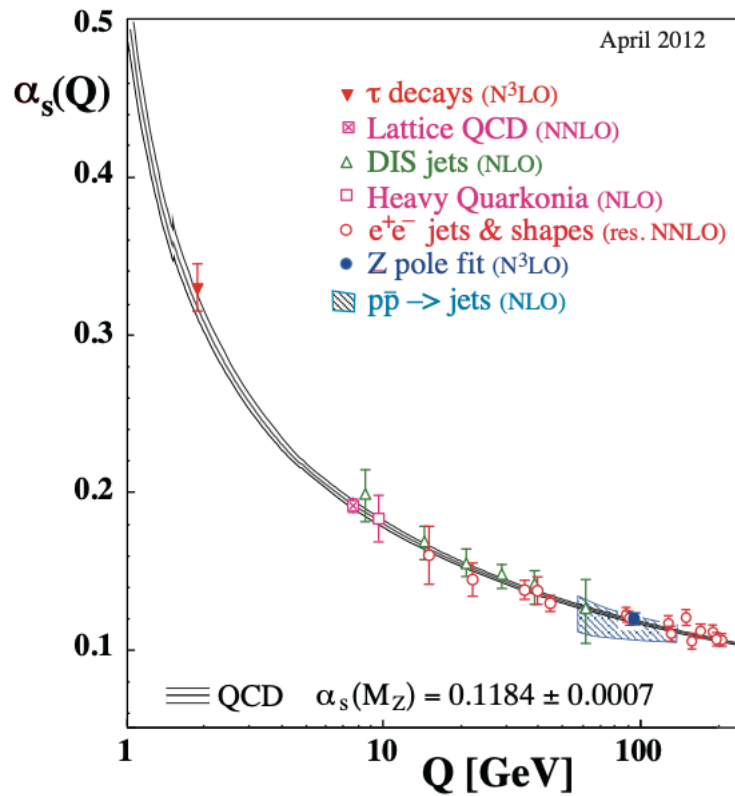


Figure 1.2: Measurements of the QCD running coupling α_s performed by SLAC, DESY, CERN’s Large Electron–Positron (LEP) collider and Fermilab’s Tevatron experiments [11], [12].

However, at shorter length scales or larger momentum transfer, the strength of the coupling becomes asymptotically weaker. As a result, partons behave as quasi-free particles. This is a fundamental characteristic of QCD known as asymptotic freedom. Due to this property, strong-force interactions can be calculated perturbatively to high accuracy with experimental measurements.

Asymptotic freedom was discovered in 1973 by David Gross and Frank Wilczek [13], and discovered independently by David Politzer [14] the same year, where all three physicists were awarded the Nobel Prize for this theoretical discovery in 2004.

1.2.2 Quark-gluon plasma

Given the distance-dependence of asymptotic freedom on parton interaction strength, a natural question occurs: If sufficiently squeezed together, could nucleons merge into a state of matter where partons move freely, similarly to a gas? Calculations from lattice QCD predict that at a temperature around $T \sim 155$ MeV or 10^{12} K (T_{pc} , or transition temperature) [15], [16] and energy density $\approx 1\text{GeV}/\text{fm}^3$ [15], [17], [18], hadronic matter transitions into a phase called a quark-gluon plasma (QGP). Analogous to an electromagnetic plasma, in a QGP phase quarks and gluons do not exist in bound states but are instead deconfined in a collective medium of quasi-free color-charged particles. The early universe is theorized to have existed in a state of quark-gluon plasma around 10 microseconds after the Big Bang [19]. QGP is also theorized to exist in the early stage of a supernova [20].

In relativistic heavy-ion collision experiments, the extreme temperature and energy density generated by two colliding atomic nuclei generates an ephemeral QGP droplet, which expands as a fireball before condensing into hadronic matter. The QGP can be characterized by its thermodynamic properties, such as the temperature and chemical potentials resulting from the conservation of quantum numbers (such as flavor or baryon number) under the strong interaction [21].

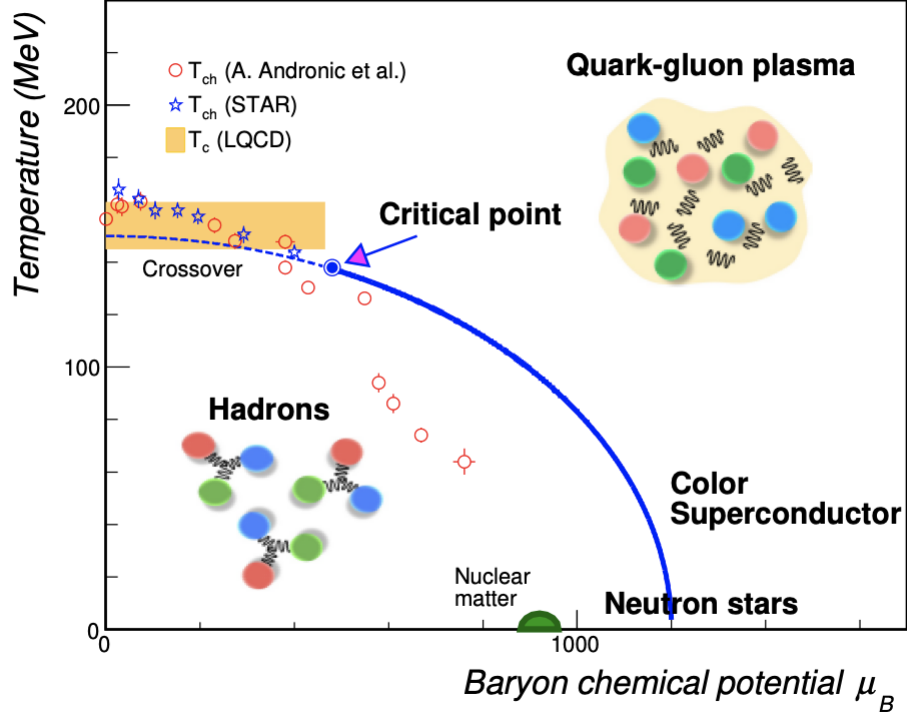


Figure 1.3: Phase diagram of QCD matter in the plane of temperature vs baryon chemical potential [22].

The development of the QGP equation of state is an ongoing subject within the field of heavy-ion physics. The phase diagram of hadronic matter in terms of baryon chemical potential, μ_B (a measure of baryon density), and temperature is given in Fig. 1.3. At approximately zero baryon chemical potential and above the critical temperature, the deconfinement transition is expected to be a smooth cross-over rather than first-order transition. It is in this high-temperature and low- μ_B region that the LHC and RHIC explore in the laboratory. At non-zero μ_B , QCD-inspired and lQCD models indicate that the hadron gas to QGP transition undergoes a first-order phase transition, which is likely to have occurred in the early universe [23]. The determination of the terminal point of the phase boundary, or critical point, is still an active area of research [24], as the phase transition depends on multiple factors, such as the number of quark flavors, the value of the pseudo-scalar meson mass, and the quark masses [17].

Early STAR experiments at RHIC indicate that the QGP is a strongly-coupled

medium [25] that rapidly undergoes thermalization [21], [26]. The medium appears to behave as a near-perfect fluid [27]. Theoretical predictions using the AdS/CFT correspondence have posited that the lowest physical limit of the shear viscosity over entropy density ratio η/s is $\frac{1}{4\pi}$ [28]. Collective flow measurements measured at both RHIC and the LHC indicate that the QGP is close to this theoretical limit [29]. The QGP offers the opportunity to study close-to-ideal hydrodynamics, which is applicable to other fields. The strongly coupled system shares a similar value of η/s with ultra-cold fermi gases [30], [31], and so offers an experimental comparison to this phase of matter in a vastly separate energy regime.

Exploring the QGP in a laboratory setting provides an environment to study an emergent phenomenon arising from QCD. Beyond the phase diagram predictions of lQCD, the QGP degrees of freedom are not completely understood at different energy scales [21]. Through studying the QGP, it is possible to learn about the QCD equation of state in a high temperature regime, which is essential for determining the QCD critical point. Studying this phase of matter also provides insight into the parton confinement process of hadron formation, or hadronization. This is a non-perturbative process which is not understood via first-principles. Also of interest in the study of the QGP is the generation mechanism of hadron mass due to the strong interaction via Chiral Symmetry Restoration [21]. The QGP generated in heavy-ion collisions offers the opportunity to study the conditions of the early universe. A realistic QGP equation of state has been used in cosmological calculations [19], as the equation of state influences the time evolution of the universe [32]. The early universe time evolution affects the spectrum of gravitational waves [23], [33] and these signatures may be experimentally measurable through laser interferometry experiments [34].

1.3 Heavy-ion collisions: “Little” bangs

The physics of the Standard Model and potentially beyond are explored in proton-proton (pp) collision experiments. The phenomena produced in proton-proton collisions occurs in a vacuum, and the measurements of this collision system are directly comparable to several models, so proton-proton collisions serve as a baseline comparison to heavy-ion (A-A) collision measurements. These comparisons facilitate the identification of final state effects due to the presence of the QGP in A-A collisions

[35]. Proton-ion collisions (p-A) serve as an intermediary between the pp and A-A collision systems. “Cold nuclear matter” (CNM) effects in the initial state of this collision system result in changes to the final state of the collision with respect to pp. These CNM effects include gluon saturation, possible color-glass condensate, and differences between the nuclear parton distribution functions (PDF) [35], and must be considered when interpreting A-A collision observables. The parton distribution function gives the probability to find partons within a hadron (or nucleus) as a function of the x (or Bjorken- x) parameter. Where x is the fraction of a hadron’s momentum carried by a constituent parton [36]. The PDF of the heavy nucleus is expected to differ with respect to the proton PDF [15]. At $x < 10^{-2}$, the nuclear PDF shows a suppression with respect to the proton PDF, which is nuclear shadowing [15].

Proton-proton and p-A collisions are not expected to generate the energy densities necessary to form a QGP [37]. However, some high-multiplicity pp [38] and p-A measurements [39] show evidence of collective flow behavior and strangeness enhancement [40], [41] along with possible jet suppression observed in high transverse momentum pion measurements in deuteron–Au collisions performed by the PHENIX experiment [42]. These findings suggest a possible “tiny” QGP created in these collision systems, but research is ongoing to confirm this theory or to determine an alternate explanation.

The heavy ions used in collision experiments are atomic nuclei which are fully stripped of their electrons and collided at ultra-relativistic velocities at 99.995% the speed of light. These experiments are performed at the Large Hadron Collider (LHC) at CERN, and the Relativistic Heavy Ion Collider (RHIC) at Brookhaven National Lab. Some ion species collided at RHIC include but are not limited to copper, gold, and uranium; while oxygen, xenon, and lead ions have been collided at the LHC.

1.3.1 Heavy-ion collision stages

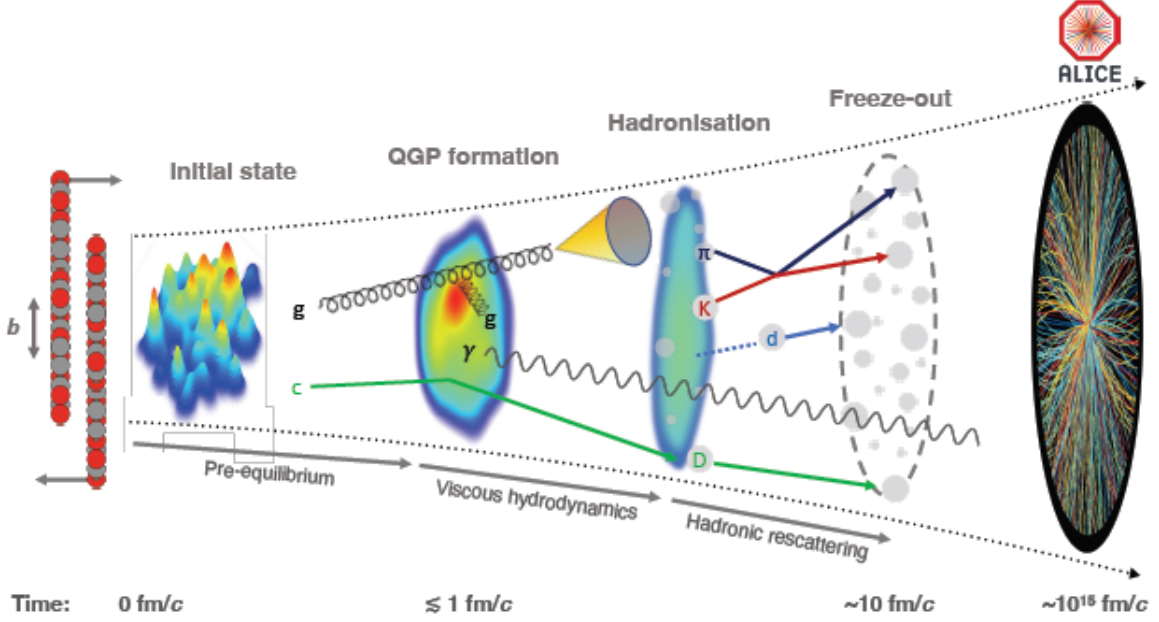


Figure 1.4: Evolution of a heavy-ion collision at LHC energies [15].

Heavy-ion collision events are characterized by multiple stages (shown in Fig. 1.4). When boosted to ultra-relativistic speeds, the ions undergo Lorentz contraction and flatten into disc-like extended objects. The diameters are about 14 fm for Pb and Au nuclei, and are only a few fractions of fm thick [43]. “Hard” particles are created in the initial collision, such as heavy-flavor quarks or jet-initiating partons, which have either a large mass or large transverse momentum ($m_{\text{HF}} \gg \Lambda_{\text{QCD}}$, $p_{\text{T}} \gg 1 \text{ GeV}/c$). Large momentum transfers, also referred to as hard scattering processes, are required to create these hard particles, being on the order of $Q^2 \sim p_{\text{T}}^2 \gg 1$. Due to the large Q^2 in these hard scattering processes, the generation of these particles can be calculated perturbatively. The hard particle production occurs on a time scale of $\tau_{\text{form}} \simeq 1/\sqrt{Q^2}$, such that for a 2 GeV particle $\tau_{\text{form}} \simeq 0.1 \text{ fm}/c$ [37], which occurs before the formation of a QGP. Due to the hard particles’ short wavelength, they can be used as probes of the QGP at short length-scales, which will be discussed in more detail in section 1.4.

When the contracted ions collide, the incident partons undergo predominantly “soft” interactions, meaning that there is little momentum transfer. The vast majority of these are small- x gluons in the nuclei [44] that undergo low- Q^2 interactions. These gluons predominantly determine the overall energy density and entropy deposition in the initial state [15] and form a weakly-coupled pre-equilibrium stage. Softer partons are created in this process and undergo further soft-scattering until reaching the energy density and temperature to form a strongly-coupled QGP [15] that is expected to undergo rapid thermalization. The transition to the QGP phase occurs within a time frame of $0.3 - 1.5$ fm/ c after the initial collision [45].

The QGP undergoes hydrodynamic expansion, which is influenced by the non-uniformity of the energy distribution of the initial state. The greater pressure at the center of the QGP compared to the outskirts produces a common velocity field outwards. This results in pressure gradients within the QGP, leading to a collective flow of the bulk. The greater pressure at the inside of the QGP results in isotropic, or radial flow of the expansion. Spatial anisotropies in the initial state such as parton fluctuations in the nucleons and the almond shape of the collision zone create a spatial anisotropy which converts to a pressure gradient that results in anisotropic flow [15]. Because the colliding nuclei have an electric charge, the beams generate a large magnetic field that influences the motion of the quarks in the medium [15].

As the QGP undergoes expansion, at around $7 - 10$ fm/ c after the initial collision, the medium cools below T_{pc} such that partons undergo confinement to form hadronic matter. This process results in a hadron gas, which is still a collective system but with different degrees of freedom from the QGP [15]. The hadronization process involves small momentum transfers, and thus cannot be described perturbatively. The hadrons can still interact via inelastic processes, and the chemical composition of the hadron gas continues to evolve. These interactions continue until reaching the chemical freeze-out temperature. At this stage, the distribution of hadron species stabilizes, with the exception of any remaining resonances. Elastic interactions continue to occur, resulting in the modification of the hadron momentum. This continues until the kinetic freeze-out, which is approximately $\gtrsim 10$ fm/ c after the initial collision [15]. At this stage, changes in particle momenta cease and these hadrons in their final state and leptons propagate toward the detector.

1.3.2 Collision kinematics

The experimental observables described in this thesis utilize multiple geometric and kinematic parameters. Fig. 1.5 shows a diagram of the collision geometry which is relevant for pp, p-A, and A-A collisions. The beam pipe for the colliding hadrons is assigned to the z -axis. The x - and y -axes define the transverse plane. Following cylindrical coordinates, the angle which sweeps from the x -axis in the transverse plane is the azimuthal angle φ , and the angle from the z -axis is the polar angle θ .

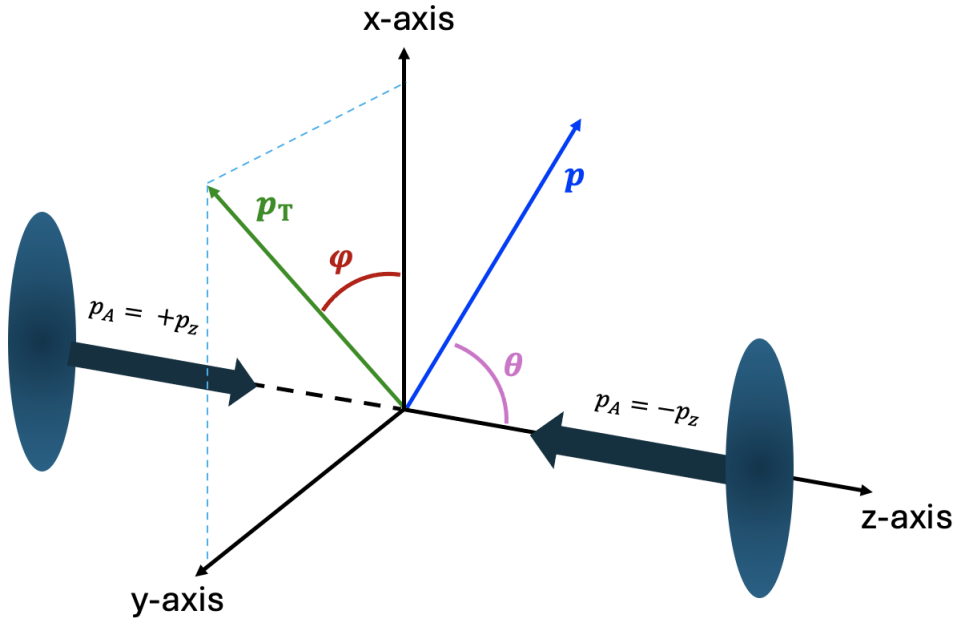


Figure 1.5: Geometry of the hadronic collision.

Many of the observables described in this text are differential in transverse momentum, or p_T . The p_T is defined as,

$$p_T = \sqrt{p_x^2 + p_y^2}. \quad (1.3)$$

The colliding hadrons undergo a Lorentz boost in the z -direction, which alters the measurement of the momentum in the laboratory frame, while the x - and y -components of the momentum are invariant between the center of mass and lab frame. Outgoing particles produced through inelastic scattering in the collision will have a

non-zero transverse momentum. This makes detection of final state particles possible, as detectors are placed around the beam pipe. Additionally, there is lower tracking resolution in the z -direction of the momentum. Therefore, p_T is more practical to use for experimental observables instead of the full momentum. A particle's azimuthal angle is determined through measurements of the momentum,

$$\varphi = \tan^{-1}\left(\frac{p_y}{p_x}\right). \quad (1.4)$$

In collider physics, rapidity (y) is the relativistic angle which parametrizes a Lorentz boost along the beam axis. The rapidity is calculated as,

$$y = \frac{1}{2} \ln\left(\frac{E + p_z c}{E - p_z c}\right). \quad (1.5)$$

The value of the rapidity gives a measure of the angle of the particle produced in the collision with respect to the beam axis. Because of the difficulty of measuring both the energy and p_z of a particle with high precision, the pseudorapidity (η) is often used experimentally. The pseudorapidity is defined as,

$$\eta = -\ln\left(\tan\frac{\theta}{2}\right). \quad (1.6)$$

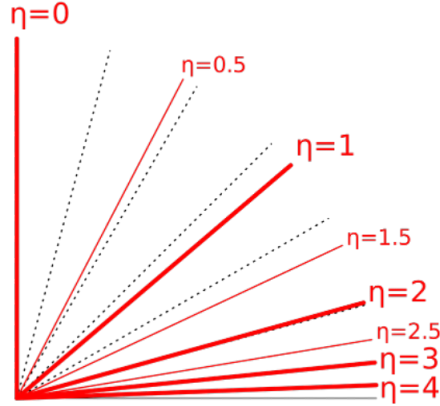


Figure 1.6: Pseudorapidity (η) values at different θ angles. A larger absolute value of η is a more “forward” measurement.

Where for particles with $m_{\text{particle}} \ll E$, $\eta \approx y$. A pseudorapidity (Fig. 1.6) value of 0 indicates that the particle is produced at 90° from the z -axis, or that

the momentum is entirely transverse. Pseudorapidities with absolute values < 1 are referred to as mid-rapidity, and the values exceeding 1 are referred to as “forward”.

1.3.3 Centrality

When accelerated to relativistic speeds, the ions undergo Lorentz-contraction, which results in the nuclei flattening into discs relative to the laboratory frame. Because the ions are extended objects, the nuclear overlap can vary, such that collisions can be more glancing or head-on. The centrality quantifies the nuclear overlap of the collision. The impact parameter (b), or the distance between the centers of the two colliding nuclei (Fig. 1.7), provides a measure of the centrality.

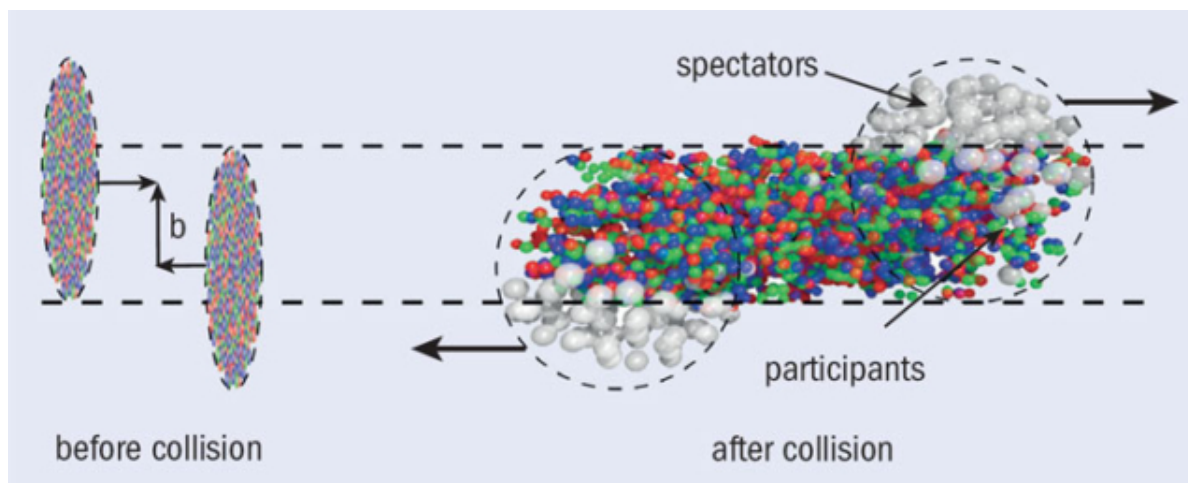


Figure 1.7: The nuclear overlap of the colliding ions determines the average number of nucleon participants [46].

The impact parameter corresponds to the number of participating nucleons (N_{part}), or the number of binary collisions among nucleons from the two nuclei (N_{coll}) [47]. Nucleons which do not participate in the interaction are referred to as the spectators (N_{spec}). Experimentally, ALICE determines the centrality by measuring the particle multiplicity in a collision event [48]. Because b , N_{part} , or N_{coll} are not directly measurable, centrality identification is performed using multiplicity measurements by VZERO detector. The multiplicity generates a specific amplitude in the detector. This amplitude is fitted to the amplitude predicted by the Glauber model, which maps the measured multiplicity to a given centrality. The Glauber model is a geo-

metric theoretical technique which treats the nuclear collision as a superposition of binary nucleon-nucleon interactions, which is used to estimate b , N_{part} , and N_{coll} from experimental data [49].

Centrality is classified into percentages to indicate the degree of overlap. The larger the percentile corresponds to a more peripheral collision. The most-central collisions are within the 0–10% centrality percentile. These collisions have the largest nuclear overlap and generate the highest energy densities and largest QGP volumes. The 30–50% centrality percentiles are classified as semi-central, which are characterized by an almond-shaped nuclear overlap and produce a smaller QGP volume than the most-central collisions.

1.4 Hard probes of the QGP

Although large length-scale behavior such as the QGP hydrodynamic properties are accessible through measurements of soft particles, the microscopic properties require a different type of method to discern. As mentioned in section 1.3.1, the production of “hard” particles with large mass $m \gg \Lambda_{\text{QCD}}$ or large transverse momentum $p_T \gg 1 \text{ GeV}/c$ are produced prior to the formation of the QGP, and lend themselves to perturbative calculations. Particles produced through hard scattering, or “hard probes”, can traverse the medium and work as probes to obtain information about the medium inaccessible to soft bulk measurements.

Hard probes can resolve shorter length scales in the QGP compared to soft particles. The accessibility of these short-length scale interactions can uncover information of the QGP and its substructure [21]. A still-unanswered question in this field is how exactly a strongly-coupled QGP emerges from asymptotic freedom. This could be answered by tracing the evolution of a QCD-colored probe in the medium over time. Information from the QGP substructure can be determined from how a hard probe scatters in the medium. Hard probes can also uncover the transport properties of the QGP, such as the values of the diffusion transport coefficients.

As a consequence of the QGP’s hydrodynamic properties, when a hard parton or jet exceeding the speed of sound in the medium propagates through the QGP, it potentially excites the medium, creating sonic booms which form structures such as a mach cone or diffusion wake [28], [50]. These sonic booms and “wake” structures

are predicted by some theoretical models, but the existence of this phenomena is still subject to debate. Sonic booms in the QGP would produce high-angle emissions of partons and a mach-cone structure [50]. This hard parton or jet potentially deposits energy into the medium and moves the medium in the mach cone scenario, and experimentally this would enhance particle production in the same direction as the parton [51]. Following the mach cone is the diffusion wake, which would experimentally be measured as a depletion of particles opposite the hard parton [52], [53]. Measurements of the wake effect can provide further information of the hydrodynamic and transport behavior, such as the speed of sound in the medium [54]. However, measuring evidence of this behavior is plagued with several difficulties: the radial flow of the hydrodynamically expanding medium can distort the Mach cone structure [52], [55]. Additionally, because a jet consists of many partons in the showering phase, these partons could induce a broad medium excitation, therefore producing no discernible structure. Also, the medium undergoes event-by-event fluctuations, which poses another difficulty in trying to identify a medium response signal on top of this fluctuating background [52].

Because hard probe production in pp collisions can be reliably calculated by pQCD, any modifications to the probe properties in an A-A collision indicate some modification through interactions with the QGP. The two relevant hard probes in this analysis are jets and heavy-flavor hadrons. In the next two sections, the theoretical and experimental description of these probes will be discussed.

1.4.1 Jets

In the context of QCD, a jet is a collimated spray of particles initiated from the fragmentation of a virtual parton generated in a hard scattering process [56]. These high-energy high-virtuality partons decay through radiated gluons at varying emission angles. These gluons split into more gluons, which continues into a cascading emission of more gluons and quark-anti-quark pairs, resulting in a cone of showering partons. This parton shower hadronizes at inter-parton distances of around 1 fm [57], resulting in a spray of hadrons. This process is jet fragmentation. Because the confinement process or hadronization is a soft interaction, hadronization has little effect on the total energy and momentum of the jets [57].

Predictions from pQCD indicate that the parton showering has an angular or-

dering, such that the leading parton generates soft gluons preferably at wide angles [58], whereas the hadrons are formed in relatively narrow angles with respect to the hadronizing parton. Overall, the angular orientation of the produced particles with respect to the leading particle is primarily determined by the showering phase of the fragmentation [59].

The type of parton which initiates the jet affects the overall jet profile. For instance, gluon jets are typically broader, undergo softer fragmentation, and have larger particle multiplicities compared to quark-initiated jets [60]. Due to their larger color factor, gluons lose more energy than quarks in the QGP [60], [61]. For both quark and gluon jets, the particle multiplicity increases as a function of jet p_T , although this increase is faster for gluon jets [60]. A quark which generates a jet preferentially ends up in the leading particle [62]. Therefore, assuming the leading particle can be used as an approximation for the leading parton, the particles correlated in $\Delta\varphi$ and $\Delta\eta$ to the leading hadron are primarily originating from the fragmentation of the leading parton [59].

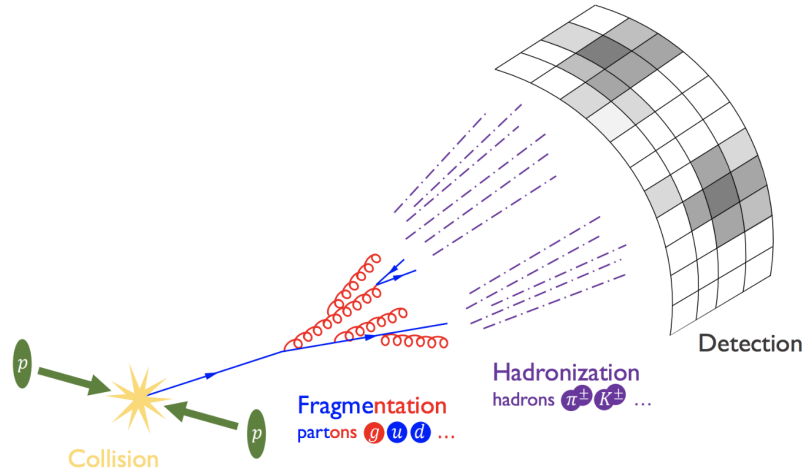


Figure 1.8: Cartoon showing the stages of jet fragmentation, where a shower of partons originate from the initiating parton which undergo hadronization. Image sourced from ericmetodiev.com [63].

Hadron production can be quantified with the parton fragmentation function (FF). The fragmentation function, $D_q^h(z)$, describes the probability for a quark q to emit a hadron h with a certain fraction z of the of the mother quark's momentum

[64]. The FF is essential for hadron production calculations with the factorization theorem. Modifications of the FF in heavy-ion collisions indicate an alteration of the jet fragmentation with respect to the vacuum.

There are two primary approaches to measure jet properties: Full jet reconstruction, and azimuthal correlation measurements (which is detailed in section 1.6.0.5). Full jet reconstruction resolves the distribution of the constituents of the jet, or the jet substructure. Jets are reconstructed using a jet-finding algorithm which clusters the fragmentation products into a jet. The most common jet-finding algorithm is the anti- k_T method [65]. The anti- k_T algorithm selects hard particles and a neighboring particle separated in Δ_{ij} , where $\Delta_{ij}^2 = (y_i - y_j)^2 + (\varphi_i - \varphi_j)^2$, and $y_{i,j}$ and $\varphi_{i,j}$ are the rapidity and azimuthal angle of particles i and j . In the algorithm, soft particles preferentially cluster with hard particles, where hard particles are used to define a jet axis. If jets contain only soft particles, the jet is reconstructed as an ideal cone. If another hard particle is present such that $R < \Delta_{12} < 2R$, where R is the jet resolution parameter ($R = \sqrt{\Delta y^2 + \Delta \varphi^2}$, with respect to the jet axis), there will be two jets defined. The difference in transverse momentum of clustered particles overall determines the number of jets and the final reconstruction, which can result in simple cones or more complex structures of overlapping cones [66]. Other reconstruction approaches include the k_T , SISCone, and Cambridge/Aachen algorithms. With these reclustering techniques, one can access different regions of the QCD phase space, such as the partonic or hadronic regime such as through jet-energy correlator measurements [67].

The influence of the QGP on jets can be quantified by the differences measured in reconstructed jets or azimuthal correlations in heavy-ion vs pp collisions. Previous measurements at the LHC and the Relativistic Heavy Ion Collider indicate that energy from the parton shower is transferred to the QGP, thereby modifying the overall fragmentation of the jet and attenuating the jet itself [65], [68]. This phenomenon is known as “jet quenching” and is a characteristic signature of the QGP formation. The high-multiplicity environment in heavy-ion collisions introduces significant background to the jet reconstruction due to the fluctuations in the underlying event, which affects the jet transverse momentum. This poses a challenge to jet reconstruction in these collision systems. However, jet quenching has been observed in a variety of measurements such as azimuthal correlations [69]–[72] and full jet reconstruction [68], [73]. Different jet quenching observations will be discussed in section 1.6.0.4.

1.4.2 Heavy flavor quarks

The heavy flavor (HF) sector of the quarks consists of the charm, beauty (bottom), and top quark. Heavy flavor quarks and subsequently their hadrons are useful QGP probes, due to their large mass in comparison to the QCD scale parameter Λ_{QCD} [74] and the medium temperature [21]. Because of this property, these quarks are primarily produced in hard scattering processes prior to QGP formation, therefore the production of heavy quarks is well-described by perturbative QCD calculations. In fact, the top quark mass is so enormous ($\sim 172m_{\text{proton}}$), that it decays rapidly into a W boson and usually a beauty quark prior to the QGP formation. Therefore, “heavy flavor” discussed in this thesis will refer to charm and beauty quarks. The beauty and charm quark lifetimes exceed that of the QGP such that they experience the full lifetime of the medium. Because heavy quark masses far exceed the pseudo-critical temperature of the QCD phase transition ($m_{c,b} \gg T_{pc}$), they “retain their identity” within the QGP and throughout hadronization [74]. These properties enable the heavy flavor sector to work as a well-defined probe of the QGP.

As heavy quarks propagate throughout the QGP, they experience energy loss. The type of energy loss is dependent on the momentum of the quark. Most heavy quarks produced have a relatively low momentum [21], and at these scales ($\lesssim 3 - 4$ GeV/ c) they diffuse through the medium and experience drag forces through elastic scattering. Charm quarks are determined to have an equilibration time τ less to the QGP lifetime [75], and thus acquire some collective behavior of the system such as anisotropic flow. However, the thermalization time for beauty quarks is expected to be longer than both the charm thermalization and the QGP lifetime, and therefore are not expected to equilibrate with the QGP. Combined measurements of heavy-flavor hadron anisotropic flow and the nuclear modification factor have constrained the value of the heavy quark spatial diffusion coefficient D_s , which is a transport property of the QGP [76].

At higher momenta ($\gtrsim 8 - 10$ GeV/ c), heavy quarks experience both collisional energy loss and radiative energy loss in the form of gluon radiation. In the parton showering phase of quark fragmentation, gluons emitted from the quark are suppressed within an angle $\theta < m_Q/E$. This angular suppression of gluon emission which is dependent on the quark mass is referred to as the “dead-cone” effect [77]. If the dead-cone effect persists in QGP-induced gluon radiation, the radiative energy loss

should follow a mass hierarchy, such that $\Delta E_b < \Delta E_c < \Delta E_l$. The dead-cone effect would result in the heavy quarks experiencing less radiative energy loss than light flavor and would ultimately alter the charged particle fragmentation spectra in HF jets compared to LF jets [78]. Additionally, heavy quarks could undergo hadronization within the QGP, which would also alter the quark fragmentation [79].

Heavy-flavor quark interactions with the QGP can be studied by measurements of heavy-flavor hadrons. Heavy-flavor hadrons such as D and B mesons are reconstructed through selections on their decay topologies, such as through their decay vertex reconstruction in conjunction with the invariant mass reconstruction of their decay daughters. Commonly studied charm hadrons include the D^0 and D^\pm mesons as well as the resonances D^* and D^{**} . The branching ratio of D^0 mesons into a $K^-\pi^+$ pair is 3.9% [11], which provides a statistically significant channel to perform an invariant mass reconstruction.

Heavy flavor hadrons can also be studied through the semi-leptonic decay channel. This channel produces a lepton along with the corresponding neutrino and a sister hadron. These decays have relatively large branching ratios, which averages about 10% for charm and beauty hadrons [11]. However, the neutrino carries a significant amount of energy from the decay and cannot be identified through conventional detectors, and so prohibits invariant mass reconstruction through this channel. However, electrons from heavy-flavor hadron decays can be identified experimentally, which allows for the study of heavy-flavor in a heavy-ion environment through measurements of these leptons.

1.5 Theoretical models and event generators

Several proton-proton collision observables have been successfully described by hadronic collision event generators, such as those based on multiple parton sub-collisions which incorporate string or cluster hadronization [80]. These models are effective at describing observables dependent on both hard and soft interactions.

In order to infer the physics mechanisms that occur within heavy-ion collisions, experimental data must be compared to theoretical models. Heavy-ion collisions are dynamic and complex systems with several confirmed and unconfirmed mechanisms that must be considered. The model must have a framework for the initial state

perhaps with or without gluon saturation, and the multi-parton interactions in the collision. Models ideally must have some description of the thermodynamic evolution of the medium. This could include a model of a non-thermalized but high-matter density environment which still describes the signatures of QGP hydrodynamics. The soft hadronization mechanisms need to be incorporated, which is typically done by including a hadronization model, for example the Lund string fragmentation [81] or cluster hadronization [82] models.

Most heavy-ion-specific models fit into three general categories: Those which include hydrodynamic evolution (EPOS, JETSCAPE), those which are transport models (PHSD), and those which are a hybrid of both (AMPT). In this section, an overview of theoretical and phenomenological models, and additionally hadronic collision event generators will be discussed. These models are discussed because they are commonly-used event generators or heavy-flavor transport models in the field of study focused on understanding the QGP, and several of these will be compared to studies discussed later in this text.

1.5.1 Lund string model

The Lund string fragmentation model [81] was developed at the University of Lund to describe quark fragmentation and hadronization. When quark and anti-quark pairs are separated, the potential between them is characterized as a narrow color field that increases in tension as the distance between them increases. The inter-quark potential is described in Eq. 1.7 as,

$$V(r) \approx \kappa r - \frac{4\alpha_s}{3r}. \quad (1.7)$$

This color field, or flux tube, acts as a string with tension of κ . The flux tube stretches until the energy required to separate the quarks “snaps” the string and produces two new quark-anti-quark pairs. This happens repeatedly, with the assumption that all fragmentation processes occur independently of each other. This results in an iterative cascade of hadrons until the final state hadrons are produced.

This phenomenological model is incorporated into hadron collision event generators, most notably PYTHIA [83], HIJING [84], and EPOS [85] with great success in describing experimental data.

1.5.2 PYTHIA

PYTHIA [83] is a widely used code library used to generate and simulate the physics processes of high-energy particle collisions, such as e^- , e^+ , p , and \bar{p} . It incorporates theory and phenomenological models for multiple physics aspects, such as the cross sections, hard and soft interactions, PDFs, hadronization/fragmentation, decays and many other aspects, with some parameters informed from data. The probability of the simulated event parameters, such as phase space variables, quantum numbers, and final-state particles are numerically determined by Markov Chain Monte Carlo techniques [86].

PYTHIA structurally consists of main parts: The process level, parton level, and hadron level. The process level includes the initial hard-scattering, and includes resonance production. The parton level involves initial- and final-state radiation, where it uses models for parton showers and multiparton interactions. This level evolves to include jets and the underlying event. The hadron level uses the Lund string fragmentation model for hadronization.

Physics models in PYTHIA operate with particular run-time parameters which determine the model’s behavior. A set of parameters which are chosen based on the comparisons of PYTHIA to the data is referred to as a “tune”. There is no single tune which inherently describes every physics process and observable with complete accuracy, but the goal of tuning is the find an “optimal” set of physics parameters which minimize the difference between simulated and experimental data [86].

The Angantyr model (which is accessible as a PYTHIA tuning), is used to simulate high energy p-A and A-A collisions. Angantyr extrapolates from pp interactions while minimizing free parameters and accounts for fluctuations and diffraction in the nucleons [87]. This model reproduces general hadron distributions to high accuracy, but it does not incorporate a simulated QGP medium or flow-like behavior observed in heavy-ion collisions.

PYTHIA has accurately recreated several proton-proton physics observables, such as particle spectra, azimuthal correlation distributions, and jet observables.

1.5.3 HIJING

The Heavy-Ion Jet INteraction generator, or HIJING [84], [88], is a Monte Carlo event generator which simulates heavy-ion collisions. HIJING is based on a pQCD-

inspired model, which incorporates minijet production (which are jets with low to moderate transverse momentum [89]) with a Lund-type model for soft interactions. A binary approximation and Glauber geometry for multiple interactions is used to simulate p-A and A-A collisions [88]. Other nuclear effects are taken into account: Parton shadowing is modeled using a parameterized parton distribution function in the nucleus. HIJING also incorporates the Cronin effect [90] and multiple parton interactions. PYTHIA is first used to generate the kinematic variables for the hard scattering process, such as jet production. This includes additional shadowing and transverse momentum exchange. The soft beam jets are modeled with diquark-quark strings with gluon kinks following the Lund FRITOF and dual parton model [91]. HIJING does not incorporate QGP hydrodynamics, although the latest version HIJING++ implements jet quenching through the Gyulassy-Lévai-Vitev [92] formalism.

1.5.4 EPOS

EPOS, which stands for Energy conserving quantum mechanical approach, based on Partons, parton ladders, strings, Off-shell remnants, and Splitting of parton ladders [85], is a heavy-ion simulation event generator. The initial collision incorporates multi-parton interactions which occur in parallel [85]. Partons undergo sub-collisions calculated via Gribov-Regge theory, and uses pomerons or “parton ladders” (modeled as Lund strings) to model elementary scatterings. EPOS separates a hadronic collision into two components: There is a high-density “core” and a low-density “corona”. Within the core, gluons form a cluster which undergoes hydrodynamic expansion until the freeze-out stage. Therefore the core acts as the “medium” within the simulation. The hadronization in the freeze-out undergoes Cooper-Frye microcanonical scheme, which is explained in detail in Ref. [93]. In the corona, the gluons fragment into hadrons [80] via through Lund string fragmentation.

EPOS-LHC is the version of EPOS developed to simulate events at LHC energies. While this version incorporates hydrodynamic expansion, this is a parameterized expansion, in contrast to EPOS 2 and 3, which develop the full hydrodynamic evolution. This update drastically decreases the runtime for a Pb–Pb collision (from 1 hour to tens of seconds), at the expense of some predictive power [94].

1.5.5 JETSCAPE

JETSCAPE, short for the Jet Energy-loss Tomography with a Statistically and Computationally Advanced Program Envelope [95], is a modular software framework used to develop event generators for simulating pp and A-A collisions [96]. The software features flexible separate modules which a user can access to simulate separate portions of a heavy-ion collisions.

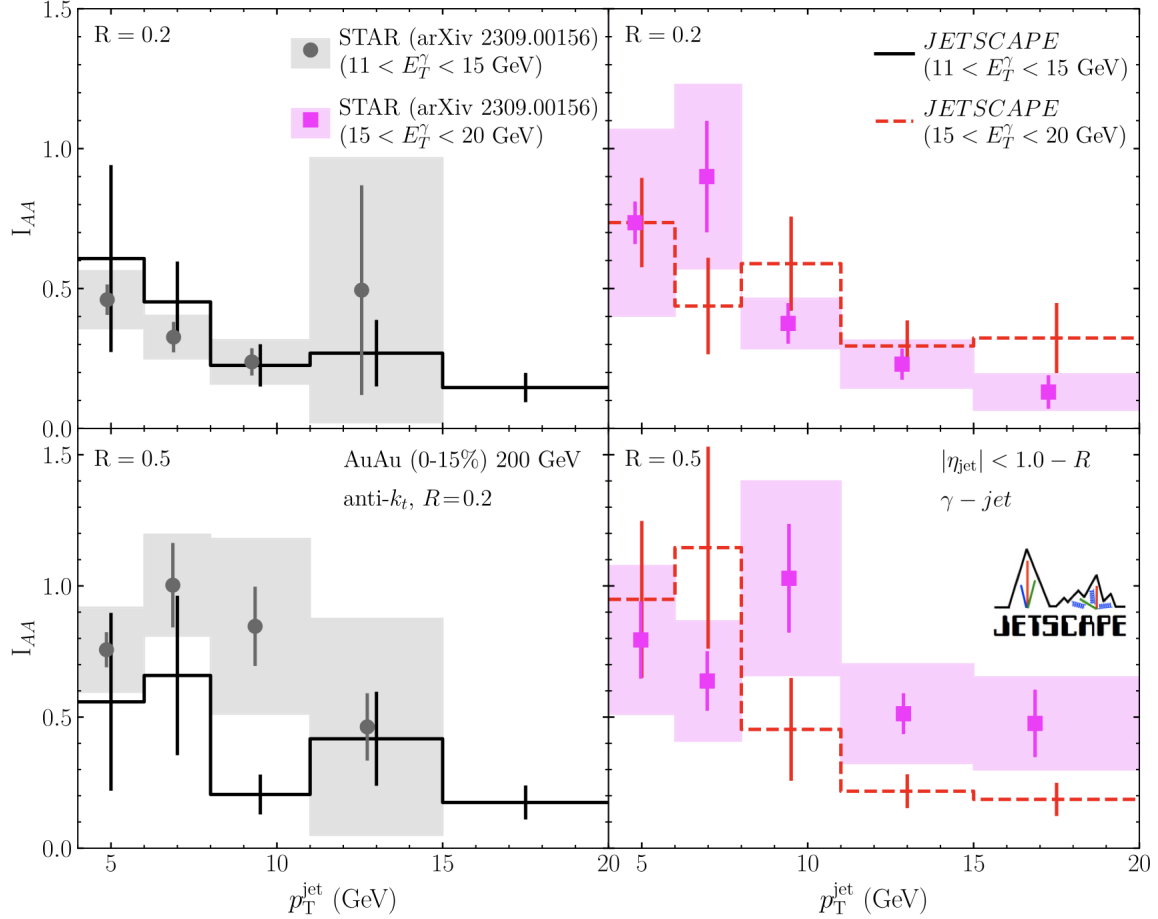


Figure 1.9: The I_{AA} of a photon-triggered charged jet in Au–Au collisions at $\sqrt{s_{NN}} = 200$ GeV measured by STAR compared to the JETSCAPE prediction [96], [97].

For instance, there are separate modules for the initial state, followed by a viscous hydrodynamic routine, and then a hadronization and hadronic afterburner [95]. Hard scatterings, or jet progenitors, have their own module which feeds into the jet-

quenching module; the latter undergoes a controlled interaction with the soft sector, and additional modules which transmit the jet energy to the fluid. JETSCAPE can be used standalone or incorporated into other existing event generator software.

Several measurements such the jet R_{AA} , jet cross-sections, and correlation measurements by ALICE, ATLAS, CMS, STAR, and PHENIX experiments have been reproduced with great accuracy by JETSCAPE. Figure 1.9 shows the per-trigger nuclear modification factor (I_{AA}) or the ratio of photon-triggered jet yields in central Au–Au and pp collisions [96], [97]. Direct photons are correlated with jets with an azimuthal angle cut of $\Delta\varphi > \frac{3\pi}{4}$ to capture the “away” side. JETSCAPE incorporates prompt and bremsstrahlung photons, which are implemented as direct photons which originate from partons with a large virtuality. As a result, the photons are well-separated from the majority of jet fragments. Despite some large uncertainties given by the data points, JETSCAPE predictions are in moderate agreement with the data for all variations of the jet radius and photon-transverse energy (E_T^γ) [96].

1.5.6 AMPT

AMPT (a multi-phase transport model for relativistic heavy ion collisions) [98] is a hybrid physics model which simulates pp and A-A collisions, where the latter includes the formation of a hot and dense QCD medium. This model contains four components: the fluctuating initial condition, the partonic rescatterings, the hadronization phase, and hadronization interactions [98], [99]. The initial parton state includes the spatial and momentum distributions of minijet partons and soft string excitations obtained from HIJING. In the second stage, scatterings occur among the partons produced from the initial nucleon-nucleon interactions following Zhang’s Parton Cascade (ZPC) model [100], which undergoes a partonic cascade. In the next stage, the quark coalescence model [101] or Lund fragmentation is used for hadronization. The dense hadronic phase undergoes dynamical evolution described via relativistic transport which includes both elastic and inelastic scatterings. These continue until the hadronic phases reaches a final state density [80].

AMPT has been used to predict a variety of experimental observables, but particularly relevant to this thesis is their extensive modeling azimuthal correlation distributions [99]. Figure 1.10 shows a correlation distributed generated by default AMPT. The AMPT predictions also extend to I_{AA} measurements, such as in π^0 correlation

measurements in Pb–Pb [71], shown later in Fig. 1.20 in Section 1.6.0.4.

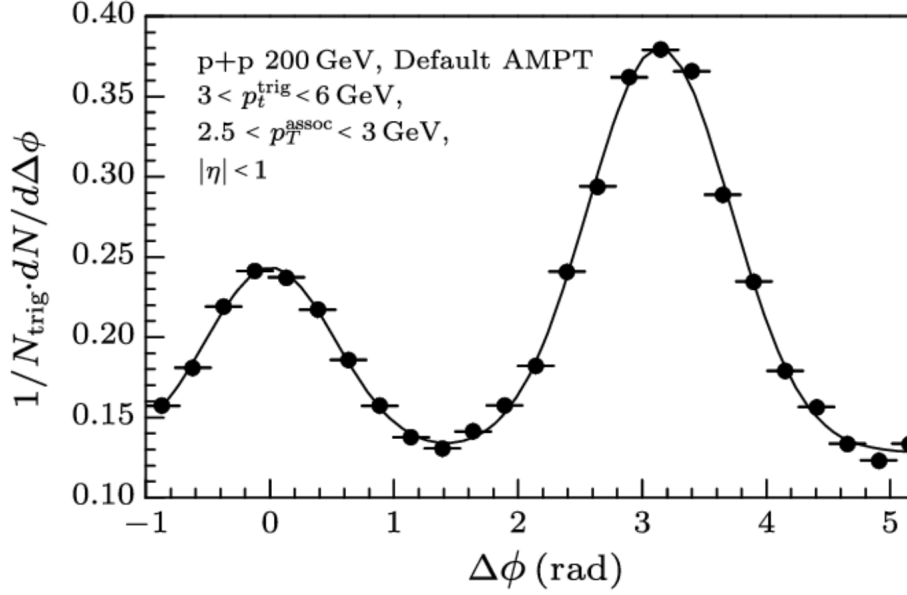


Figure 1.10: Dihadron correlation distribution for pp collisions at $\sqrt{s_{\text{NN}}} = 200$ generated by AMPT [102].

1.5.7 PHSD

The Parton-Hadron-String Dynamics (PHSD) framework [103] is a microscopic transport model which simulates the evolution of heavy-ion collision through modeling individual particle interactions. Particles encompass strings, partons, or hadrons, and their transport is derived from the Kadanoff-Baym (KB) equations [104], which is a non-perturbative transport of strongly-interacting particles. The framework consists of a 3D grid of cells which contain particles that evolve with time. In the initial state, nucleons form pre-hadrons and hadrons and undergo transport using Hadron-String-Dynamics [105]. The QGP phase occurs when the energy density of a given cells increases past the critical energy density of $\epsilon_c = 0.5$ GeV/c/fm³, which causes any hadrons or prehadrons to devolve into partons. These partons interact via the dynamical quasi-parton model (DQPM) [106] model. When the energy density falls below this value, the partons undergo hadronization.

1.5.8 JEWEL

JEWEL [107] is a Monte Carlo jet event generator which serves as a fully dynamical perturbative framework for jet quenching. In JEWEL, hard-scattering partons undergo a virtuality-ordered shower, which undergo jet evolution with elastic and inelastic rescattering. JEWEL offers different operational modes in the generated medium. This model assumes that the medium encounters the jet as a collection of quasi-free partons, and the interaction is treated as background partons recoiling from jet-medium scattering [108]. Events can be generated without saving the recoil information, thereby removing the medium effects. Alternatively, the recoil partons can be kept in the event to provide a prediction of medium effects on the jet. After scattering, the recoiling partons do not undergo any further interaction and free-stream towards hadronization.

1.5.9 TAMU

The TAMU (Texas A&M University) [109] model is focused on describing heavy flavor quark dynamics within the QGP. This model utilizes nonperturbative transport coefficients for heavy-flavor diffusion through the QGP, and for hadronization and hadronic matter. The elastic heavy-quark scattering within the QGP is determined via a thermodynamic T -matrix approach. In this method, resonances close to T_{cr} are utilized for recombination into D and B mesons. This is followed by hadronic diffusion using effective hadronic scattering amplitudes. The transport coefficients are determined from Fokker-Planck Langevin dynamics within hydrodynamic simulations of the bulk medium. Collisional energy loss of the heavy quark is considered, but not radiative. This model incorporates a strongly coupled medium in bulk and heavy quark dynamics which evolves thermally, with the inclusion of hadronization models such as recombination.

1.5.10 LGR

The Langevin-transport with Gluon Radiation (LGR) model [110], [111] describes heavy-quark transport within the QGP. The model uses the Langevin approach to describe heavy quark propagation in the QGP, which assumes there is small momentum transfer in the scattering processes between heavy quarks and the QGP. The

entropy distribution of the initial state is applied to the input of the hydrodynamic evolution. The medium evolves through a 3+1D relativistic viscous hydrodynamics, vHLLE [112]. LGR considers both elastic and inelastic (such as gluon radiation and absorption) energy loss processes. Additionally, hadronization mechanisms are incorporated such as the quark coalescence/recombination model. LGR is quite useful for heavy flavor measurement comparisons in that certain parameters can be tuned. For instance, the initial nPDF, energy loss due to the quark mass, and coalescence model can be altered to determine the effect of these processes.

1.6 Experimental signatures of the QGP

The formation of the QGP is characterized by specific experimental signatures. These signatures include jet-quenching, collective flow, quarkonia suppression, and strangeness enhancement. Jet quenching and collective flow are the most relevant QGP signatures for this thesis, and will be discussed in detail in the following sections.

1.6.0.1 Strangeness enhancement

Because the critical transition temperature to form a QGP exceeds the mass of the strange quark ($m_s \approx 95 \text{ MeV}/c^2 < T_c$), strange quarks can be produced within the QGP itself. In heavy-ion collisions, the production and equilibration of strangeness occurs due to the large gluon density and high energy threshold in the medium [113]. This is measured as an enhancement of strange particle yields in comparison to pp collisions.

Figure 1.11 shows the strangeness enhancement factor in two collision systems [114]. The strangeness enhancement factor E is defined as the yield (dN/dy) per mean number of nucleon participants ($\langle N_{\text{part}} \rangle$), divided by the value in pp collisions. This measurement shows the deviation of the strange particle yields with respect to pp. The relative abundance of the particles increases as a function of $\langle N_{\text{part}} \rangle$, indicating strangeness enhancement in these collision systems.

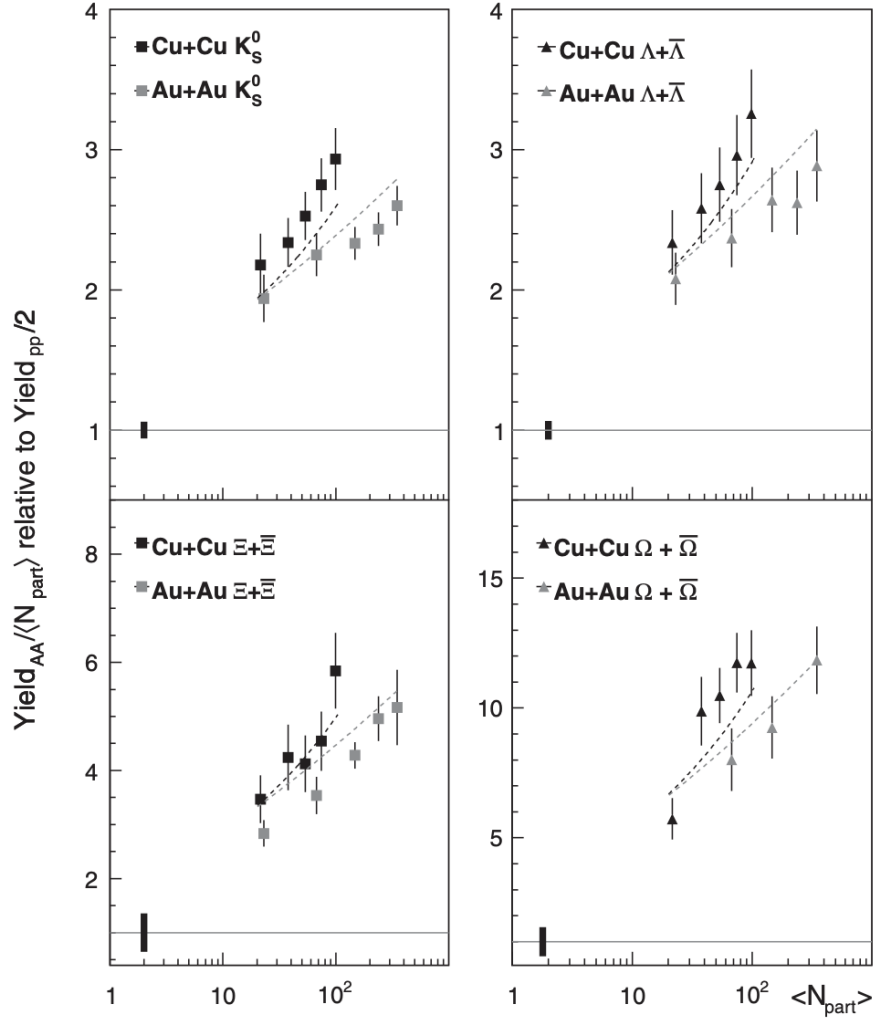


Figure 1.11: Measurements of the strangeness enhancement factor for (multi-)strange particles in Cu–Cu and Au–Au collisions at $\sqrt{s_{NN}} = 200$ measured by STAR [114].

1.6.0.2 Collective flow

As mentioned earlier, in the formation of the QGP after the initial collision, the greater pressure at the center of the QGP compared to the outskirts produces a common velocity field outwards. The initial spatial anisotropy of the collision and the initial state fluctuations convert to momentum anisotropy, ultimately resulting in a directional flow of the bulk medium [56]. The geometrical shape of the flow can be parameterized by a Fourier expansion of the flow coefficients,

$$\frac{dN}{d\varphi} \propto 1 + 2 \sum_{n=1}^{\infty} v_n \cos[n(\varphi - \Psi_n)]. \quad (1.8)$$

Where Eq. 1.8 represents the azimuthal angular (φ) dependence of the produced particle density [15]. The indices n correspond to the order of the flow harmonics, and v_n are the anisotropic flow coefficients, and Ψ_n is the symmetry plane angle, which is the angular direction of anisotropic flow for the corresponding order. The magnitude of the v_2 is directly related to the almond shape of the nuclear overlap region, while v_3 and the higher order coefficients (particularly the odd-numbered) are determined by the event-by-event fluctuations of the colliding nuclei.

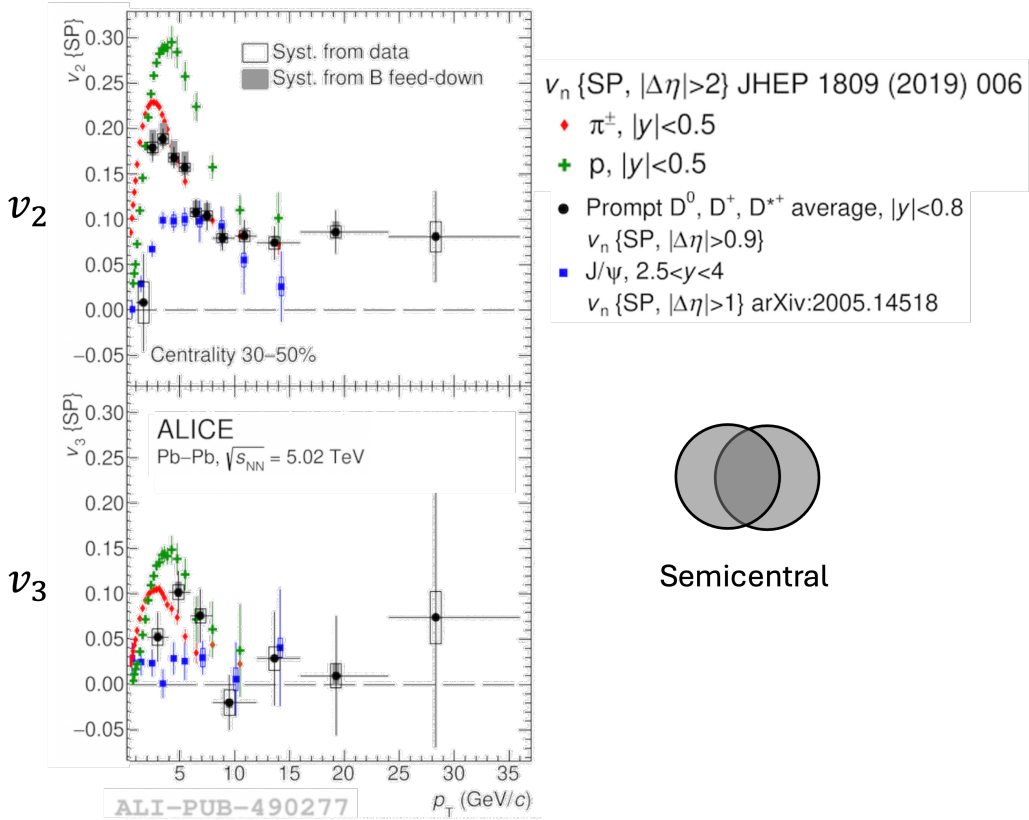


Figure 1.12: Measurements of v_2 and v_3 flow coefficients of inclusive D mesons [115], inclusive J/ψ [116], π^\pm , and protons [117] at $\sqrt{s_{NN}} = 5.02$ TeV measured by ALICE.

Figure 1.12 shows the v_2 and v_3 flow coefficients for different hadron species [115] in both the light and heavy flavor sector. Light-flavor quarks are expected to quickly achieve thermal equilibrium in the medium, whereas charm quarks are expected to

thermalize at a later time. The v_n values follow a mass-ordering when comparing light flavor to heavy flavor, where the D meson and J/ψ values are lower than light flavor. However, there is a noticeable difference between the D meson and J/ψ , which is due to the light quark in the D meson contributing its anisotropic flow to the hadron. The v_n also scales with the number of constituent quarks, as evidenced by the larger value in the proton values compared to the π^\pm . At around p_T of $8 - 10$ GeV/ c , all v_n values approach a similar value due to path-length dependent energy loss [118].

1.6.0.3 Quarkonium suppression

The binding energy between a heavy quark pair is affected by the presence of a QGP medium. Heavy quarkonia are expected to experience collisional dissociation in the QGP, as well as color screening, which weakens the strong force interaction between quarks and gluons due to the presence of the QGP. This phenomenon results in their suppression in heavy-ion collisions [119].

Figure 1.13 shows the dependence of J/ψ suppression [120] on the collision centrality via the J/ψ R_{AA} measurement. The nuclear modification factor (R_{AA} , Eq. 1.9) is a measurement which can be used to investigate energy loss, as well as other effects such as nuclear-shadowing, hadronization modification, and anisotropic flow [74]. It is defined as the ratio of the p_T -differential production yield (dN_{AA}/dp_T) in heavy-ion collisions to the production cross-section ($d\sigma_{pp}/dp_T$) in proton-proton collisions scaled by the average nuclear overlap ($\langle T_{AA} \rangle$).

$$R_{AA} = \frac{1}{\langle T_{AA} \rangle} \frac{dN_{AA}/dp_T}{d\sigma_{pp}/dp_T} \quad (1.9)$$

The $\langle T_{AA} \rangle$ is defined as the average of N_{coll} divided by the inelastic nucleon-nucleon cross-section. This factor scales the observable in pp to the equivalent number of nuclear interactions in Pb–Pb. An $R_{AA} < 1$ indicates medium suppression, where an $R_{AA} = 1$ indicates no modification.

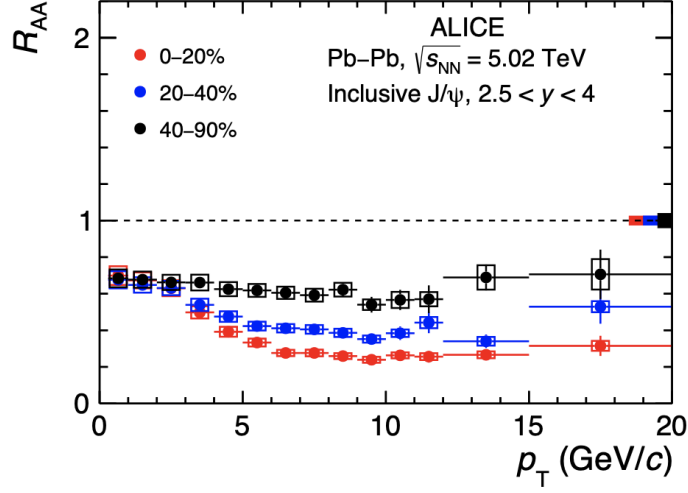


Figure 1.13: R_{AA} measurements of J/ψ in different centrality percentiles at $\sqrt{s_{NN}} = 5.02$ TeV measured by ALICE [120].

Figure 1.13 shows the R_{AA} of inclusive J/ψ [120]. The greater suppression observed in Fig. 1.13 in increasing centrality indicates that a higher-temperature QGP is generated in more central collisions, which suppresses the number of J/ψ .

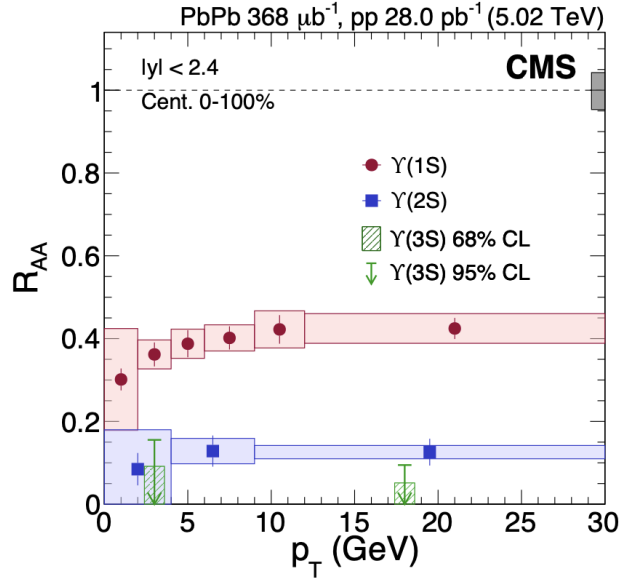


Figure 1.14: R_{AA} measurements of $\Upsilon(1S)$ and the bottomonium resonances at $\sqrt{s_{NN}} = 5.02$ TeV measured by CMS [121]. The measurement shows a hierarchy of suppression dependent on the quarkonium binding energy.

Figure 1.14 shows the R_{AA} of bottomonium states in Pb–Pb collisions, measured by CMS [121]. The R_{AA} measurement in Fig. 1.14 shows a sequential suppression as the binding energy of the bottomonium state decreases [121]. The dissociation temperatures of the Υ states are expected to be correlated with their binding energies, where $T_{dissoc.} \approx 2T_c$, $1.2T_c$, and $1T_c$ for $\Upsilon(1S)$, $\Upsilon(2S)$, and $\Upsilon(3S)$ respectively, where T_c is the critical deconfinement temperature [122].

1.6.0.4 Parton energy loss measured with R_{AA}

Partons within jets interact with the QGP via elastic and inelastic scatterings in the medium, which results in transverse momentum broadening and parton energy loss [65], which is experimentally found via jet-quenching measurements. The fast parton's color charge interacts with the color charges of the medium, which induces radiative energy loss in the form of a bremsstrahlung gluon experienced by the jet parton. The radiative energy loss is expected to have a mass-dependence, such that heavy quarks would lose less energy compared to light flavor. Additionally, jet partons lose energy through elastic collisions. For quarks, this energy loss dE/dx increases monotonically with quark velocity. Although for a given QGP temperature and quark momentum, the quark with a larger mass has a smaller velocity. This results in beauty quarks losing less collisional energy than charm, and charm losing less energy than light flavor [123]. These energy-loss processes result in the modification of the jet fragmentation function with respect to the vacuum. The fragmentation function parametrizes the non-perturbative transition of a heavy quark into a hadron, and these are determined experimentally [124]. This modification results in a suppression of the yield of high p_T hadrons and modifications of the jet topologies [125]. Jet quenching and the modification of the fragmentation is measured in jet observables such as the jet momentum spectra, azimuthal correlation distributions, and through the nuclear modification factor, or R_{AA} .

Figure 1.15 is the R_{AA} distribution for different hadron species in all Pb–Pb centrality classes measured by CMS [126]. There is a noticeable mass-ordering between the light and heavy-flavor sector, where the charged hadron R_{AA} experiences a greater suppression compared to the heavy-flavor hadrons. This is expected due to the light quarks experiencing a greater energy loss compared to heavy flavor.

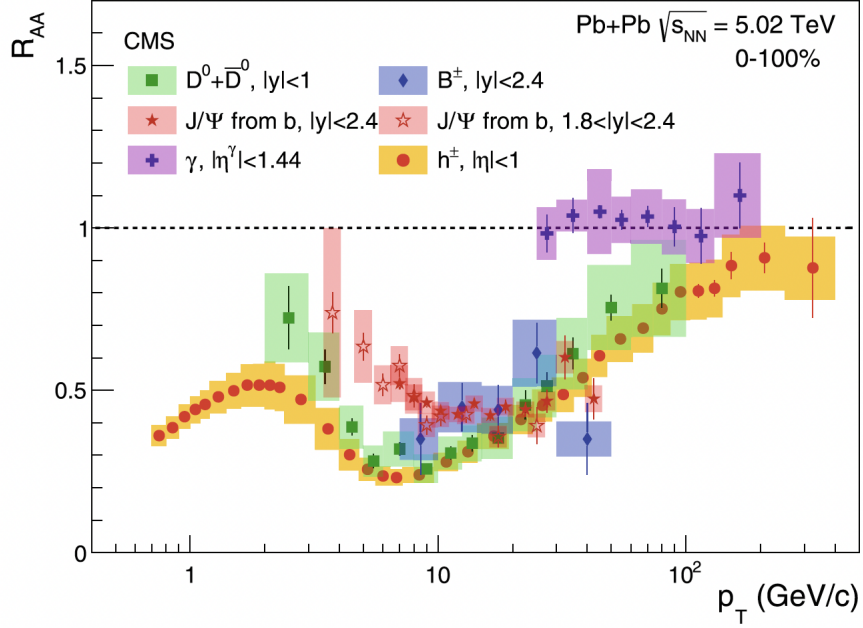


Figure 1.15: CMS measurement of the R_{AA} of different species [126]–[130] at $\sqrt{s_{NN}} = 5.02$ TeV for the full spectrum of Pb–Pb centrality classes.

Figure 1.16 shows a closer look at the differences between beauty and charm via the R_{AA} of prompt and non-prompt D^0 mesons [76], [131]. Prompt D mesons hadronized from charm quarks produced in the initial collision, while non-prompt D mesons originate from beauty hadrons which have decayed into D mesons. The beauty quark’s lifetime exceeds that of the QGP, therefore it has experienced the full medium evolution which will be reflected in the R_{AA} of the non-prompt D meson. Albeit with some uncertainties, there is a consistent mass-ordering of the R_{AA} in all p_T intervals, where the prompt D mesons experience a larger suppression. In $3 < p_T < 10$ GeV/c, collisional energy loss dominates, where the beauty quark loses less energy from collisional due to its larger mass. At $p_T > 10$ GeV/c, energy loss is dominated by radiative processes. The larger suppression in the prompt D meson is likely due to the difference in gluon radiation from the “dead-cone” effect.

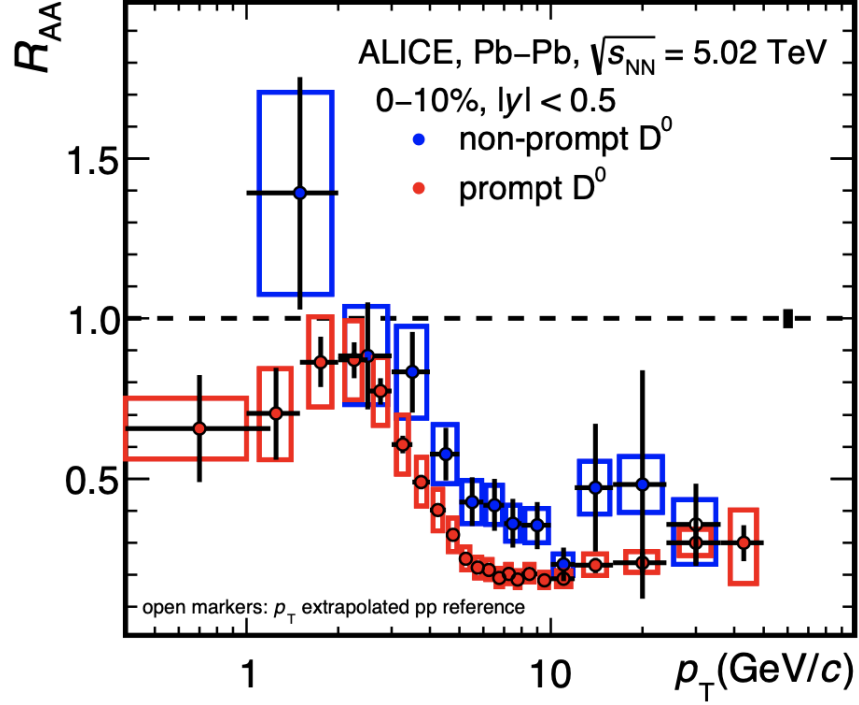


Figure 1.16: Comparison of prompt vs non-prompt D^0 R_{AA} measured by ALICE [131].

In Fig. 1.17, the ratio of the prompt to non-prompt D meson R_{AA} is compared to the LGR, MC@sHQ+EPOS2, and TAMU models as a function of p_T . In the top portion, all models describe the p_T -dependent shape and predict a value close to unity at $2 < p_T < 3$ GeV/ c and increases towards higher p_T . At $p_T > 10$ GeV/ c , the models appear consistent with the measurements, although there is a large uncertainty in the highest p_T regions measured. In the bottom portion of the figure, some physics mechanisms are altered in the LGR model and compared to data. The comparison indicates that nuclear shadowing does not influence the measurement, or it is effectively canceled in the ratio. When the beauty quark is modeled to experience the charm energy loss, the LGR model deviates from the measurement at $3 < p_T < 10$ GeV/ c . The coalescence hadronization model can be turned on and off, which describes the probability for quarks to hadronize together dependent on their phase space. The close agreement with data indicates that the coalescence hadronization model [101] is required to explain the data, and that the difference in the quark masses does not

significantly affect coalescence. All models in both sections of the figure are consistent with the measurement at high- p_T where radiative energy loss (in the form of jet quenching) is expected to dominate. Although the R_{AA} provides a measurement of jet quenching, the observable is influenced by a variety of other factors such as nuclear shadowing, the anisotropic flow, and hadronization mechanisms.

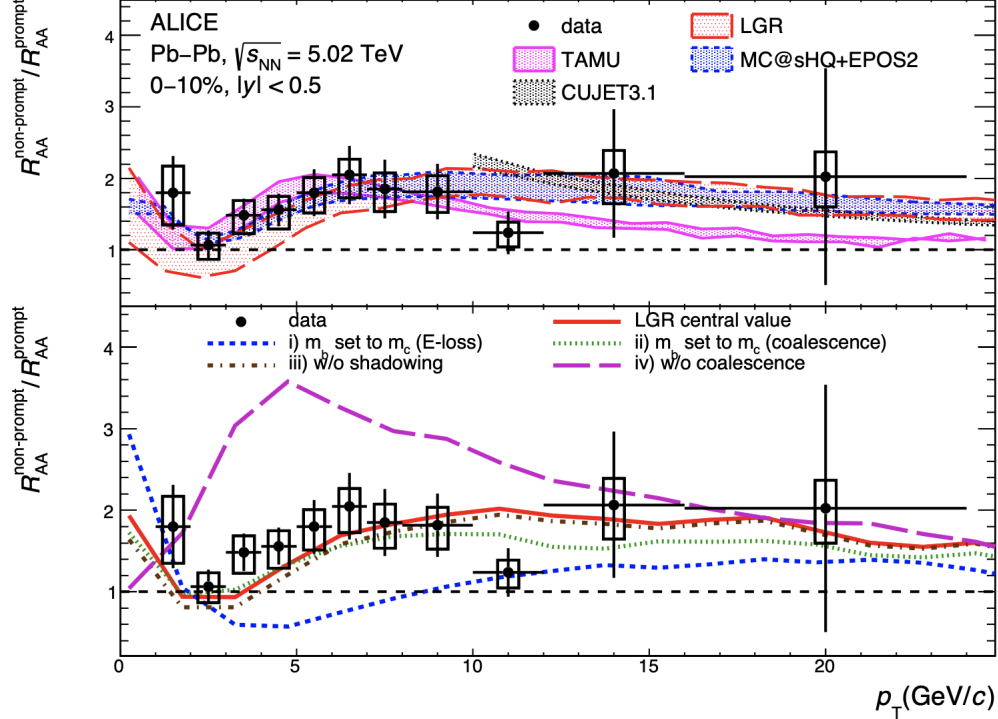


Figure 1.17: Ratio of non-prompt [131] and prompt [76] D^0 R_{AA} at $\sqrt{s_{NN}} = 5.02$ TeV measured by ALICE compared to theoretical models.

1.6.0.5 Jet quenching measured with azimuthal correlations

Azimuthal correlations are a type of differential jet measurement which accesses different momentum scales of the angular distribution of particles. Particles produced in a jet are correlated in azimuthal angle, and this measurement reflects the fragmentation of outward-traveling partons produced primarily in dijet events [132]. When measured in heavy-ion collisions, the back-to-back correlation strength indicates sensitivity to the in-medium path length of the parton [132], and therefore is used to study jet quenching. This type of measurement complements full jet reconstruction,

in that it does not rely on jet clustering algorithms and can be used to investigate the fragmentation of jets in a wide kinematic range.

This measurement consists of selecting a “trigger” particle of a specific $p_T^{\text{trig.}}$ to act as the proxy for the jet. Particles “associated” with the trigger are selected in different $p_T^{\text{assoc.}}$ intervals, where typically $p_T^{\text{assoc.}} < p_T^{\text{trig.}}$ to avoid self-correlating the trigger particle. The difference in azimuthal angle $\Delta\varphi$ is taken between the trigger particle and the associated particles to obtain a correlation distribution in each selected $p_T^{\text{assoc.}}$ range.

$$\Delta\varphi \equiv \varphi^{\text{Trig.}} - \varphi^{\text{Assoc.}} \quad (1.10)$$

$$\Delta\eta \equiv \eta^{\text{Trig.}} - \eta^{\text{Assoc.}} \quad (1.11)$$

The resulting distributions of $\Delta\varphi$ and $\Delta\eta$ are plotted, which give a two-dimensional picture of the correlation measurement (see Fig. 1.18). The correlation distribution is then normalized by the number of trigger particles (see Eq. 1.12), so that the measurement represents the distribution of associated particles with respect to a single trigger. This also makes the measurement independent of the total number of trigger particles.

$$C(\Delta\varphi, \Delta\eta) = \frac{1}{N_{\text{trig}}} \frac{dN_{\text{assoc}}}{d\Delta\varphi d\Delta\eta} \quad (1.12)$$

Although the 2D correlation is often sufficient for physics observations, usually the 2D correlation is projected in $\Delta\varphi$ to obtain a 1D distribution (Eq. 1.13). This has the benefit of reducing statistical fluctuations in the correlation distribution. The 1D distribution is shown in the right on Fig. 1.18.

$$C(\Delta\varphi) = \frac{1}{N_{\text{trig}}} \frac{dN_{\text{assoc}}}{d\Delta\varphi} \quad (1.13)$$

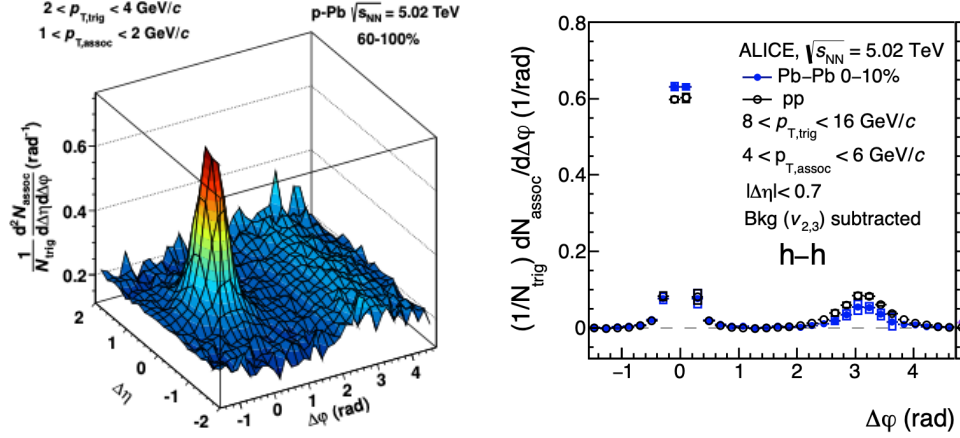


Figure 1.18: (Left) 2D ($\Delta\varphi\Delta\eta$) azimuthal correlation distribution of charged particles in p-Pb collisions measured by ALICE at $\sqrt{s_{NN}} = 5.02$ TeV [133], [134]. (Right) 1D ($\Delta\varphi$) hadron-triggered correlation distribution in pp and Pb-Pb at $\sqrt{s_{NN}} = 5.02$ TeV measured by ALICE shown together [70]. In the right figure, there is a noticeable difference in the near- and away-side peaks between the two collision systems.

The typical structure of the correlation distribution features a “near-side” peak at $(\Delta\varphi, \Delta\eta) = (0, 0)$, and an “away-side” peak at $\Delta\varphi = \pi$ which extends over a wide $\Delta\eta$ range. The near-side peak reflects the fragmentation of the jet which contains the trigger. The away-side peak provides information from the recoil jet, but is also influenced by other jet events in the hard scattering. The azimuthal correlation distribution offers multiple observables which can be compared to models. These observables include the distribution itself, the per-trigger associated particle yield, the peak width, and the per-trigger nuclear modification factor (I_{AA}).

$$I_{AA} = \frac{Y_{PbPb}}{Y_{pp}} \quad (1.14)$$

The I_{AA} , shown in Eq. 1.14, is defined as the ratio of the per-trigger particle yield in the correlation peak measured in Pb-Pb to pp. The I_{AA} is sensitive to modifications in the parton fragmentation function, jet-quenching, and the overall jet-medium interaction in heavy-ion collisions.

Figure 1.19 shows the azimuthal correlation distribution of π^0 triggers in four different $p_T^{\text{assoc.}}$ intervals, measured in central Pb-Pb collisions [71]. The shape of the correlation distribution peaks vary in the p_T slices. At low- $p_T^{\text{assoc.}}$, the away-side

peak is visible and gradually disappears as $p_T^{\text{assoc.}}$ increases. This indicates the jet-initiating parton energy loss in the medium, and the potential modification of the jet fragmentation.

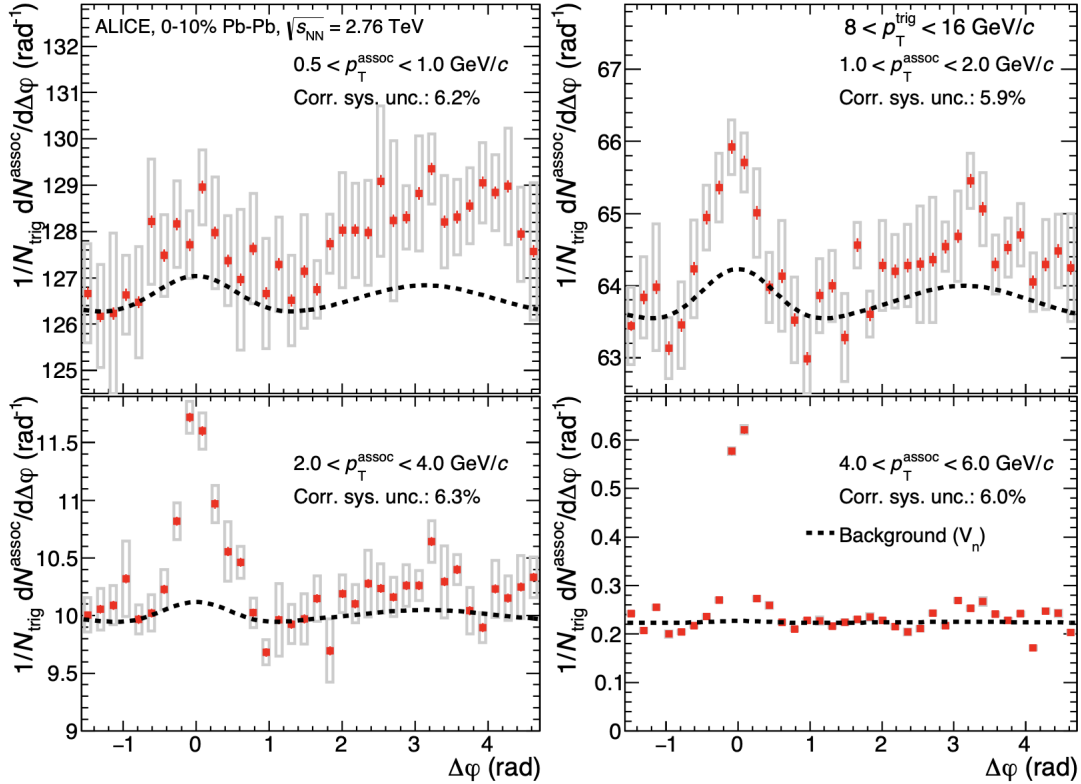


Figure 1.19: The π^0 correlation distribution in Pb-Pb collisions $\sqrt{s_{NN}} = 5.02$ TeV in the 0-10% central collisions measured by ALICE [71]. The depletion of the away-side peak observed in $4 < p_T^{\text{assoc.}} < 6$ GeV/c is evidence of jet-quenching.

The extent of the jet quenching can be observed in the measurement of the $\pi^0 I_{AA}$. Fig. 1.20 shows the I_{AA} for the two correlation peaks compared to the AMPT and JEWEL models. The near-side peak shows a slight enhancement at low- $p_T^{\text{assoc.}}$ and approaches unity at high- $p_T^{\text{assoc.}}$. In the away-side, there is a significant enhancement at low- $p_T^{\text{assoc.}}$ and approaches unity between $3 < p_T^{\text{assoc.}} < 4$ GeV/c where it then displays a suppression that evens out at $I_{AA} \approx 0.5$.

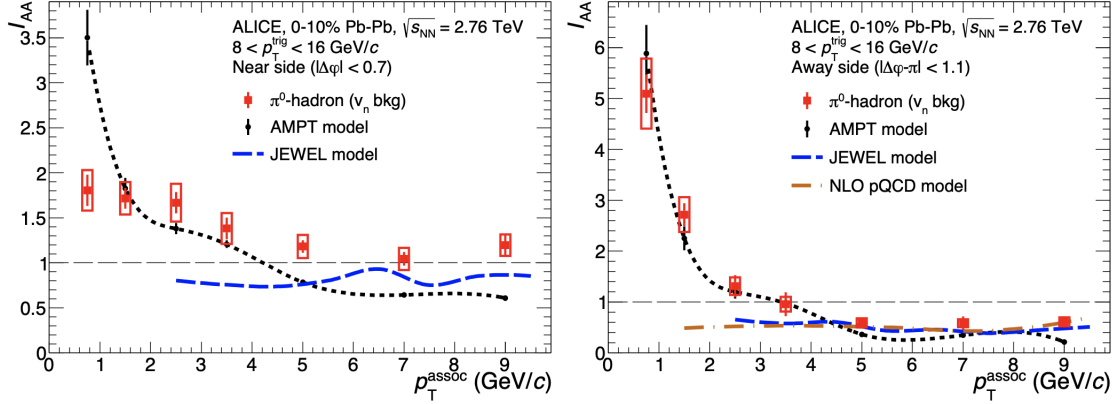


Figure 1.20: The near- (left) and away-side (right) $\pi^0 I_{AA}$ at $\sqrt{s_{NN}} = 2.76$ TeV measured by ALICE [71] compared to the AMPT and JEWEL model predictions.

The AMPT model predicts a strong enhancement on the near-side at low- $p_T^{\text{assoc.}}$, but this is not shared with the data. JEWEL predicts jet-quenching on the near-side peak, but this is not shared with data. Both models can replicate the suppression on the away-side due to jet quenching, but only the AMPT model recreates the enhancement. This is attributed to the increase of soft particles resulting from the jet-medium interactions.

1.7 Measuring heavy-flavor jet-fragmentation in heavy-ion collisions

The objective of this thesis is to investigate the modification of heavy-flavor jet fragmentation in the presence of the quark-gluon plasma. This is performed via an analysis of jet-like azimuthal correlations between electrons from heavy-flavor hadron decays with associated charged particles measured in Pb–Pb collisions.

There are several questions this measurement seeks to answer: To what extent does the QGP affect the heavy-flavor jet? Does this only result in a reduction of the jet constituents due to jet quenching, or is there an enhancement of associated particles? In what $p_T^{\text{assoc.}}$ is the jet modified? What are the differences between the profile of a heavy-quark-initiated jet and jets which originate from light quarks and gluons? Would the smaller energy loss experienced by the heavy quark result in a quantifiable difference in the distribution compared to light flavor? What does that indicate about

how the fragmentation of the different species is modified? How does the p_T , therefore the energy of the heavy flavor jet, affect the profile, and does the fragmentation of jets in varying energy experience different modifications from the QGP? How does the modification of the jets differ when originating from predominantly charm vs beauty quark fragmentation? How does the modification differ with respect to the size of the QGP? Does the jet induce wake structures within the medium, and does that influence the observables in this measurement?

Azimuthal correlation measurements illustrate the angular distribution of jet constituents, which is determined by the initial jet fragmentation pattern. This measurement can be performed in several associated- p_T regions, which provides a differential view of the associated particle distribution as a function of $p_T^{\text{assoc.}}$. Therefore, this measurement characterizes the jet profile in different regions of phase space.

The species of the jet-initiating parton determines the jet properties, such as the fragmentation function, the jet width, and the expected energy loss in the QGP. Performing this measurement in the heavy-flavor sector gives insight into these jet properties in the heavy-ion environment. The measurement in this thesis will be compared to correlation measurements in the light-flavor sector, which allows for a comparison between the jet fragmentation profile of heavy quark-initiated jets to light quark and gluon jets.

Electrons from the semileptonic decay of heavy-flavor hadrons are used as the trigger particle of this correlation study for several reasons. The relatively large branching ratio ($\sim 10\%$) of heavy-flavor semileptonic decays allows for sufficient statistics to perform this measurement in a heavy-ion environment. This is advantageous over other heavy-flavor correlation measurements that use reconstructed hadrons as the triggers, which suffer from significant combinatorial background from the invariant-mass reconstruction. These increased statistics allow for a more differential investigation of the jet modification. Additionally, electrons are charged final-state particles, which make them amenable to tracking and they are also identifiable through calorimetric detection. Therefore, electrons are experimentally easy to identify. For brevity, the term “electron” encompasses both electrons and positrons, and will be used for the remainder of this text, except when explicitly distinguished for a specific procedural step.

This measurement is performed in Pb–Pb collisions and builds off the equivalent measurement in the proton-proton and proton-Pb collision systems [135]. The az-

azimuthal correlation measurement of electrons from heavy-flavor hadron decays was performed in pp to obtain a baseline measurement of the correlation to compare to Pb–Pb, such that the pp measurement describes the heavy-flavor fragmentation in vacuum. This measurement was performed in p–Pb collisions to determine how and if cold-nuclear effects affect the correlation distribution observables, which must be considered before performing the analysis in Pb–Pb. Thus, the comparison of this measurement to the smaller collision systems illustrates how the QGP influences the fragmentation of the jet-initiating parton. The per-trigger associated yields of the distributions can be compared in Pb–Pb to pp by taking the ratio, or the I_{AA} . The I_{AA} is sensitive to changes in the heavy quark fragmentation function, therefore a suppression or enhancement of the I_{AA} provides a quantifiable difference in the heavy quark jet fragmentation between these collision systems.

Two centrality percentiles were selected to perform this measurement: 0–10% (central) and 30–50% (semicentral) Pb–Pb collisions. This is done for the purpose of observing the effect of jet fragmentation modification as the size, density, and temperature of the QGP differ due to collision centrality [74].

In the following chapters of this thesis, the experimental apparatus, the procedural steps, and the systematic checks of this analysis will be outlined. This culminates in the results of the first jet-like Pb–Pb azimuthal correlation measurement by ALICE in the heavy-flavor sector.

Chapter Two: Experimental Apparatus

This chapter provides an overview of the Large Hadron Collider (LHC), ALICE experiment, and the specific detectors used for this analysis measurement.

2.1 The LHC

The Large Hadron Collider (LHC) is the largest and most powerful particle accelerator on Earth [136]. The accelerator complex is operated and overseen by CERN, the European Organization for Nuclear Research. The LHC is situated 100 meters underground in a tunnel overlapping the French-Swiss border, and consists of a 16 mile (27 km) circumference ring stringing a collection of superconducting magnets and accelerating structures with the purpose of accelerating and colliding high-energy particle beams at ultra-relativistic speeds [136], [137]. The main structures of the accelerator complex are underground, where the linear accelerator 4 (Linac4) produces the proton beam sources by accelerating negative hydrogen ions, before they are stripped of the of their electrons to expose the bare protons and transferred to the Proton Synchrotron Booster (PSB). These protons are accelerated to 2 GeV for injection into the Proton Synchrotron (PS) 528 m circumference ring, which then accelerates the proton beam to 26 GeV before entering the Super Proton Synchrotron (SPS) 7 km circumference ring, which accelerates the beams to 450 GeV. The proton beams are split and enter the two beam pipes of the main ring (LHC), where the beams circulate clockwise and counterclockwise to converge at intersection points for each main experiment. For the lead-ion source, vaporized lead enters the Linac3 and is accelerated in the Low Energy Ion Ring (LEIR) before entering the PS and following the same route as the proton beams [138].

There are four major CERN experiments, each having their own respective focus in experimental particle or nuclear physics, situated at the intersection points along the LHC beamline. These are ALICE (A Large Ion Collider Experiment), ATLAS (A Toroidal LHC ApparatuS), CMS (Compact Muon Solenoid), and LHC-b (LHC-beauty).

2.2 The ALICE Detector

The ALICE program is dedicated to studying the physics of strongly-interacting matter and the quark–gluon plasma via heavy-ion collision experiments. The experiment consists of a 10,000 ton, 26 m long, 16 m high, and 16 wide detector located along the beam-line on the French side of the LHC apparatus. The detector is specially optimized for the measurement of heavy-ion collision data, due to its high-precision tracking and vertexing of low-momentum particles in a high-multiplicity environment [139].

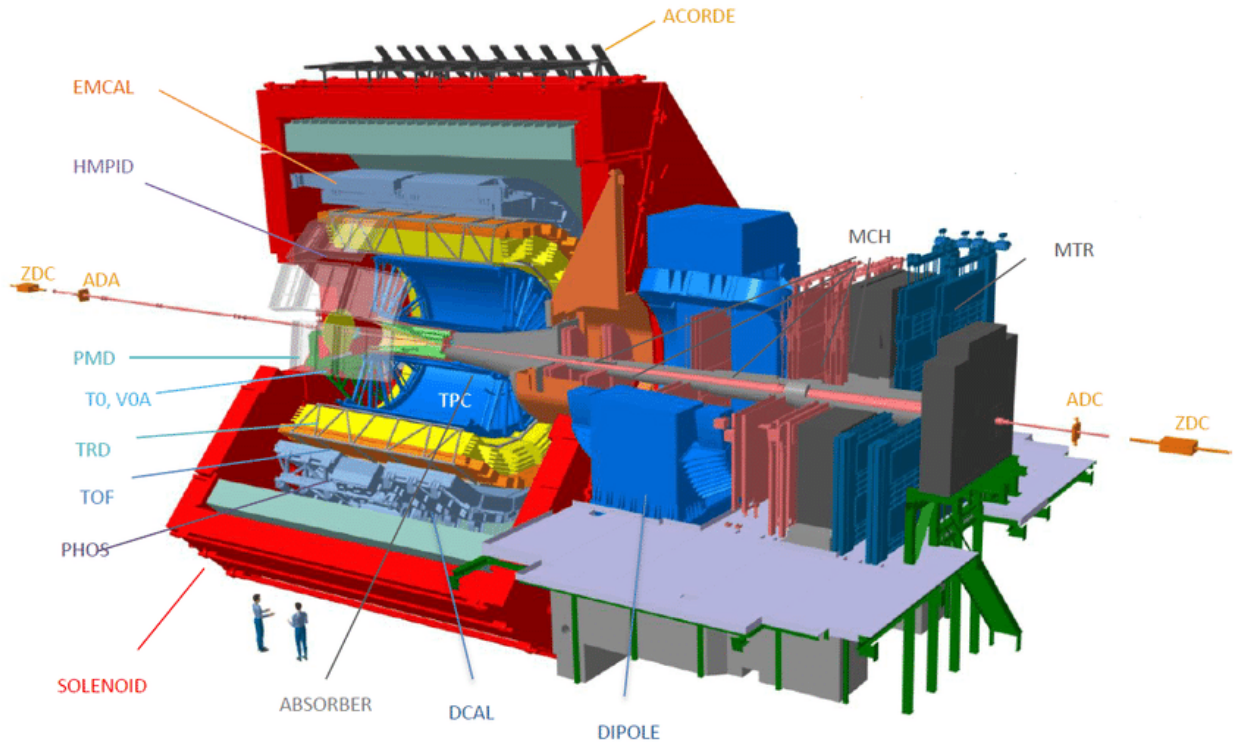


Figure 2.1: ALICE Detector during the Run 2 (2015 - 2018) data collection period.

The ALICE detector consists of a central barrel with several sub-detectors for the purposes of track and vertex resolution, particle identification, event triggering; and several smaller detectors located at forward angles used for global event characterization and triggering.

The central barrel of the detector is located at midrapidity ($|\eta| < 0.9$), covers the full azimuth, and is embedded within the large L3 magnet. The L3 magnet is a

cylindrical solenoid which produces a magnetic field of 0.5 T parallel to the direction of the beam. The central barrel is composed of the Inner Tracking System (ITS) of high-resolution silicon detectors, the gas-filled Time Projection Chamber (TPC), the Time-of-Flight (TOF), the Ring Imaging Cherenkov (HMPID), the Transition Radiation (TRD) detectors, the single-arm photon spectrometer (PHOS), and the electromagnetic calorimeter and Dijet calorimeter (EMCal and DCal, which will collectively be referred to as EMCal). On top of the central magnet is the ALICE COsmic Ray DEtector (ACORDE), which acts as a cosmic ray trigger for ALICE calibration and the study of high energy cosmic rays.

There are additional subdetectors in the forward and backward rapidity regions. Muons are detected by the muon spectrometer, located $-4.0 \leq \eta \leq -2.5$, which consists of a passive front absorber, high-granularity tracking system, a large dipole magnet, a filter wall with four planes of trigger chambers, and an inner beam shield to protect the chambers from particles and secondaries. The Zero Degree Calorimeters (ZDC) are located at 112.5 m from both sides of the interaction point, which are utilized for rejecting electromagnetic interactions and beam-induced background in Pb–Pb collisions. This is done by measuring spectator nucleons for centrality and reaction plane determination. The remaining forward subdetectors are the Photon Multiplicity Detector (PMD); the V0 system; the T0 detector, and the Forward Multiplicity Detector (FMD) [139].

The first operation of the LHC, or Run 1, began in 2009 and continued until 2013 [140], which consisted of a proton-proton (pp), proton-Lead (p–Lead), and Lead-Lead (Pb–Pb) collisions for the first physics campaign of the apparatus. For the first run, pp beams were collided at center-of-mass energies of 0.9 TeV. The pp beams ultimately reached energies of 2.76 and 7-9 TeV. Pb–Pb collisions with $\sqrt{s_{NN}} = 2.76$ TeV were recorded at a maximum of 3-4 kHz interaction rate; and p–Pb beam collisions were recorded at $\sqrt{s_{NN}} = 5.02$ TeV [140]. Events were recorded based on a trigger decision system, which is the Central Trigger Processor (CTP) of ALICE. In this run period, events were recorded by triggering on “minimum bias” events, which utilizes signals from the SPD and V0, triggers based on heavy-ion centrality, or EMCal-signal triggers [140]. Run 1 continued until 2013, which marked the end of the first physics campaign of the LHC. This was followed by Long Shutdown 1 (LS1), where planned upgrades of the LHC and the experiments took place.

LS1 culminated in a number of enhancements to the ALICE experiment, which

included but was not limited to: completion of the TRD; CTP upgrades; and the addition of the DCal, which extended the acceptance of the EMCal [141]. The Run 2 data collection period (beginning June 2015) consisted of higher center-of-mass energies and increased luminosities for all collision systems compared to Run 1 and the addition of Xenon-Xenon collisions to the heavy-ion program. For pp collisions, the highest energies reached in Run 2 was $\sqrt{s} = 13$ TeV. Both Pb–Pb and pp collisions were recorded at $\sqrt{s_{\text{NN}}} = 5.02$ TeV, facilitating the direct comparison of measurements between these systems. The Pb–Pb interaction rate in Run 2 reached 8 kHz, which meant an overall $2\times$ greater number of collisions per second compared to Run 1 [142]. The dataset used for this thesis is LHC Lead ion (Pb–Pb) collision data with center of mass per nucleon energy of 5.02 TeV, acquired by the ALICE detector in 2018 during the Run 2 data-taking period.

The primary detectors used for this analysis are the ITS, the TPC, the EMCal, and V0 detectors, which will each be discussed in further detail in the next sections.

2.2.1 Inner Tracking System

The Inner Tracking System (ITS) consists of six cylindrical layers located coaxially around the beam pipe and covers the full azimuth and pseudorapidity range of $|\eta| < 0.9$. Its primary tasks are to reconstruct the primary and secondary vertices of the event and for low-momentum charged-particle tracking.

The ITS (Fig. 2.2) utilizes three different silicon-tracking technologies: The two inner layers are composed of Silicon Pixel Detectors (SPD), the two middle layers are Silicon Drift Detectors (SDD), and Silicon Strip Detectors (SSD) make up the outer two layers [143]. The ITS was designed to improve the position, angle, and momentum resolution for tracks reconstructed in the TPC, and to identify the secondary vertices from the decay of hyperons and heavy-flavored hadrons.

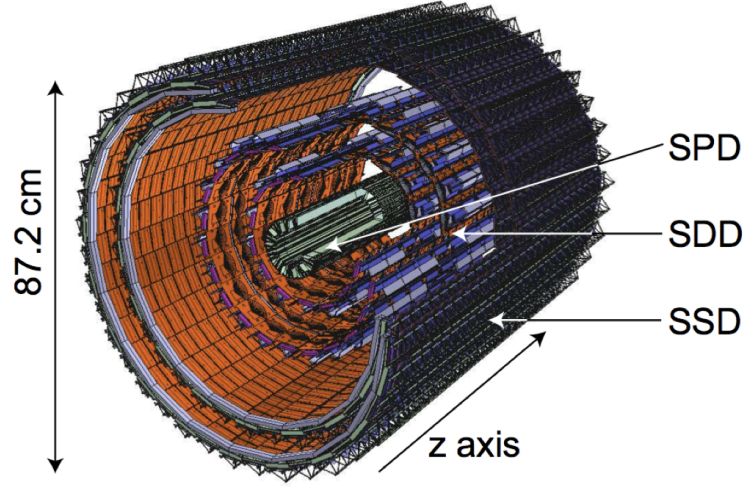


Figure 2.2: Layout of Inner Tracking System during Run 2 [144].

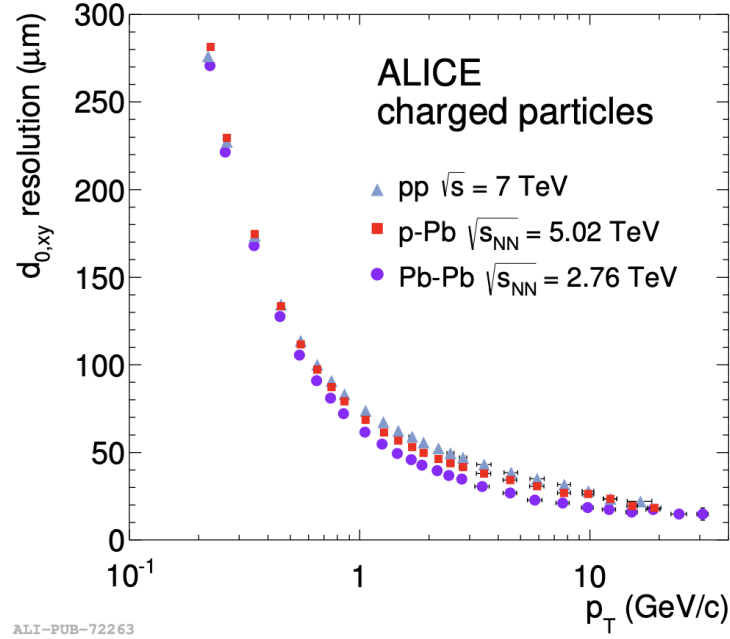


Figure 2.3: Impact parameter resolution performance of the ITS in the x-y plane as a function of p_T for pp, p-Pb, and Pb-Pb collisions provided publicly by ALICE [145].

The resolution of the impact parameter in the transverse plane ($d_{0,xy}$) can be used

as a benchmark quantity for track and vertex reconstruction precision of the ITS. The transverse impact parameter is defined as the distance between the extrapolation of a track in the transverse plane to the reconstructed primary vertex [145], [146]. For heavy-flavor analyses, the $d_{0,xy}$ is essential for identifying secondary tracks originating from charm and beauty hadron decays. For example, the resolution required for a D^0 analysis is $\langle d_{0,xy} \rangle(r\phi) \approx c\tau(D^0) \approx 124 \mu\text{m}$ for the kaon and pion tracks originating from the $D^0 \rightarrow K^- \pi^+$ decay channel [146]. A performance plot of the $d_{0,xy}$ resolution in μm is given in Fig. 2.3.

2.2.2 Time Projection Chamber

The Time Projection Chamber (TPC) [147] is the core of the ALICE tracking system, providing three-dimensional information of particle momenta and charged-particle identification (PID) [148].

The detector is a gas-filled cylindrical chamber surrounding the ITS with an inner radius of approximately 85 cm and an outer radius of 250 cm, and 500 cm in length along the beam direction, at $|\eta| < 0.9$. The chamber consists of nested field cages, while a conducting electrode at the cylinder center provides a voltage of 500 kV, which provides an axial electric field of 400 V/cm. Charged particles ionize the gas with a curved trajectory within the magnetic field and undergo an average energy loss $\langle dE/dx \rangle$ characteristic of specific charged particle species, shown in 2.5. The TPC readout chambers (ROC) are designed based on the Multi-Wire Proportional Chamber (MWPC) technique with pad readouts (readout channels) [149]. There are a total of 72 ROCs with 63 total pad rows consisting of 6×10 and $6 \times 15 \text{ mm}^2$ -sized pads [147].

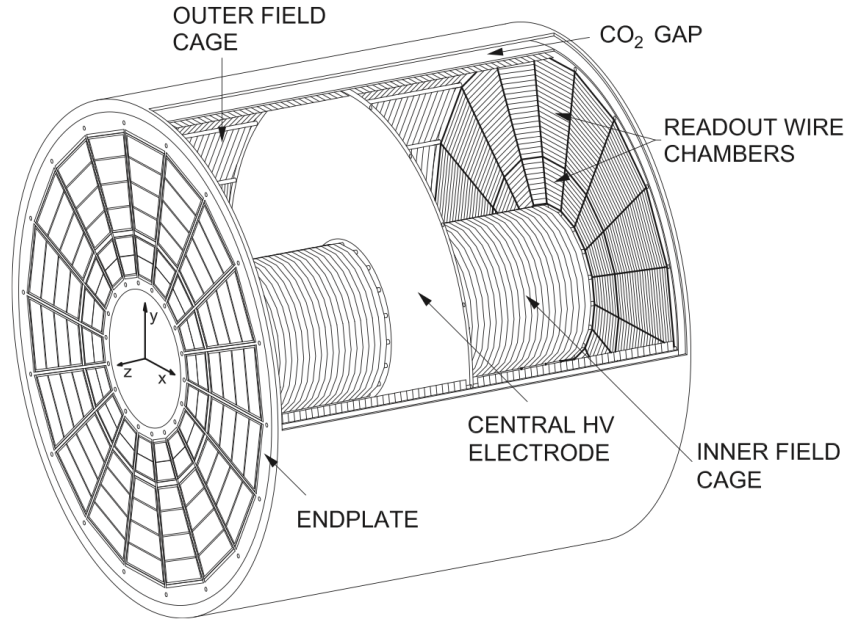


Figure 2.4: 3D Schematic of the TPC field cage provided by ALICE [147].

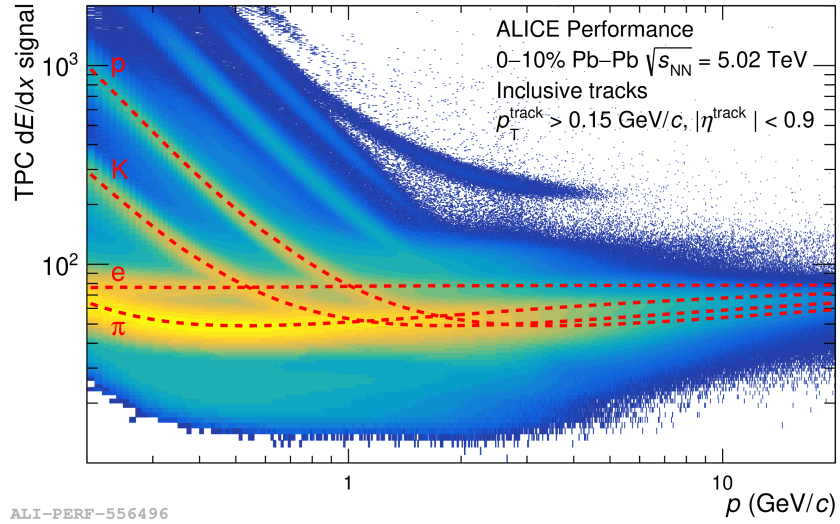


Figure 2.5: TPC performance plot for Pb-Pb collisions in 0–10% centrality class at $\sqrt{s_{\text{NN}}} = 5.02$ TeV provided by ALICE, illustrating the tracks for charged particle species.

The characteristic energy-loss within the TPC is parameterized by the Bethe-

Bloch function:

$$\left\langle \frac{dE}{dx} \right\rangle = \frac{4\pi N e^4}{m c^2} \frac{Z^2}{\beta^2} \left(\ln \frac{2 m c^2 \beta^2 \gamma^2}{I} - \beta^2 - \frac{\delta(\beta)}{2} \right) \quad (2.1)$$

Where distributions of particle tracks can be distinguished as a function of momentum (seen in Fig. 2.5 for most-central Pb–Pb collisions). The energy-loss distributions of protons, electrons, deuterons, some Hydrogen and Helium isotopes, and charged pions and kaons are well-documented for the TPC.

2.2.3 Electromagnetic Calorimeter

The electromagnetic calorimeter (EMCal) detector is designed for identification of electrons, direct jet measurements, and to enhance the measurement of the spectra of high p_T photons and neutral mesons, and event triggering by providing a direct energy measurement of particle tracks. The detector is a Lead-Scintillator sampling calorimeter utilizing Shashlik-technology [150]. The EMCal covers a pseudorapidity and azimuthal angle of ($|\eta| < 0.7$ and $80^\circ < \varphi < 187^\circ$), and the DCal covers ($0.22 < \eta < 0.7$ and $260^\circ < \varphi < 320^\circ$, $|\eta| < 0.7$ and $320^\circ < \varphi < 327^\circ$).

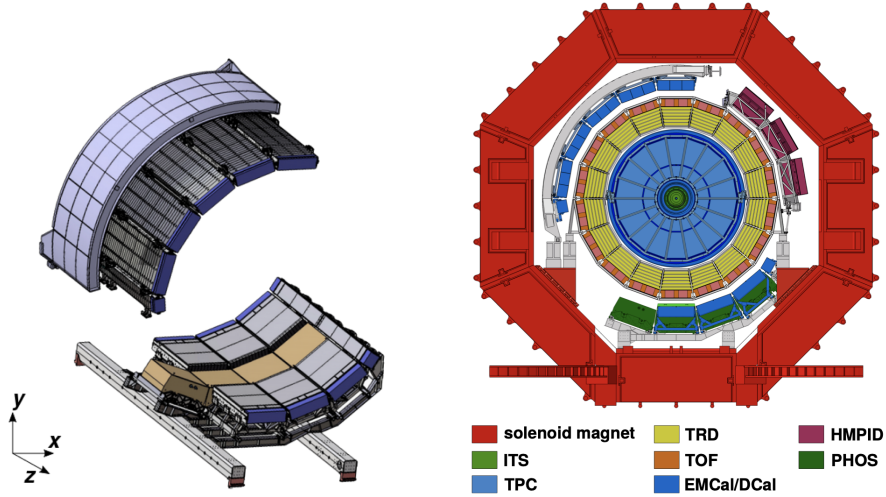


Figure 2.6: Schematic of the electromagnetic calorimeter, which shows the components approximately opposite in azimuth provided by ALICE [151].

The EMCal is composed of modules, which are 2×2 optically isolated towers which span a region of $\Delta\eta \times \Delta\varphi \simeq 0.0143 \times 0.0143$ and consists of 76 lead layers and

77 scintillator layers. Modules have a fixed width in the φ direction and a tapered width in the η direction with an angle of 1.5° . Modules are assembled into Super Modules, which are stacked strips consisting of 12 identical modules along φ and are approximately projective in η . The strip structure is shown in Fig. 2.7. The EMCal modules have an effective radiation length (X_0) of 12.3 mm and 20.1 radiation lengths [150].

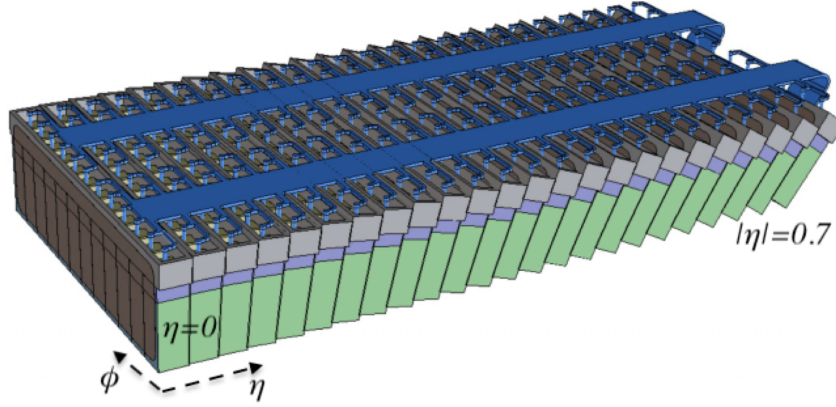


Figure 2.7: Schematic of the EMCal full-size super modules, which shows the strip structure composed of 24 strips, provided by ALICE [151].

When a particle interacts with the EMCal cell material, this produces a shower which spreads its energy over neighboring cells. When adjacent calorimeter cells contain an energy above the noise threshold, this is designated as a calorimeter “cluster”. These clusters are reconstructed with a clusterization algorithm, and can be produced by a single particle but can be the product of multiple particles interacting with the cell material. For particles which deposit their full energy in the calorimeter, such as electrons or photons, the reconstructed cluster energy is approximately equal to the particle’s energy [151], thus allowing for the direct identification of electrons. Tracks reconstructed with the ITS and TPC can be matched with EMCal clusters via track-matching algorithms. The distribution of the energy within a cluster, or the “shower shape”, is parameterized by an ellipse with short and long axes. Clusters from background particle species, such as slow neutrons, can be discarded by selecting clusters within a specific long axis range for analysis [151].

2.2.4 VZERO System

The V0 system is used for multiple roles for the ALICE experiment. It provides a minimum bias trigger for the central barrel detectors, provides centrality triggers in Pb–Pb collisions, acts as a centrality indicator, validates the signal for the muon trigger, and measures the luminosity for the experiment [139], [152].

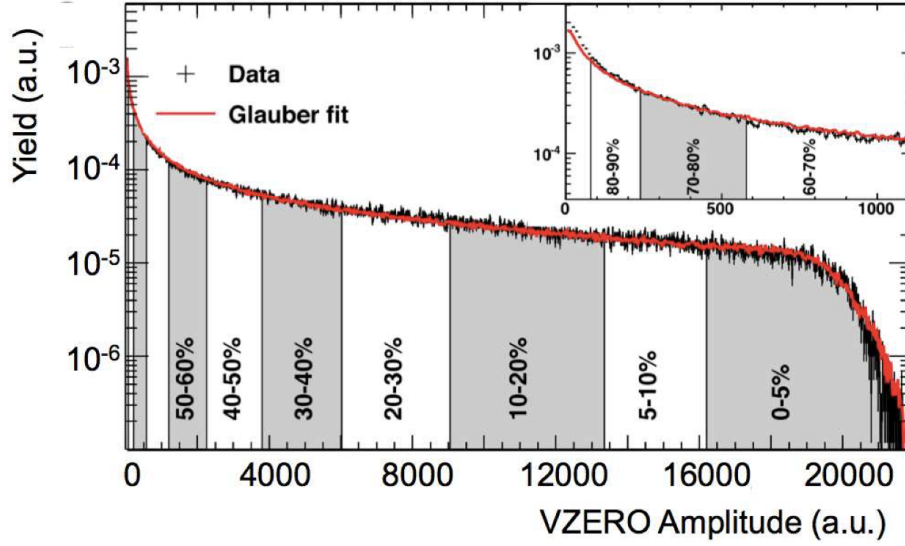


Figure 2.8: Distribution of the sum of amplitudes from the VZERO arrays (black) in Pb–Pb collisions at $\sqrt{s_{\text{NN}}} = 2.76$, where the red line is the Glauber model fit, provided by ALICE [152].

The V0 is composed of two scintillator arrays on each side of the interaction point, which cover the pseudorapidity ranges of $2.8 < \eta < 5.1$ (V0A) and $-3.7 < \eta < -1.7$ (V0C) [152]. Particle multiplicity is determined by the energy deposited in the VZERO scintillators, which is mapped to specific amplitudes in the arrays.

Heavy-ion collisions are classified into centrality percentiles by using the VZERO system multiplicity amplitudes fitted with the Glauber model [49], as seen in Fig. 2.8. The Glauber model serves to estimate the number of participating nucleons and binary nucleon-nucleon collisions as a function of the impact parameter in heavy-ion collisions [47], [49].

2.3 Data Acquisition and Processing

Recording, processing, and storing LHC collision data is a computationally monumental task. By 2015, the ALICE experiment alone recorded about 10 petabytes (10 million gigabytes) of collision data within a year [153]. Data acquisition for ALICE by Run 1 required a maximum aggregate bandwidth of 1.25 GB/s, for the purpose of transferring heavy-ion events with an average size of 12.5 MB at a rate of 100 Hz [154]. Data reconstruction in ALICE utilizes the computational resources of the Worldwide LHC Computing Grid (A.K.A. “the Grid”) via the framework of the ALICE LEGO Train system.

2.3.1 Worldwide LHC Computing Grid

The computational and memory demands of the LHC required at the beginning of LHC operation was roughly 15 petabytes of data, which was generated from the four major experiments. To address the computational demands to handle this data, the Worldwide LHC Computing Grid project was started in tandem with the operation of the LHC. This computational infrastructure was built to facilitate data analysis and storage for the LHC-affiliated physics community [154]. By 2004, the reconstruction and analysis of the data, which includes comparisons to theoretical simulations, requires of the order of 100,000 CPUs. Rather than centralizing this computing capacity at one site near the experiments, the LHC utilizes a globally distributed model for data storage and analysis: a computing grid [154].

The Grid consists of data acquisition systems and computational centers at 4 different tiers: Tier-0 centers are located at CERN, which perform the first-pass reconstruction and copies this data for storage. Further copies of the reconstructed data are passed on to the Tier-1 centers; this role of Tier-1 centers also vary by experiment. Generally, the Tier-1 centers are used for managing permanent data storage, which includes the raw, simulated, and processed data. Tier-2 centers are used to provide additional computational capacity and provide storage for Monte Carlo simulation and user-level analysis. By 2005, there were more than 100 Tier-2 centers distributed globally. At the Tier-3 level, the computing facilities at universities and laboratories perform additional processing and analysis of LHC data [154].

2.3.2 ALICE LEGO Train System

Analyzing a single dataset in ALICE generated in 2015 requires reading on the order of 10^5 files with a general size of 50 TB. Analysis jobs to be performed on the Grid were completed with the ALICE analysis (ALIPhysics) framework, where jobs were monitored and submitted using the MonALISA monitoring service. On top of these frameworks is the Lightweight Environment for Grid Operators (LEGO) train system. The purpose of the train system is to act as a workflow to increase the CPU efficiency of the analysis jobs on the Grid, with the intent to maximize the number of user analyses performed with the computing resources allotted. The system accomplishes this by reading the dataset once and running multiple combined analysis tasks on this set, which avoids the computational and memory requirements of loading and reading the data for every task separately [153].

The train system is divided into trains separated by physics working groups (such as jet analysis, heavy-flavor, correlations, etc.) and by collision datasets (pp, p–Pb, Pb–Pb, data or Monte Carlo). A user’s analysis code is submitted to the ALIPhysics repository. Once in the repository, the code is configured in a train “wagon” on the LEGO train web page, where user-defined parameters for the analysis are set. Multiple wagons containing one or more analysis tasks each are combined to create the entire train. The train is first tested with an automated procedure, and if the test is successful the train can run on the Grid. The full train contains all train wagons, but all wagons are tested individually and assigned their own memory allocation for analysis jobs. These jobs are merged together, and their output is linked to the LEGO train web page, where all successful train jobs and output are accessible to all ALICE users [153].

Chapter Three: Analysis Procedure

This chapter details the analysis procedure to obtain the azimuthal correlation measurement of electrons from heavy-flavor hadron decays in Pb–Pb collisions. First, an overview of the analysis is presented, which includes the momentum intervals chosen for this analysis and the motivation for this selection. This is followed by a high-level description of the analysis, a description of the dataset, and the steps of the formal procedure.

3.1 Analysis Overview

As described in Introduction section 1.7, the azimuthal correlation distribution provides a differential measurement of the jet angular profile. The correlation distribution is obtained by taking the difference of the azimuthal angle ($\Delta\varphi$) between a trigger particle (electron from heavy-flavor hadron decays) and the particles associated with that trigger (charged particles). The independent variable of the resulting correlation distribution is $\Delta\varphi$, and the dependent variable is the average number of associated particles (N). The distribution is normalized with respect to the number of trigger particles ($N^{\text{trig.}}$), such that the measurement is the angular distribution of the average number of particles associated with the trigger. The general form of the final distribution is represented in Eq. 3.1,

$$C(\Delta\varphi) \equiv \frac{1}{N^{\text{trig.}}} \frac{dN}{d\Delta\varphi}, \quad (3.1)$$

In this study, trigger electrons were selected in three p_{T}^{e} intervals: $4 - 12$, $4 - 7$, and $7 - 16$ GeV/ c . The latter two $p_{\text{T}}^{\text{trig.}}$ intervals will be referred to as the “split” intervals. The correlation was performed in five $p_{\text{T}}^{\text{assoc.}}$ intervals within $1 - 7$ GeV/ c to provide a measurement of the distributions in low to moderate associated p_{T} . A constraint of $p_{\text{T}}^{\text{trig.}} > p_{\text{T}}^{\text{assoc.}}$ is imposed to capture associated particles originating from the fragmentation of the same jet as the trigger. The $4 < p_{\text{T}}^{\text{e}} < 12$ correlations are shown to demonstrate all steps, but the split p_{T}^{e} intervals will also be discussed when the differences of electron p_{T} are relevant. These $p_{\text{T}}^{\text{trig.}}$ intervals were chosen due to two

related but distinct reasons: The first is to study the differences in jet fragmentation as a function of p_T by selecting trigger particles of high- vs low- p_T . The higher- p_T triggers are more likely to originate from high- p_T jets, therefore samples jets of different energies, and potentially different fragmentation profiles. The second reason was informed by previous studies of electrons from semi-leptonic hadron decays [155], which investigated the fraction of beauty hadron decays as a function of p_T . The fraction of electrons descending from beauty-hadron decays is approximately 40% of the electron yield at $p_T^e = 4$ GeV/ c , and increases to 60-70% at $p_T^e > 8$ GeV/ c . By studying azimuthal correlations in the split p_T^e ranges of $4 - 7$ vs $7 - 16$ GeV/ c , the corresponding correlations sample predominantly from charm vs beauty quark-initiated jets, respectively. Differences in the correlation observables could indicate a mass-dependence of the initiating quark on the jet fragmentation.

To obtain the correlation measurement, first, electron candidates are selected and correlated with associated charged particles in a two-dimensional correlation distribution ($S(\Delta\eta, \Delta\varphi)^{\text{ele. cand.}}$, Eq. 3.2),

$$S(\Delta\eta, \Delta\varphi)^{\text{ele. cand.}} \equiv \frac{d^2 N}{d\Delta\eta d\Delta\varphi}, \quad (3.2)$$

The 2D distribution is then corrected for the acceptance and detector effects. To reduce the fluctuations of the correlation, the 2D distribution is projected within $|\Delta\eta| < 1$. This results in a one-dimensional azimuthal distribution,

$$S(\Delta\varphi)^{\text{ele. cand.}} \equiv \frac{dN}{d\Delta\varphi}. \quad (3.3)$$

The $S(\Delta\varphi)^{\text{ele. cand.}}$ correlation distribution is composed of correlations of electrons as well as hadrons incorrectly identified as electrons. To remove the correlation contribution from these “contaminant” hadrons, a scaled azimuthal correlation distribution between hadrons and charged particles ($S(\Delta\varphi)^{\text{hadron}}$) is subtracted from the electron candidate distribution,

$$S(\Delta\varphi)^{\text{ele. cand.}} - S(\Delta\varphi)^{\text{hadron}} = S(\Delta\varphi)^{\text{electron}}. \quad (3.4)$$

The resulting distribution $S(\Delta\varphi)^{\text{electron}}$ contains trigger electrons from heavy-flavor (HFe) and non-heavy-flavor sources (non-HFe). To obtain the correlation distributions of electrons from heavy-flavor hadron decays, the correlation distribution of non-heavy-flavor electrons are subtracted from the electron distributions,

$$S(\Delta\varphi)^{\text{electron}} - S(\Delta\varphi)^{\text{Non-HFe}} = S(\Delta\varphi)^{\text{HFe}}. \quad (3.5)$$

The heavy-flavor decay electron distribution is normalized by the number of heavy-flavor decay electrons (N^{HFe}). After normalization, the associated particle efficiency and secondary contamination corrections are applied. The resulting distribution reflects the correlation of electrons with associated charged particles, but this correlation sits on a background of two sources: uncorrelated combinatorial pairs (which is expected to have a flat background), and the anisotropic flow (which contributes to the distribution peaks). These background sources to the correlation distribution are removed by means of a baseline function $B(\Delta\varphi)$,

$$B(\Delta\varphi) = b(1 + 2 \sum_n v_n^{\text{HFe}} v_n^{\text{assoc}} \cos(n\Delta\varphi)). \quad (3.6)$$

The correlation background described by the baseline is subtracted from the distribution. This results in the final distribution,

$$C(\Delta\varphi)^{\text{HFe}} \equiv \frac{1}{N^{\text{trig.}}} \frac{dN}{d\Delta\varphi}. \quad (3.7)$$

3.2 Dataset

Events from Pb–Pb collisions recorded by the ALICE experiment in the `LHC18q_pass3` and `LHC18r_pass3` run lists were selected to perform this measurement. These events were recorded after fulfilling the minimum-bias and centrality software trigger criteria. Minimum-bias-triggered events require a simultaneous signal in the ITS SPD and the V0 system [152] to initiate recording. Centrality-triggered events require the V0 system amplitude to fulfill the desired centrality criteria to initiate event recording. Each run, which typically consists on the order of thousands of collision events, are assigned a run number. After recording, each run was assessed for detector quality, and categorized accordingly. Because this analysis utilizes the central-barrel detectors for particle tracking and identification (ITS, TPC, and EMCal), only run numbers designated with high-quality readouts from these detectors were used. Events from these runs were selected when the reconstructed primary vertex was within ± 10 cm from the nominal interaction point ($z = 0$) along the beam axis. The analysis task

for this measurement was run on the ALICE LEGO train framework, which resulted in a total number of events: $N^{\text{events}} = 41.5 \times 10^6$ for the most-central collisions, and $N^{\text{events}} = 62.3 \times 10^6$ semicentral events.

Four simulated event datasets were used for this analysis. These samples were created from Monte Carlo event generators which are configured for the LHC18q_pass3 and LHC18r_pass3 datasets. The datasets LHC23d8a (0–10%) and LHC23d8b (30–50%) contain HIJING Pb–Pb-simulated events with additional heavy-flavor hadron semi-leptonic decays, and additional π^0 and η particles. This is used for obtaining the photonic electron tagging efficiency (described in section 3.6). The datasets LHC20e3b (0–10%) and LHC20e3c (30–50%) are general-purpose HIJING Pb–Pb-simulated events used for applying associated particle efficiency corrections (described in section 3.7).

3.2.1 Integrated Luminosity

The probability for two lead nucleons to undergo any interaction is the total Pb–Pb cross section, $\sigma_{\text{total}}^{\text{Pb–Pb}}$. This is a geometrical value determined from the largest Pb–Pb impact parameter which facilitates a nucleon-nucleon collision [48], [49]. The cross-section is related to the number of particles produced in a given unit of time, shown in Eq. 3.8:

$$\frac{dN}{dt} = \mathcal{L} \cdot \sigma_{\text{total}}^{\text{Pb–Pb}} \quad (3.8)$$

Where $\frac{dN}{dt}$ is the number of events per second, and \mathcal{L} is what is called the instantaneous luminosity [156]. Given in units of $\text{cm}^{-2}\text{s}^{-1}$, the instantaneous luminosity is a proportionality between the cross-section and the rate of events and is a measure of the number of beam interactions. The instantaneous luminosity can be used to quantify the performance of the experiment within a given data-taking period by calculating the integrated luminosity (\mathcal{L}^{int}) [156],

$$\mathcal{L}^{\text{int}} = \int_0^T \mathcal{L} dt \equiv \frac{N}{\sigma_{\text{total}}^{\text{Pb–Pb}}}. \quad (3.9)$$

Using equation 3.9, the total integrated luminosity for Pb–Pb collisions in a given centrality class is calculated as:

$$\mathcal{L}^{\text{int}} = \frac{N^{\text{events}}}{\sigma_{\text{total}}^{\text{Pb-Pb}} f^{\text{cent}}} \quad (3.10)$$

Where $\sigma_{\text{total}}^{\text{Pb-Pb}}$ is equal to $7.67 \pm 0.16(\text{syst.})\text{b}$ for $\sqrt{s_{\text{NN}}} = 5.02$ [48]; f^{cent} is the fraction of the centrality (0.1 and 0.2 for 0–10% and 30–50% percentile classes, respectively); and N^{events} is the number of events for each centrality class. For $N^{\text{events}} = 41.5 \times 10^6$ in the 0–10% centrality class, the corresponding integrated luminosity is $54 \mu\text{b}^{-1}$. For the $N^{\text{events}} = 62.3 \times 10^6$ in the 30–50% centrality class, the integrated luminosity is $41 \mu\text{b}^{-1}$.

3.3 Particle Tracking

Experimentally, particles are first distinguished by their tracks. Track reconstruction begins with finding the track clusters in the ITS and TPC. In the ITS, the clusters are generated from particles passing through the silicon sensors. As particles pass through the TPC, they ionize the gas and the electrons produced in this ionization drift to the endplates where they generate clusters in the TPC readout chambers. The coordinates of the crossing points are calculated as the cluster center of gravity. The crossing points in the first two layers of the SPD are used to reconstruct the primary vertex. The seeds of primary particle tracks are constructed from the two outer TPC pad rows and the primary vertex. Tracks are traced from the outer pad rows towards the primary vertex, which selects for more space points along the way and updates the track parameters and covariance matrix using the Kalman filter. The tracks are extrapolated down using the distance of closest approach (DCA) to the collision vertex, then propagated outwards through the ITS, TPC, and TRD. The track parameters are recalculated back to the DCA of the primary vertex. Using the Kalman filter, the primary vertex undergoes a final refitting using the reconstructed tracks and the beam-beam interaction information [157]. To ensure track quality for particle identification, there must be $50 < N^{\text{TPC clusters}} < 160$ associated with the track [147]. The number of crossed TPC pad rows by a track as well as the ratio of the number of clusters to crossed pad rows can be used as variables by which to make track quality cuts.

To facilitate measuring the jet fragmentation profile, both trigger and associated particles in this measurement must qualify as physical primaries. Physical primaries

are particles which originate from the primary vertex or from short-lived particles produced in the initial collision (in contrast to particles produced in later decay chains, which are secondary particles). Particles are defined as primary if they have a mean proper lifetime $\tau > 1 \text{ cm}/c$ and are produced directly in the collision. A particle is also classified as primary if its parent has $\tau < 1 \text{ cm}/c$ and the parent originates from a decay chain arising from the collision [158].

3.3.1 Electron candidate tracks

For the electron candidate tracks in this analysis, at least 70 pad rows must be crossed by the tracks, and a ratio cut of 0.8 crossed rows over findable clusters is imposed. These cuts select for high-quality tracks for reconstruction, and in tandem with the p_T^e ranges of the electrons measured, selects for tracks which are likely to reach the EMCal. Additionally, electrons are selected in the pseudorapidity region of $|\Delta\varphi| < 0.6$ to fall within the EMCal acceptance. Strict DCA cuts of 0.5 cm (in the x, y -plane) and 1.0 cm (on the z -axis) are applied to the electron candidate tracks to select for physical primaries, which captures electrons originating from heavy-flavor hadron decays. Particles produce a shower in the EMCal detector material, which is reconstructed into a cluster. TPC tracks and EMCal clusters are paired by the cluster-matching algorithm, where tracks and clusters must be within $\Delta\phi < 0.01$ and $\Delta\eta < 0.01$ [151] to be matched as pair. The total list of track selections for electron candidates is reported in Table 3.1.

3.3.2 Associated particle tracks

Charged particle tracks are selected as the associated particles in the correlation. Because they are identified using the TPC and do not need to be identified in the EMCal, they are selected in the pseudorapidity range of $|\Delta\eta| < 0.8$ and also have less TPC cut requirements compared to the trigger electrons. This allows for greater associated particle statistics for the correlation measurement and covers the full range of the central-barrel pseudorapidity acceptance. Similar DCA cuts are applied to the associated particle tracks to select for physical primaries.

The track cuts for associated charged particles are listed in Table 3.2.

Table 3.1: Track cuts used for electron candidate tracks.

Track property	Cut applied
Minimum number of ITS clusters	2
Minimum NCrossedRowsTPC	70
Minimum RatioCrossedRowsOverFindableClustersTPC	0.8
Maximum χ^2 per TPC cluster	4
ITS and TPC refit	yes
Hit on SPD layer	kAny
Maximum χ^2 per ITS cluster	36
EMCAL acceptance	$ \eta < 0.6, 80 < \phi < 187$
DCAL acceptance	$0.22 < \eta < 0.6, 260 < \phi < 320$
	$ \eta < 0.6, 320 < \phi < 327$
Pseudorapidity	$-0.6 < \eta < 0.6$
Maximum DCAxy	0.5
Maximum DCAz	1.

Table 3.2: Track selection cuts for associated particles.

Track property	Cut applied
Minimum NCrossedRowsTPC	60
Minimum RatioCrossedRowsOverFindableClustersTPC	0.6
Min number of TPC clusters	50
Maximum χ^2 per TPC cluster	4
Pseudorapidity	$-0.8 < \eta < 0.8$
DCAxy	0.5
DCAz	1.

3.4 Electron Identification

Electron identification is performed using the particle identification (PID) information from the TPC and EMCal. First, electron candidates are identified in the TPC based on their energy loss (dE/dx) in the detector gas. Then the energy measured from the EMCal clusters matched to the tracks is used with the track momentum to apply an EID selection. Additionally, a geometric selection based on the shape of the EMCal cluster is applied to increase the electron purity of the candidate track. The details of this process are elaborated in the following subsections.

3.4.1 TPC Selection

Electron candidates are identified using the number of standard deviations $n\sigma_e^{\text{TPC}}$ with respect to the average electron energy loss $\langle dE/dx \rangle$ in the TPC gas. Where $\langle dE/dx \rangle$ is the characteristic electron energy loss expected from Bethe-Bloch function described in 2.2.2. The distribution of $n\sigma_e^{\text{TPC}}$ for all tracks as a function of momentum is shown in Fig. 3.1.

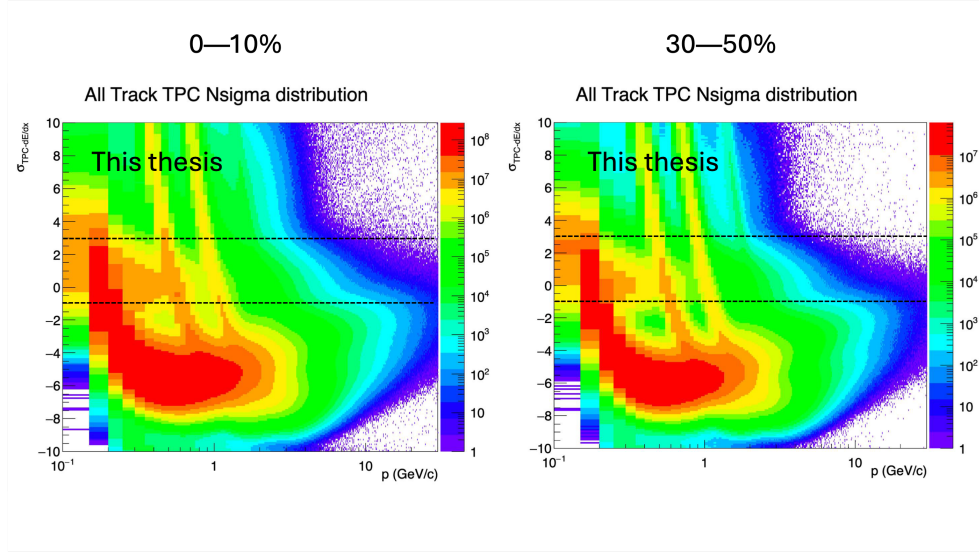


Figure 3.1: σ_e^{TPC} distribution as a function of p_T for 0–10% collisions (left) and for 30–50% collisions (right) measured for this thesis. The electron TPC cut is shown with a black dotted line.

As p_T increases, the dE/dx signal for some particle species overlaps with the electron signal. At $< 1 \text{ GeV}/c$ in momentum, the kaon signal overlaps with the electron, and eventually the pion and proton signals overlap as well. The dE/dx signal for all four particles (and eventually the deuteron) overlap within the other particles' respective $n\sigma^{\text{TPC}}$ distributions. This inevitably results in the signal of one particle contaminating the signal of a different species; in the context of this analysis, the electron signal is subject to contamination from hadrons. Electrons are selected by applying an asymmetric cut of $-1 < n\sigma_e^{\text{TPC}} < 3$. This cut removes a significant portion of pion contamination, which dominates in the range of $-3 < \sigma_e^{\text{TPC}} < -1$ at the p_T^e ranges measured for this analysis. Applying the $n\sigma_e^{\text{TPC}}$ effectively captures

the electron signal, but the hadron contamination that remains must still be dealt with.

3.4.2 EMCal Selection

The EMCal is used in tandem with the TPC for electron PID. Energy deposited in the EMCal and the momentum of the track can be utilized for electron PID by exploiting the E/p ratio for electrons. For electrons at relativistic energies, $E = \sqrt{m^2 + p^2} \approx p$, due to their low mass. This results in the E/p ratio of electrons to approximately equal 1. Therefore, a PID cut of $0.8 < E/p < 1.2$ was applied to select for electron candidate tracks.

Recall in chapter 2, when a particle interacts with the EMCal, the particle produces a shower in the detector material, which is reconstructed into a cluster. The EMCal clusterizer parameterizes clusters into an ellipse shape. The short axis (M20), and long axis (M02) of the clusters are used as additional selection criteria to resolve the electron signal. A shower shape of $0.02 < M02 < 0.9$ is applied to clusters belonging to electron candidate tracks to serve as an additional PID cut. This serves to capture the electron signal while removing the signal contamination from neutral particles [151]. If one wanted to select for hadrons, a TPC cut of $-10 < \sigma_e^{\text{TPC}} < -4$ and a shower shape cut of $0.2 < M02$ would be used. All specific electron ID cuts are reported in Table 3.3.

Table 3.3: Electron identification cuts

Cut parameters	Cut applied
σ_e^{TPC}	(-1, 3)
Shower shape long axis (M02)	(0.02, 0.9)
E/p	(0.8, 1.2)

3.4.3 Hadron contamination subtraction

Trigger electron candidates are composed of both electrons and hadrons incorrectly identified as electrons. The hadron contamination is evident in the E/p distribution of electron candidates shown in Fig. 3.2.

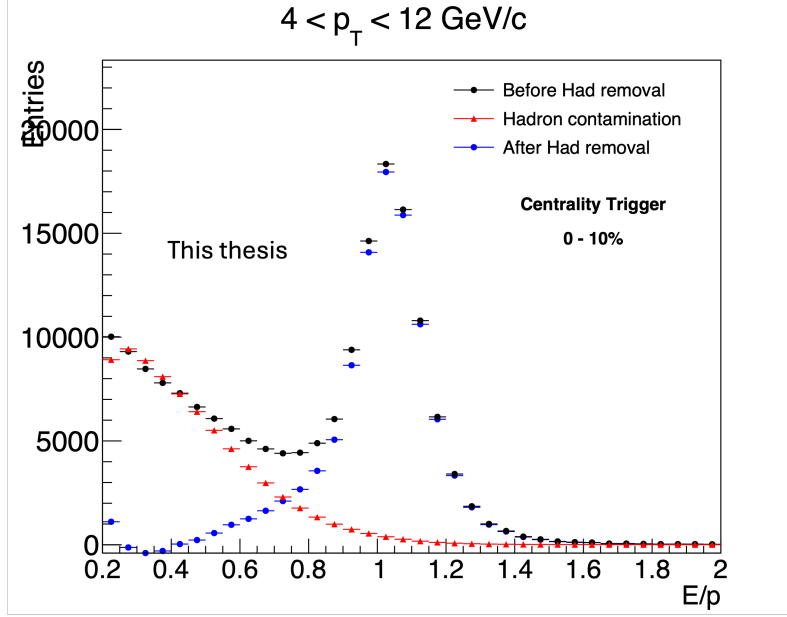


Figure 3.2: E/p distribution of electron candidates with $4 < p_T^e < 12$ GeV/ c , in the 0–10% centrality class. The black points are the distribution before hadron contamination subtraction. The red-point distribution is the E/p of particles selected with $-10 < \sigma_e^{\text{TPC}} < -4$ scaled to match the black distribution. Blue is after the contamination subtraction.

As expected of the electron E/p signal, the distribution exhibits a peak centered at 1. At $E/p < 1$, there is a second peak due to the hadron contribution. To account for this contamination, first trigger hadrons are selected using the same tracking, E/p , and shower shape cuts as the electron candidates, but which have a TPC cut of $-10 < \sigma_e^{\text{TPC}} < -4$ to select only hadron tracks. An E/p distribution is obtained for these trigger hadrons, which exhibits a similar peak in the low E/p region, but has a significantly larger magnitude. A scaling factor α is used to scale the hadron-trigger E/p to approximate the hadron contribution in the electron candidate E/p . To obtain α , the particle yield from the electron candidate E/p is obtained by integrating within the ranges of $0.25 < E/p < 0.5$ and is divided by the yield obtained in the hadron E/p in the same integration region. The $\alpha E/p$ (hadron) (red points in Fig. 3.2) is subtracted from the electron E/p to obtain the “pure” electron signal. This is repeated for all p_T^e intervals in both collision centrality classes.

The percentage of true electrons in the electron candidate sample, or the purity, can subsequently be quantified. This is defined as,

$$Purity^{\text{electron}} = \frac{\int_{0.8}^{1.2} E/p^{\text{had. subtracted}}}{\int_{0.8}^{1.2} E/p}. \quad (3.11)$$

Where the percentage of hadron contamination is $Contamination^{\text{hadron}} = 1 - Purity^{\text{electron}}$. For $4 < p_T^e \leq 12$ GeV/ c in the 0–10% (30–10%) centrality percentiles, the purity is valued at 95% (96%). As p_T^e decreases, the purity slightly increases, such as 97% for the $4 < p_T^e \leq 7$ GeV/ c , and the purity decreases with respect to increasing p_T^e , where it is valued at 93% for $7 < p_T^e \leq 16$ GeV/ c .

The electron candidate correlation distribution undergoes a similar correction. A hadron correlation distribution $S(\Delta\varphi)^{\text{hadron}}$ (which has undergone corrections described in section 3.5) is obtained by correlating the trigger hadrons with charged particles. The hadron distribution is scaled by a factor $N^{\text{Had. electron } E/p} / N^{\text{hadrons}}$. Where $N^{\text{Had. electron } E/p}$ is the number of hadrons from the scaled electron E/p distribution, and N^{hadrons} is the number of trigger hadrons. The scaled hadron correlation distribution is subtracted from the electron candidate distribution (Eq. 3.12) to obtain the inclusive electron distribution, seen in Fig. 3.3.

$$S(\Delta\varphi)^{\text{electron}} = S(\Delta\varphi)^{\text{ele. cand.}} - S(\Delta\varphi)^{\text{hadron}}. \quad (3.12)$$

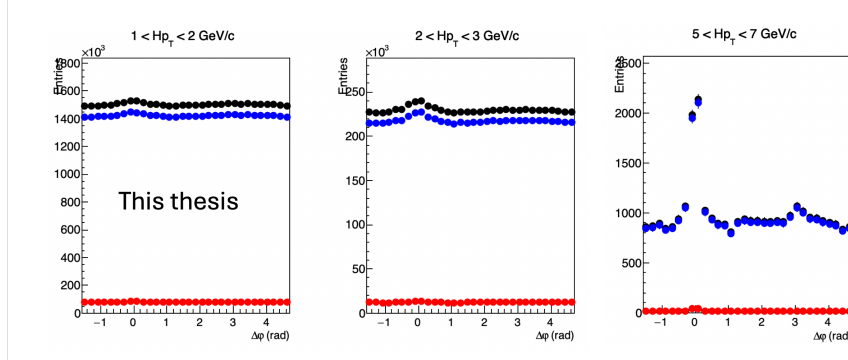


Figure 3.3: Correlation distributions for inclusive electrons before (black) and after (blue) subtraction of hadron contamination (red) for events in the 0–10% centrality class.

3.5 Mixed-event Correction

Electron candidates are correlated with associated charged particles both in azimuth ($\Delta\varphi$) and pseudorapidity ($\Delta\eta$) to obtain the 2D correlation distribution. This is shown for different $p_T^{\text{assoc.}}$ intervals in Fig. 3.4,

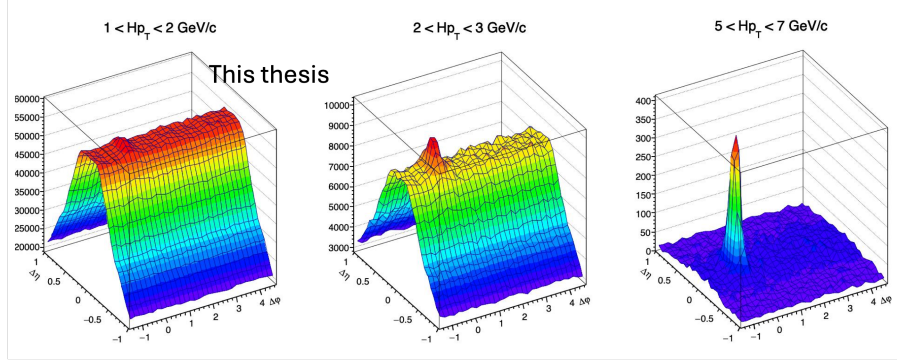


Figure 3.4: Two-dimensional ($\Delta\eta, \Delta\varphi$) correlation distribution of electron candidates with charged particles, for $4 < p_T^e < 12$ GeV/c in the most-central events. The triangular shape of the distribution in $\Delta\eta$ is due to the limited rapidity coverage of the detector. The distribution is also affected by detector inefficiencies and inhomogeneities.

The limited acceptance range of the detectors, along with other effects such as dead or noisy channels will affect the distribution $C(\Delta\varphi)^{\text{HFe}}$ if not corrected. These effects can be removed by performing a mixed-correction procedure: This correlates associated particles with triggers from separate but similar events, resulting in a distribution which captures the acceptance and detector effects. This mixed event distribution $ME(\Delta\eta, \Delta\varphi)$ is used to correct the same event ($SE(\Delta\eta, \Delta\varphi)$) distributions [159] such as in Fig. 3.4.

The events are categorized into pools which group similar VtxZ (z -vertex) positions and centrality classes. The ranges of the event pools are binned as follows:

- 0–10% centrality events
 - Centrality percentile bin : (0,1), (1,2), (2,3), (3,5), (5,7.5), (7.5,10)
 - VtxZ(cm) bin : (-10,-5), (-5,-2), (-2,0.5), (0.5,3), (3,6), (6,10)
- 30–50% centrality events

- Centrality percentile bin : (30,32), (32,35), (35,38), (38,41), (41,45), (45,50)
- VtxZ(cm) bin : (-10,-5), (-5,-2), (-2,0.5), (0.5,3), (3,6), (6,10)

The size of the centrality pool bin decreases as the collision percentile increases. This is done to account for the higher particle multiplicity in the lower percentile (greater centrality) events. The asymmetry in the VtxZ bins accounts for the shift in the VtxZ distribution centered around $VtxZ = 0.5$ for Pb–Pb collisions. A minimum of three events are required in each pool before the corresponding particles can be selected.

Electron candidates are correlated with associated particles from their common event pools to create the mixed-event distributions, $ME(\Delta\eta, \Delta\varphi)$. Figure 3.5 shows $ME(\Delta\eta, \Delta\varphi)$, which exhibits the same triangular structure as $SE(\Delta\eta, \Delta\varphi)$, minus the correlation peaks.

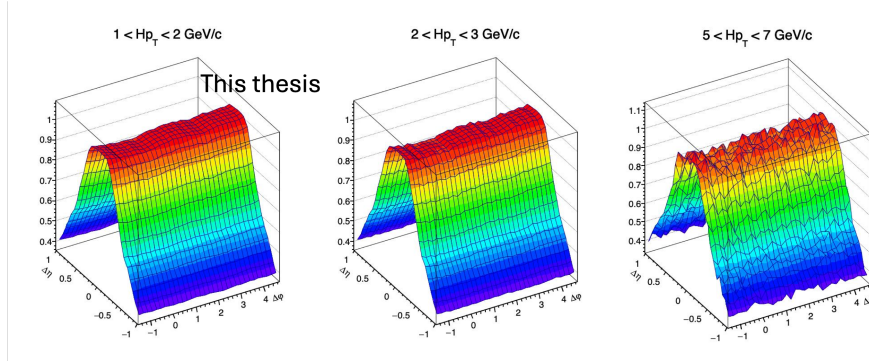


Figure 3.5: Mixed event $(\Delta\eta, \Delta\varphi)$ distribution between inclusive electrons and charged particles normalized by β (yield from $(\Delta\eta, \Delta\varphi) = (0,0)$) for $4 < p_T^e < 12$ GeV/c and in different associated charged particle p_T intervals for 0–10% centrality class events.

At $\Delta\varphi, \Delta\eta \approx 0$, the trigger electron and associated particles experience the same detector effects. By exploiting this property, a β factor is obtained to normalize the mixed-event distribution. β is calculated as particle yield at $(\Delta\eta, \Delta\varphi) = (0,0)$. The mixed event distribution is divided by the β factor to obtain the normalized mixed-event distribution, $ME_{\text{Norm}}(\Delta\eta, \Delta\varphi)$,

$$ME_{\text{Norm}}(\Delta\eta, \Delta\varphi) = \frac{1}{\beta} ME(\Delta\eta, \Delta\varphi). \quad (3.13)$$

The acceptance-corrected signal distribution ($S(\Delta\eta, \Delta\varphi)$) is obtained by dividing the same-event distribution by the normalized mixed-event distribution, seen in Fig. 3.6:

$$S(\Delta\eta, \Delta\varphi) = \beta \times \frac{SE(\Delta\eta, \Delta\varphi)}{ME(\Delta\eta, \Delta\varphi)} \quad (3.14)$$

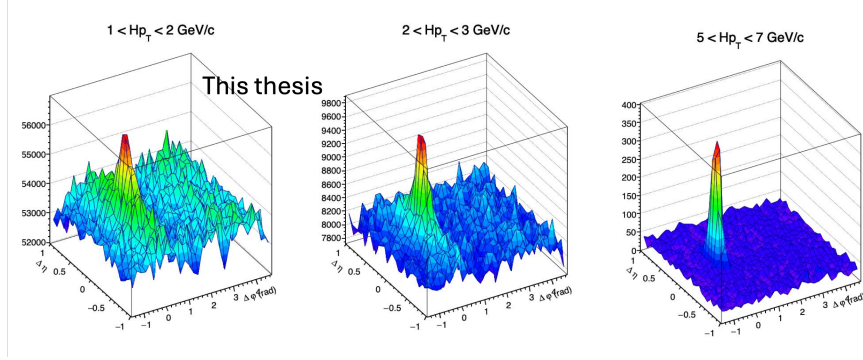


Figure 3.6: Mixed-event-corrected 2D correlation distribution between inclusive electrons and charged particles for $4 < p_T^e < 12$ GeV/ c and in different associated charged particle p_T ranges for 0–10% centrality class events.

The mixed-event correction procedure is applied to the distributions in every associated $p_T^{\text{assoc.}}$ interval for all correlation distributions measured in the analysis. The one-dimensional azimuthal correlation distribution $S(\Delta\varphi)^{\text{ele. cand.}}$ is obtained by integrating over the range $|\Delta\eta| < 1$, which reduces the fluctuations of the measurement.

3.6 Non-HFe Background Subtraction

There are multiple sources which contribute to the electron spectrum produced in hadronic collisions. The electrons may originate from:

- The semi-leptonic decay of heavy-flavor hadrons
- Dalitz decays of light neutral mesons
- Photon conversion within the detector material
- The weak decays of K mesons and the di-electron decays of light vector mesons

- Di-electron decays of quarkonia
- Partonic hard scattering, such as Drell-Yan production and prompt photon production
- W^\pm , Z, and Higgs boson decays

In the trigger p_T ranges studied in this analysis, electrons from the semi-leptonic decay of HF hadrons, electrons from Dalitz decays, and from photon conversion in the detector material dominate, while the other sources are negligible. For brevity, these electrons from Dalitz decays and photon conversion will be referred to as the “photonic” electron background. Electrons from the semi-leptonic HF hadron decays are produced individually, whereas photonic electrons are produced in pairs. This property can be exploited to identify and separate these background electrons.

3.6.1 Photonic electron production

Electron-positron pair production can occur from photons above energies of $2m_e c^2$ (> 1.022 MeV) when the photon interacts with the Coulomb field of an atomic nucleus [160]. Photons measured by ALICE predominantly originate from π^0 and η mesons, which both have a $meson \rightarrow \gamma\gamma$ decay channel branching ratio of approximately 99% and 39%, respectively [11], [161]. These photons can then interact with the detector material of the ALICE central barrel and convert to an electron-positron pair [161], [162].

In addition to the di-photon decay, the η and π^0 mesons also undergo Dalitz decays. A Dalitz decay is the three-body decay of electrically neutral pseudoscalar mesons into a di-lepton pair which are accompanied by a sister photon or vector meson [163]. For π^0 , the branching ratio of the $\pi^0 \rightarrow \gamma e^- e^+$ Dalitz decay is approximately 1%. The equivalent decay for η has a branching ratio of 7×10^{-3} . However, the branching ratio of $\eta \rightarrow 3\pi^0$ is 33%, which would significantly contribute to the number of π^0 mesons and their subsequent decays. Despite these relatively small branching fractions, because both π^0 and η are produced in such large quantities in hadronic collisions, electrons from the Dalitz decays provide a significant contribution to the photonic electron spectra.

3.6.2 Unlike-sign and Like-sign correlations

To estimate the photonic electron contribution, electrons (or positrons) which pass the trigger electron tracking and electron ID cuts are paired with a partner electron (or positron) in two ways: partners which have opposite charges (dubbed unlike-sign pairs, ULS) or which have the same charge (like-sign, LS) to the trigger electron. The partner electrons are identified by a loose dE/dx cut of $-3 < \sigma_e^{\text{TPC}} < 3$ and undergo similar tracking cut criteria to the associated charged particles and are not identified in the EMCal. Due to the drop in detector tracking performance at very low p_T , partner electrons have minimum p_T requirement of $> 0.3 \text{ GeV}/c$. Additionally, χ^2/NDF cuts are imposed on the reconstructed parent vertex to ensure that the electron pairs originate from photon conversion or Dalitz decays. The partner electron cuts are summarized in Table 3.4.

Table 3.4: Additional track selection cuts used for associated electrons.

Track property	Cut applied
Minimum NCrossedRowsTPC	60
Min number of TPC clusters	50
Minimum RatioCrossedRowsOverFindableClustersTPC	0.6
Maximum χ^2 per TPC cluster	4
Min p_T (GeV/ c)	0.3
Pseudorapidity	$-0.9 < \eta < 0.9$
PID cut	$-3 < \sigma_e^{\text{TPC}} < 3$
Maximum DCAxy	0.5
Maximum DCAz	1.

The invariant mass is calculated from the electron pairs. The invariant mass spectrum of unlike-sign pairs is characterized by a peak at $\text{GeV}/c \approx 0$ (shown in Fig. 3.7, plotted in blue). Because the additional photon is not reconstructed with the pairs originating from the Dalitz decays, there are no characteristic invariant mass peaks for the π^0 and η . However, the electrons from these sources contribute to the invariant mass up to approximately $0.14 \text{ GeV}/c^2$ [164].

In the invariant mass reconstruction process, random combinations of electron-positron pairs result in combinatorial background to the distribution. The combinatorial background is estimated with the LS invariant mass distribution (shown in Fig. 3.7, plotted in red).

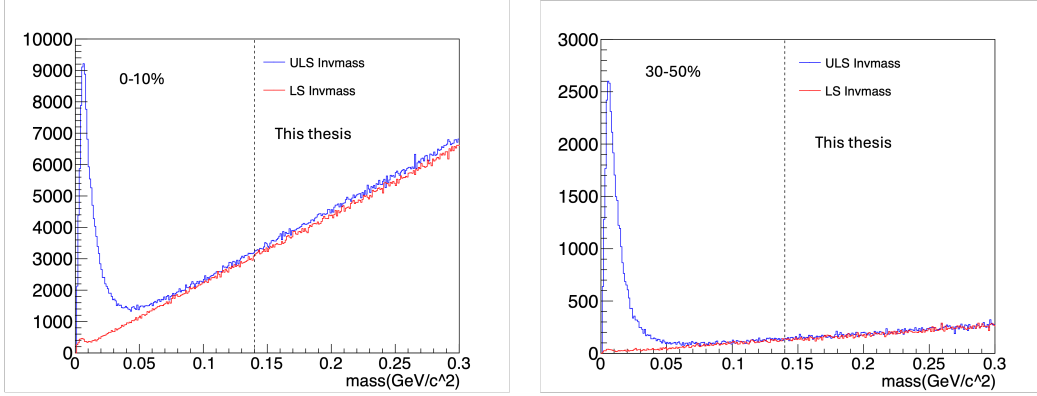


Figure 3.7: Invariant mass distribution for the like-sign (red) and unlike-sign (blue) electron pairs for $4 < p_T^e < 12$ GeV/c for 0–10% (left) and 30–50% (right) centrality collisions. The difference between the like-sign and unlike-sign distribution is more noticeable in the 0–10% centrality.

The like-sign invariant mass spectra has no characteristic peak at $\text{GeV}/c \approx 0$, but it does contain the combinatorial background from the reconstruction. However, experimentally the combination of $e^\mp e^\pm$ exceeds the $e^\mp e^\mp$ combinations. Therefore, due to the large background accumulated in the Pb–Pb environment, the asymmetry of these pairs are amplified, so the LS distribution does not entirely match the ULS contribution. Therefore, the LS invariant mass distribution is scaled to match the ULS within the range $0.2 < \text{GeV}/c^2 < 0.25$, seen in Figure 3.7. This range was chosen because it fit outside of the Dalitz decay contribution to the invariant mass. The values of the scaling factors are 1.045 for both the 0–10% and 30–50% centrality classes of electrons with $4 < p_T^e < 12$. Figure 3.8 shows the invariant mass distributions after the scaling factors are applied.

A cut of $m_{e^-e^+} < 0.14 \text{ GeV}/c^2$ is applied to both the ULS and LS invariant mass distributions to obtain the photonic electron signal. This upper threshold of $0.14 \text{ GeV}/c^2$ was chosen because this captures approximately 98% of π^0 and η Dalitz decays [164]. The number of the reconstructed photonic electrons is estimated by subtracting LS from the ULS signal.

Electrons which pass the trigger electron criteria and are successfully matched with ULS and LS partners which fulfill $m_{e^-e^+} < 0.14 \text{ GeV}/c^2$ are correlated with charged particles to obtain the $S(\Delta\varphi)^{\text{ULS}}$ and $S(\Delta\varphi)^{\text{LS}}$ distributions, respectively. To account for photonic electrons lost due to the reconstruction procedure, the dis-

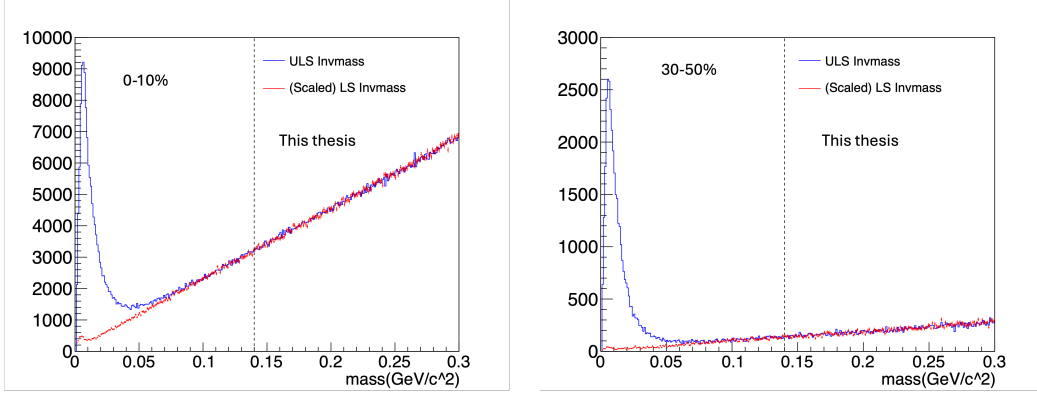


Figure 3.8: Invariant mass distribution for the like-sign (red) (after scaling) and unlike-sign (blue) electron pairs for $4 < p_T^e < 12$ GeV/ c for 0–10% and 30–50% collisions.

tribution $(S(\Delta\varphi)^{\text{ULS}} - S(\Delta\varphi)^{\text{LS}})$ is corrected by the tagging efficiency (ϵ_{tag}). This efficiency is obtained from Monte Carlo simulations using electrons “tagged” as originating from Dalitz decays and photon conversion.

3.6.3 Tagging efficiency

The specific datasets used to estimate the tagging efficiency are listed in section 3.2 and consist of events generated with HIJING v.136 [84] simulations of Pb–Pb collisions. Particle propagation through the ALICE detector is simulated using GEANT3 [165]. For the purpose of improving the statistical precision of the tagging efficiency, additional π^0 and η mesons are generated with PYTHIA 6.4.25 [83] and are embedded within the simulated sample, which extends the p_T spectra of both particles to 50 GeV/ c . These high p_T spectra is required to account for decay chains such as $\eta \rightarrow \pi^0 \rightarrow \gamma \rightarrow e^\pm$ that produce up to 16 GeV/ c electrons. However, this artificially injected spectra is flat as a function of p_T (Figure 3.9) and must be corrected using a weighting factor before the tagging efficiency can be calculated. For the Monte Carlo reconstruction, the following decay channels were taken into account when selecting photonic electrons:

1. $\gamma \rightarrow e^-e^+$
2. $\pi^0 \rightarrow \gamma\gamma$

3. $\pi^0 \rightarrow \gamma e^- e^+$
4. $\eta \rightarrow \gamma\gamma$
5. $\eta \rightarrow \gamma e^- e^+$
6. $\eta \rightarrow 3\pi^0$

Where this list is not entirely exhaustive, since the photonic electrons can also originate from very rare decays such as $\eta \rightarrow 2e^- 2e^+$, but decays such as these are automatically included in the reconstruction.

The weights to apply to the embedded π^0 and η spectra are obtained by taking the ratio of the π^0 and η which originate from HIJING to the flat spectra (HIJING/embedded). This ratio is fit with the Hagedorn function ($f = p_0 \times (e^{-p_1 x - p_2 x^2} + \frac{x}{p_3})^{-p_4}$) to parameterize the enhanced sample, which is shown in Figure 3.10 for 0–10% collisions.

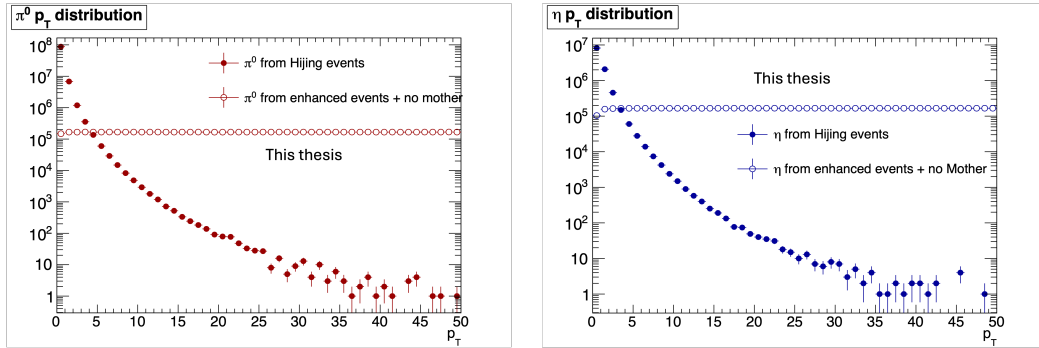


Figure 3.9: Spectra of π^0 and η from HIJING compared to the spectra of the artificially embedded spectra generated by PYTHIA.

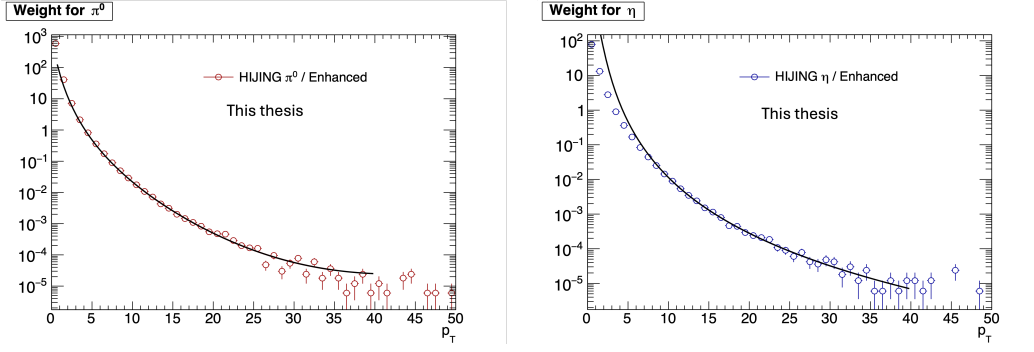


Figure 3.10: Ratio of HIJING to PYTHIA spectra of π^0 and η fit with the Hagedorn function.

Applying the weighting factor to correct the flat π^0 and η spectra subsequently changes the daughter electron p_T spectra to create an unbiased distribution. The effect on the electron p_T spectra is seen in Fig. 3.11; the weighting procedure is repeated for the 30–50% centrality class MC sample.

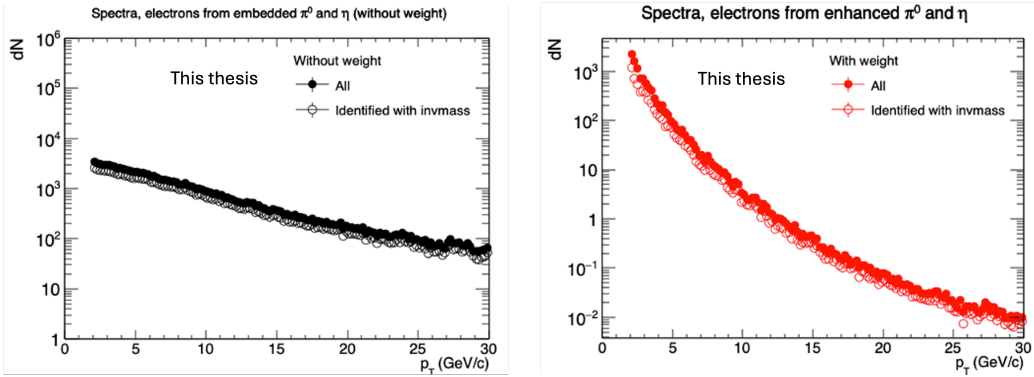


Figure 3.11: Monte Carlo p_T spectra of electrons from π^0 and η . (Left) shows the spectra of electrons when no weight is applied to the parent particles. (Right) shows the spectra of electrons after the weight is applied. Open circles for both figures represent electrons which pass the reconstruction procedure, and closed circles are all electrons identified as photonic.

The tagging efficiency is defined by the ratio of photonic electrons which pass the reconstruction procedure to all photonic electrons in the Monte Carlo sample. The numerator and denominator spectra are shown in Fig. 3.11, where the open circle distributions are the spectra of the reconstructed photonic electrons, and the closed circles represent the spectra of all photonic electrons in the sample. Figure 3.12 shows

the resulting tagging efficiency obtained from these two spectra. For collisions in the 0–10% (30–50%) centrality interval, the tagging efficiency is $57 \pm 1\%$ ($61 \pm 1\%$) at $p_T^e = 4 \text{ GeV}/c$, and approximately $65 \pm 1\%$ ($68 \pm 1\%$) at $p_T^e = 7 \text{ GeV}/c$. For $p_T^e > 8 \text{ GeV}/c$, the tagging efficiency is approximately constant with a value of $70 \pm 1\%$ for both centrality classes.

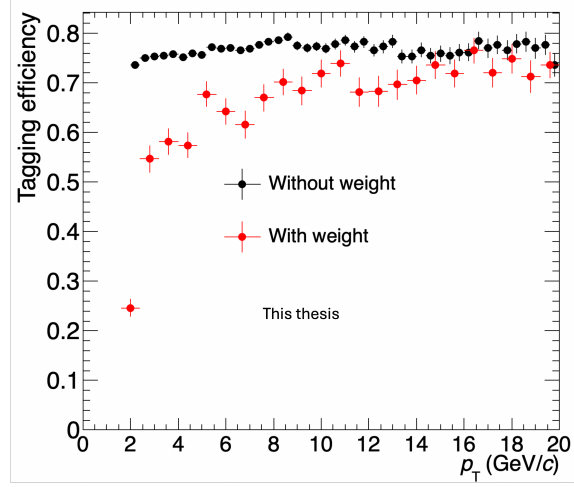


Figure 3.12: Tagging efficiency distribution for the photonic electron reconstruction for 0–10% events.

The resulting photonic electron (Non-HFe) correlation distribution, which consists of electrons tagged as photonic are correlated with charged particles are given as:

$$S(\Delta\varphi)^{\text{Non-HFe}} = \frac{1}{\epsilon_{\text{tag}}} [S(\Delta\varphi)^{\text{ULS}} - S(\Delta\varphi)^{\text{LS}}]. \quad (3.15)$$

And the number of photonic electrons ($N^{\text{Non-HFe}}$) are determined via:

$$N^{\text{Non-HFe}} = \frac{1}{\epsilon_{\text{tag}}} (N^{\text{ULS}} - N^{\text{LS}}). \quad (3.16)$$

Where N^{LS} is corrected by the same scaling factor used for the invariant mass distribution. After this procedure, the correlation distributions of heavy-flavor hadron decays can be determined,

$$S(\Delta\varphi)^{\text{HFe}} = S(\Delta\varphi)^{\text{electron}} - S(\Delta\varphi)^{\text{Non-HFe}}. \quad (3.17)$$

And the N^{HFe} is determined by:

$$N^{\text{HFe}} = N^{\text{electron}} - N^{\text{Non-HFe}}. \quad (3.18)$$

3.7 Associated particle corrections

The electron from heavy-flavor hadron decay correlation distribution is normalized by N^{HFe} such that the distribution reflects the number of associated particles in $\Delta\varphi$ per HF electron.

$$C(\Delta\varphi)^{\text{HFe}} = \frac{1}{N^{\text{HFe}}} S(\Delta\varphi)^{\text{HFe}} \quad (3.19)$$

Due to the track selections applied to the associated particles, some particles are lost in the track reconstruction process. Additionally, some secondary particles end up contaminating the associated particle signal. The efficiency and secondary contamination must be corrected to obtain the final distribution.

3.7.1 Charged particle tracking efficiency

To correct for the particles lost in reconstruction, a tracking efficiency is applied to the $C(\Delta\varphi)^{\text{HFe}}$ distribution for each associated p_{T} interval to account for associated particles missed in the track reconstruction. The associated particle tracking efficiency is estimated using general purpose Monte Carlo samples mentioned in section 3.2. This is obtained by taking the ratio of charged particles which pass the track reconstruction over all charged particles in the Monte Carlo sample (Fig. 3.13).

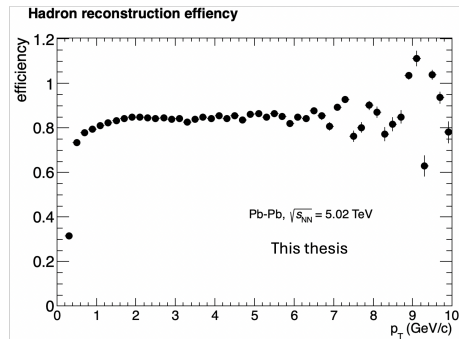


Figure 3.13: Tracking efficiency distribution for associated charged particles in the 0–10% centrality class.

This is performed for both centrality percentiles, and an efficiency is obtained for the five associated p_T intervals (1 - 2, 2 - 3, 3 - 4, 4 - 5, 5 - 7 GeV/ c). This is repeated for both centrality classes. In the interval $1 < p_T^{\text{assoc.}} < 7$ GeV/ c , for 0–10% (30–50%) collisions, the efficiency is 82–85% (86–87%).

3.7.2 Secondary particle contamination

To estimate the contamination of the secondary particles in the associated particle sample, a physical primary purity distribution is determined. This is done by taking the ratio of the p_T spectra of charged particles which are designated “Physical Primary” to the spectra of all charged particles. This is shown in Fig. 3.14.

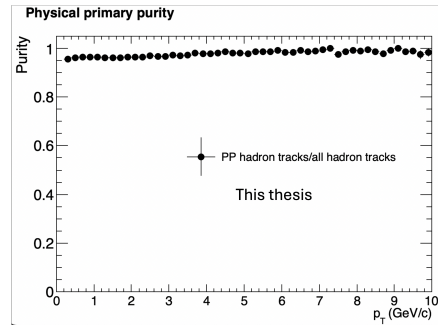


Figure 3.14: Physical primary fraction distribution of charged particles in the 0–10% centrality class.

For the 0–10% centrality class, the estimated amount of secondary hadrons is 2–4% (1–4%) for 0–10% (30–50%) collisions. Similarly to the tracking efficiency, the secondary particle contamination ($Purity^{\text{assoc.}}$) correction is applied to $C(\Delta\varphi)^{\text{HFe}}$ in each associated p_T interval. This is shown in Eq. 3.20,

$$\left(\frac{Purity^{\text{assoc.}}}{Efficiency^{\text{assoc.}}}\right)C(\Delta\varphi)^{p_T^{\text{assoc.}}}. \quad (3.20)$$

3.8 Correlation Background Subtraction

After all corrections are applied, the correlation distribution contains both correlated signal and a distribution background. This background must be fit with a baseline function $B(\Delta\varphi)$ and subtracted from the correlation distribution to obtain the final

distribution from which the per-trigger yields can be extracted. In comparison to pp and p–Pb collisions, Pb–Pb collisions are characterized by a large background of uncorrelated pairs due to the particle multiplicity, which is one background source. An additional background source is from anisotropic flow. To estimate these background contributions, the baseline function is defined as,

$$B(\Delta\varphi) = b(1 + 2 \sum_n v_n^{\text{HFe}} v_n^{\text{assoc}} \cos(n\Delta\varphi)). \quad (3.21)$$

Where b is the pedestal parameter of the background, and v_n^{HFe} and v_n^{assoc} are the n -th order harmonic flow coefficients of the trigger and associated particles. The background due to uncorrelated pairs is assumed to be flat and contributes to a non-zero b value. The anisotropic flow contribution results in a modulation seen in $\Delta\phi$ which contributes to the correlation peak shapes. The values of v_n^{HFe} and v_n^{assoc} are taken from previous measurements, but the value of b is not known *a priori* and must be estimated.

3.8.1 Anisotropic flow estimation

Only the v_2 and v_3 flow coefficients are considered for this study, due to the negligible effect the higher order coefficients ($n > 3$) would have on the correlation. The heavy flavor electron flow coefficients used in this analysis are taken from measurements of the ATLAS experiment on muons from HF decay measured at 0–10% and 30–40% centrality classes [166] due to the lack of electron measurements in this full centrality range. Because v_n is a measure of anisotropic flow as a function of p_T , the electrons and muons from heavy-flavor hadron decays are expected to have similar kinematics. Therefore, the heavy-flavor decay muon v_n can be used in place of the heavy-flavor decay electron. The spectra of heavy-flavor decay muons are also taken from an ATLAS measurement [167] for the purpose of obtaining a statistically weighted flow coefficient corresponding to the p_T ranges used in this analysis. The flow coefficients and spectra of charged particles were measured by ALICE in 0–10% and 30–50% centrality percentiles and are used for this analysis [168], [169].

To obtain the statistically-weighted v_n values, the spectra measured in the papers are weighted by the inverse of the measured variance to create the corresponding spectra in the p_T intervals that the v_n are measured.

$$yield^{combined} = \frac{\sum_{i=1} (\frac{1}{\sigma_i^2}) (yield)_i}{\sum_{i=1}^i \frac{1}{\sigma_i^2}} \quad (3.22)$$

For the charged particles, the v_n values are measured in centrality intervals 0–5%, 5–10% and 30–40%, 40–50%. The v_n for these intervals are combined to match the analysis centrality by obtaining spectra-weighted average. The v_2 and v_3 distributions are shown for charged particles in Figs. 3.15 and 3.16.

$$\nu_n^{combined} = \frac{\sum_{i=1} (\nu_2^i \times yield^i)}{\sum_{i=1} yield^i} \quad (3.23)$$

The measured statistical and systematic errors from the v_n measurements are combined in quadrature and are combined following a similar spectra-weighted average.

$$\sigma_{v_n^{combined}}^{stat} = \frac{\sum_{i=1} (\sigma_{v_n^i}^{stat} \times yield^i)}{\sum_{i=1} yield^i} \quad (3.24)$$

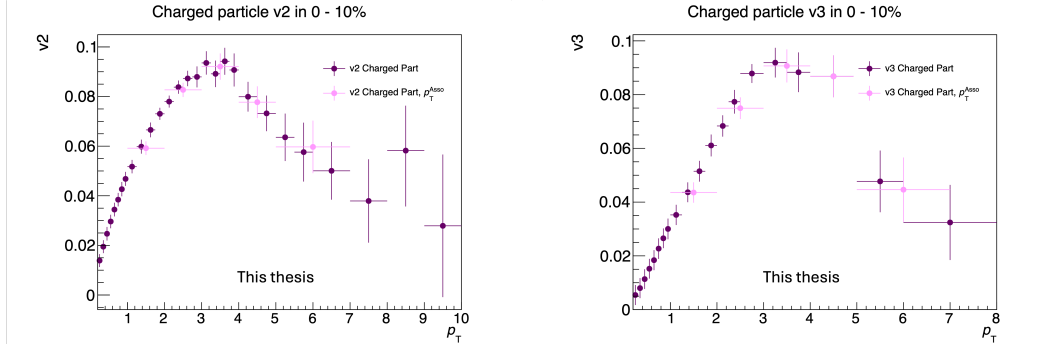


Figure 3.15: The p_T distribution of charged particle v_2 (left) and v_3 (right) shown for the 0–10% centrality percentile.

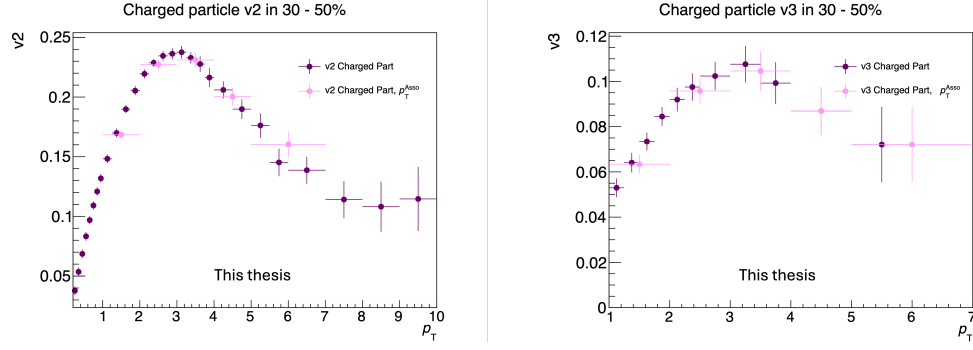


Figure 3.16: The p_T distribution of charged particle v_2 (left) and v_3 (right) shown for the 30–50% centrality percentiles. Notice the larger magnitude of v_2 for this centrality.

Both the v_2 and v_3 for all p_T^e intervals are shown in Figs. 3.17 and 3.18.

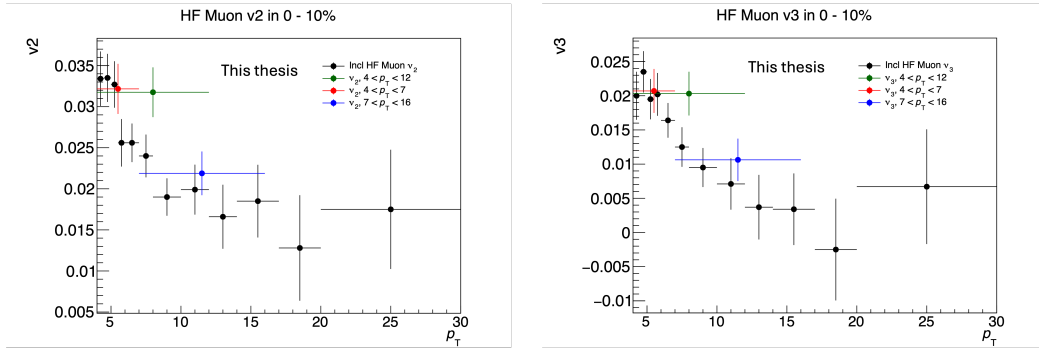


Figure 3.17: The flow coefficients v_2 (left) and the v_3 (right), calculated for the three trigger p_T^e ranges studied in this analysis using a statistically-weighted average in the 0–10% centrality class.

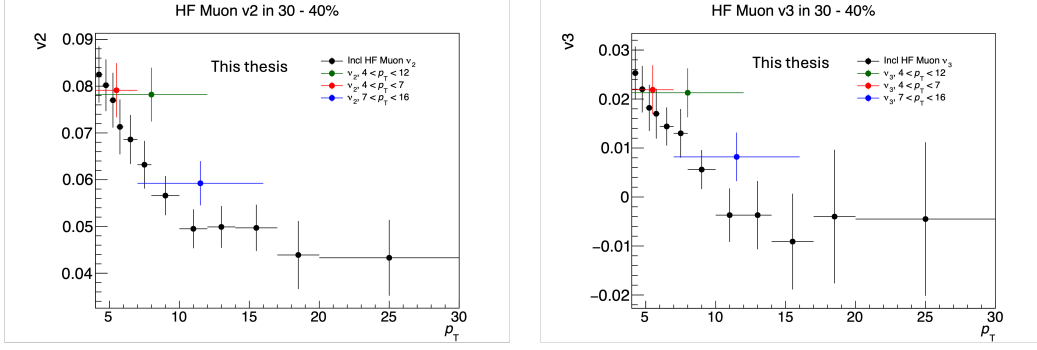


Figure 3.18: The flow coefficients v_2 (left) and the v_3 (right), calculated for the three trigger p_T^e ranges studied in this analysis using a statistically-weighted average in the 30–50% centrality class.

Tables 3.5 through 3.8 report the final v_n values used in the analysis along with the corresponding uncertainty.

Table 3.5: Values for v_2 used in baseline function in 0–10% centrality.

Particle	p_T range (GeV/c)	v_2	Error
HF hadron decay electron	4 – 12	0.03176	+ / – 0.00303
HF hadron decay electron	4 – 7	0.032163	+ / – 0.00305
HF hadron decay electron	7 – 16	0.02188	+ / – 0.00266
Charged particle	1 – 2	0.05918	+ / – 0.00276
Charged particle	2 – 3	0.08269	+ / – 0.00287
Charged particle	3 – 4	0.09207	+ / – 0.00531
Charged particle	4 – 5	0.07773	+ / – 0.00639
Charged particle	5 – 7	0.05970	+ / – 0.01060

Table 3.6: Values for v_2 used in baseline function in 30–50% centrality.

Particle	p_T range (GeV/c)	v_2	Error
HF hadron decay electron	4 – 12	0.07820	+ / – 0.00576
HF hadron decay electron	4 – 7	0.07913	+ / – 0.00581
HF hadron decay electron	7 – 16	0.05923	+ / – 0.00474
Charged particle	1 – 2	0.16839	+ / – 0.00363
Charged particle	2 – 3	0.22720	+ / – 0.00383
Charged particle	3 – 4	0.23105	+ / – 0.00583
Charged particle	4 – 5	0.20037	+ / – 0.00756
Charged particle	5 – 7	0.16031	+ / – 0.01082

Table 3.7: Values for v_3 used in baseline function in 0–10% centrality.

Particle	p_T range (GeV/ c)	v_3	Error
HF hadron decay electron	4 – 12	0.04367	+ / – 0.003803
HF hadron decay electron	4 – 7	0.02070	+ / – 0.00321
HF hadron decay electron	7 – 16	0.01063	+ / – 0.00310
Charged particle	1 – 2	0.043567	+ / – 0.003803
Charged particle	2 – 3	0.07495	+ / – 0.004040
Charged particle	3 – 4	0.09068	+ / – 0.006163
Charged particle	4 – 5	0.08680	+ / – 0.007807
Charged particle	5 – 7	0.04463	+ / – 0.011987

Table 3.8: Values for v_3 used in baseline function in 30–50% centrality.

Particle	p_T range (GeV/ c)	v_3	Error
HF hadron decay electron	4 – 12	0.02128	+ / – 0.00500
HF hadron decay electron	4 – 7	0.02190	+ / – 0.00501
HF hadron decay electron	7 – 16	0.06341	+ / – 0.00418
Charged particle	1 – 2	0.06341	+ / – 0.00418
Charged particle	2 – 3	0.09577	+ / – 0.00572
Charged particle	3 – 4	0.10462	+ / – 0.00854
Charged particle	4 – 5	0.08691	+ / – 0.01058
Charged particle	5 – 7	0.07206	+ / – 0.01667

3.8.2 Pedestal parameter Estimation

There are different approaches to estimating the pedestal parameter (b) of the baseline function 3.21 for the purpose of removing the uncorrelated background. A common method performed in correlation analyses is to fit and characterize the correlation peaks with probability density functions (PDFs) with the baseline simultaneously [135], [170]. Another approach is to make a zero yield at minimum assumption, which involves fitting only the transverse region of the correlation distribution with a baseline function, leaving only the correlation peaks, from which the peak yields can be obtained [70]. Some of the challenges with the pedestal parameter estimation procedure in this analysis include:

- Correlation background is not flat
- Large background in some $p_T^{\text{assoc.}}$ intervals affect the stability of fitting algorithms
- Fluctuations in the correlation distribution, which particularly affect the transverse region
- Broad or sometimes nonexistent away-side peak is difficult to fit with some probability density functions

In the remainder of this section, an overview of how to characterize correlation distribution peaks is discussed, different methods to estimate the baseline and how those may or may not work in this analysis due to these difficulties, followed by the final method used to estimate the baseline pedestal parameter.

3.8.2.1 Probability density functions

As mentioned in section 1.6.0.5 of the introduction, the azimuthal correlation distribution is characterized by at least one, or most often two peaks, with means (μ) at 0 and π . Barring fluctuations in the distribution, these peaks are assumed to be symmetric about their means and can be characterized by probability density functions. By fitting the correlation peaks with PDFs, both the distribution peak yields and peak widths become observables from the correlation which can be compared to model simulations. Since these observables are affected by the underlying physics

of jet fragmentation, PDFs offer a quantitative way to characterize the distribution peaks.

The normal or Gaussian distribution [171] is used in some correlation analyses [172] to characterize the peaks. This is a continuous probability distribution, which is described by a PDF in the form:

$$f(x) = \frac{1}{\sqrt{2\pi\sigma^2}} e^{-\frac{(x-\mu)^2}{2\sigma^2}}. \quad (3.25)$$

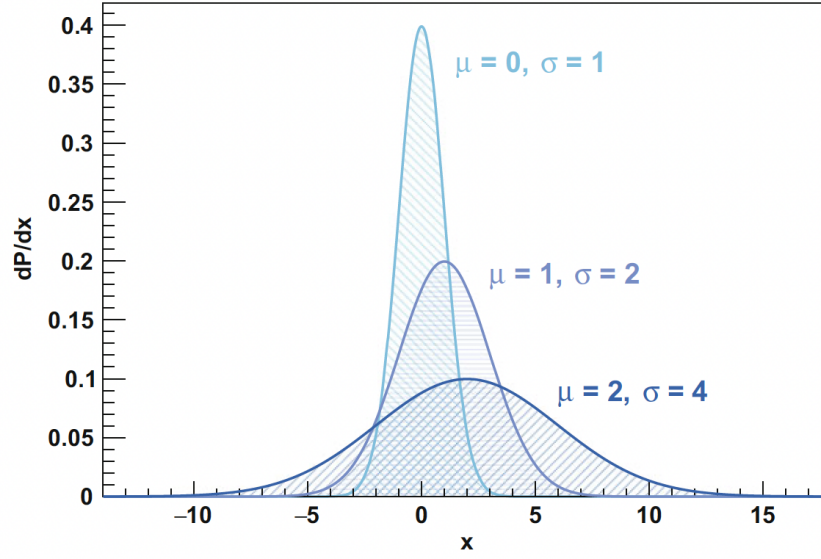


Figure 3.19: Gaussian distributions with different mean (μ) and standard deviation (σ) values [171].

Where the variable σ , or square root of the variance, is used to characterize the peak width. Given that the Gaussian PDF is normalized, such that the integral of the function from $(-\infty, \infty)$ outputs a value of 1, the Gaussian distribution can be modified to include an amplitude term Y_{peak} such that the modified PDF becomes,

$$f(x) = \frac{Y_{\text{peak}}}{\sqrt{2\pi\sigma^2}} e^{-\frac{(x-\mu)^2}{2\sigma^2}}. \quad (3.26)$$

Where the amplitude Y_{peak} quantifies the per-trigger yield of the correlation peak. However, one cannot assume that the azimuthal correlation peaks exhibit a purely

Gaussian shape. An alternative PDF is the generalized normal/generalized Gaussian distribution, with a characteristic function:

$$f(x) = \frac{\beta}{2\alpha\Gamma(1/\beta)} e^{-(\frac{|x-\mu|}{\alpha})^\beta}. \quad (3.27)$$

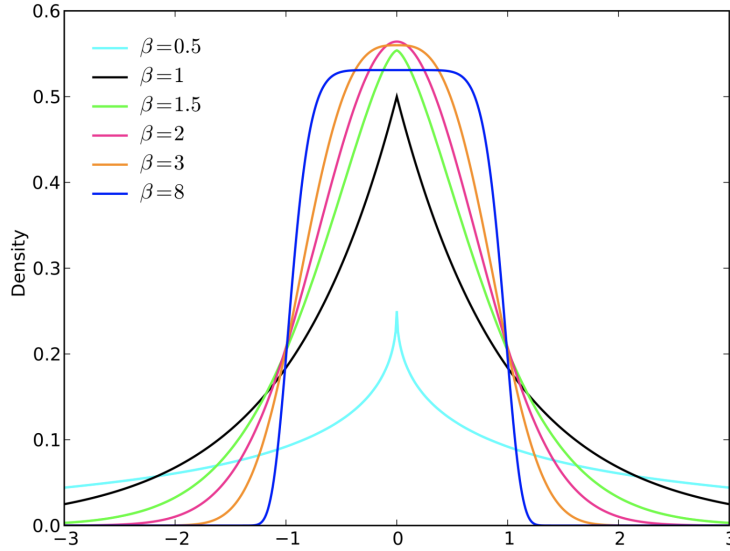


Figure 3.20: Generalized Gaussian distribution with different β values.

The generalized Gaussian [173] offers more degrees of freedom with the α and β variables, which makes the PDF more adaptable to a larger number of correlation peak shapes. Like the Gaussian PDF, this function can be modified to include a yield term,

$$f(x) = \frac{Y_{\text{peak}}\beta}{2\alpha\Gamma(1/\beta)} e^{-(\frac{|x-\mu|}{\alpha})^\beta}. \quad (3.28)$$

The peak width from the generalized Gaussian PDF is $\sigma = \alpha\sqrt{\Gamma(3/\beta)/\Gamma(1/\beta)}$. This has been used to characterize the near-side peak in D-meson correlation studies [172]. However, the variables α and β are not known *a priori*, and they can have a range of values which could be similarly valid to describe the peak width. These two variables contribute a possible source of systematic uncertainty via this characterization method.

One of the difficulties with using the Gaussian and generalized Gaussian PDFs is the periodic nature of the correlation distribution. Because the distribution is on the full circular azimuth, it repeats such that, $C(-\frac{\pi}{2}) = C(\frac{3\pi}{2})$. The characteristic function of the distribution must also express this same periodicity. When using the Gaussian or generalized Gaussian PDFs to fit the distribution, the characteristic function must impose an artificial periodicity to fulfill this criteria. This issue can be addressed by utilizing a periodic probability density function.

One such example of a periodic PDF is the von Mises distribution, which is a continuous probability distribution on a circle. The distribution originates from the field of directional statistics, which focuses on circular data, with examples such as wind or wave directions, or a 24-hour time cycle [174]. The von Mises distribution is generally characterized as the normal distribution on the circle, with a PDF of the following form,

$$f(x) = \frac{e^{\kappa \cos(x-\mu)}}{2\pi I_0(\kappa)}. \quad (3.29)$$

Where I_0 is the modified Bessel function of the first kind of order 0 evaluated at κ . The variable κ is a measure of concentration, where $1/\kappa$ is analogous to the variance σ^2 . This distribution has the benefit of being directly applicable to the periodic domain of the correlation distribution, and thus fulfills the $C(-\frac{\pi}{2}) = C(\frac{3\pi}{2})$ requirement. In the range of $(-\pi, \pi)$, the distribution sums to unity. Therefore, like the other PDFs, the von Mises function can be modified to account for the peak yield:

$$f(x) = \frac{Y_{\text{peak}} e^{\kappa \cos(x-\mu)}}{2\pi I_0(\kappa)}. \quad (3.30)$$

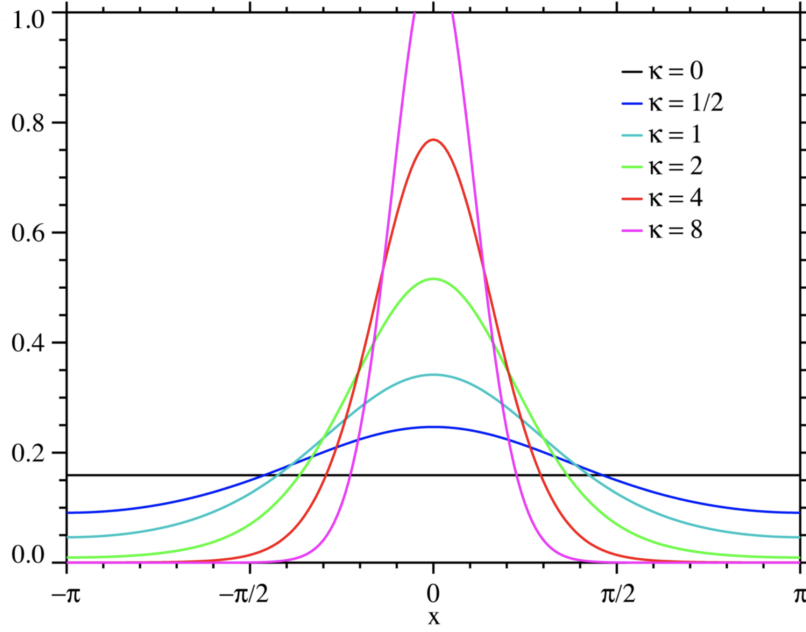


Figure 3.21: von Mises distribution with different κ values.

The von Mises PDF has been successfully implemented to characterize the correlation distributions of electrons from heavy-flavor hadron decays in pp and p-Pb [135]. The corresponding width from this PDF is given by,

$$\sigma = \sqrt{-2 \log \frac{I_1(\kappa)}{I_0(\kappa)}}. \quad (3.31)$$

Where $I_1(\kappa)$ is the first-order modified Bessel function evaluated at κ . Like the Gaussian distribution, the von Mises PDF has only one unknown variable to consider when fitting the distribution. For this analysis, the von Mises PDF will be used for characterizing the azimuthal distribution.

3.8.2.2 Methods to estimate the correlation distribution baseline

In previous correlation measurements within the heavy-flavor sector, such as electrons from heavy-flavor hadron decays in pp and p-Pb [135], the D-meson [170], [172], [175], and the Λ_c [176], all analyses fit both the correlation peaks and the underlying background of the distribution. This is given by the following general form of the distribution characteristic function,

$$f(\Delta\varphi) = \text{PDF}(NS) + \text{PDF}(AS) + b. \quad (3.32)$$

Where the PDF is one of the previously mentioned probability density functions which are used to characterize the near- and away-side peaks. The pedestal parameter b functions the same in this analysis, such that this represents the uncorrelated background. However, since there is no assumed modulated flow component to the background, the standalone b in the function represents a flat line. This is a valid assumption in pp and p-Pb analyses, but not in Pb-Pb where a nonzero flow contribution to the background has been experimentally measured in the centrality classes used in this analysis. Since in this analysis we are considering both the v_2 and v_3 flow coefficients for the trigger and associated particles, the characteristic function takes the general form of,

$$f(\Delta\varphi) = \text{PDF}(NS) + \text{PDF}(AS) + b(1 + 2\nu_2^{\text{HFe}}\nu_2^{\text{ChPart}}\cos(2\Delta\varphi) + 2\nu_3^{\text{HFe}}\nu_3^{\text{ChPart}}\cos(3\Delta\varphi)). \quad (3.33)$$

When attempting to fit this function on the correlation distributions in this analysis, a reoccurring issue would appear in several $p_{\text{T}}^{\text{assoc.}}$ intervals in both centrality classes, shown in Fig. 3.22. When fitting the near- and away-side peaks as a combined function such as Eq. 3.33, the resulting baseline $B(\Delta\varphi)$ would be placed either unphysically too low or high from the correlation distribution. This issue would occur when using different PDF configurations for the peaks. The $p_{\text{T}}^{\text{assoc.}}$ intervals where this occurred were often the intervals with the largest background contribution, but this was not exclusive to those correlations.

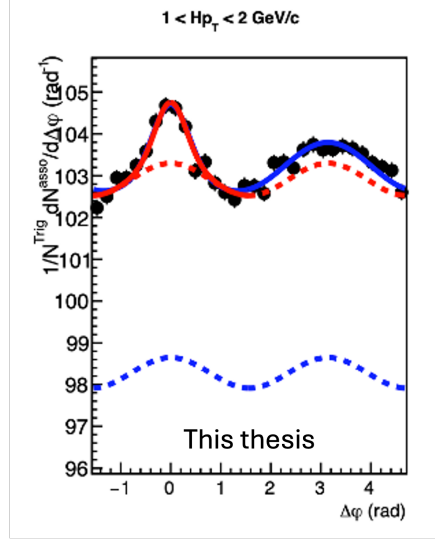


Figure 3.22: Correlation distribution in the lowest $p_T^{\text{assoc.}}$ interval for the most-central collisions. The solid red line is only the near-side peak fitted with a von Mises PDF, and the dotted line is the corresponding baseline. The blue solid line is the characterization function using the von Mises PDF for both peaks. The blue dotted line represents the resulting baseline from the fit, which is unphysical.

The unphysical baseline occurred due to the fit instability of the characteristic function Eq. 3.33. Most of the difficulty with obtaining a stable fit was due to the away-side peak. In some $p_T^{\text{assoc.}}$ intervals, the peak width was so wide that it overlapped into the near-side peak region, resulting in an unstable fit (such as what is seen in Fig. 3.22). In other $p_T^{\text{assoc.}}$ intervals, the AS peak was either non-existent or undetectable within the correlation fluctuations, which could not be accurately characterized by a PDF. For these reasons, a reasonable pedestal parameter b could not be consistently obtained from this method. Although this method of fitting the distribution with a full characteristic function was not used in the final analysis procedure, the cross-checks performed on this method demonstrated that the near-side peak was well-defined in all p_T^e and $p_T^{\text{assoc.}}$ intervals. Such that it is consistently well-described by a von Mises function.

An alternative to fitting the entire distribution to obtain the b parameter is to fit only the baseline function ($B(\Delta\varphi)$) in the parts of the distribution where there are no peaks, the transverse region. This part of the correlation distribution is approximately around $\Delta\varphi \approx \frac{\pi}{2}$ and $\Delta\varphi \approx -\frac{\pi}{2}/\frac{3\pi}{2}$ (depending on the peak width). With this method,

one assumes the absence of the jet in the transverse regions of the distribution, or that there is zero peak yield at the minimum of the distribution (ZYAM method) [177]. This approach has been used successfully in Λ , K , and hadron correlation analyses [70]. There are two primary issues with the ZYAM method: When the correlations peaks are relatively large in width, it can be difficult to define exactly where the transverse region ends and the peak begins, and vice versa. Additionally, the statistical uncertainty on the pedestal parameter b increases when fewer points of the distribution are fitted.

3.8.2.3 Analysis characterization function

For this analysis, the value of the pedestal parameter b was estimated by a combination of the aforementioned methods. Because the near-side peak is consistently well-defined in all correlations, this was fit with a von Mises PDF, while the away-side was not fit with any function. The transverse region of the distribution was fit with the baseline function $B(\Delta\varphi)$, which was informed by the ZYAM method. This is done with the final characterization function,

$$f(\Delta\varphi) = B(\Delta\varphi) + \frac{e^{\kappa_{NS} \cos(\Delta\varphi)}}{2\pi I_0(\kappa_{NS})}. \quad (3.34)$$

The resulting function Eq. 3.34 fits both the transverse region of the distribution and near-side peak. This approach minimizes some of the issues with the other methods: The near-side peak is fully characterized, which allows for the extraction of the peak width, and one method to obtain the near-side peak yield. This also serves to "anchor" the b parameter, so that the baseline function is not significantly influenced by the fluctuations in the transverse region. A maximum number of distribution points are included when fitting Eq. 3.34 on the near-side peak and transverse region, resulting in the smallest uncertainty on the parameter b as possible. Because this method involves assumptions about where exactly the transverse region resides, a systematic study was performed to determine the total uncertainty of the baseline estimation, which is described in the next chapter in section 4.3.6.

The $B(\Delta\varphi)$ placement obtained from the fit is subtracted from the correlation $C^*(\Delta\varphi)^{\text{HFe}}$, which is then used to obtain the final correlation distribution. This is shown in Fig. 3.23:

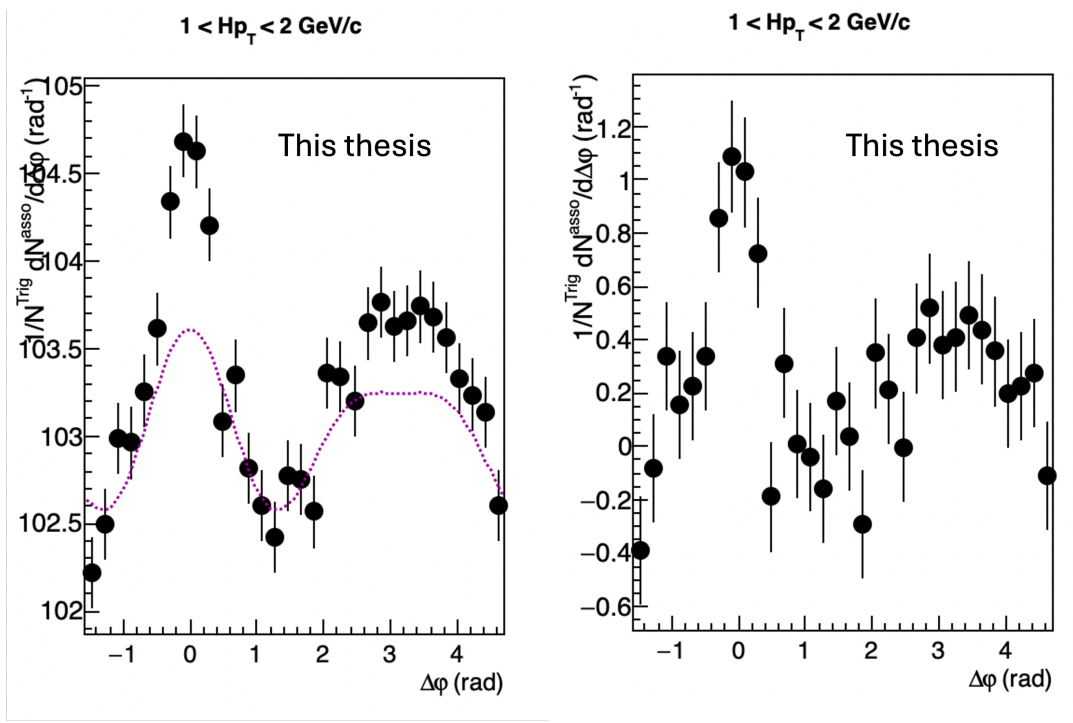


Figure 3.23: Correlation distribution in the 0–10% centrality class. The left figure shows the distribution fitted with $B(\Delta\phi)$ before subtraction. The right shows the distribution after $B(\Delta\phi)$ subtraction.

Chapter Four: Systematic Uncertainties

Every measurement taken with the ALICE detector, or similarly, any measurement taken with an experimental apparatus in the realm of particle or nuclear physics or beyond, has an uncertainty associated with the measurement. There are multiple sources of this uncertainty: For a collider measurement, an uncertainty arises in the form of the Poisson variance due to measuring several million independent discrete events. There is also an uncertainty associated with the confluence of a detector imprecision and the experimenter's limited knowledge of the system.

For example, to measure the p_T spectra of electrons produced in a pp collision, the electrons are isolated using well-known cuts in the TOF or TPC and EMCal. Some of the particles in this signal are pions or kaons misidentified as electrons because their signals overlap in the detector. There are also electrons which do not originate from the collision itself but from the decay of direct photons interacting with the detector. These are background electrons which must be removed from the signal. Additionally, some electrons are lost due to the tracking selections or the limited acceptance of the detector, therefore affecting the total number of electrons measured. To address these problems, multiple assumptions about the analysis must be made, which include but are not limited to:

- The E/p cut fully removes the hadron contamination
- The background electrons are well-described by Monte Carlo, such that their simulated spectra can be subtracted from the total measured electron spectra
- The Monte Carlo simulation used to correct for lost electrons correctly recreates the correct proportion lost in reconstruction

All of these assumptions listed carry with them a degree of uncertainty. Effects such as these necessitate that results are expressed as both the measured values *and* error bars which encapsulate the total uncertainty of those measured values. The uncertainties related to the measurement of this analysis are distinguished by two types: Statistical and systematic. To describe in simple terms, the statistical component of the uncertainty is as it sounds, the uncertainty as a consequence of measuring a large

finite sample of events. The uncertainty due to an event occurring with Poissonian probability is a *statistical* uncertainty. The uncertainty “associated with the nature of the measurement apparatus, assumptions made by the experimenter, or the model used to make inferences based on the observed data” [178] such as the uncertainties associated with the direct electron identification are *systematic* uncertainties. Put another way, the systematic uncertainty is the uncertainty resulting from *how* the measurement is performed, the *assumptions* made in the measurement process, and the *limited knowledge* of the measurement process. However, the systematic uncertainty is linked to the statistical, in that statistical fluctuations or the finite number of events influence the magnitude of the systematic uncertainties. Understanding and estimating the uncertainty due to systematic effects is fundamentally different from determining the statistical uncertainty, and requires a careful approach to quantify.

The focus of this chapter is to detail the systematic uncertainties associated with this analysis. First, the systematic sources for these uncertainties are listed and how they are expected to affect the observables. Next, the procedure to estimate the systematic uncertainties are described. Finally, the estimation procedure for these systematic uncertainties are shown, and the final estimated uncertainty tables.

4.1 Systematic Sources

In the previous section, the systematic uncertainty was defined as the degree of uncertainty attributed to the choice imposed on the measurement procedure. In every step of the analysis, from the correlation distribution corrections to the tracking, etc., these choices contribute to the overall uncertainty of the measurement. The following list contains the sources of systematic uncertainties in this analysis:

1. Electron track selection
2. Electron identification
3. Associated particle track selection
4. Non-HF hadron decay electron identification
5. Mixed event correction

6. Baseline estimation

These systematic sources affect the following observables:

- $\Delta\varphi$ correlation distribution
- The peak widths
- Near-side per-trigger associated yield (Y_{NS})
- Away-side per-trigger associated yield (Y_{AS})

In the following sections, the estimation procedure is discussed as well as the effects of these sources on the analysis and their estimated uncertainty on the distribution and yields.

4.2 Systematic Uncertainty Estimation

Disentangling the systematic uncertainty from the statistical is an art as much as it is a science. The process for determining the uncertainty for all systematic sources (with the exception of the uncertainty due to the estimation of the baseline, discussed in section 4.3.6) is as follows:

1. Select a reasonable variation of the selection criteria (or “cut”) for a systematic source.
2. Perform the analysis procedure using the variation.
3. Take the ratio of the observable ($\Delta\varphi$ distribution or yield) using the “default” cut described in the analysis chapter to the observable identified with the variational cut. This is performed for one variation at a time.
4. Repeat with additional reasonable variations related to the systematic source.
5. After evaluating the cut variation ratios and other checks, assign an uncertainty value to the systematic source.

What constitutes a “reasonable” variation is inherently subjective and relies on the knowledge of how each selection in the analysis procedure affects the measurement, which will be elaborated in the following sections.

A detail of note: The baseline estimation is a significant source of uncertainty of the analysis. However, the baseline must be subtracted to obtain the per-trigger yields. To minimize the effect of the baseline uncertainty on the yields, a flat background is subtracted from the correlation distributions for all different systematic cuts. An example is shown in Fig. 4.1.

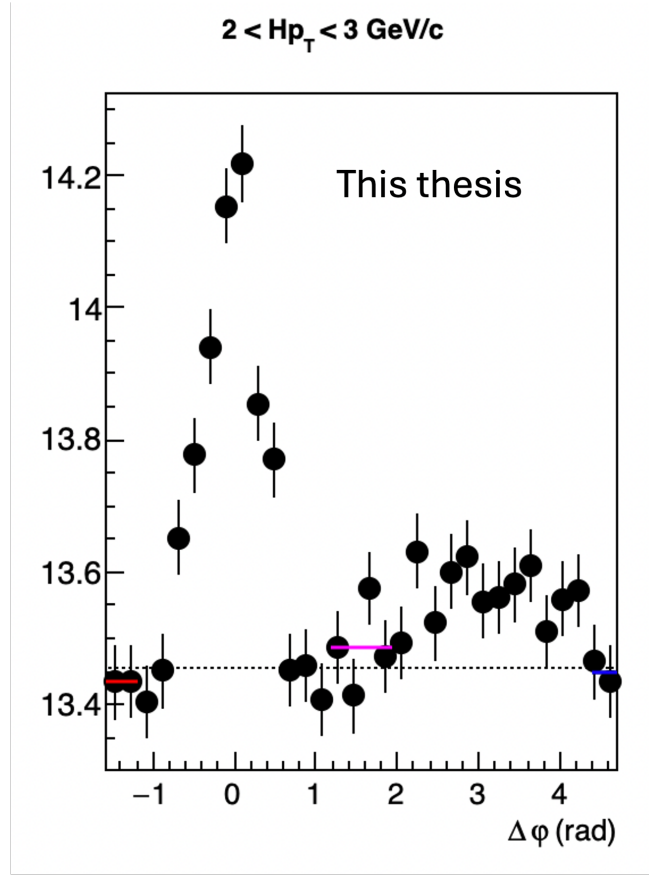


Figure 4.1: $\Delta\phi$ Correlation distribution of inclusive electrons with charged particles in the $p_T^{\text{assoc.}}$ interval of 2 - 3 GeV/c. The average of three values of the distribution around $-\frac{\pi}{2}$, $\frac{\pi}{2}$, and $\frac{3\pi}{2}$ are used to obtain the flat pedestal b , which is subtracted from the distribution. This is performed for the distributions the default and variation cuts before the systematic estimation.

Subtracting a flat background from the distribution minimizes the effect of the

distribution fluctuations which would be amplified by subtracting the full baseline function $B(\Delta\varphi)$. This decision is made with the assumption that the correlated flow in the N distribution is the same as the correlated flow in the V distributions. By taking the ratio of the distributions and yields after a flat background subtraction, the effect of the flow should cancel, leaving only the effect of the systematic source determined by the choice of the varied cut.

When evaluating the ratios of the correlation distributions, the transverse region is subject to larger fluctuations than the distribution peaks, making it difficult to ascertain the systematic effect on the distribution. Therefore, only the regions corresponding to the signal (distribution peaks) are considered when estimating the uncertainty.

In section 2.3 of the ALICE detector chapter, a brief overview of the LEGO train and wagon system are discussed. A consequence of studying Pb–Pb collisions is the large computational and memory demand for these high-multiplicity environments. For this reason, all of the variations for the most-central events are reconstructed in separate wagons, and in semicentral events some of the variations are reconstructed in the same wagons. Additionally, the variations in the semicentral events are performed on both the LHC18q_pass3 and LHC18r_pass3 datasets, where the most-central events are only evaluated on the LHC18r_pass3 dataset. This was done to minimize the computational requirements of this analysis. As a result, statistical fluctuations unrelated to the systematic effects appear in the systematic checks. These must be accounted for when assigning the uncertainty values.

4.3 Systematic studies

In the following subsections, the effect of each systematic source is determined from the estimation procedure, and the effect of that source on the measurement observables is discussed.

4.3.1 Electron tracking

Particle tracks must first pass quality selection criteria before applying electron identification cuts to find electron candidates. When the potential electron track reaches the TPC, the nominal requirement is that track must interact with at least 70 readout

pads in the detector. The particle track is highly unlikely to be detected by every pad row in the TPC so this requirement ensures a high-quality track without removing all track signals. The 0.8 ratio of the number of crossed TPC pad rows over the number of clusters found also ensures track quality. “Tighter” cuts than the nominal 70 crossed rows or 0.8 crossed rows over findable clusters result in higher-quality tracks being analyzed, but this will inevitably remove some of the signal—resulting in fewer electron candidates considered for the analysis. However, a looser cut can result in selecting a track which does not reach the EMCal. Because the EMCal cluster matching is required for electron candidates, this wastes computational resources on tracks which won’t be used in the correlation. These nominal cuts are informed by previous successful measurements of heavy-flavor hadron decay electrons [135] and the effects of these cuts are reproducible in Monte Carlo simulations of the detector, but the cost to benefit for these track selection cuts has a level of subjectivity. Reasonably tighter or looser cuts could have also been valid selections for this analysis. For this reason, the following variations were used to determine the systematic effect of the electron tracking:

Table 4.1: Electron tracking systematic uncertainties

Minimum number of TPC crossed rows required for the track
60
80
TPC crossed row over findable clusters
0.9
0.7

Because the electron track selections affect all electrons equally, regardless of their source, the systematic study on the electron tracking is performed at the inclusive electron level. This avoids the fluctuations introduced from subtracting the non-heavy-flavor electron distributions. The cut to default ratios of the inclusive-electron $\Delta\varphi$ correlation distribution for electrons in the trigger interval $4 < p_{\text{T}}^e < 12$ GeV/ c are shown in Fig. 4.2, and the per-trigger yields are shown in Fig. 4.3.

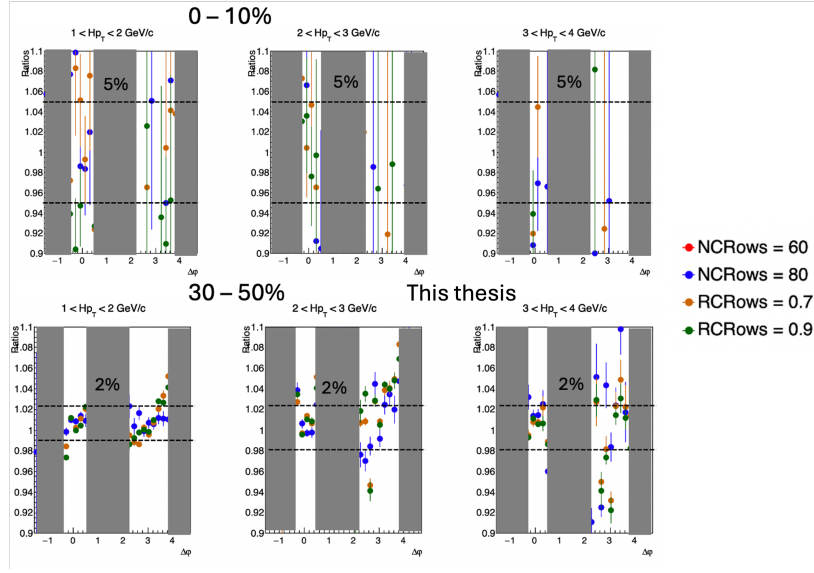


Figure 4.2: Electron tracking systematic uncertainty estimation on the $\Delta\varphi$ correlation distribution, measured in the 0–10% centrality class (top) and the 30–50% centrality class (bottom).

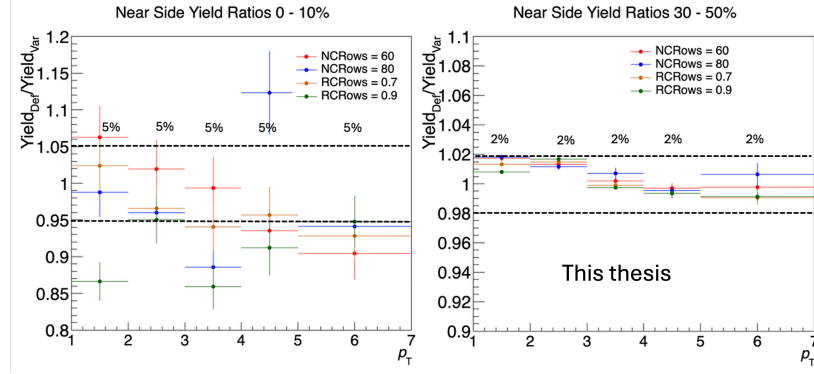


Figure 4.3: Electron tracking systematic uncertainty estimation on the per-trigger yields, measured in the 0–10% centrality class (left) and the 30–50% centrality class (right).

Comparing first the two centrality classes, there is an obvious difference in the spread of the variations when they are included in the same wagon vs when they are in separate wagons. This discrepancy gives an idea of how the fluctuations might affect the other systematic sources. Additionally, the electron tracking is not expected to differ significantly between centrality classes, so the semicentral ratios can be

used to inform the uncertainty values for the most-central events. The ratio values for the $\Delta\varphi$ distributions was obtained by fitting the distribution ratios with a flat line in $-0.4 < \Delta\varphi < 0.4$ and $2.2 < \Delta\varphi < 3.8$ (which is repeated for the other systematic sources described later). To aid in quantifying the systematic uncertainty, the root mean square and the standard deviation of the variation ratios were computed for the systematic sources. The ratios are assumed to follow a continuous uniform distribution, such that the standard deviation is calculated as:

$$\text{One standard deviation \%} = |(\frac{\text{MaximumVariation} - \text{MinimumVariation}}{\sqrt{12}} - 1) \times 100| \quad (4.1)$$

After considering the distribution and yield ratios, as well as the RMS and σ_{sys} values, the estimated relative systematic uncertainty in the central (semicentral) events for this electron trigger interval is 5% (2%) for the near-side peak, and 5% (3%) for the away-side peak. Accounting for the added fluctuations, in the most-central collisions the uncertainty due to the electron track is estimated to be 5% (2%) for the $\Delta\varphi$ distribution.

The systematic estimation procedure was repeated for the $4 < p_{\text{T}}^e < 7 \text{ GeV}/c$ and $7 < p_{\text{T}}^e < 16 \text{ GeV}/c$. The ratios for these trigger intervals follow a similar behavior as the $4 < p_{\text{T}}^e < 12 \text{ GeV}/c$, and their values are reported in the tables in section 4.4.

4.3.2 Electron identification

For a track to be considered an electron candidate, the track must exhibit an energy loss in the TPC within a certain number of standard deviations from the expected electron signal. This corresponds to the asymmetric cut of $-1 < \sigma_{\text{e}}^{\text{TPC}} < 3$, which captures the electron signal while removing a significant portion of the hadron contamination. A tighter selection of the negative value is expected to increase the overall purity of the electron sample, with the drawback of removing more of the true electron candidates. A looser selection has the opposite effect.

This track must also reach the EMCal, where it deposits its remaining energy into the detector material and generates an identifiable cluster. This energy taken with the momentum produces an E/p ratio around 1. The nominal cut of $0.8 < E/p < 1.2$ captures the electron signal, but a systematic study tests if this is the “optimum”

value for this analysis. The nominal interval of $0.25 < E/p < 0.5$ used to scale down the hadron E/p signal was selected because it is sufficiently displaced from the electron signal, however this is not the only interval which could have been used. Additionally, a geometric selection is imposed on the cluster shape in the EMCal to increase the purity of the electron signal.

The following variations were selected to estimate the systematic effect of the electron identification procedure:

Table 4.2: Electron identification systematic uncertainties

σ_e^{TPC}
$-0.75 < \sigma_e^{\text{TPC}} < 3$
$-1.25 < \sigma_e^{\text{TPC}} < 3$
E/p
$0.75 < E/p < 1.2$
$0.85 < E/p < 1.2$
$0.9 < E/p < 1.2$
Shower shape long-axis (M02)
$0.02 < \text{M02} < 0.8$
$0.02 < \text{M02} < 0.95$
E/p -scale change
(0.4, 0.65)

This systematic study was performed at the inclusive electron level. The uncertainty observed for the correlation distribution in the most-central (semicentral) collisions is 3% (1%), 3% (2%) for the near-side yield and 4% (2%) for the away-side yield.

4.3.3 Background electron identification

As described in the methodology section 3.6, the non-heavy flavor background of the electron samples are attributed primarily to electrons from Dalitz decays and photon conversions in the detector material (collectively referred to as “photonic” electrons). Electron candidates are matched with partner electrons and reconstructed to obtain an invariant mass distribution. This invariant mass distribution is cut at a threshold of $140 \text{ MeV}/c^2$ to select the electrons originating from the photonic background. In

the process of estimating the photonic background, there are two systematic sources which contribute to the uncertainty of the photonic background estimation:

- The partner electron tracking
- The reconstruction selections

In regards to the electron tracking, partner electrons are selected with tracking cuts similar to the associated charged particles to maximize the number of candidates. The corresponding systematic uncertainty can be estimated similarly, by increasing the minimum number of crossed pad rows from the nominal 60 value, and requiring a larger minimum ratio of pad rows to findable clusters from the nominal 0.6 value. The uncertainty arising from the reconstruction selections depend on the choices made regarding the p_T cutoff of the partner electron and the precise value of the invariant mass cut. To investigate the effect of the tracking and reconstruction choices, the following variations were made regarding the photonic electron estimation in order to estimate the corresponding systematic uncertainty:

Table 4.3: Background electron systematic uncertainties

Electron invariant mass threshold (MeV/ c^2)
130
150
Minimum partner electron p_T (MeV/ c)
100
200
400
Minimum number of crossed pad rows in TPC
70
80
Minimum crossed TPC pad rows over findable clusters
0.7
0.8

An important note for this estimation, is that in order to estimate the photonic background uncertainty, the correlation distributions must be compared at the heavy-flavor decay electron correlation level. So in contrast to the other systematic estimations which could be performed at the inclusive electron level, this systematic

estimation is prone to a larger number of statistical fluctuations. Additionally, for all the variations listed for the photonic electron systematic estimation, a corresponding tagging efficiency was generated using these cut variations so that the correct efficiency could be applied to the distributions. This compensates for the effect these cuts would have on the tagging efficiency.

The ratios of the correlation distributions and the yields are presented in Figs. 4.4 and 4.5. For the 0–10% (30–50%) centrality class, systematic uncertainties of 5% (3%) are assigned for the $\Delta\varphi$ correlation distribution. For the near-side yield, uncertainties of 5% (3%) are assigned and 5% (4%) for the away-side yield.

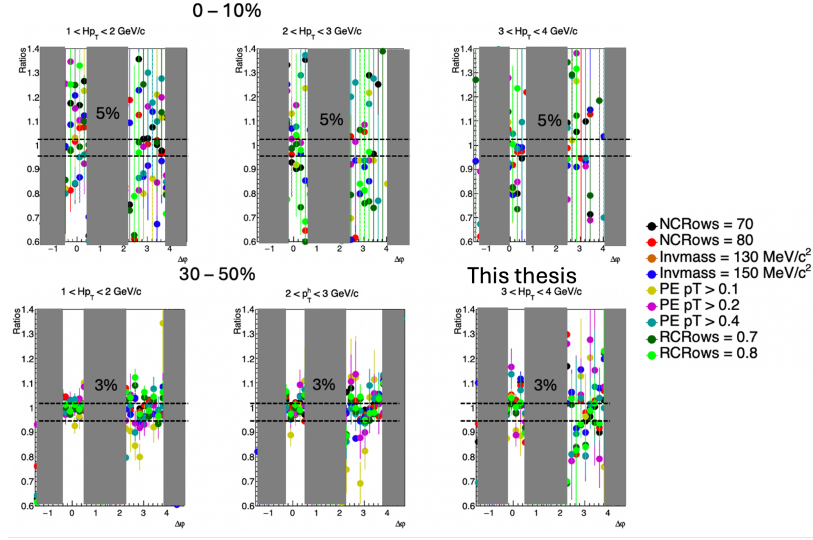


Figure 4.4: Photonic electron systematic uncertainty estimation on the $\Delta\varphi$ correlation distribution, measured in the 0–10% centrality class (top) and 30–50% centrality class (bottom).

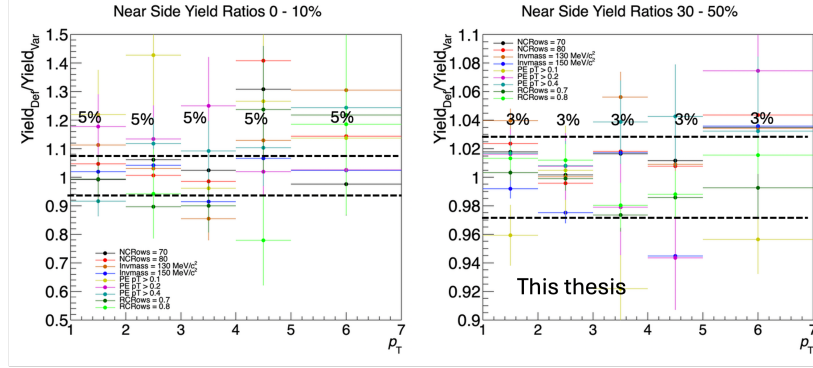


Figure 4.5: Photonic electron systematic uncertainty estimation on the near-side per-trigger yields, measured in the 0–10% centrality class (left) and 30–50% centrality class (right).

4.3.4 Associated particle tracking

Selections of at least 60 crossed TPC pad rows, and a ratio of 0.6 crossed rows over findable clusters were required for the associated particle tracks. Additionally, a pseudorapidity selection of $|\eta| < 0.8$ was imposed on the associated particle tracks. Because the charged associated particles are not required to reach the EMCal, the associated particle track cuts are looser relative to the same type of selections for the electron tracks. Recall that the TPC covers a pseudorapidity of $|\eta| < 0.9$, while the EMCal covers $|\eta| < 0.7$. This wider range in pseudorapidity allows for the selection of associated particles in a larger η region than the electrons. However, the looser TPC selection requirements could result in low-quality reconstructed tracks. As a systematic check, tighter TPC selection cuts are applied to the associated charged particles. Both looser and a tighter cuts are applied to the pseudorapidity to determine the systematic uncertainty associated with the η requirement.

Table 4.4: Associated particle tracking systematic uncertainties

Minimum number of TPC crossed rows required for the track
70
80
90
TPC crossed row over findable clusters
0.7
0.8
0.9
η cut
$ \eta < 0.7$
$ \eta < 0.85$

The uncertainties related to the associated particle tracking were evaluated to be 5% in $\Delta\varphi$ for all $p_T^{\text{assoc.}}$ intervals for the most-central collisions, and 3% for semicentral collisions. The per-trigger yields were similarly valued, with the uncertainties valuated at 5% (3%) for the near-side yield and 5% (3%) for the away-side yield for the most-central (semicentral) collisions.

Because the associated particle tracking efficiency is applied as a flat value to the final correlation distribution, all points in the resulting distribution change by the same magnitude. Because of this, the associated particle tracking uncertainty is an uncertainty that is *correlated* in $\Delta\varphi$.

4.3.5 Mixed-event correction

Events selected for mixing to create the mixed-event correlation distributions are matched via similar Z-vertex and centrality class. This is done by creating event mixing pools of specific bin sizes. The choice to divide the pools for the nominal selection was done to achieve a balance of maximizing the statistics for each bin while remaining differential. A variation for the binning of the Z-vertex and centrality pools was created to determine the systematic effect.

The nominal binning of the Z-vertex mixed event pools is:

- (-10,-5), (-5,-2), (-2,0.5), (0.5,3), (3,6), (6,10)

For the systematic check, the Z-vertex bins were changed to:

- (-10,-5), (-5,-2.5), (-2.5,0), (0,2.5), (2.5,5), (5,10)

The nominal binning of the 0–10% centrality class mixed event pools is:

- (0,1), (1,2), (2,3), (3,5), (5,7.5), (7.5,10)

The variation binning becomes:

- (0,2.5), (2.5,5), (5,7.5), (7.5,10)

Similarly for the 30–50% centrality class events, the original centrality binning is:

- (30,32), (32,35), (35,38), (38,41), (41,45), (45,50)

And the variation is:

- (30,34), (34,39), (39,44), (44,50)

In addition to the event mixing pool variation, the method to estimate the normalization factor β was modified. Recall that β is used to scale the mixed-event distribution before the distribution can be used to correct for the detector and acceptance effects of the same-event distribution. The normalization factor for the nominal method is:

$$\beta = \text{Average}(\Delta\varphi \approx 0, \Delta\eta \approx 0)$$

For the full variation, the entire η range is considered:

$$\beta = \text{Average}(\Delta\varphi \approx 0, |\Delta\eta| < 1)$$

After considering both variational methods to estimate the mixed event systematic effect, the total systematic uncertainty due to the mixed-event correction for the three measured p_T^e interval for both centrality classes is given as a flat 2% in all associated particle p_T intervals for the 4–12 p_T^e ranges in both centrality classes. This 2% value was observed in both the $\Delta\varphi$ distribution and the per-trigger yields. Performing this same check on the 4–7 p_T^e interval yielded similar results. Whereas in the 7–16 p_T^e interval, the systematic uncertainty was observed to be 2% in $p_T^{\text{assoc.}} < 3 \text{ GeV}/c$, and 5% $> 3 \text{ GeV}/c$. Overall, the uncertainty due to the mixed-event

correction amounts to a smaller contribution compared to the previously discussed systematic sources. In addition, the mixed-event systematic uncertainty affects the entire the correlation distribution equally. Similar to the associated particle tracking uncertainty, the mixed-event systematic uncertainty is a correlated uncertainty. The contribution of the correlated uncertainties are reported in the final $\Delta\varphi$ correlation distribution results.

4.3.6 Baseline estimation

The largest source of systematic uncertainty in this analysis originates from the estimation of the baseline of the correlation distribution.

Recall that the baseline function takes the form:

$$B(\Delta\varphi) = b(1 + 2\nu_2^{HFe}\nu_2^{ChPart}\cos(2\Delta\varphi) + 2\nu_3^{HFe}\nu_3^{ChPart}\cos(3\Delta\varphi)) \quad (4.2)$$

Where the flow coefficients (v_n) of the baseline function are taken from previous studies of heavy-flavor hadron decay muons [166] and charged particles [168]. The parameter b is a free parameter which is not known *a priori*, and must be determined experimentally. Both the flow coefficients and the b value are sources of systematic uncertainty. These systematic sources are examined separately and then compared to determine if one contribution dominates the total baseline uncertainty or if both should be equally considered.

In the following sections, studies to estimate the systematic effect of the flow coefficients and b are shown.

4.3.6.1 “Pedestal” parameter b

As described in the analysis procedure section 3.8, the high-multiplicity environment and the potential jet-medium interactions change the shape and background contribution of the Pb–Pb correlation distribution with respect to pp collisions. In both collision centrality classes measured, statistical fluctuations plague the distribution, particularly in the transverse region. At low $p_T^{\text{assoc.}}$ in the most-central collisions, or high $p_T^{\text{assoc.}}$ in the semicentral collisions, the away-side peaks cannot be fully fit by a Gaussian or Generalized Gaussian distributions simultaneously with the near-side peak and transverse region. Additionally, there are no away-side peaks in some $p_T^{\text{assoc.}}$

intervals. Perhaps the peaks themselves are nonexistent due to jet-quenching or other effects, or the fluctuations of the measurement drown out what is potentially a small signal peak. Whatever the physics reason, no assumptions can be made regarding the shape of the away-side peak itself, so the method of fitting both peaks with the background done in the conventional manner seen in Refs. [70], [170] is not performed.

$$f(\Delta\varphi) = b(1 + 2\nu_2^{HFe}\nu_2^{ChPart}\cos(2\Delta\varphi) + 2\nu_3^{HFe}\nu_3^{ChPart}\cos(3\Delta\varphi)) + \frac{e^{\kappa_{NS}\cos(\Delta\varphi)}}{2\pi I_0(\kappa_{NS})}. \quad (4.3)$$

The distribution is fitted with Eq. 4.3 in the ranges $(-\frac{\pi}{2}, \frac{\pi}{2} + 0.4)$ and $(\frac{3\pi}{2} - 0.4, \frac{3\pi}{2})$ radians, which fits the well-defined near-side peak and the transverse region as a combined von Mises + zero-yield-at-minimum (ZYAM) approach. As a systematic check, a conventional ZYAM approach is used to create additional baseline variations. This is done by fitting only the transverse region with the baseline function $B(\Delta\varphi)$, creating a first variation (2 - 4 - 2) by fitting the same transverse region as Eq. 4.3. This fit is symmetric, such that this variation covers the four points centered around $\frac{\pi}{2}$, the two points to the right of $-\frac{\pi}{2}$ and the two points to the left of $\frac{3\pi}{2}$ to mirror the four center points. Additional baseline variations were created by slightly varying the fitting regions by ± 0.2 radians to create a total of 4 ZYAM variations. The ranges for the variations are listed as:

1. 2 - 4 - 2: $(-\frac{\pi}{2}, -\frac{\pi}{2} + 0.4)$, $(\frac{\pi}{2} - 0.4, \frac{\pi}{2} + 0.4)$ and $(\frac{3\pi}{2} - 0.4, \frac{3\pi}{2})$
2. 3 - 6 - 3: $(-\frac{\pi}{2}, -\frac{\pi}{2} + 0.6)$, $(\frac{\pi}{2} - 0.6, \frac{\pi}{2} + 0.6)$ and $(\frac{3\pi}{2} - 0.6, \frac{3\pi}{2})$
3. 2 - 2 - 2: $(-\frac{\pi}{2}, -\frac{\pi}{2} + 0.4)$, $(\frac{\pi}{2} - 0.2, \frac{\pi}{2} + 0.2)$ and $(\frac{3\pi}{2} - 0.4, \frac{3\pi}{2})$
4. 3 - 3 - 2: $(-\frac{\pi}{2}, -\frac{\pi}{2} + 0.6)$, $(\frac{\pi}{2} - 0.6, \frac{\pi}{2})$ and $(\frac{3\pi}{2} - 0.4, \frac{3\pi}{2})$

Variation 4 (3 - 3 - 2) was motivated by the shape of the distributions, which overall among $p_T^{\text{assoc.}}$ appears to have a narrow near-side peak compared to the away-side (when the away-side peak is visible), hence the slight asymmetry of the fit.

Much of the difficulty with the b value estimation is the effect the statistical fluctuations have on the baseline fits. The aforementioned ZYAM variations are made with the assumption that the true b value must lie within the range of the variations. However, fluctuations have strong effects on the fits, such as driving the fits either

upwards or downwards with respect the nominal fit, and this is compounded when fitting a smaller number of points. This fact coincides with the assumption that the nominal b taken from the von Mises + ZYAM method is likely the closest to the “true” b value since that method fits the most points in the distribution and has the smallest statistical uncertainty of all the fits. However, whether the nominal b value is the closest to the true value is unknown. Taken altogether, there is an intrinsic statistical-dependence on the systematic estimation of the b parameter.

To take into account the inherent uncertainty of the b parameter using the nominal method, two more variations were created. This is done by creating two baseline functions where the b value is assigned the new value $b \pm b_{error}$, where b_{error} is the error taken from the parameter of the nominal fit.

The list of seven systematic b variations of the baseline are thus:

1. ZYAM 2 - 4 - 2
2. ZYAM 3 - 6 - 3
3. ZYAM 2 - 2 - 2
4. ZYAM 3 - 3 - 2
5. $b_N + b_{error}$
6. $b_N - b_{error}$

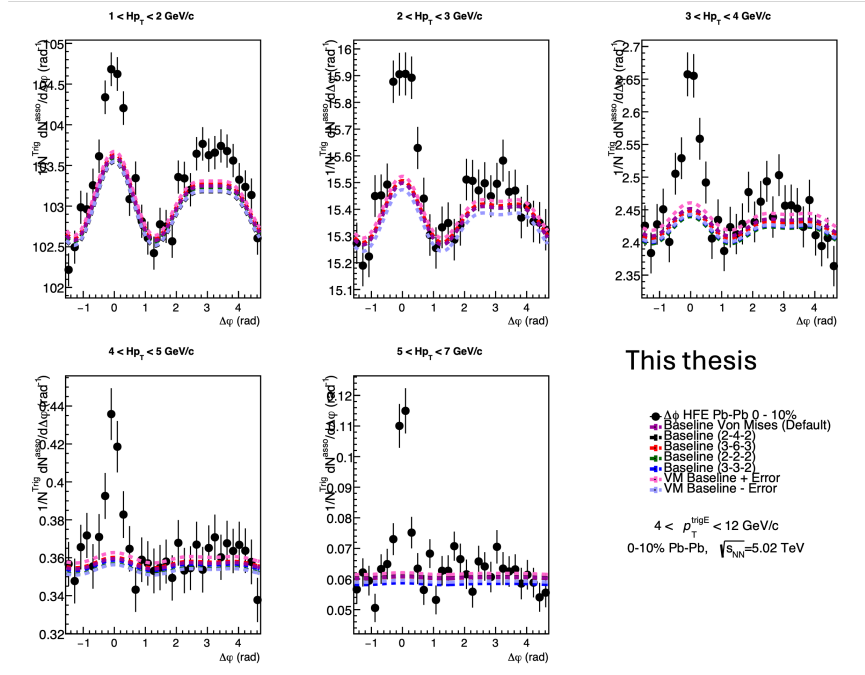


Figure 4.6: Six b parameter variations in the $4 < p_T^e < 12 \text{ GeV}/c$ trigger interval for the most-central collision events.

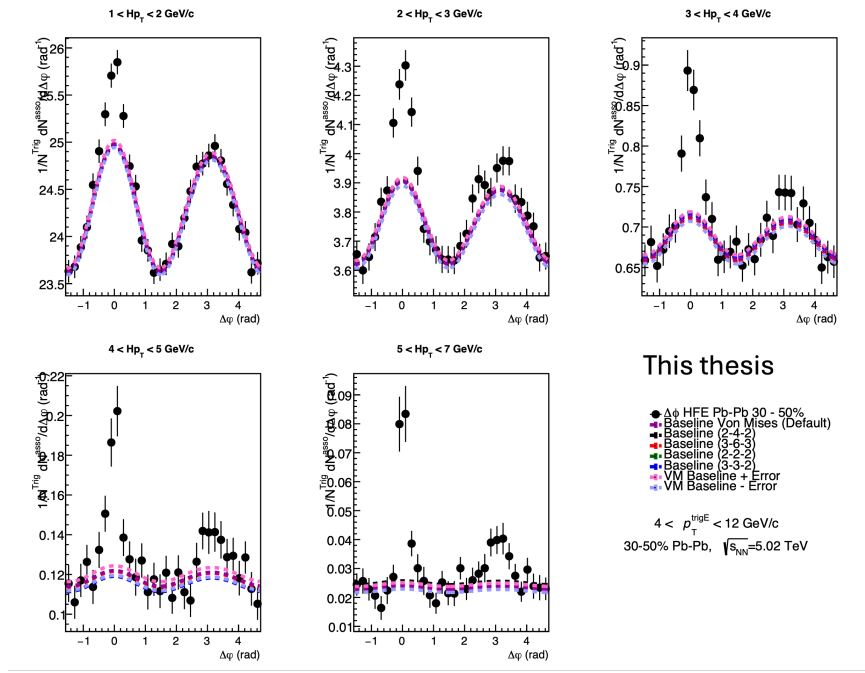


Figure 4.7: Six b parameter variations in the $4 < p_T^e < 12$ GeV/ c trigger interval for the semicentral collision events.

In Figs.4.6 and 4.7, all seven b variations are shown together (and will be referred to by their number in the list). In both centrality classes, the variations 5 and 6 appear to capture all of the other variations in almost every $p_T^{\text{assoc.}}$ intervals. Since the error on the b parameter is dependent on the number of points fitted and the size of the error bars, this indicates that the statistical uncertainty of the b value overwhelms the systematic uncertainty, but there is a high likelihood that the true baseline b value is within variations 5 and 6. In Figs. 4.8 and 4.9, the highest and lowest baseline in each $p_T^{\text{assoc.}}$ interval is subtracted from the correlation distribution (to obtain the “global” variation distributions) and are plotted with the nominal distribution. Figs. 4.10 and 4.11 illustrate the ratios of the per-trigger yield using the “maximum” and “minimum” correlation distributions.

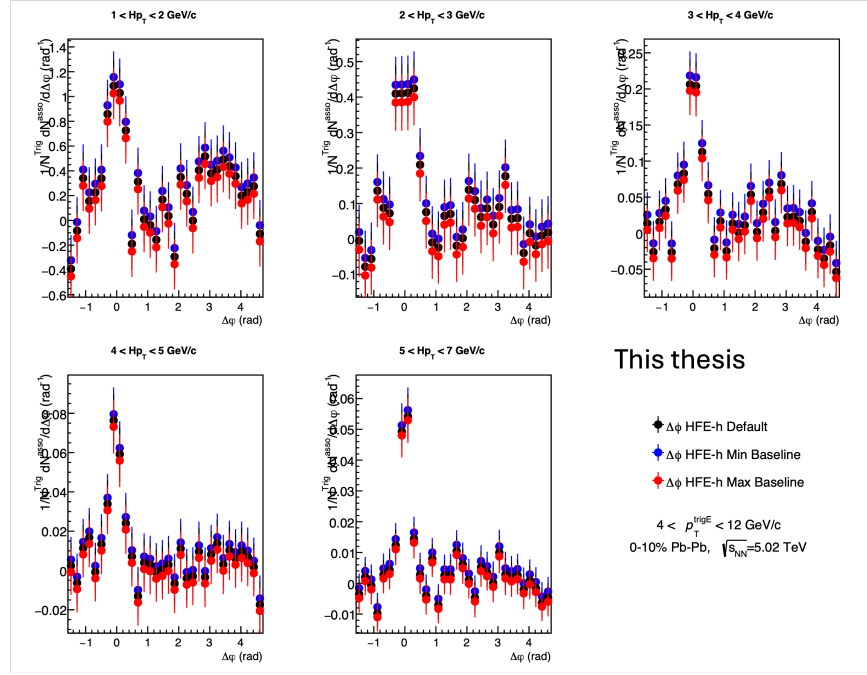


Figure 4.8: $\Delta\phi$ correlation distributions after subtracting the highest and lowest baseline in all $p_T^{\text{assoc.}}$ intervals. Shown for the most-central collision events.

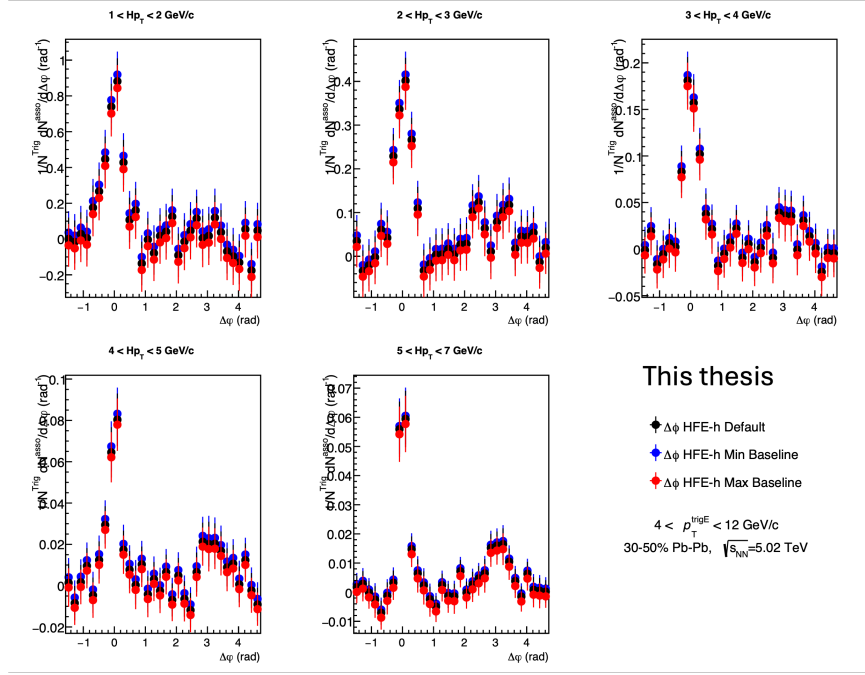


Figure 4.9: $\Delta\varphi$ correlation distributions after subtracting the highest and lowest baseline in all $p_T^{\text{assoc.}}$ intervals. Shown for semicentral collision events

After subtracting the highest and lowest baselines, the points in the resulting distributions are well-within the uncertainty of the nominal distribution. However, for points which fluctuate around 0, subtracting the highest baseline drives these points further downwards. This is especially apparent in the intervals where the away-side peaks are non-existent.

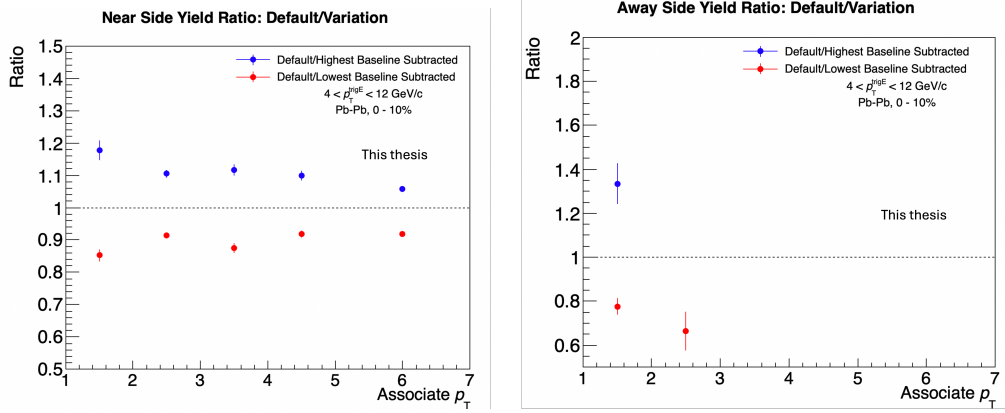


Figure 4.10: Ratios of the per-trigger yields of the b parameter variations to the nominal yields in the 0–10% centrality class.

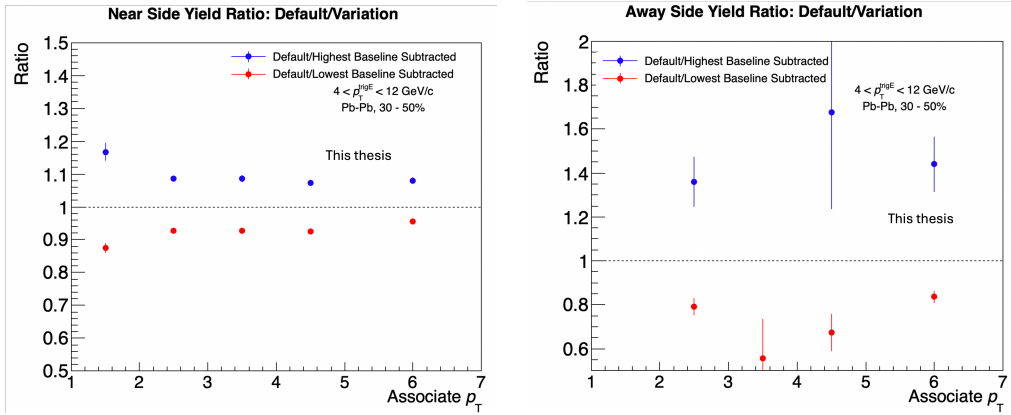


Figure 4.11: Ratios of the per-trigger yields of the b parameter variations to the nominal yields in the 30–50% centrality class.

When comparing the near-side yields for the 0–10% centrality class, the ratios appear to be confined within a $\leq 20\%$ deviation from the nominal value. This difference of 20% is only seen in the lowest $p_T^{\text{assoc.}}$ interval after subtracting the highest global baseline, and the difference between the nominal decreases at the higher $p_T^{\text{assoc.}}$ intervals. The 30–50% centrality class follows a similar behavior and shows a clearly decreasing trend as a function of $p_T^{\text{assoc.}}$.

However, the ratio for the away-side yield is not-well defined in most $p_T^{\text{assoc.}}$ intervals, because there is a small to non-existent away-side peak in several $p_T^{\text{assoc.}}$ intervals after the baseline subtraction. When a higher baseline is subtracted, more of the

away-side is removed, resulting in a ratio between two numbers very close to zero. Therefore, the ratio blows up to a large value, or the variational yield was negatively valued, resulting in a negative ratio. This indicates that the ratio method cannot quantify the uncertainty associated with the away-side peak.

4.3.6.2 Anisotropic Flow contribution

The baseline function $B(\Delta\varphi)$ uses the central values of the flow coefficients (after determining the weighted values using the particle spectra), but does not take into account the associated statistical and systematic uncertainties of the measurements. Following the same procedure to determine the central values of v_n described in section 3.8.1, the statistical and systematic errors for the coefficients reweighted for the p_T^e and $p_T^{\text{assoc.}}$ intervals are determined as reported in tables 3.5 through 3.8 in the analysis methodology section.

For the systematic study of the flow coefficients, the statistical and systematic uncertainties associated with v_n are combined in quadrature to obtain a total systematic uncertainty σ_{v_n} ,

$$\sigma_{v_n} = \sqrt{(\sigma_{v_n}^{\text{stat.}})^2 + (\sigma_{v_n}^{\text{sys.}})^2}. \quad (4.4)$$

The systematic study for the v_n contribution makes two assumptions:

- The true value of v_n for the heavy-flavor hadron decay electrons and the charged particles is within $1 \times \sigma_{v_n}$.
- Of the four separate flow coefficient values used in the baseline function, one or two of the true σ_{v_n} values at a time is $1 \times \sigma_{v_n}$ from the central value.

Using these assumptions, 16 variations of the baseline were created, using the same b parameter taken from the nominal baseline function used in the analysis. Eight variations change only one value of v_n to $v_n \pm \sigma_{v_n}$, and the remaining eight variations change two values of v_n to $v_n \pm \sigma_{v_n}$. This results in the following baseline variations:

1. $v_2^{\text{HFe}} \rightarrow v_2^{\text{HFe}} + \sigma_{v_2}^{\text{HFe}}$
2. $v_2^{\text{HFe}} \rightarrow v_2^{\text{HFe}} - \sigma_{v_2}^{\text{HFe}}$

3. $v_3^{\text{HFe}} \rightarrow v_3^{\text{HFe}} + \sigma_{v_3}^{\text{HFe}}$
4. $v_3^{\text{HFe}} \rightarrow v_3^{\text{HFe}} - \sigma_{v_3}^{\text{HFe}}$
5. $v_2^{\text{Ch.Part.}} \rightarrow v_2^{\text{Ch.Part.}} + \sigma_{v_2}^{\text{Ch.Part.}}$
6. $v_2^{\text{Ch.Part.}} \rightarrow v_2^{\text{Ch.Part.}} - \sigma_{v_2}^{\text{Ch.Part.}}$
7. $v_3^{\text{Ch.Part.}} \rightarrow v_3^{\text{Ch.Part.}} + \sigma_{v_3}^{\text{Ch.Part.}}$
8. $v_2^{\text{Ch.Part.}} \rightarrow v_2^{\text{Ch.Part.}} - \sigma_{v_2}^{\text{Ch.Part.}}$
9. $v_2^{\text{HFe}} \rightarrow v_2^{\text{HFe}} + \sigma_{v_2}^{\text{HFe}}, v_2^{\text{Ch.Part.}} \rightarrow v_2^{\text{Ch.Part.}} + \sigma_{v_2}^{\text{Ch.Part.}}$
10. $v_2^{\text{HFe}} \rightarrow v_2^{\text{HFe}} - \sigma_{v_2}^{\text{HFe}}, v_2^{\text{Ch.Part.}} \rightarrow v_2^{\text{Ch.Part.}} - \sigma_{v_2}^{\text{Ch.Part.}}$
11. $v_3^{\text{HFe}} \rightarrow v_3^{\text{HFe}} + \sigma_{v_3}^{\text{HFe}}, v_3^{\text{Ch.Part.}} \rightarrow v_3^{\text{Ch.Part.}} + \sigma_{v_3}^{\text{Ch.Part.}}$
12. $v_3^{\text{HFe}} \rightarrow v_3^{\text{HFe}} - \sigma_{v_3}^{\text{HFe}}, v_3^{\text{Ch.Part.}} \rightarrow v_3^{\text{Ch.Part.}} - \sigma_{v_3}^{\text{Ch.Part.}}$
13. $v_2^{\text{HFe}} \rightarrow v_2^{\text{HFe}} + \sigma_{v_2}^{\text{HFe}}, v_2^{\text{Ch.Part.}} \rightarrow v_2^{\text{Ch.Part.}} - \sigma_{v_2}^{\text{Ch.Part.}}$
14. $v_2^{\text{HFe}} \rightarrow v_2^{\text{HFe}} - \sigma_{v_2}^{\text{HFe}}, v_2^{\text{Ch.Part.}} \rightarrow v_2^{\text{Ch.Part.}} + \sigma_{v_2}^{\text{Ch.Part.}}$
15. $v_3^{\text{HFe}} \rightarrow v_3^{\text{HFe}} + \sigma_{v_3}^{\text{HFe}}, v_3^{\text{Ch.Part.}} \rightarrow v_3^{\text{Ch.Part.}} - \sigma_{v_3}^{\text{Ch.Part.}}$
16. $v_3^{\text{HFe}} \rightarrow v_3^{\text{HFe}} - \sigma_{v_3}^{\text{HFe}}, v_3^{\text{Ch.Part.}} \rightarrow v_3^{\text{Ch.Part.}} + \sigma_{v_3}^{\text{Ch.Part.}}$

Figures 4.12 and 4.13 illustrate the the 16 different baselines created by the flow coefficient variations. In both centrality classes, the variations appear to differ in the lowest $p_{\text{T}}^{\text{assoc.}}$ interval, with the greatest difference seen in the troughs and peaks near $-\frac{\pi}{2}$, 0 , $\frac{\pi}{2}$, around π , and $\frac{3\pi}{2}$. As $p_{\text{T}}^{\text{assoc.}}$ increases, the variations all appear to approach the same shape to a near flat line at the highest interval. This follows the expectations of the behavior, given that the b parameter affects the magnitude of the modulation, and a larger background (therefore larger b) would result in a more dramatic flow contribution.

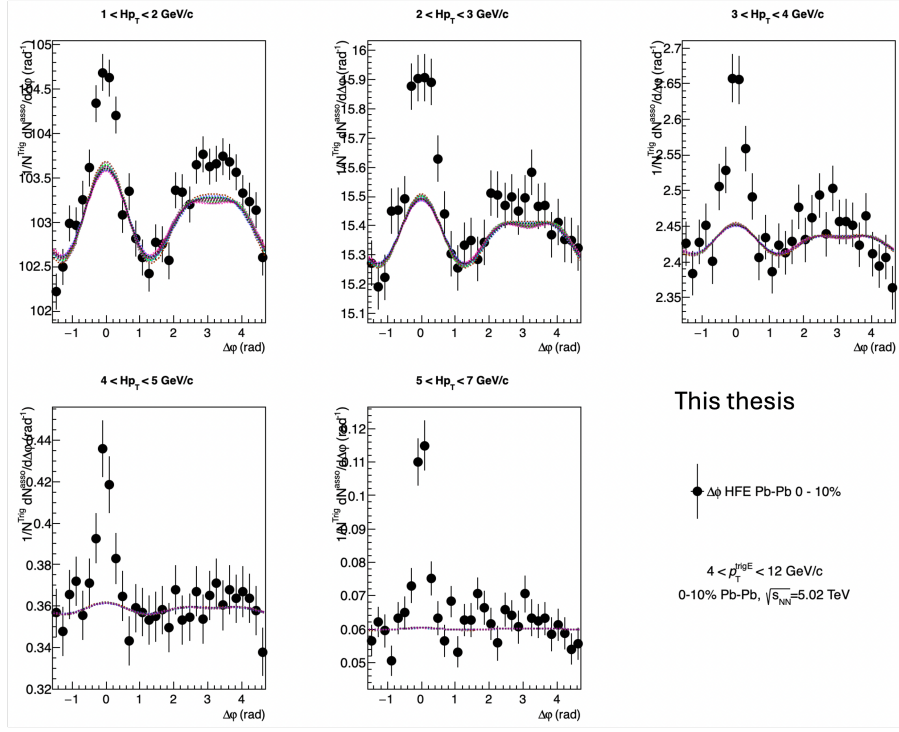


Figure 4.12: 16 separate baseline variations made from the v_n variations in the $4 < p_T^e < 12 \text{ GeV/c}$ trigger interval for the most-central collision events.

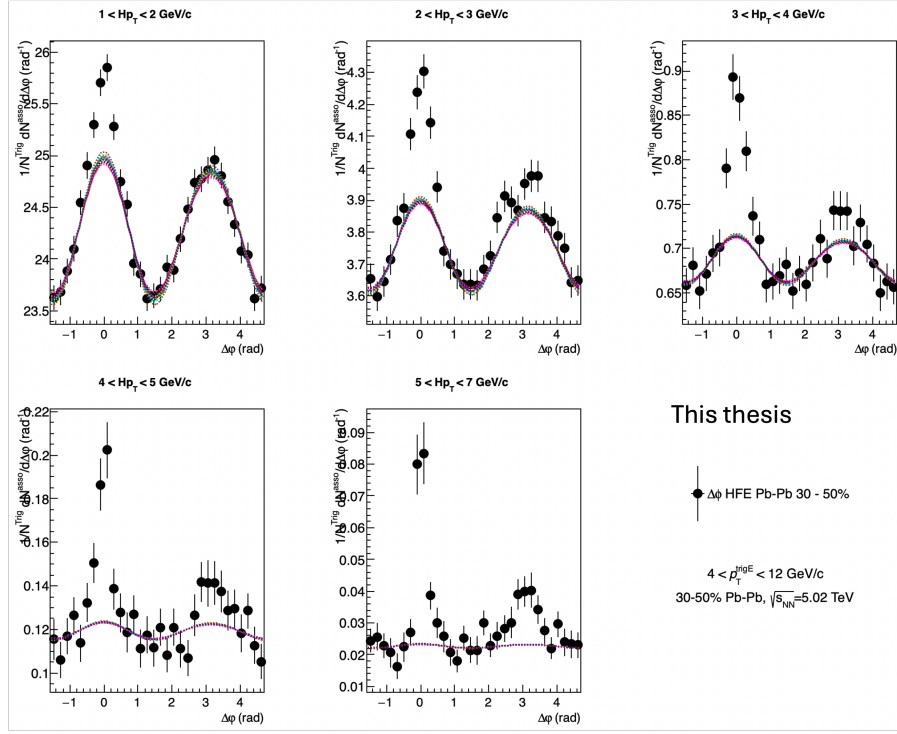


Figure 4.13: 16 separate baseline variations made from the v_n variations in the $4 < p_T^e < 12$ GeV/ c trigger interval for the semicentral collision events.

To check the systematic effect of the v_n variations, the per-trigger yields were obtained for these 16 baseline variations and compared to the per-trigger yields from the 6 b parameter variations after taking the ratio to the nominal yields. These are shown for Figs. 4.14 and 4.15 with the corresponding legend in Fig. 4.16, where the closed circles represent the v_n variations the open circles represent the b parameter variations.

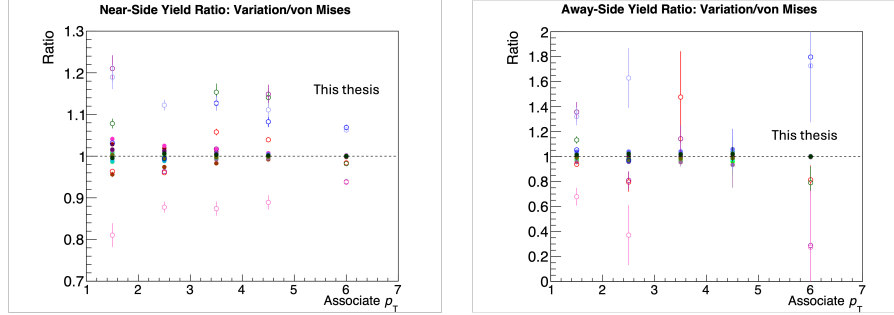


Figure 4.14: Ratios of the per-trigger yields of the baseline variations to the nominal yields in the 0–10% centrality class.

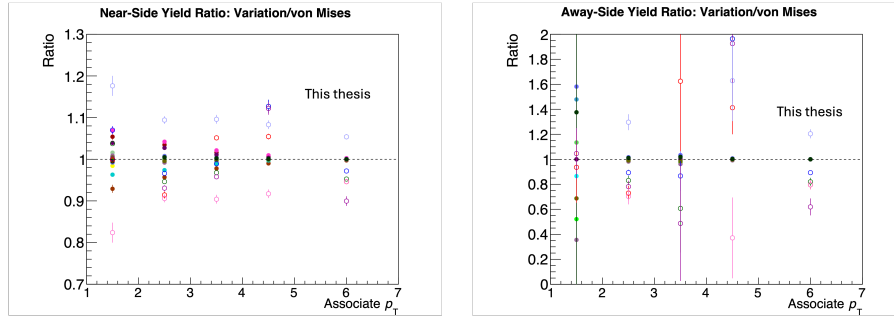


Figure 4.15: Ratios of the per-trigger yields of the baseline variations to the nominal yields in the 30–50% centrality class.

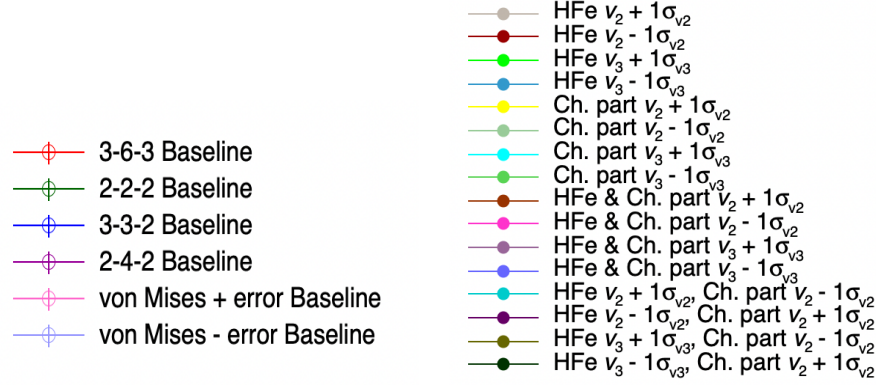


Figure 4.16: List of the 16 v_n variations and the 6 b parameter variations for the systematic baseline study.

On the near-side, the baselines corresponding to the v_n variations deviate from the nominal yield by a maximum of 8%, with this difference in the lowest $p_T^{\text{assoc.}}$ interval, and decreasing to $< 1\%$ at the highest interval. On the away-side yields, some of the adjusted v_n values cause the yield to be negatively-valued (which are not shown in the figures). The positively-valued ratios are well-constrained under 10% relative to the nominal yield. By comparison, the b parameter variations encapsulate the v_n variations by a wide margin for both the near- and away-side yields, averaging to about 20% relative uncertainty, indicating that the uncertainty attributed to the baseline is determined overwhelmingly by the b value uncertainty.

4.3.6.3 Baseline Uncertainty Expression

Following the baseline systematic studies focusing on the contribution of the b value and the flow coefficients, the magnitude of the baseline systematic uncertainty is determined by the uncertainty of the b parameter. However, much of this uncertainty is attributed to the statistical fluctuations in the distributions, making the b value estimation difficult using conventional means. Because the systematic uncertainties from other sources such as the electron and associated particle tracking, photonic electron background, etc., are well-defined, these systematic uncertainties can be grouped together conventionally. Therefore, the decision was made to separate the baseline uncertainty into its own error bar for the final results. Instead of plotting the baseline uncertainty as a percentage of the total yield, it was instead reported as $\frac{1}{2}$ the difference between the absolute value of the maximum or minimum of the variations. This was repeated for the correlations in the other p_T^e ranges.

For the correlation distribution, the baseline uncertainty is conveyed by a band along $\Delta\varphi$ (see Fig. 4.17). This band is created by determining the following:

- $\text{band width}(p_T^{\text{assoc.}}) = \frac{b_{\text{highest}}(p_T^{\text{assoc.}}) - b_{\text{lowest}}(p_T^{\text{assoc.}})}{2}$

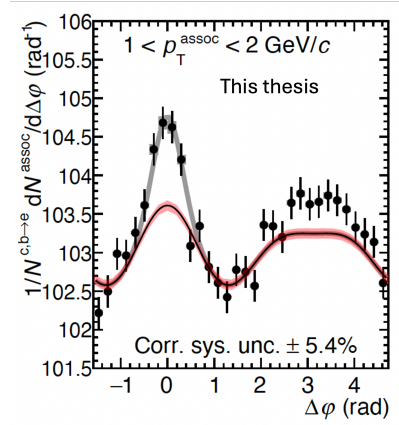


Figure 4.17: Baseline uncertainty represented with a red band along $\Delta\varphi$, taken from the b variations. Shown is the correlation distribution for 0–10% centrality collisions in the $1 < p_T^{\text{assoc.}} < 2 \text{ GeV}/c$ interval.

Where this is performed for every $p_T^{\text{assoc.}}$ interval.

To convey the baseline uncertainty of the per-trigger yields, the maximum and minimum yields from the correlation distributions shown in the section 4.3.6.1 (the

distributions resulting from subtracting the highest and lowest baselines in every $p_T^{\text{assoc.}}$ interval) and taking the difference between them. This done as:

- $\frac{Yield_{\text{Highest}} - Yield_{\text{Lowest}}}{2}$

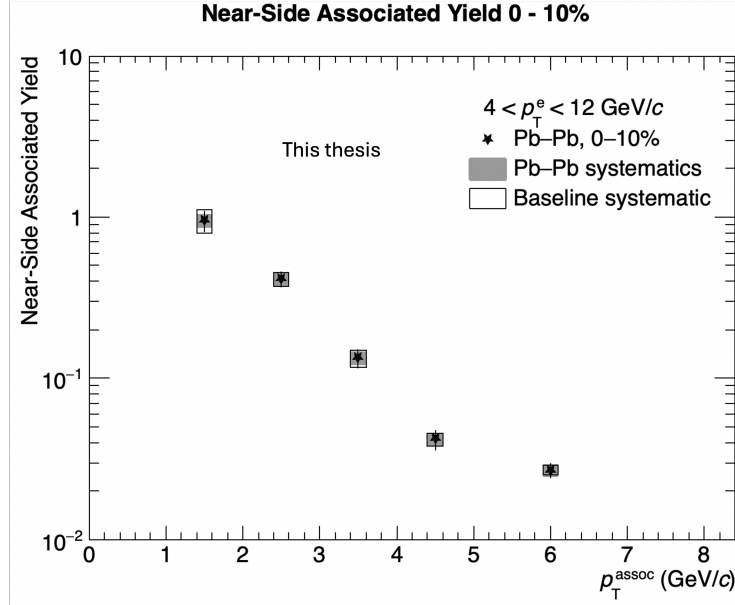


Figure 4.18: Baseline uncertainty represented with an open box, taken from the b variations. Shown is the correlation distribution for 0–10% centrality collisions.

All of these systematic values are reported in the updated systematic tables in section 4.4.

4.4 Final Systematic Tables

The final systematic values determined in the analysis are reported in Tables 4.5 through 4.22. All uncertainties except for those which relate to the baseline are conveyed as solid error bars in the final results.

Table 4.5: $\Delta\varphi$ Systematic Relative Error for $4 < p_T^{\text{trig.e}} < 12$ in 0 - 10%

Systematic	p_T^h in GeV/c				
0 - 10% $\Delta\varphi$	1 - 2	2 - 3	3 - 4	4 - 5	5 - 7
Associate Tracking	5%	5%	5%	5%	5%
Mixed Event	2%	2%	2%	2%	2%
Electron Tracking	5%	5%	5%	5%	5%
EID	3%	3%	3%	3%	3%
Photonic Ele	5%	5%	5%	5%	5%
Max - Default baseline	0.0609	0.0248	0.0088	0.0032	0.0013
Min - Default baseline	-0.0699	-0.0248	-0.0121	-0.0032	-0.0020

Table 4.6: Near Side Yield Systematic Relative Error for $4 < p_T^{\text{trig.e}} < 12$ in 0 - 10%

Systematic	p_T^h in GeV/c				
0 - 10% NS yield	1 - 2	2 - 3	3 - 4	4 - 5	5 - 7
Associate Tracking	5%	5%	5%	5%	5%
Mixed Event	2%	2%	2%	2%	2%
Electron Tracking	5%	5%	5%	5%	5%
EID	3%	3%	3%	3%	3%
Photonic Ele	5%	5%	5%	5%	5%
(Max Yield - Min Yield)/2	0.1543	0.0391	0.0165	0.0038	0.0019

Table 4.7: Away Side Yield Systematic Relative Error for $4 < p_T^{\text{trig.e}} < 12$ in 0 - 10%

Systematic	p_T^h in GeV/c				
0 - 10% AS yield	1 - 2	2 - 3	3 - 4	4 - 5	5 - 7
Associate Tracking	5%	5%	5%	5%	5%
Mixed Event	2%	2%	2%	2%	2%
Electron Tracking	5%	5%	5%	5%	5%
EID	4%	4%	4%	4%	4%
Photonic Ele	5%	5%	5%	5%	5%
(Max Yield - Min Yield)/2	0.2056	0.0778	0.0328	0.0100	0.0051

Table 4.8: $\Delta\varphi$ Systematic Relative Error for $4 < p_T^{trig.e} < 12$ in 30 - 50%

Systematic	p_T^h in GeV/ c				
30 - 50% $\Delta\varphi$	1 - 2	2 - 3	3 - 4	4 - 5	5 - 7
Associate Tracking	3%	3%	3%	3%	3%
Mixed Event	2%	2%	2%	2%	2%
Electron Tracking	2%	2%	2%	2%	2%
EID	1%	1%	1%	1%	1%
Photonic Ele	3%	3%	3%	3%	3%
Max - Default baseline	0.0366	0.0136	0.0057	0.0023	0.0017%
Min - Default baseline	-0.0366	-0.0136	-0.0057	-0.0028	-0.0011

Table 4.9: Near Side Yield Systematic Relative Error for $4 < p_T^{trig.e} < 12$ in 30 - 50%

Systematic	p_T^h in GeV/c				
30 - 50% NS yield	1 - 2	2 - 3	3 - 4	4 - 5	5 - 7
Associate Tracking	3%	3%	3%	3%	3%
Mixed Event	2%	2%	2%	2%	2%
Electron Tracking	2%	2%	2%	2%	2%
EID	2%	2%	2%	2%	2%
Photonic Ele	3%	3%	3%	3%	3%
(Max Yield - Min Yield)/2	0.0870	0.0219	0.0092	0.0031	0.0016

 Table 4.10: Away Side Yield Systematic Relative Error for $4 < p_T^{trig.e} < 12$ in 30 - 50%

Systematic	p_T^h in GeV/c				
30 - 50% AS yield	1 - 2	2 - 3	3 - 4	4 - 5	5 - 7
Associate Tracking	3%	3%	3%	3%	3%
Mixed Event	2%	2%	2%	2%	2%
Electron Tracking	3%	3%	3%	3%	3%
EID	2%	2%	2%	2%	2%
Photonic Ele	4%	4%	4%	4%	4%
(Max Yield - Min Yield)/2	0.1152	0.0428	0.0179	0.0080	0.0043

 Table 4.11: $\Delta\varphi$ Systematic Relative Error for $4 < p_T^{trig.e} < 7$ in 0 - 10%

Systematic	p_T^h in GeV/c				
0 - 10% $\Delta\varphi$	1 - 2	2 - 3	3 - 4	4 - 5	5 - 7
Associate Tracking	5%	5%	5%	5%	5%
Mixed Event	2%	2%	2%	2%	2%
Electron Tracking	5%	5%	5%	5%	5%
EID	6%	6%	6%	6%	6%
Photonic Ele	5%	5%	5%	5%	5%
Max - Default baseline	0.0679	0.0270	0.0098	0.0035	0.0016
Min - Default baseline	-0.0679	-0.0270	-0.0098	-0.0035	-0.0011

Table 4.12: Near-Side Yield Systematic Relative Error for $4 < p_T^{trig.e} < 7$ in 0 - 10%

Systematic	p_T^h in GeV/ c				
0 - 10% NS yield	1 - 2	2 - 3	3 - 4	4 - 5	5 - 7
Associate Tracking	5%	5%	5%	5%	5%
Mixed Event	2%	2%	2%	2%	2%
Electron Tracking	5%	5%	5%	5%	5%
EID	5%	5%	5%	5%	5%
Photonic Ele	5%	5%	5%	5%	5%
(Max Yield - Min Yield)/2	0.1602	0.0426	0.0155	0.0041	0.0016

Table 4.13: Away-Side Yield Systematic Relative Error for $4 < p_T^{trig.e} < 7$ in 0 - 10%

Systematic	p_T^h in GeV/c				
0 - 10% AS yield	1 - 2	2 - 3	3 - 4	4 - 5	5 - 7
Associate Tracking	5%	5%	5%	5%	5%
Mixed Event	2%	2%	2%	2%	2%
Electron Tracking	5%	5%	5%	5%	5%
EID	7%	7%	7%	7%	7%
Photonic Ele	5%	5%	5%	5%	5%
(Max Yield - Min Yield)/2	0.2134	0.0849	0.0308	0.0109	0.0042

Table 4.14: $\Delta\varphi$ Systematic Relative Error for $4 < p_T^{trig.e} < 7$ in 30 - 50%

Systematic	p_T^h in GeV/c				
0 - 10% $\Delta\varphi$	1 - 2	2 - 3	3 - 4	4 - 5	5 - 7
Associate Tracking	4%	4%	4%	4%	4%
Mixed Event	2%	2%	2%	2%	2%
Electron Tracking	2%	2%	2%	2%	2%
EID	2%	2%	2%	5%	5%
Photonic Ele	4%	4%	4%	4%	4%
Max - Default baseline	0.0491	0.0248	0.0081	0.0031	0.0014
Min - Default baseline	-0.0491	-0.0195	-0.0081	-0.0036	-0.0011

Table 4.15: Near-Side Yield Systematic Relative Error for $4 < p_T^{trig.e} < 7$ in 30 - 50%

Systematic	p_T^h in GeV/c				
0 - 10% NS yield	1 - 2	2 - 3	3 - 4	4 - 5	5 - 7
Associate Tracking	4%	4%	4%	4%	4%
Mixed Event	2%	2%	2%	2%	2%
Electron Tracking	2%	2%	2%	2%	2%
EID	2%	2%	2%	2%	2%
Photonic Ele	3%	3%	3%	3%	3%
(Max Yield - Min Yield)/2	0.1165	0.0356	0.0130	0.0040	0.0015

Table 4.16: Away-Side Yield Systematic Relative Error for $4 < p_T^{trig.e} < 7$ in 30 - 50%

Systematic	p_T^h in GeV/ c				
0 - 10% AS yield	1 - 2	2 - 3	3 - 4	4 - 5	5 - 7
Associate Tracking	4%	4%	4%	4%	4%
Mixed Event	2%	2%	2%	2%	2%
Electron Tracking	3%	3%	3%	3%	3%
EID	4%	4%	4%	4%	4%
Photonic Ele	4%	4%	4%	4%	4%
(Max Yield - Min Yield)/2	0.1542	0.0696	0.0254	0.0104	0.0038

Table 4.17: $\Delta\varphi$ Systematic Relative Error for $7 < p_T^{trig.e} < 16$ in 0 - 10%

Systematic	p_T^h in GeV/c				
0 - 10% $\Delta\varphi$	1 - 2	2 - 3	3 - 4	4 - 5	5 - 7
Associate Tracking	5%	5%	5%	5%	5%
Mixed Event	2%	2%	2%	2%	2%
Electron Tracking	5%	5%	5%	5%	5%
EID	6%	6%	6%	6%	6%
Photonic Ele	5%	5%	5%	5%	5%
Max - Default baseline	0.1231	0.0523	0.0186	0.0079	0.0050
Min - Default baseline	-0.1231	-0.0725	-0.0209	-0.0080	-0.0095

Table 4.18: Near-Side Yield Systematic Relative Error for $7 < p_T^{trig.e} < 16$ in 0 - 10%

Systematic	p_T^h in GeV/c				
0 - 10% NS yield	1 - 2	2 - 3	3 - 4	4 - 5	5 - 7
Associate Tracking	5%	5%	5%	5%	5%
Mixed Event	2%	2%	2%	2%	2%
Electron Tracking	5%	5%	5%	5%	5%
EID	5%	5%	5%	5%	5%
Photonic Ele	5%	5%	5%	5%	5%
(Max Yield - Min Yield)/2	0.2902	0.0983	0.0311	0.0093	0.0086

Table 4.19: Away-Side Yield Systematic Relative Error for $7 < p_T^{trig.e} < 16$ in 0 - 10%

Systematic	p_T^h in GeV/c				
0 - 10% AS yield	1 - 2	2 - 3	3 - 4	4 - 5	5 - 7
Associate Tracking	5%	5%	5%	5%	5%
Mixed Event	2%	2%	2%	2%	2%
Electron Tracking	5%	5%	5%	5%	5%
EID	7%	7%	7%	7%	7%
Photonic Ele	5%	5%	5%	5%	5%
(Max Yield - Min Yield)/2	0.3868	0.1961	0.0621	0.0248	0.0228

Table 4.20: $\Delta\varphi$ Systematic Relative Error for $7 < p_T^{trig.e} < 16$ in 30 - 50%

Systematic	p_T^h in GeV/ c				
0 - 10% $\Delta\varphi$	1 - 2	2 - 3	3 - 4	4 - 5	5 - 7
Associate Tracking	4%	4%	4%	4%	4%
Mixed Event	2%	2%	5%	5%	5%
Electron Tracking	2%	2%	2%	2%	2%
EID	3%	3%	3%	3%	3%
Photonic Ele	3%	3%	3%	3%	3%
Max - Default baseline	0.1320	0.0338	0.0333	0.0070	0.0087
Min - Default baseline	-0.1320	-0.0379	-0.0142	-0.0070	-0.0051

Table 4.21: Near-Side Yield Systematic Relative Error for $7 < p_T^{trig.e} < 16$ in 30 - 50%

Systematic	p_T^h in GeV/ c				
0 - 10% NS yield	1 - 2	2 - 3	3 - 4	4 - 5	5 - 7
Associate Tracking	4%	4%	4%	4%	4%
Mixed Event	2%	2%	5%	5%	5%
Electron Tracking	2%	2%	2%	2%	2%
EID	2%	2%	2%	2%	2%
Photonic Ele	3%	3%	3%	3%	3%
(Max Yield - Min Yield)/2	0.3129	0.0573	0.0380	0.0084	0.0082

Table 4.22: Away-Side Yield Systematic Relative Error for $7 < p_T^{trig.e} < 16$ in 30 - 50%

Systematic	p_T^h in GeV/ c				
0 - 10% AS yield	1 - 2	2 - 3	3 - 4	4 - 5	5 - 7
Associate Tracking	4%	4%	4%	4%	4%
Mixed Event	2%	2%	5%	5%	5%
Electron Tracking	2%	2%	2%	2%	2%
EID	4%	4%	4%	4%	4%
Photonic Ele	4%	4%	4%	4%	4%
(Max Yield - Min Yield)/2	0.4149	0.1127	0.0746	0.0220	0.0217

Chapter Five: Measurement Results

After following each step of the analysis procedure and estimating the systematic uncertainties, the final results emerge. At this point, it is useful to review the motivation for the analysis and discuss the published correlation measurement in pp and p–Pb collisions [135], which is done in section 5.1. In section 5.2, the correlation distributions of heavy-flavor hadron decay electrons with charged particles are shown for Pb–Pb collisions measured in the 0–10% and 30–50% centrality classes at $\sqrt{s_{\text{NN}}} = 5.02$ TeV. The subsequent sections include the correlation distributions after the baseline subtraction and the per-trigger associated particle yields, which are the first HF azimuthal correlation measurements performed on Pb–Pb collisions measured by the ALICE experiment. The distributions and yields for the near- and away-side peaks are compared to the same measurements in pp collisions, first comparatively and then directly through the ratio of the yields in the different collision systems. Next, the correlation results are shown for two non-overlapping trigger electron p_{T} ranges. Finally, the correlation results are compared to light-flavor results to investigate the flavor-dependence of the modification of the peak yields in Pb–Pb collisions.

5.1 Electron from HF hadron decay correlations in pp and p–Pb

At leading order (LO), heavy quark pairs are produced 180° in azimuth in hard-scattering processes. Given a sufficiently large momentum transfer, these quarks can initiate back-to-back jets. The fragmentation pattern of the initiating heavy quark determines the angular orientation of the jet parton shower. This heavy quark preferentially hadronizes into the leading particle of the jet [62]. Because the hadrons in the jet are produced in small angle relative to the parent partons [179], the final angular orientation of hadrons with respect to the leading particle is primarily determined by the parton shower phase of the heavy quark fragmentation [59]. Azimuthal correlation measurements of electrons from the decay of heavy flavor hadrons in different $p_{\text{T}}^{\text{assoc.}}$ regions can be used to study the angular profile of particles correlated with

the original HF quark as a function of p_T . Although the decay of the HF hadron to electron results in the electron deviating from the parent hadron axis, this electron maintains its correlation with the heavy quark fragmentation products.

This measurement in proton-proton collisions provides the azimuthal distribution of the particles associated with the electron in vacuum. This serves as the baseline for comparison to the same analysis in p-Pb and Pb-Pb collisions, and is directly comparable to different Monte Carlo event generators. Performing this measurement in p-Pb collisions introduces cold-nuclear matter effects, which can affect the jet fragmentation pattern in the initial state. In Fig. 5.1, the heavy-flavor decay electron correlation distributions are shown for pp (black) and p-Pb (red) [135].

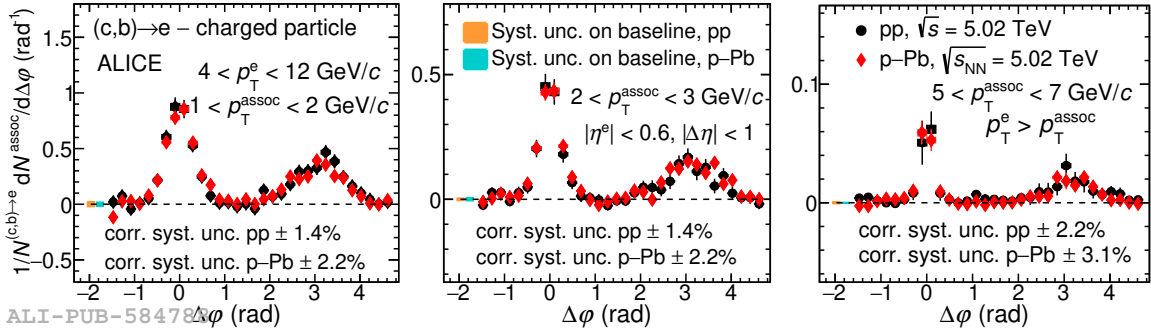


Figure 5.1: Azimuthal-correlation distribution of heavy-flavor hadron decay electrons and charged particles measured pp (black) and p-Pb collisions (red) at $\sqrt{s_{NN}} = 5.02$ TeV by ALICE [135]. The distributions are shown in the trigger range of $4 < p_T^e < 12$ GeV/c and three p_T^{assoc} intervals.

Observing the near-side peaks of the $\Delta\phi$ correlation distributions in both collision systems, it appears that for both pp and p-Pb, the overall peak heights decrease and become more collimated as p_T^{assoc} increases. This behavior of the near-side peak indicates that the higher- p_T associated particles are closer to the jet axis of the leading heavy-flavor hadron, which can be due to the high- p_T emissions being more collinear to the initiating heavy quark. As p_T^{assoc} increases, the away-side peaks generally decrease in size. The AS peaks can have multiple contributions, such as the fragmentation of the opposite quark, or from particles originating from a recoil gluon, or from other separate processes in the event. Generally, even in a pure back-to-back process, the correlation of the trigger with associated particles in the away-side jet is weaker than the correlation in the near-side jet. The shape and amplitude of the

the associated yields show that within uncertainty, the values for pp and p—Pb are consistent. In terms of the peak widths, the pp and p—Pb widths both decrease with $p_T^{\text{assoc.}}$ on the near-side peak, where both are close to 0.3 at $1 < p_T^{\text{assoc.}} < 2$ GeV/ c , decreasing to about 0.15 at $4 < p_T^{\text{assoc.}} < 7$ GeV/ c . For the away-side peak width, there is no discernible trend due to the uncertainty of the measurements.

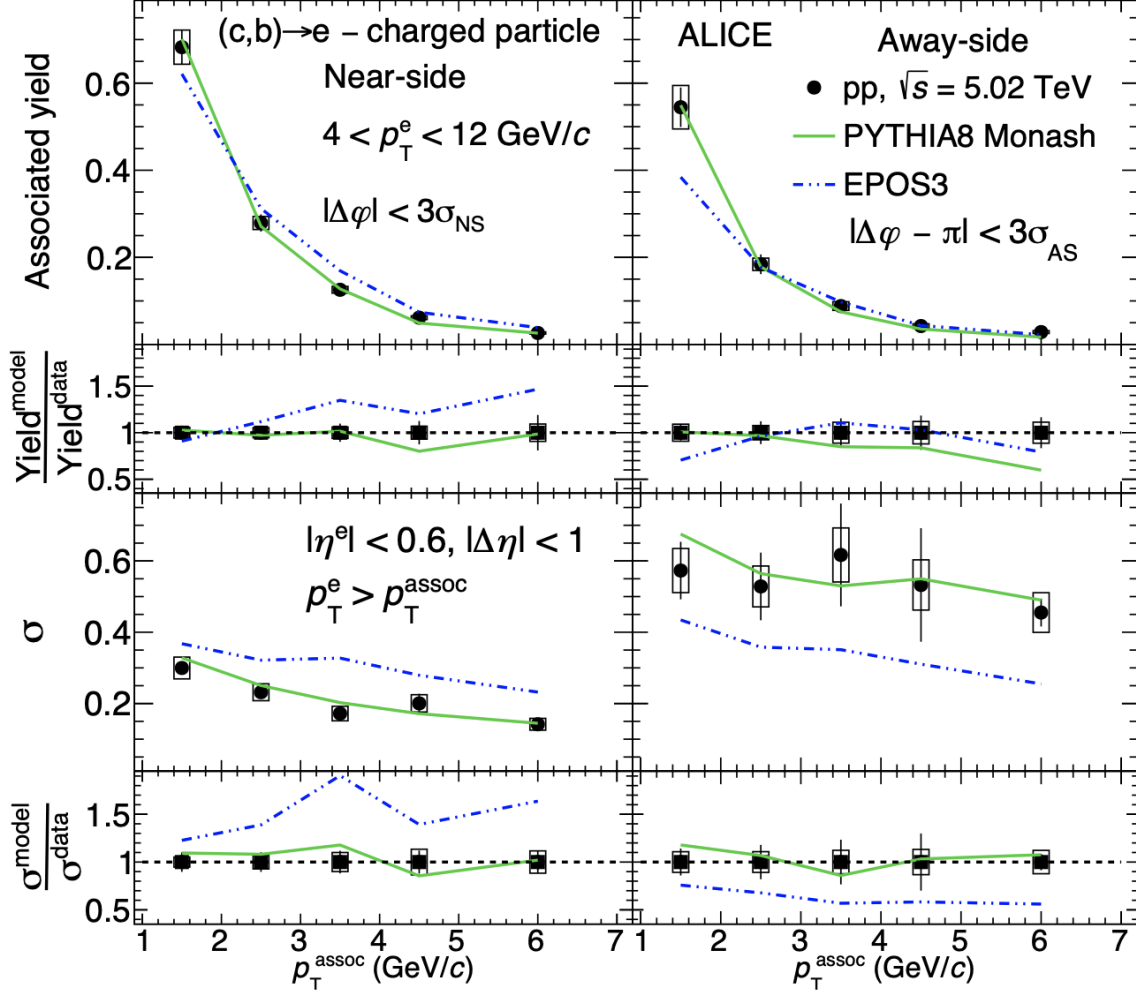


Figure 5.3: Per-trigger associated yields and peak widths in pp compared to PYTHIA8 Monash and EPOS3 in $4 < p_T^e < 12$ GeV/ c and all $p_T^{\text{assoc.}}$ intervals at $\sqrt{s_{\text{NN}}} = 5.02$ TeV measured by ALICE [135].

Figure 5.3 shows the pp yield and widths in comparison to the PYTHIA8 with Monash tune and EPOS3 event generators. PYTHIA is commonly used to describe

high-energy proton-proton collisions with high accuracy. EPOS3 is primarily used for heavy-ion collision simulation, which it does by using a core-corona model to simulate the hydrodynamic behavior of the QGP. Both event generators describe the overall trends of the observables, but PYTHIA provides a closer estimate to the measured values. EPOS3 predicts the overall observable distributions, but it produces less-accurate descriptions of the near-side widths than PYTHIA, and entirely underpredicts the away-side peak.

5.2 $\Delta\varphi$ Correlation Distributions in Pb–Pb

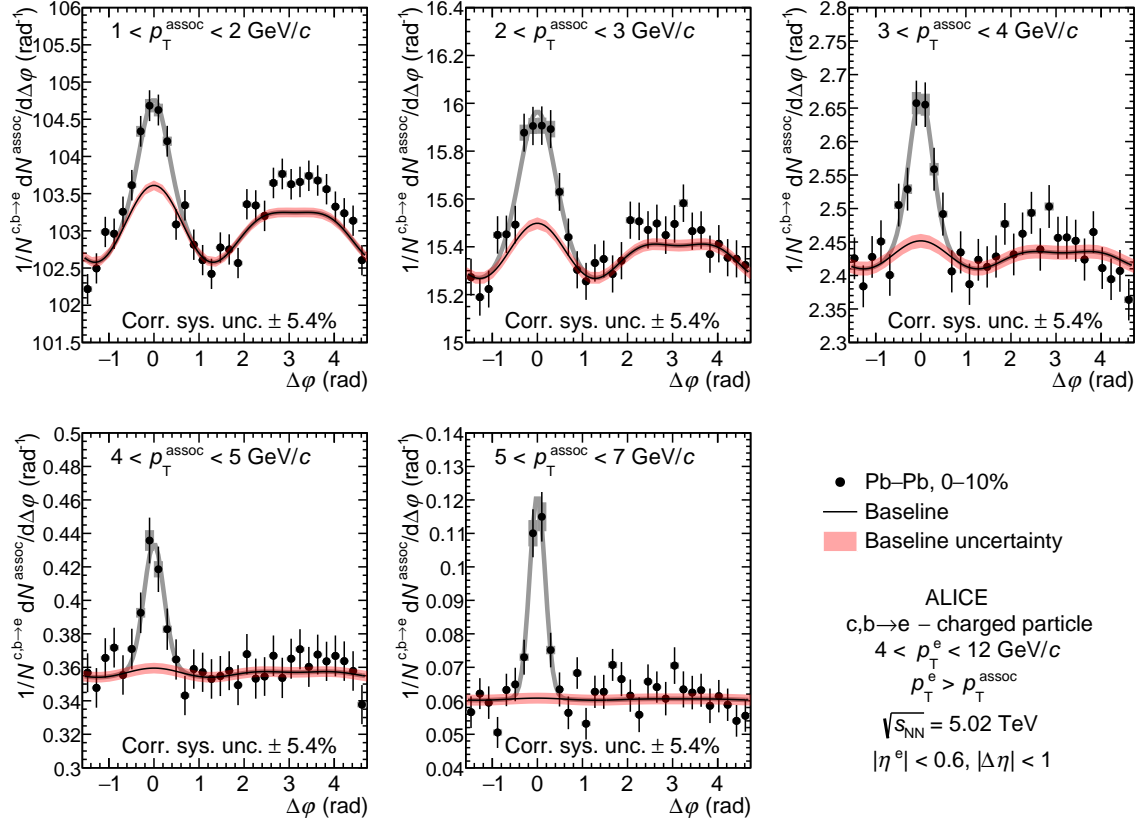


Figure 5.4: Azimuthal-correlation distribution of heavy-flavor hadron decay electrons and charged particles measured in 0–10% central Pb–Pb collisions before background subtraction publicly available by ALICE [180]. The distributions are shown in the trigger range of $4 < p_T^e < 12$ GeV/c and all p_T^{assoc} intervals. The near-side peak and transverse range of the $\Delta\varphi$ distribution is fit with a von Mises function (solid gray line), and the resulting baseline is shown with a solid black line. The statistical (uncorrelated systematic) uncertainties are shown as vertical lines (filled boxes). The uncertainties on the baseline are shown with the dotted lines.

Azimuthal correlation distributions of heavy-flavor hadron decay electrons with charged particles measured in Pb–Pb collisions in both the 0–10% and 30–50% centrality classes are shown in Figures 5.4 and 5.5.

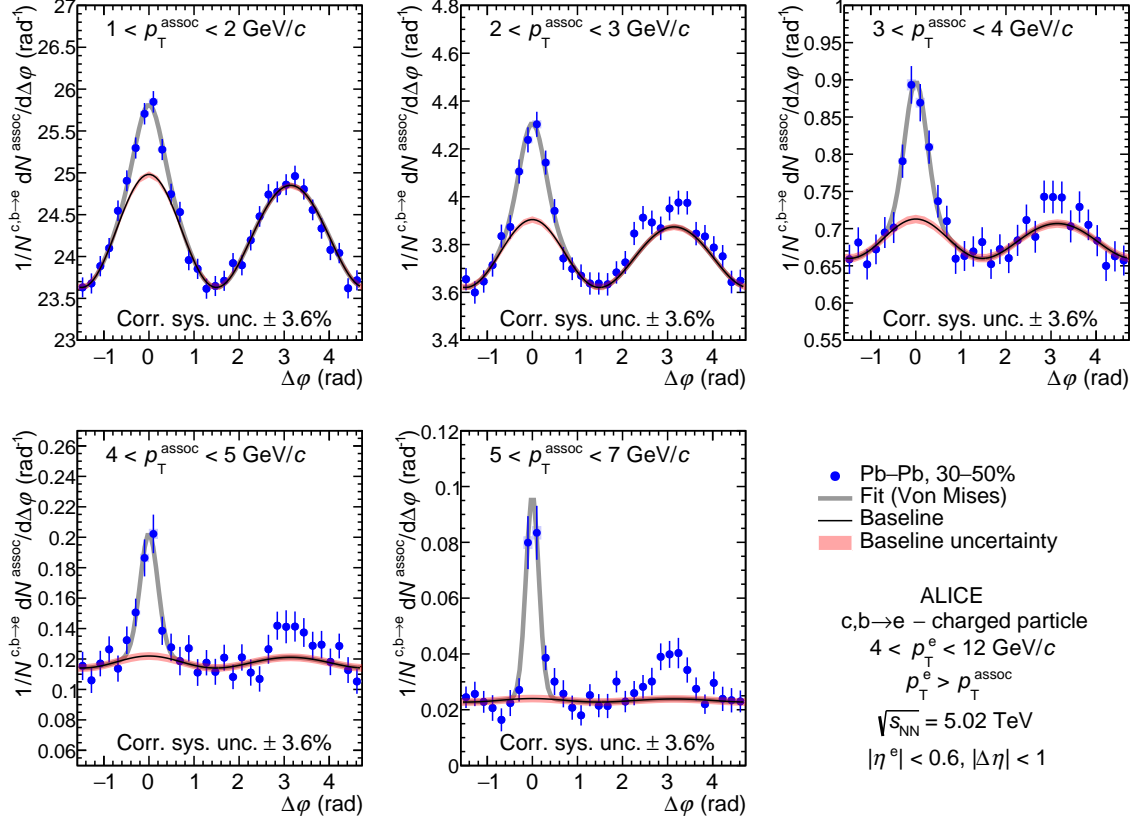


Figure 5.5: Azimuthal-correlation distribution of heavy-flavor hadron decay electrons and charged particles measured in 30–50% central Pb–Pb collisions before background subtraction publicly available by ALICE [180]. The distributions are shown in the trigger range of $4 < p_T^e < 12$ GeV/c and all p_T^{assoc} intervals. The near-side peak and transverse range of the $\Delta\phi$ distribution is fit with a von Mises function (solid gray line), and the resulting baseline is shown with a solid black line. The statistical (uncorrelated systematic) uncertainties are shown as vertical lines (filled boxes). The uncertainties on the baseline are shown with the dotted lines.

These distributions are shown before the uncorrelated background and anisotropic flow contributions are subtracted. A solid black line indicates the function of the baseline which separates the correlation peaks from the background. The uncertainty of the baseline fit is shown with red and blue dotted lines. Immediately evident is the magnitude of the background component increasing at decreasing p_T^{assoc} . This is expected, due to the larger number of low p_T particles relative to high p_T , but the background number in the central collisions is roughly $4\times$ the background in semicentral collisions in the lowest interval. This relative difference in background remains

roughly the same in the $2 < p_T^{\text{assoc}} < 3$ interval and approximately $3\times$ higher in the highest p_T^{assoc} interval. The variation in the background in different p_T^{assoc} intervals and centrality classes is due to the different multiplicity in the collisions. Most particles measured in a heavy-ion collision will be low in p_T , and so will contribute a larger background as the p_T^{assoc} interval decreases. The particle multiplicity has a centrality dependence, such that the total number of particles produced in the central collisions is larger than in semicentral collisions. This is seen when comparing the distributions in the same p_T^{assoc} intervals between the centrality classes, where the background in 0–10% events exceeds the background of 30–50% in all corresponding intervals.

The near-side peaks in both centrality classes become more collimated at increasing p_T^{assoc} , similar to what was seen in the pp and p–Pb distributions. This observation will be discussed further upon direct comparison of the Pb–Pb distributions to pp.

A notable feature in the away-side distribution peaks is an opposing behavior occurring in the two measured centrality classes. For the 0–10% distribution, there is a visible away-side peak sitting on the background in the lowest p_T^{assoc} interval, but at increasing p_T^{assoc} , the peak flattens and becomes indiscernible from the background. For the 30–50% distribution, the shape of the background due to the flow (originating primarily from v_2) appears to entirely describe the away-side peak. However, as p_T^{assoc} increases, the away-side peak emerges and forms a noticeable peak.

An explanation for the away-side behavior in the 10% most-central collisions could be that high- p_T jets on the away-side experience jet-quenching, which would suppress the peak. Alternatively, the near-side jet could impart energy on the QGP and create a diffusion wake on the away-side, resulting in a suppression. However, because the 30–50% centrality class collisions do not exhibit the same behavior, this could indicate that there could be competing mechanisms occurring. Although, one must consider that the QGP size between the two-classes of collisions would differ. However, at the time of this writing there are currently no models which would offer a sufficient comparison to the Pb–Pb correlation distributions. This is due to the computational demand of the extreme multiplicity environment of the collision system, and the need for several million events of sufficiently high- p_T heavy flavor mesons, as well as the computational requirement of incorporating hydrodynamic effects. Direct comparisons to pp and other correlation measurements may give further insight into what could be occurring in these centrality classes.

5.3 $\Delta\phi$ Correlation Distributions in Pb–Pb and pp

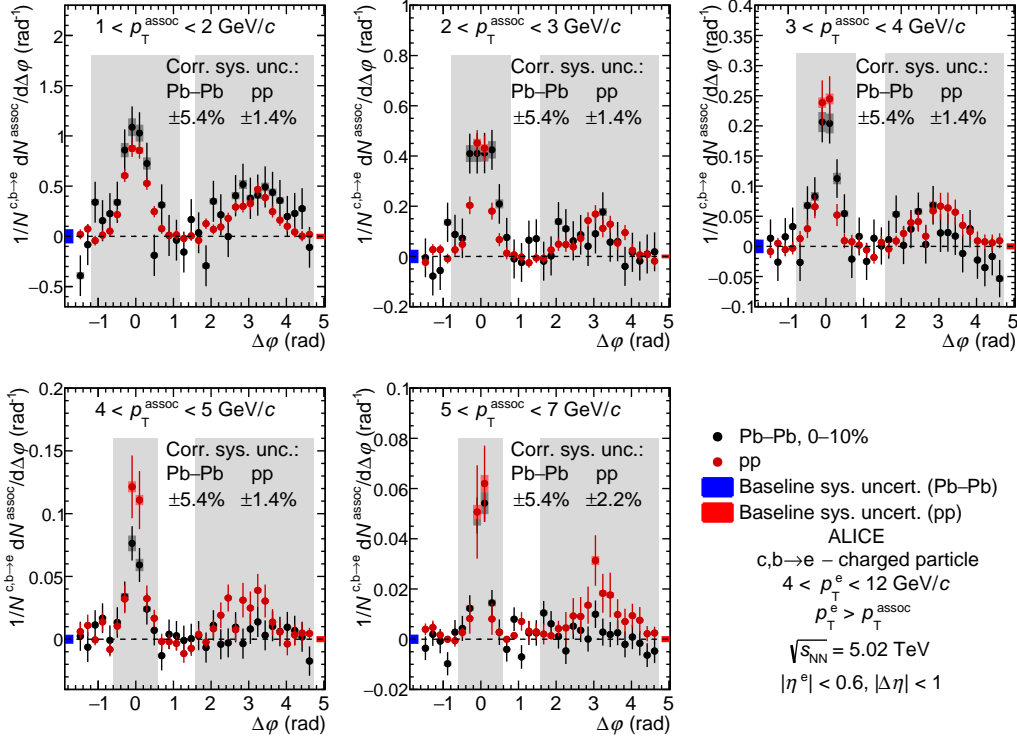


Figure 5.6: Comparison of the azimuthal-correlation distribution of heavy flavor hadron decay electrons with charged particles measured in 0–10% central Pb–Pb collisions and in pp collisions publicly available by ALICE [180]. Uncorrelated background has been subtracted (both), as well as flow contribution (Pb–Pb), for $4 < p_T^e < 12$ GeV/c and different associated p_T ranges. The statistical (uncorrelated systematic) uncertainties are shown as vertical lines (filled boxes). The uncertainties on the baseline estimation are shown as solid boxes at $\Delta\phi \sim -2$ and 5 rad.

The background from uncorrelated pairs and the flow are subtracted from the correlation distributions in the two centrality classes, and they are compared directly to pp distributions in Fig. 5.6 and Fig. 5.7.

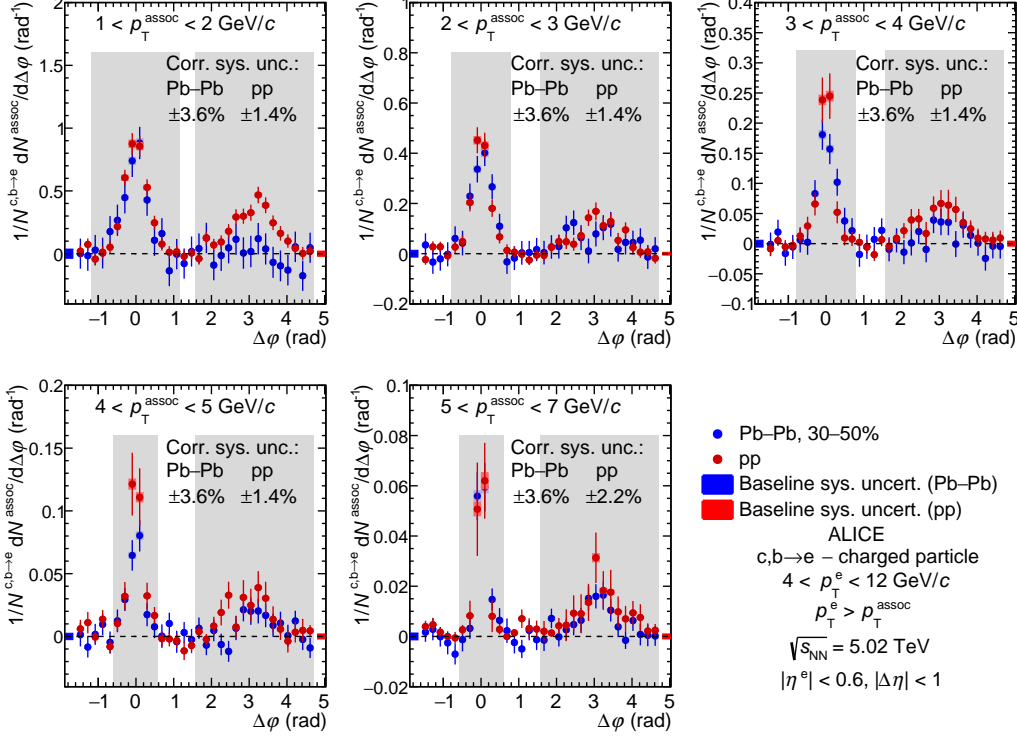


Figure 5.7: Comparison of the azimuthal-correlation distribution of heavy flavor hadron decay electrons with charged particles measured in 30–50% central Pb–Pb collisions and in pp collisions publicly available by ALICE [180]. Uncorrelated background has been subtracted (both), as well as flow contribution (Pb–Pb), for $4 < p_T^e < 12$ GeV/c and different associated p_T ranges. The statistical (uncorrelated systematic) uncertainties are shown as vertical lines (filled boxes). The uncertainties on the baseline estimation are shown as solid boxes at $\Delta\varphi \sim -2$ and 5 rad.

Immediately, it is evident that the near-side peak shape is similar in pp and Pb–Pb for both centrality classes. Focusing first on the 0–10% centrality, the near-side peak in Pb–Pb appears to be slightly larger compared to pp in the lowest $p_T^{\text{assoc.}}$ interval, but as $p_T^{\text{assoc.}}$ increases, the near-side peak in pp becomes similar in size and shape to Pb–Pb. The differences between the two systems are more apparent on the away-side peak. In Pb–Pb in the lowest $p_T^{\text{assoc.}}$ interval, the peak is slightly wider, although due to the fluctuations it is difficult to make a clear distinction. The size of the away-side peak relative to pp clearly decreases with respect to $p_T^{\text{assoc.}}$.

When comparing the 30–50% Pb–Pb distribution to pp, as seen in Fig. 5.7, the near-side peaks are generally consistent between both collision systems. However, the

similar shape at the highest $p_T^{\text{assoc.}}$ interval could indicate that the 30–50% collisions experience less jet-quenching for high- p_T particles compared to the 0–10% collisions.

5.4 Per-Trigger Associated Width

The peak width of a correlation distribution is dependent on multiple factors. NLO effects such as gluon radiation can broaden the near- and away-side peaks [181]. In Pb–Pb collisions, this effect can be enhanced due to the presence of the medium inducing large-gluon angle emission [182]. In the event of gluon splitting, heavy-quark pairs can be produced with a small opening angle, causing the subsequent jets to produce overlapping sprays of hadrons and influence the shape of the peaks [181].

Since the near-side peaks in the Pb–Pb correlation distributions are clearly defined in all $p_T^{\text{assoc.}}$ intervals, this peak was amenable to fitting to obtain the width. Recall from the procedure section 3.8.2.3, the near-side peak is characterized by a von Mises distribution,

$$NS(\Delta\varphi) = \frac{e^{\kappa_{NS} \cos(\Delta\varphi)}}{2\pi I_0(\kappa_{NS})}. \quad (5.1)$$

Where the κ_{NS} is the dependent variable which characterizes the peak width. Also recall that the peak width is obtained from the κ_{NS} factor by,

$$\sigma_{NS} = \sqrt{-2 \log \frac{I_1(\kappa_{NS})}{I_0(\kappa_{NS})}}. \quad (5.2)$$

This method to characterize the peak was done for the correlation distributions of all three collision systems. The pp widths taken from Fig. 5.2 are compared directly to the widths measured in the Pb–Pb system.

5.4.1 Per-trigger Width Comparison to pp

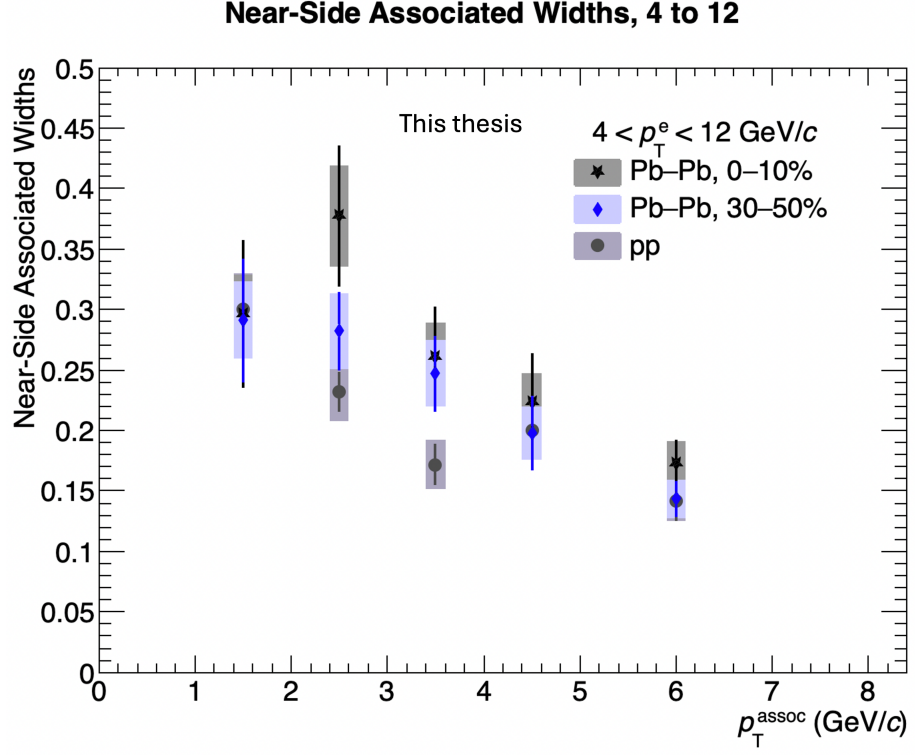


Figure 5.8: Near-side widths from Pb–Pb collisions in the central and semicentral centrality classes compared to pp, for $4 < p_T^e < 12 \text{ GeV}/c$ and all p_T^{assoc} intervals measured for this thesis. The systematic uncertainty was not determined for the Pb–Pb width, so the largest uncertainty on the width in p–Pb collisions was used (11%).

In the comparison of the pp to p–Pb per-trigger widths, Fig. 5.2 shows that the observable in the two collision systems is consistent with each other. In Fig. 5.8 above, the Pb–Pb widths in both centrality classes also appear consistent with pp, and all points generally decrease as a function of p_T^{assoc} . The semicentral distribution follows a very smooth trend and the central widths are almost identical in value with the exception of the $2 < p_T^e < 3$ point, which is likely an upwards fluctuation (given the size of the statistical error bar). The pp widths follow the same overall behavior as a function of p_T^{assoc} and although the possibly fluctuating points between 2 and 4 GeV/c have a relatively small error bar, they are still consistent with the Pb–Pb widths. The close values of the near-side widths suggest that the width of the near-side jet is not significantly modified by the QGP. However, the correlation

distributions are influenced by a surface bias [183], [184], such that the trigger particle in the measurement originates from a heavy quark closer to the surface of the QGP, resulting in a minimal path-length through the medium, which could potentially minimize the effect of medium-induced modifications to the jet.

5.5 Per-Trigger Associated Yield

Associated particle yields are obtained by integrating the correlation distributions in $p_T^{\text{assoc.}}$ ranges motivated from the pp and p—Pb measurements. In the pp correlation analysis, the per-trigger yields were obtained from integrating $\pm 3\sigma$ of the measured σ around the $\Delta\varphi$ distribution peaks. To maintain consistency with the pp and p—Pb measurements, the yield was calculated in the same way for Pb—Pb. The yield extraction for the near-side yields is as follows:

$$Y_{NS} = \int_{-3\sigma_{NS}}^{3\sigma_{NS}} \frac{dN}{d\Delta\varphi} d\Delta\varphi \quad (5.3)$$

And similarly for the away-side yields:

$$Y_{AS} = \int_{\pi-3\sigma_{AS}}^{\pi+3\sigma_{AS}} \frac{dN}{d\Delta\varphi} d\Delta\varphi \quad (5.4)$$

Because there is a clear trend in the near-side σ as a function of $p_T^{\text{assoc.}}$ measured in pp, the integration range varies per associated p_T interval. The same sigma value is used for all $p_T^{\text{assoc.}}$ ranges for the away-side peak. Table 5.1 provides the σ values used in the analysis, which were taken from the PYTHIA width predictions shown in Fig. 5.3.

Table 5.1: σ values used for the yield integration. Associated yields are obtained by integrating $\pm 3\sigma$ from the mean peak values of 0 (near-side) and π (away-side)

$p_T^{\text{assoc.}}$ (GeV/c)	near-side (radians)	away-side (radians)
$1 < p_T^{\text{assoc.}} < 2$	0.33	0.5
$2 < p_T^{\text{assoc.}} < 3$	0.25	0.5
$3 < p_T^{\text{assoc.}} < 4$	0.2	0.5
$4 < p_T^{\text{assoc.}} < 5$	0.175	0.5
$5 < p_T^{\text{assoc.}} < 7$	0.15	0.5

To ensure that the measurements from pp are directly comparable to Pb—Pb, the yields shown for pp are not taken from the relevant analysis paper, but are instead calculated again for this analysis. Therefore, all statements and physics conclusions regarding the similarities or differences between collision systems pertains to observations are made on equal integration ranges. What this analysis is not accounting for are the difference in the peak widths for the collision systems, due to the following reasons:

- By constraining the $\Delta\varphi$ integration range parameter, we can make physics observations about the correlation peaks that are not inherently dependent on another measured observable (peak width)
- As discussed in the analysis procedure section (3.8.2.3), the away-side peak was not fit with a characteristic function for the final results. Therefore, we could not extract a definite peak width to compare to pp or p—Pb

5.5.1 Per-trigger Yield Comparison to pp

The near- and away-side per-trigger associated peak yields in Pb—Pb in both centrality classes are compared to pp in Fig 5.9. Statistical errors are shown with a solid line, systematic errors are shown with a shaded box, and the uncertainty due to the baseline uncertainty estimation is shown as an open box. For ease of observation, the 30–50% values are shifted $-0.2 \text{ GeV}/c$.

Observing first the near-side yields in Fig. 5.9, the values decrease with increasing p_T^{assoc} . The yields in Pb—Pb appear to be consistent with pp within 1 standard deviation. The pp yield in the $4 - 5 \text{ GeV}/c$ interval appears slightly higher than Pb—Pb, although still within uncertainty. This is similar to what is seen in Fig.5.2 where the pp yield is just slightly higher than p—Pb in this interval. Additionally, in Fig. 5.3 which shows the ratio of the measured pp yield to PYTHIA, the value of the ratio is slightly < 1 , suggesting that the pp yield in this interval is a fluctuation.

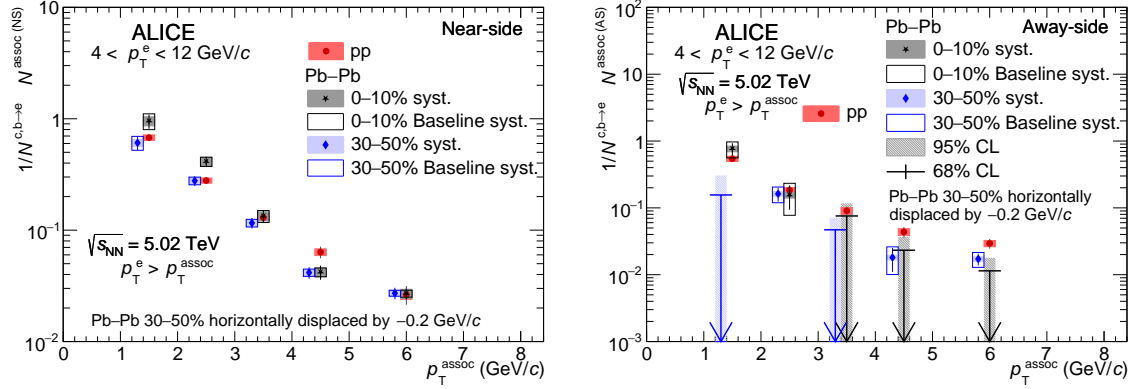


Figure 5.9: Per-trigger associated yields of the near- (left) and away-side (right) peaks for $4 < p_T^e < 12$ GeV/c as a function of p_T^{assoc} in 0–10% and 30–50% central Pb–Pb collisions compared to those obtained from pp collisions publicly available by ALICE [180]. The statistical (systematic) uncertainties are shown as vertical lines (empty boxes). In some p_T^{assoc} intervals, the away-side yield is consistent with zero within one standard deviation of statistical and systematic uncertainties added in quadrature. For those intervals, upper limits on the yields for 68% (95%) confidence levels are evaluated, and are shown with arrows (boxes).

The away-side yield values that are consistent with 0 within one standard deviation (where statistical, systematic, and baseline systematic uncertainties are combined in quadrature) are shown as upper-limit confidence intervals. This is to account for small yield values relative to their measured uncertainty. The 68% and the 95% confidence limits illustrate the intervals for $(0, \mu + 1\sigma]$ (arrow) and $(0, \mu + 2\sigma]$ (solid box) respectively. Where μ is the measured value of the yield and σ is the total-combined uncertainty. The Feldman-Cousins method [185] was also performed as an additional check on the confidence limits, and was found to be consistent in value. Accounting for the confidence limits on the Pb–Pb yields, the pp yields are still within 1 to 2 standard deviations from the 95% upper limits, and all appear to decrease at increasing p_T^{assoc} .

5.6 Per-Trigger Nuclear Modification Factor (I_{AA})

Using the per-trigger associated yields in Fig. 5.9, the per-trigger nuclear modification factor (I_{AA}) can be used to perform a more direct observation on the effect of the QGP medium on the jets. This is defined as the ratio of the Pb–Pb associated yield

to the pp yield. Similar to the R_{AA} , a measurement of > 1 (< 1) of the I_{AA} indicates an enhancement (suppression) of the yield. The I_{AA} is sensitive to a change in the initiating parton fragmentation function, the change of the quark/gluon jet ratio in the final state, and any bias on the parton p_T spectrum after energy loss from the trigger particle selection [72]. Changes in the fragmentation function of the jet, or a wake front in the medium [50], the jet depositing energy in the medium [51], or k_T -broadening would manifest as an enhancement on the near-side. A suppression observed in the near- or away-side is likely due to jet-parton energy loss [35], [125], [186] or from the depletion due to a diffusion wake [187].

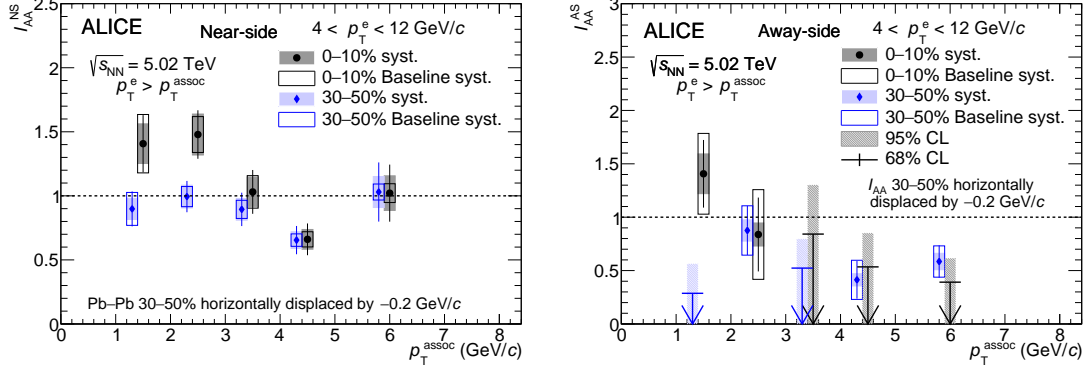


Figure 5.10: Per-trigger nuclear modification factor (I_{AA}) of near- (left) and away-side (right) associated yields, for $4 < p_T^e < 12$ GeV/c as a function of p_T^{assoc} in 0–10% and 30–50% central Pb–Pb collisions publicly available by ALICE [180]. The statistical (systematic) uncertainties are shown as vertical lines (empty boxes). In some p_T^{assoc} intervals the away-side yield is consistent with zero within one standard deviation of total uncertainty. For those intervals, upper limits on the I_{AA} for 68% (95%) confidence levels are shown with arrows (boxes).

Figure 5.10 shows the near- and away-side I_{AA} , respectively, with both centrality classes. For the 0–10% centrality, the near-side I_{AA} shows a slight enhancement at low p_T^{assoc} , with a significance of about 1.27σ , before approaching unity at higher p_T^{assoc} . The 30–50% centrality I_{AA} distribution overlaps with unity well within uncertainty. For both centrality classes, the 4–5 GeV/c interval does show a possible suppression, but given what was previously seen with pp yield in this interval compared to p–Pb, this is possibly due to an upwards fluctuation in pp. Because both centralities are divided by this same value in pp, the same behavior occurs for both in this interval.

The away-side I_{AA} measurements in Fig. 5.10 do not tell a straight-forward story. There is possibly an away-side enhancement at low $p_T^{\text{assoc.}}$ for the 0–10% centrality class, but due to the uncertainty that can't be stated for certain. However, the second interval's consistency with unity followed by the remaining intervals overlapping with zero point to a gradual suppression at higher associated p_T , but again, due to the uncertainties this is inconclusive. The 30–50% away-side I_{AA} measurement appears to fluctuate up to unity (in the 2 – 3 GeV/ c interval) and down such that some points are consistent with 0. Taken as a whole, the 30–50% away-side I_{AA} points to an overall suppression. A possible explanation could be that the QGP medium in semicentral events is significant enough to induce jet-quenching throughout the entire p_T spectra, or that the higher- p_T associated particles lost energy (similarly to the central events) and that these now lower- p_T jet constituents thermalized with the medium.

5.6.1 I_{AA} measured in 2σ intervals

To maintain consistency with the measurement in the pp and p–Pb collision systems, the per-trigger yield was obtained by integrating within 3σ in the Pb–Pb collision system. However, the Pb–Pb correlation distributions have significant fluctuations compared to the other two collision systems, particularly in the transverse region. These fluctuations contribute to the statistical and baseline uncertainties, and these uncertainties may be reduced by integrating in a smaller region. For this reason, the per-trigger yields and I_{AA} were obtained by integrating within 2σ of the peak means.

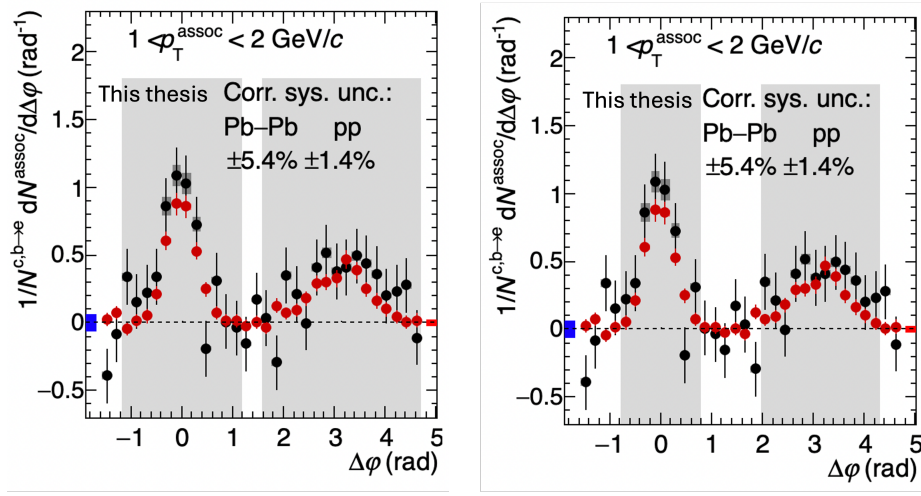


Figure 5.11: (Left) 3σ integration region of the $\Delta\phi$ correlation. (Right) 2σ integration region of the $\Delta\phi$ correlation.

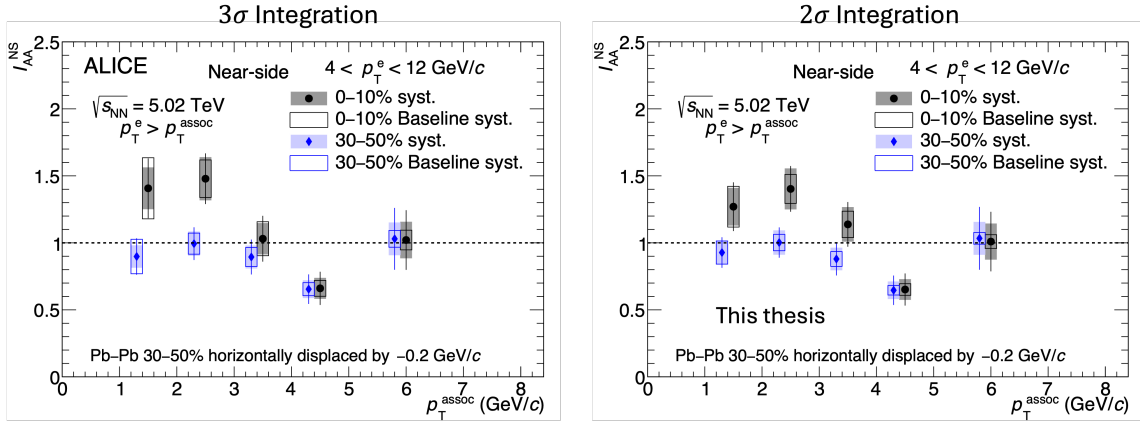


Figure 5.12: Per-trigger nuclear modification factor (I_{AA}) of the near-side peak for $4 < p_T^e < 12$ GeV/c as a function of p_T^{assoc} . (Left) the near-side I_{AA} obtained from integrating within 3σ , publicly available by ALICE [180]. (Right) is the near-side I_{AA} obtained from integrating in 2σ measured for this thesis.

A comparison of the 3σ and 2σ integration regions are shown in Fig. 5.11. The near-side I_{AA} in the two different integration ranges are shown in Fig. 5.12. As expected, the uncertainties of the values are reduced in the 2σ -integrated yields. This is more dramatic in the baseline systematic uncertainty, but overall the updated measurement is consistent with the original. The significance of the near-side I_{AA} in

the $< 3 \text{ GeV}/c$ $p_T^{\text{assoc.}}$ for the 2σ is 1.20σ , which is consistent with the original I_{AA} value of 1.27σ .

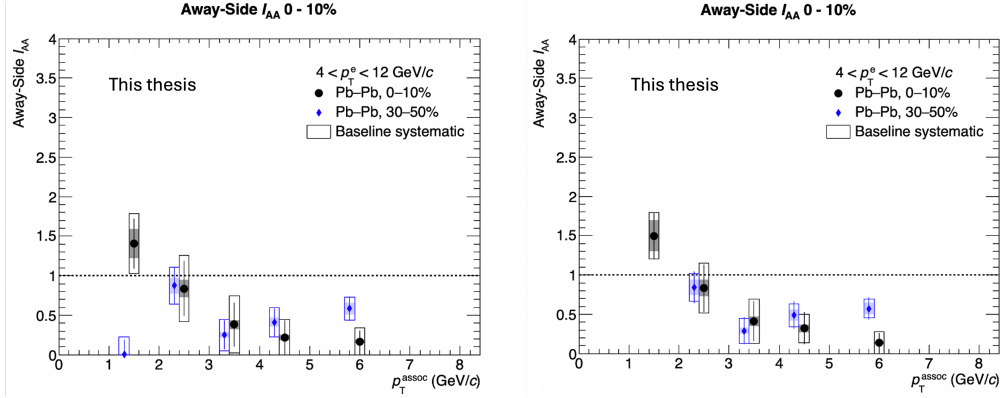


Figure 5.13: Per-trigger nuclear modification factor (I_{AA}) of the away-side peak for $4 < p_T^e < 12 \text{ GeV}/c$ as a function of $p_T^{\text{assoc.}}$. The left is the near-side I_{AA} obtained from integrating within 3σ . The right is the near-side I_{AA} obtained from integrating in 2σ . The confidence intervals are not plotted in the left plot for ease of comparison.

The away-side I_{AA} is pictured in Fig. 5.13 without the confidence intervals shown in Fig. 5.10. Similarly to the near-side I_{AA} , the 2σ I_{AA} has a reduced uncertainty compared to the original measurement and the values are consistent with the original values, although the fluctuations in the away-side in the semicentral centrality has cause the Pb-Pb yield to be negatively-valued in the lowest $p_T^{\text{assoc.}}$ interval.

This 2σ cross-check was performed on the $4 < p_T^{\text{trig.e}} < 7 \text{ GeV}/c$ and $7 < p_T^{\text{trig.e}} < 16 \text{ GeV}/c$ correlation measurements. The observables in these p_T^e ranges were similarly consistent to the original 3σ measurements, albeit with slightly smaller uncertainties, but did not change the overall physics message. However, the 2σ measurement will be considered in comparison to light-flavor measurements in a later section.

5.7 Correlation $p_T^{\text{trig.e}}$ -dependence

Previous measurements of electrons from heavy-flavor decays indicate a mass-dependence of the originating heavy quark on the electron p_T spectra. The fraction of electrons originating from beauty decays, either through the $b \rightarrow e$ or non-prompt D channel ($b \rightarrow c \rightarrow e$) are the predominant heavy quark parent species ($> 50\%$) of the decay electron at high p_T^e ($> 5 \text{ GeV}/c$) [155]. Therefore, selecting different p_T ranges of the

trigger electron provides insight to the fragmentation profile of different heavy flavor species. Additionally, selecting trigger particles in different kinematic intervals samples jets of differing p_T , and therefore parent partons of differing energy. Therefore, one can investigate how the p_T of the jet influences any experimental signatures of jet-medium interactions.

The analysis procedure was repeated for trigger electrons in the “split” kinematic intervals of $4 < p_T^{\text{trig.e}} < 7 \text{ GeV}/c$ and $7 < p_T^{\text{trig.e}} < 16 \text{ GeV}/c$, with the intention of studying the correlation distributions of HF decay electrons originating predominantly from charm and beauty, respectively. However, given that the electrons in this analysis are not explicitly separated by parent quark species, the correlations are a reflection of only the relative fraction HF quark. The fraction of beauty decays in at $p_T = 4 \text{ GeV}/c$ accounts for approximately 40% of the decay electron spectra, so it can account for almost half of the electrons measured in the lower $p_T^{\text{trig.e}}$ interval. At the higher p_T spectra, beauty decays account for approximately 70% of the decay electrons at $p_T^e = 7 \text{ GeV}/c$. Keep in mind that due to the $p_T^{\text{trig}} > p_T^{\text{assoc}}$ requirement, there is a kinematic bias on the distribution where the trigger and associated p_T intervals overlap. The observables in the semicentral centrality was measured for these p_T^e ranges, however these measurements had relatively large uncertainties. Therefore, the measurements in the split p_T^e ranges in the most-central collisions will be discussed.

5.7.1 Split $p_T^{\text{trig.e}}$ Correlation Distributions

Figures 5.14 and 5.15 show the correlation distribution for $4 < p_T^{\text{trig.e}} < 7 \text{ GeV}/c$ and $7 < p_T^{\text{trig.e}} < 16 \text{ GeV}/c$ in Pb–Pb collisions compared to pp. The $4 < p_T^e < 7 \text{ GeV}/c$ correlation distribution follows similar trends to what was observed in the $4 < p_T^e < 12 \text{ GeV}/c$ distribution.

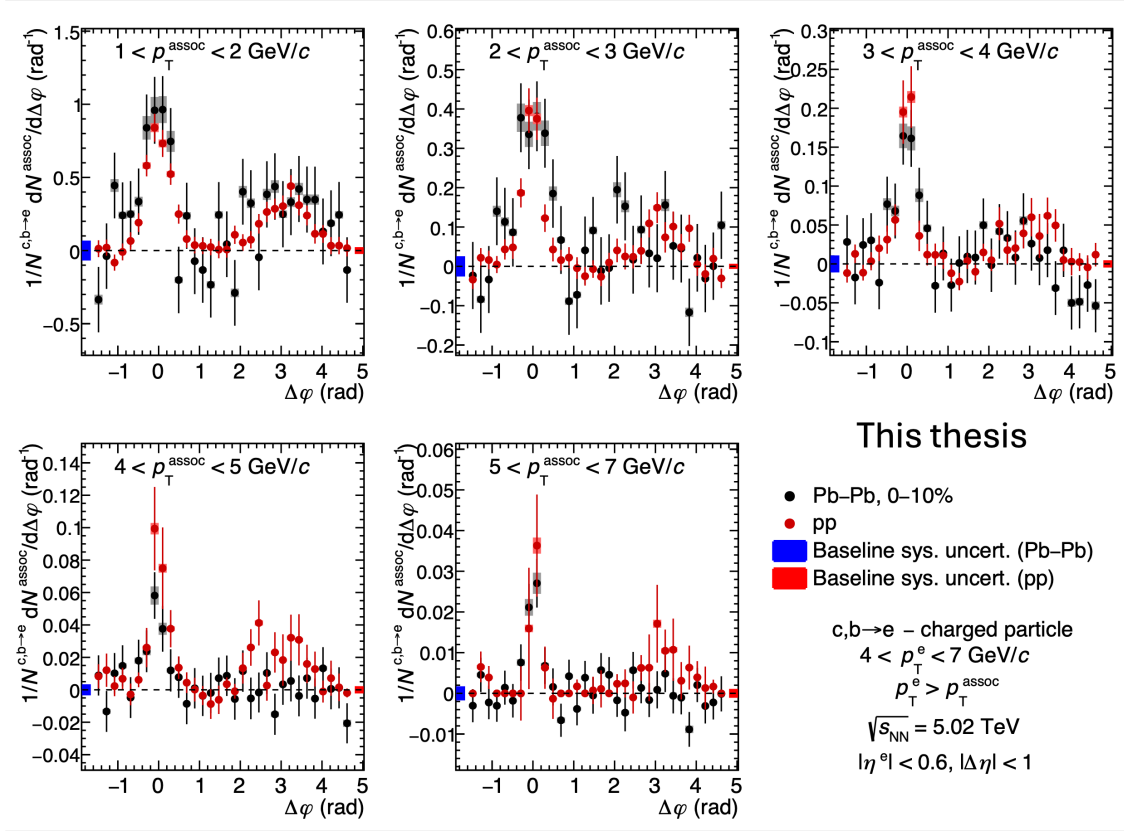


Figure 5.14: Azimuthal-correlation distribution of heavy-flavor hadron decay electrons and charged particles measured in 0–10% central Pb–Pb collisions. The distributions are shown in the trigger range of $4 < p_T^e < 7 \text{ GeV}/c$ and all p_T^{assoc} intervals.

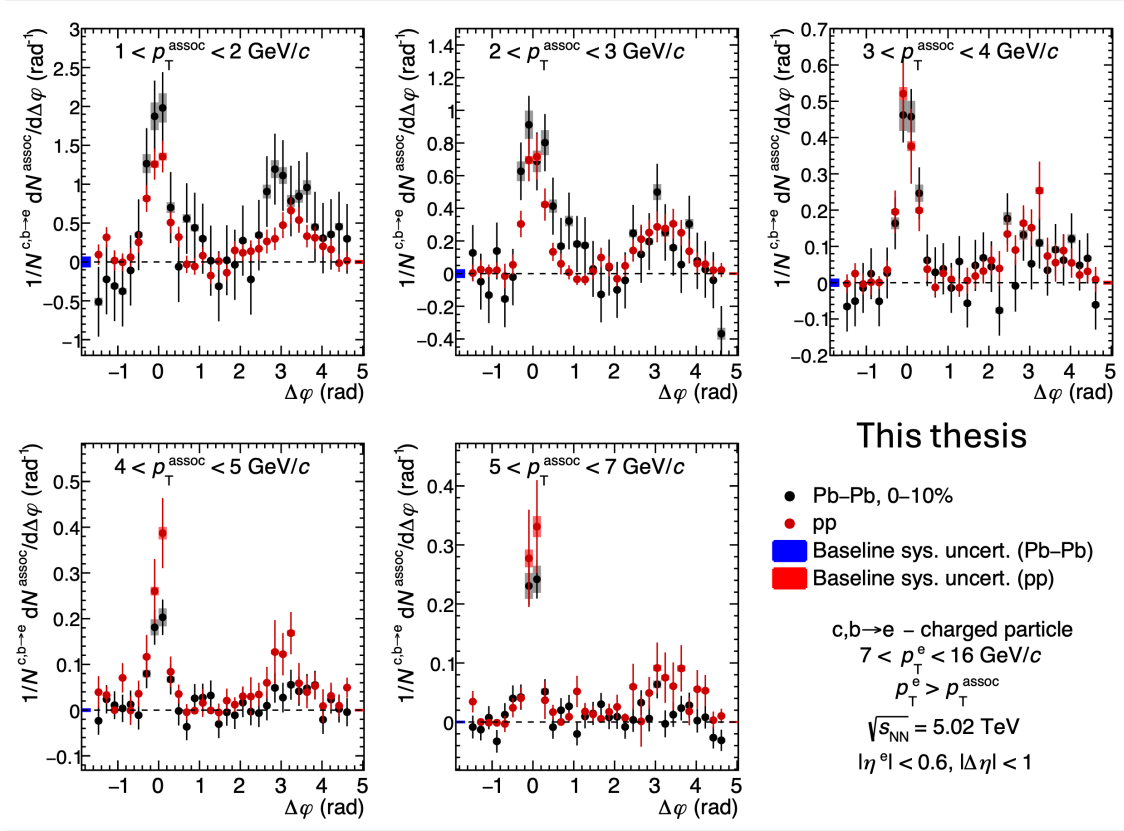


Figure 5.15: Azimuthal-correlation distribution of heavy-flavor hadron decay electrons and charged particles measured in 0–10% central Pb–Pb collisions. The distributions are shown in the trigger range of $7 < p_T^e < 16$ GeV/ c and all p_T^{assoc} intervals.

In both Figs. 5.14 and 5.15, the distributions exhibit behavior similar to the $4 < p_T^e < 12$ GeV/ c measurement, where the near-side peak becomes more collimated at increasing p_T^{assoc} , and the peaks appear consistent with pp within uncertainty. In Fig. 5.15, the near-side peaks in both collision systems appear slightly narrower than their counterparts in the $4 < p_T^e < 7$ GeV/ c at low p_T^{assoc} , although any differences at higher p_T^{assoc} are less clear. For the away-side peak, the Pb–Pb peak appears slightly higher than the pp peak in the lowest p_T^{assoc} , albeit with somewhat larger uncertainties in Pb–Pb. Although trigger electrons in this higher p_T^e interval samples higher-energy jets than the lower interval, the disappearance of the away-side peak remains similar to the $4 < p_T^e < 7$ GeV/ c interval, with even smaller statistical uncertainties.

5.7.2 Split $p_T^{\text{trig.e}}$ Per-trigger associated widths

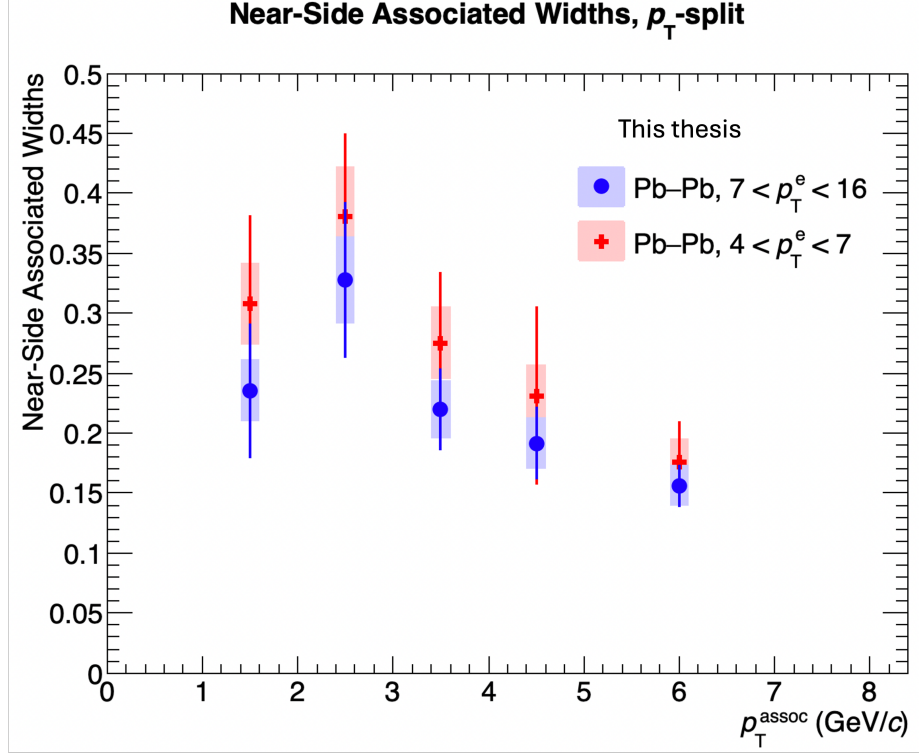


Figure 5.16: Per-trigger associated near-side peak width in $4 < p_T^e < 7$ GeV/c (red) and $7 < p_T^e < 16$ GeV/c (blue) measured for this thesis.

Figure 5.16 shows the associated widths for the split p_T^e measurements. What is immediately evident is that the per-trigger widths for both $p_T^{\text{trig.e}}$ intervals are consistent within uncertainty for all $p_T^{\text{assoc.}}$ intervals. Not pictured is the pp comparison, but the Pb-Pb measurements were consistent with those widths as was in the case for the $4 < p_T^e < 12$ GeV/c interval. Although the values between the split p_T^e regions are consistent within uncertainty, the central value of the $4 < p_T^e < 7$ GeV/c measurement is higher in all $p_T^{\text{assoc.}}$ intervals. When comparing the same measurement in pp in Fig. 5.17, the near-side widths between the split $p_T^{\text{trig.e}}$ regions are similar in value.

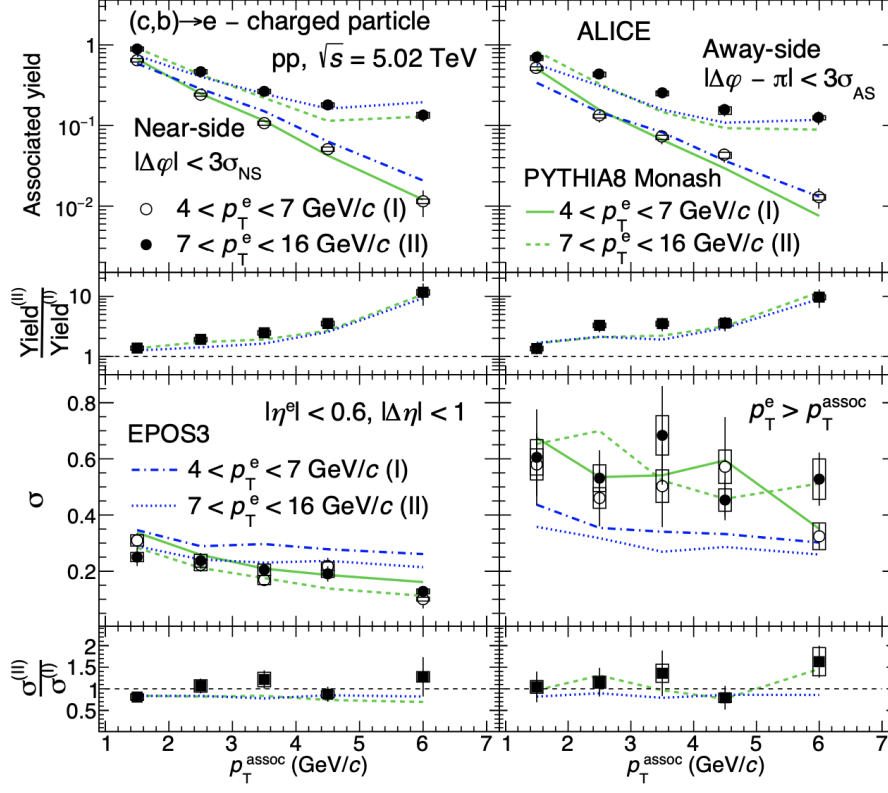


Figure 5.17: Per-trigger associated yields and widths in pp collisions for $4 < p_T^e < 7$ GeV/c and $7 < p_T^e < 16$ GeV/c measured by ALICE compared to PYTHIA8 Monash and EPOS3 predictions [135].

To investigate the effect of the electron's parent hadron flavor or $p_T^{\text{trig.e}}$ on the peak widths, a study was performed in the pp correlation paper using PYTHIA with the Monash tuning, shown in Fig. 5.18. The largest near-side peak width is from the $4 < p_T^e < 7$ GeV/c correlations where the electron originates from beauty (solid squares). The next-largest near-side width belongs to the $7 < p_T^e < 16$ GeV/c from beauty (open squares). The electrons from charm have smaller widths but follow a similar ordering. This indicates that the size of the width due to the flavor of the parent hadron competes with the width determined by the $p_T^{\text{trig.e}}$. This competing effect results in the split- p_T^e widths being so similar in pp, and would be present in the Pb-Pb measurement as well.

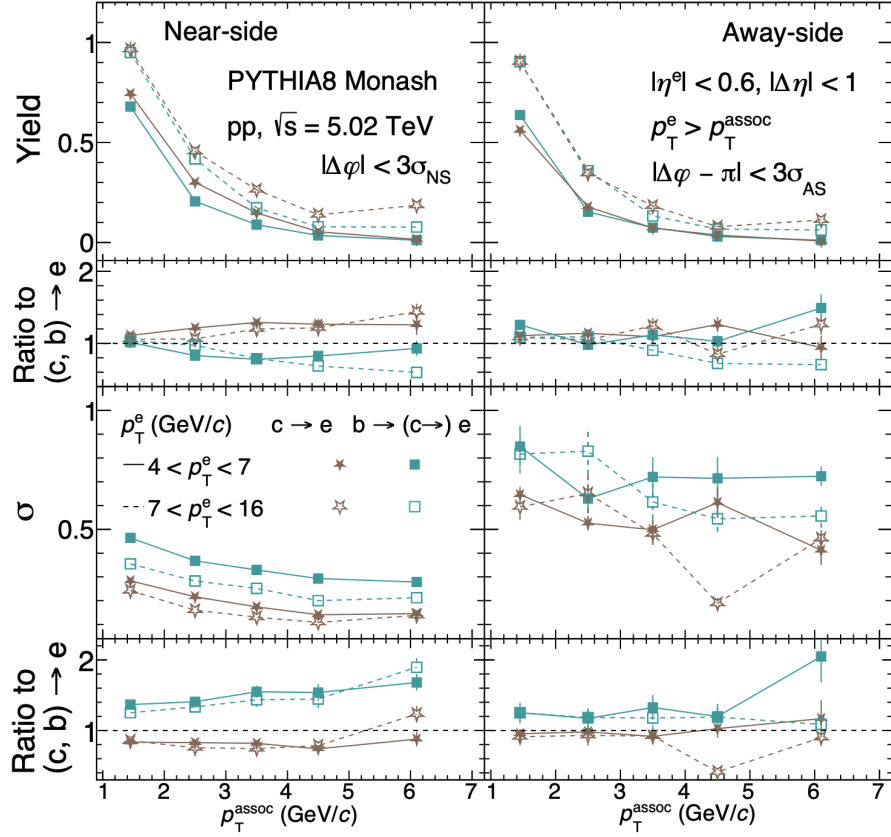


Figure 5.18: Per-trigger associated yields and widths in pp collisions for $4 < p_T^e < 7$ GeV/c and $7 < p_T^e < 16$ GeV/c generated with PYTHIA8 Monash [135]. Associated peak widths are dependent on both the flavor of the electron's parent hadron and the trigger p_T .

5.7.3 Split $p_T^{\text{trig.e}}$ Per-trigger associated yields

The correlation distributions are integrated following the same procedure in 5.5 for both trigger ranges. The per-trigger associated yields for the near- and away-side peaks are shown in Fig. 5.19 compared to the corresponding correlations in pp collisions.

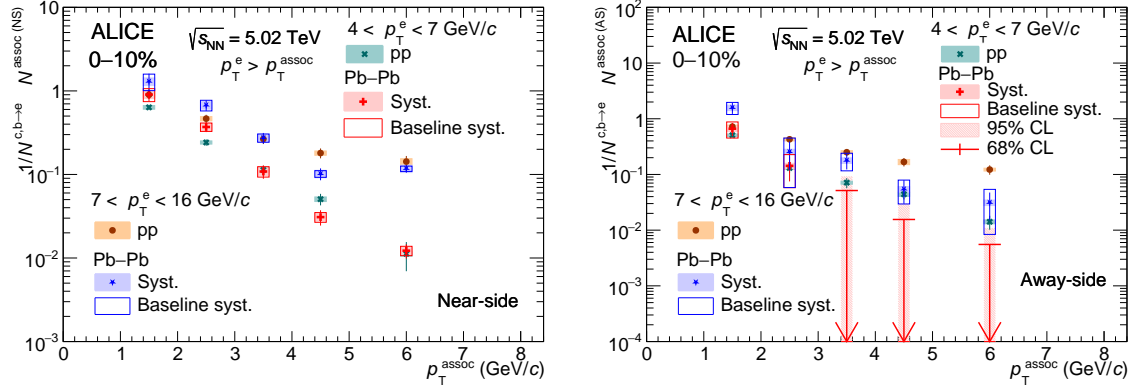


Figure 5.19: Per-trigger near- (left) and away-side (right) associated peak yields for $4 < p_T^{\text{trig},e} < 7 \text{ GeV}/c$ and $7 < p_T^{\text{trig},e} < 16 \text{ GeV}/c$ as a function of $p_T^{\text{assoc.}}$ in 0–10% central Pb–Pb collisions, compared to measurements in pp collisions publicly available by ALICE [180]. The statistical (systematic) uncertainties are shown as vertical lines (boxes). In some $p_T^{\text{assoc.}}$ intervals the away-side yield is consistent with zero within one standard deviation of total uncertainties. For those intervals, upper limits on the yields for 68% (95%) confidence levels are shown with arrows (boxes).

The associated yields measured in Pb–Pb in the two $p_T^{\text{trig},e}$ ranges (shown only for the 0–10% centrality class) follow the same relative trend as seen in pp. The $7 < p_T^{\text{trig},e} < 16 \text{ GeV}/c$ near-side yields in Pb–Pb decreases with increasing $p_T^{\text{assoc.}}$, however the yield in the $5 - 7 p_T^{\text{assoc.}}$ interval is similar in value to the previous interval (which is also observed in pp). For both collision systems, the $4 < p_T^{\text{trig},e} < 7 \text{ GeV}/c$ yields follow the same continuously decreasing distribution. The near-side widths for the Pb–Pb measurements are overall consistent with pp. For the away-side yields, in the lowest $p_T^{\text{assoc.}}$ interval the $7 < p_T^{\text{trig},e} < 16 \text{ GeV}/c$ Pb–Pb appears higher than pp, and noticeably decreases in comparison with increasing $p_T^{\text{assoc.}}$. The $4 < p_T^{\text{trig},e} < 7 \text{ GeV}/c$ yields appear generally consistent with pp in the lowest two $p_T^{\text{assoc.}}$ intervals, although the values were low compared to the uncertainty in the higher intervals. However, the upper limit of these yield confidence intervals are still consistent with pp.

5.7.4 I_{AA} Comparison of different $p_T^{\text{trig},e}$

The I_{AA} measurements of the $4 < p_T^{\text{trig},e} < 7 \text{ GeV}/c$ and $7 < p_T^{\text{trig},e} < 16 \text{ GeV}/c$ measurements are shown in Fig. 5.20.

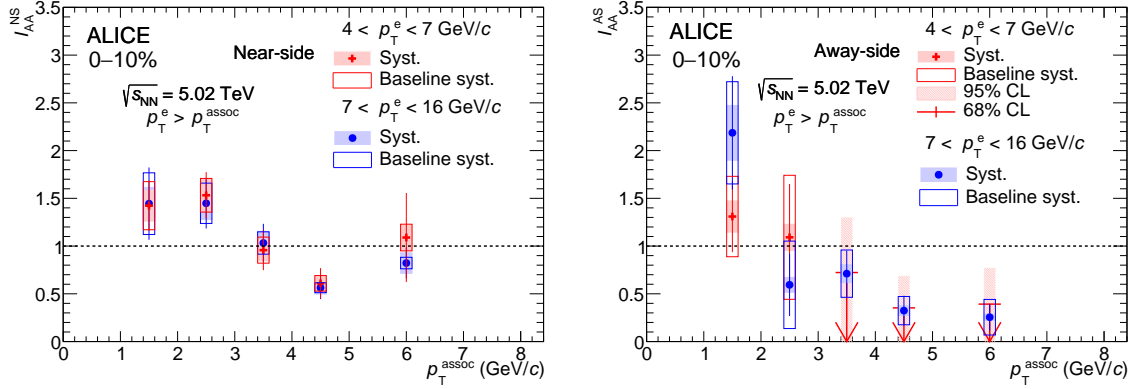


Figure 5.20: I_{AA} of the near- (left) and away-side (right) associated peak yields for $4 < p_T^{\text{trig.e}} < 7 \text{ GeV}/c$ and $7 < p_T^{\text{trig.e}} < 16 \text{ GeV}/c$ as a function of $p_T^{\text{assoc.}}$ in 0–10% central Pb–Pb collisions publicly available by ALICE [180]. The statistical (systematic) uncertainties are shown as vertical lines (boxes). In some $p_T^{\text{assoc.}}$ intervals the away-side yield is consistent with zero within one standard deviation of total uncertainty. For those intervals, upper limits on the I_{AA} for 68% (95%) confidence levels are shown with arrows (boxes).

What is immediately evident in the near-side I_{AA} measurement for the two $p_T^{\text{trig.e}}$ ranges is how the data points are essentially on top of each other. This seems to indicate that for the near-side peak, there does not appear to be a p_T -dependence of the I_{AA} . Given the larger proportion of charm-initiated jets in the lower $p_T^{\text{trig.e}}$ measurement, the number of associated particles appears to be flavor (specifically mass) independent. The I_{AA} appear similar to the $4 < p_T^{\text{trig.e}} < 12 \text{ GeV}/c$ near-side I_{AA} , where there is a slight enhancement at low $p_T^{\text{assoc.}}$ and is consistent with unity at higher $p_T^{\text{assoc.}}$. Comparing the away-side I_{AA} , although for the three highest $p_T^{\text{assoc.}}$ intervals the $4 < p_T^{\text{trig.e}} < 7 \text{ GeV}/c$ interval is expressed via an upper limit, the two measurements still follow similar trends. Due to the size of the uncertainty for the lower $p_T^{\text{trig.e}}$ interval, it is inconclusive to determine that there is an enhancement at low $p_T^{\text{assoc.}}$, but there does appear to be a suppression of the I_{AA} at high $p_T^{\text{assoc.}}$. The larger $p_T^{\text{trig.e}}$ measurement follows similarly, but with a more pronounced sign of enhancement at low $p_T^{\text{assoc.}}$. Since these trigger electrons would originate from heavy-flavor quark-initiated jets, jet quenching is occurring in these central collisions, and this evidence manifests similarly for the two $p_T^{\text{trig.e}}$ measurements in the high- $p_T^{\text{assoc.}}$ region. However, by sampling a low- p_T trigger, there are less low- p_T particles associated with this trigger on the away-side jet, resulting in less evidence of enhancement (vs the high-

p_T trigger). Or, the enhancement mechanism for the away-side is weaker for charm-initiated jets compared to beauty-initiated jets. Similarly to the $4 < p_T^{\text{trig.e}} < 12$ GeV/ c I_{AA} measurement, the I_{AA} for these $p_T^{\text{trig.e}}$ intervals were calculated by integrating within 2σ of the mean. The I_{AA} from this method was consistent with the values shown in Fig. 5.20 such that the $4 < p_T^{\text{trig.e}} < 7$ GeV/ c measurement offered no new information, but the uncertainty reduction in the $7 < p_T^{\text{trig.e}} < 16$ GeV/ c I_{AA} offers a better comparison to light-flavor measurements.

5.8 I_{AA} Comparison to Light-Flavor

I_{AA} measurements have been previously conducted in the light-flavor sector by the ALICE experiment [70]–[72]. The electron from heavy-flavor hadron decay I_{AA} measurement for the $7 < p_T^{\text{trig.e}} < 16$ GeV/ c interval (calculated by integrating the distribution in 2σ around the peak mean) is compared to K_s^0 and charged hadron triggered near- and away-side I_{AA} in Fig. 5.21.

The K_s^0 and charged hadron correlation measurements are obtained using a trigger range of $8 < p_T^{\text{trig.}}$ < 16 GeV/ c , measured in associated p_T intervals of 1 – 2, 2 – 3, 3 – 4, 4 – 6, and 6 – 8 GeV/ c [70]. A note to consider is that the decay electron correlation is compared to hadron correlations, and that due to the decay kinematics, the originating heavy-flavor hadron will have a higher p_T than the electron.

The near-side I_{AA} distribution of the electron is overall consistent to the I_{AA} of light-flavor. At low $p_T^{\text{assoc.}}$, the central value of the electron I_{AA} is ≈ 1.5 , and overlaps in uncertainty to the light-flavor I_{AA} , valued at ≈ 1.9 . Although the electron correlation is subject to larger uncertainty, it is within uncertainty of light flavor measurements at low $p_T^{\text{assoc.}}$, hinting towards an enhancement. There are multiple possible explanations for this. The fragmentation function of the heavy-quark is modified in the QGP, causing this deviation from unity. A softer fragmentation function in heavy-ion collisions results in hadrons carrying a smaller fraction of the initial parton momentum compared to pp, which could be the cause of an enhancement in the low- p_T region. Alternatively, hadrons with a p_T which fit the trigger criteria would originate from a relatively larger-momentum parton, resulting in more associated particles and an enhancement [72]. Although the measurement discussed in this thesis focuses on the the decay electron, this effect would carry over from the

heavy-flavor hadron parents.

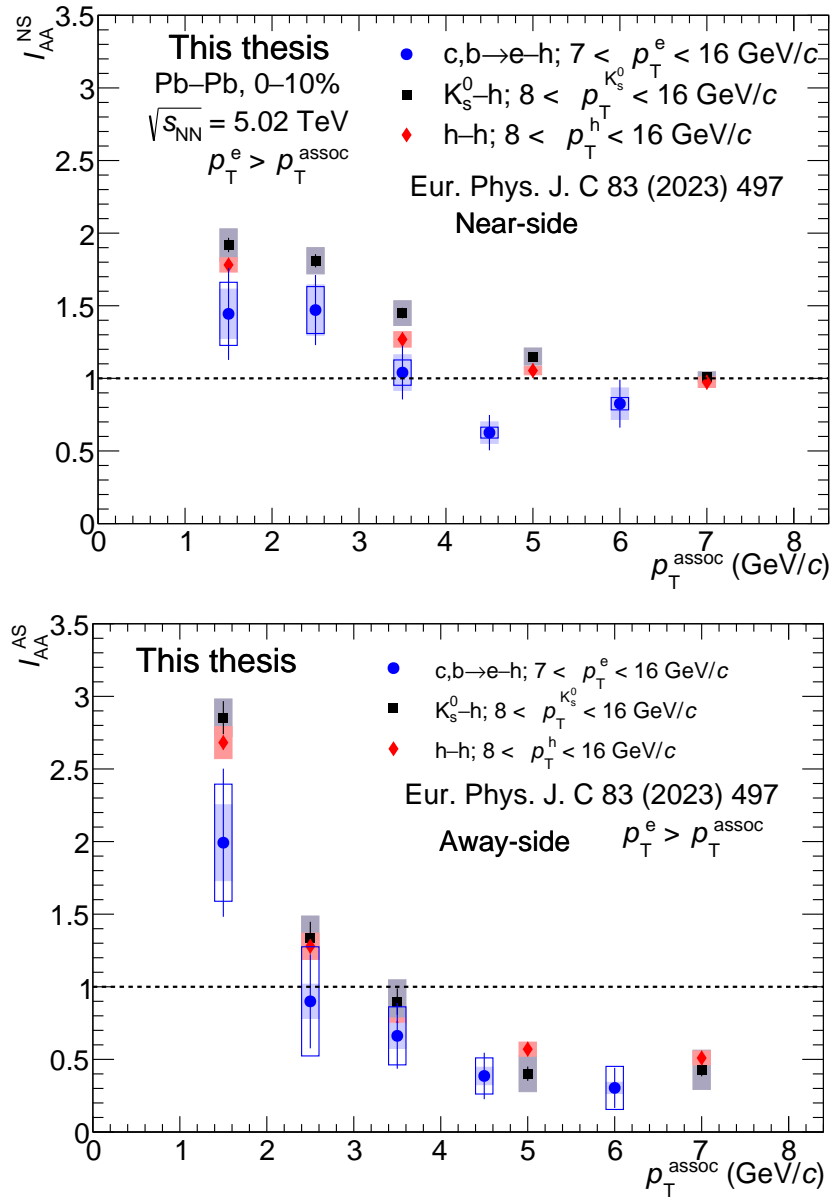


Figure 5.21: I_{AA} of near- (top) and away-side (bottom) associated peak yield from correlation distribution of electron from heavy-flavor hadron decays as the trigger particle ($7 < p_T^e < 16$ GeV/c) measured for this thesis compared with that of charged hadrons and K_s^0 as trigger particles ($8 < p_T^{trig} < 16$ GeV/c) measured by ALICE [70]. The electron I_{AA} is calculated using the 2σ method.

An alternative explanation for the near-side enhancement would be due to the

medium excitation from the deposition of jet energy. In this scenario, the medium experiences a larger energy density at the front of the mach-cone like structure formed by the parton in the medium and enhances particle production collinear with the hard parton jet in comparison to the vacuum [50], [51].

While approaching high $p_T^{\text{assoc.}}$, all three near-side I_{AA} measurements trend towards unity (considering that the pp yield fluctuation is affecting the $4 - 5 p_T^{\text{assoc.}}$ interval), indicating no alteration of the per-trigger yield in Pb–Pb compared to pp. This is likely due to the near-side jet being produced close to the surface of the medium. If the jet undergoes little to no interaction with the medium, the parton shower experiences little to no energy loss, resulting in a similar fragmentation with respect to the vacuum and likely would cause minimal medium excitation. Theoretical models predict that high- p_T hadrons are more likely to originate from narrow, hard-fragmenting jets which would encounter less interactions with the QGP [188], [189]. This prediction is supported by the presence of collimated near-side peaks in the correlation distribution at higher $p_T^{\text{assoc.}}$.

The heavy-flavor decay electron away-side I_{AA} shows an enhancement at low- $p_T^{\text{assoc.}}$ and becomes a suppression at higher $p_T^{\text{assoc.}}$, with all values consistent to the I_{AA} in the light-flavor measurements. The suppression in the I_{AA} measurement is expected, given that the away-side jet on average traverses through a longer path in the medium than the near-side jet. In low- $p_T^{\text{assoc.}}$, the electron I_{AA} central point is ≈ 2 , and is within uncertainty of the light-flavor measurements, which are $I_{AA} \approx 2.75$. Both the light-flavor and electron I_{AA} values are ≈ 0.4 in $p_T^{\text{assoc.}} > 4 \text{ GeV}/c$, where the heavy flavor has a significance of 2.9 below unity. The close consistency in these I_{AA} values suggest that there is no flavor-dependence of the I_{AA} . The term “flavor-dependence” is stated instead of solely “mass-dependence” because the heavy-flavor correlations will inevitably originate from heavy-quark initiated jets, whereas the light-flavor correlations can originate from both quark and gluon jets. Figure 5.22 is taken from the light-flavor correlation paper [70], which also includes the I_{AA} of $\Lambda/\bar{\Lambda}$ correlations measured in the same study, and additionally includes the I_{AA} measurements of π^0 [71] and di-hadron correlations [72]. The $\Lambda/\bar{\Lambda}$ I_{AA} is consistent with all other measurements within uncertainty. An important note is that baryons are predominantly produced from gluon jets [61]. Due to the larger color factor of gluon jets, they are expected to lose more energy than quark-initiated jets. One would then expect the $\Lambda/\bar{\Lambda}$ I_{AA} to potentially differ from the other measurements,

in particular the electron I_{AA} . However, the $\Lambda/\bar{\Lambda}$ I_{AA} measurement shows a similar magnitude of enhancement and suppression to the other measurements for both the near- and away-side peaks.

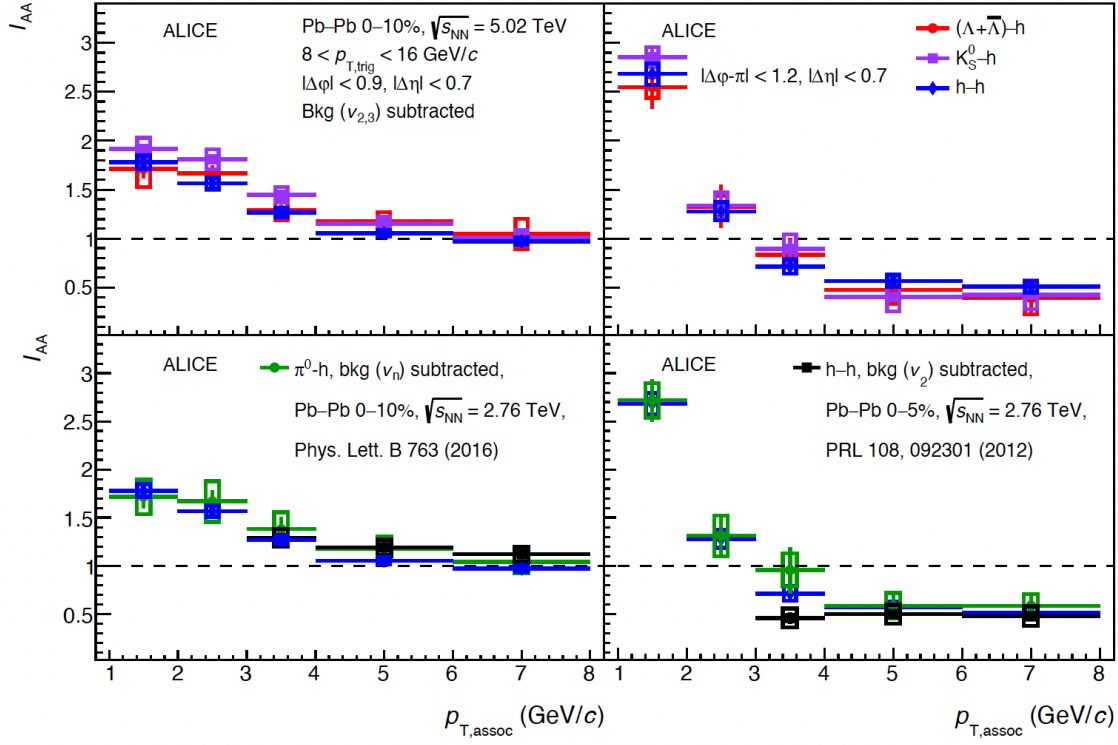


Figure 5.22: Figure showing all I_{AA} measurements by ALICE [70]–[72].

The measurements shown in Ref. [70] were compared to HIJING [84] and AMPT [98] models, seen in Fig. 5.23. HIJING is an event generator used for simulating heavy-ion collision environments which models jet interactions and particle production. AMPT is multi-phase transport model which includes initial partonic and final hadronic interactions and the phase transition between them. The initial conditions are taken from HIJING and it includes parton and hadron cascades with elastic scatterings for the final state interactions. For the near-side, HIJING predicts an $I_{AA} \approx 1$ for all p_T^{assoc} intervals, which is not shared with data. AMPT predicts an enhancement at low- p_T^{assoc} , but incorrectly predicts a suppression at high- p_T^{assoc} . The away-side is well-reproduced by AMPT, with the exception for the magnitude of enhancement in the low- p_T^{assoc} region. The HIJING prediction shows no change as a function of

$p_T^{\text{assoc.}}$, which conflicts with data. This indicates that medium effects are necessary to describe the data.

The away-side I_{AA} likely shows evidence of jet-quenching in the higher $p_T^{\text{assoc.}}$ intervals, although there is no clear explanation for why the suppression would have a similar magnitude for both light and heavy flavor. The enhancement at low $p_T^{\text{assoc.}}$ could indicate that the partons which have lost energy in the medium have hadronized into lower-momentum hadrons, and so are occupying the lowest $p_T^{\text{assoc.}}$ intervals. Overall, this deviation from the pp value indicates that the fragmentation function of the jets producing these triggers has been modified.

Another possible explanation for the away-side measurement would be due to a diffusion wake from the jet producing an enhancement in the low- $p_T^{\text{assoc.}}$ region and a depletion in the high- $p_T^{\text{assoc.}}$ region. However, a dijet event such as heavy-quark production would produce a wake in opposite directions, which would potentially negate the effect in the measurement. Additionally, because the distributions are so well-described by the AMPT model, this would support the theory that the partons which have lost energy in the medium have hadronized into more low- p_T particles relative to the vacuum.

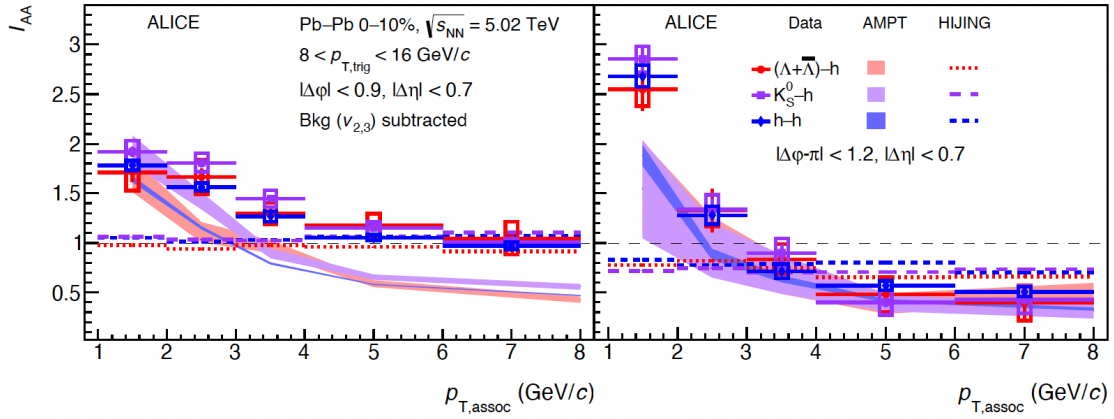


Figure 5.23: Light-flavor I_{AA} measurements compared to AMPT and HIJING models [70].

5.9 Comparison to Z-boson-triggered measurements

Because electroweak bosons do not interact strongly with the QGP, they can be used as trigger particles to closely study the mechanisms of jet-medium interactions on the away-side jet. These measurements do not suffer from the uncertainties of a harmonic flow background [190]. Additionally, because the electroweak bosons will have a large mean-free path in the medium, these measurements aren't influenced by the surface bias of the trigger seen in hadron-triggered correlations. In these correlation measurements, evidence of the mach cone or diffusion wake in the QGP would be unobscured and are ideal to compare to models which incorporate medium excitation.

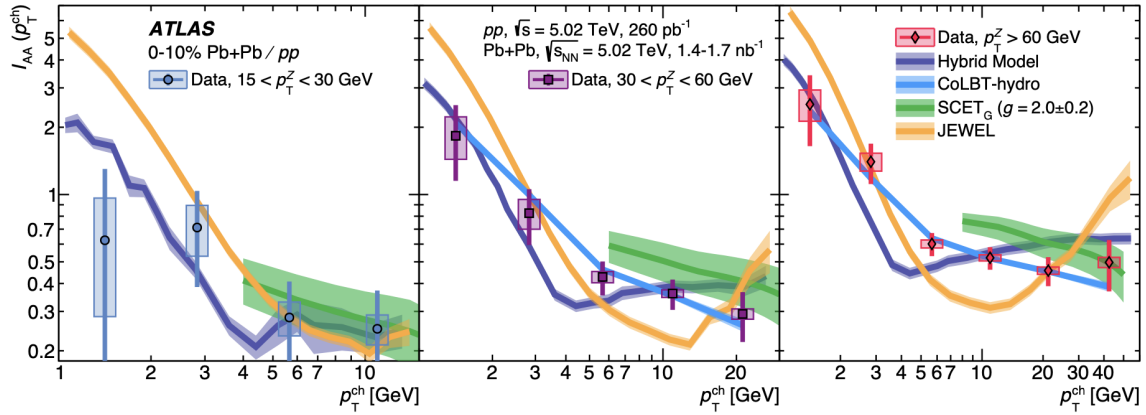


Figure 5.24: Z-boson-triggered away-side I_{AA} in 0–10% Pb–Pb collisions in three different p_T^Z intervals measured by ATLAS [191].

Z-triggered correlations have been studied by both the ATLAS [191] and CMS [192] experiments, and γ -triggered measurements have been performed by the STAR [193] and PHENIX [194] experiments at RHIC. Figure 5.24 shows the away-side I_{AA} of Z bosons triggered with associated charged particles measured by ATLAS [191]. The ATLAS measurement is conducted in three p_T^Z intervals in the 0–10% centrality interval and is compared to the Hybrid, CoLBT-hydro, SCET, and JEWEL models. The Hybrid models considers “wake” effects from jet propagation through the QGP. In CoLBT-hydro, the jet energy lost to the medium is fed as a source term into the medium evolution. JEWEL models the medium interaction with the jet as parton

“recoils”, and these recoils do not undergo any further interactions and hadronize. The SCET model does not consider medium response to the jet propagation. All I_{AA} distributions exhibit the same pattern of increasing suppression at high- $p_T^{\text{assoc.}}$. The $60 < p_T^Z \text{ GeV}/c$ interval appears to show an enhancement at very low $p_T^{\text{assoc.}}$. This follows the same pattern as the heavy-flavor I_{AA} and is consistent with previous measurements of the γ -triggered I_{AA} [193], [194]. The I_{AA} distribution is relatively well-described by models which include medium excitation, such as the Hybrid, JEWEL, and CoLBT.

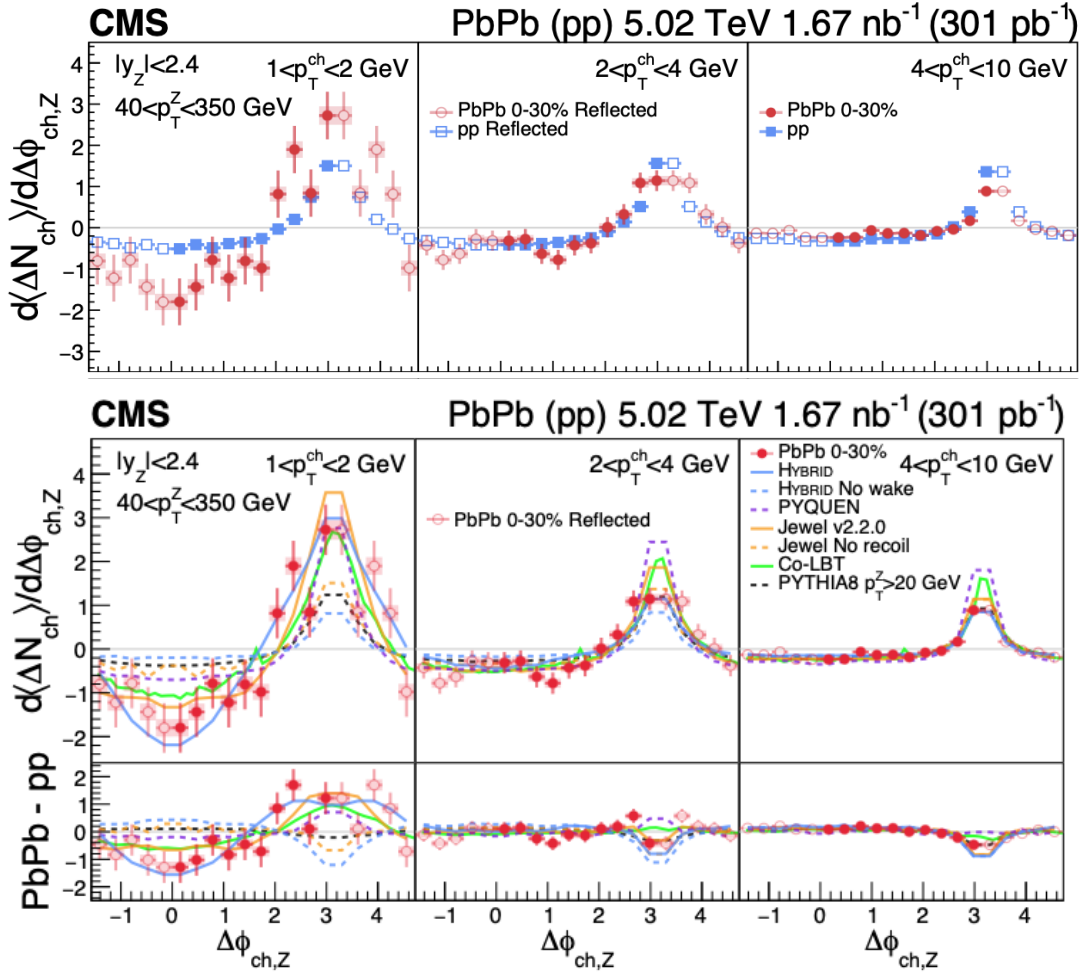


Figure 5.25: Z-boson-triggered correlation distribution in Pb–Pb collisions measured by CMS [192]. (Top) The correlation measurement in pp is compared to Pb–Pb. (Bottom) The correlation measurement is compared to theoretical models.

Another correlation measurement of note is the Z-boson-triggered azimuthal correlation performed by the CMS experiment [192], shown in Fig. 5.25. In this measurement, high- p_T trigger Z bosons ($40 < p_T^Z < 350$ GeV/ c) are correlated with hadrons in low $p_T^{\text{assoc.}}$ intervals. Medium excitation from the jet would manifest as an enhancement compared to pp on the away-side peak in low $p_T^{\text{assoc.}}$. This is observed in the correlation, as well as a noticeable suppression of the near-side peak. Like the ATLAS measurement, the CMS measurement suggests medium-excitation. The away-side peak enhancement potentially originates from a mach cone or wave front in the QGP formed by the away-side jet. The suppression seen on the near-side peak would in turn be produced by the diffusion wake behind the wave front, which would suppress the number of particles on the side of the Z boson. Similarly to the ATLAS measurement, the CMS measurement is qualitatively well-described by models which incorporate medium excitation.

The results of the ATLAS and CMS measurements do not necessarily invalidate the likelihood of jet partons which have lost energy to the QGP producing lower- p_T hadrons solely by means of the modified fragmentation. By triggering the correlation with such a high p_T^Z , these measurements are selecting highly-energetic jets. If the medium is modified by the jet such that these structures are formed, evidence of this phenomena may be only observable with these highly-energetic probes, which is somewhat supported by the lowest- $p_T^{\text{trig.}}$ of the ATLAS I_{AA} which shows no enhancement at low- $p_T^{\text{assoc.}}$, albeit with large uncertainties. If there is medium excitation present in the events selected in the heavy-flavor correlation measurement, experimental evidence of this effect is likely overshadowed by the fragmentation modification of the jet itself.

Chapter Six: Conclusion and Outlook

6.1 Analysis summary and conclusion

This thesis details the two-particle azimuthal correlation measurement of electrons from heavy-flavor hadron decays with charged particles in Pb—Pb collisions using the ALICE detector at the LHC. This measurement investigates the possible modification of the charm and beauty quark-initiated jet fragmentation or excitation of the medium due to the jet interactions with the quark-gluon plasma. Electrons from the semi-leptonic decay channel of heavy-flavor hadrons are used because of the relatively high decay branching ratio and the straightforward reconstruction of the electron signal by the ALICE detector. The correlation distribution provides a differential view of the jet phase space by correlating the trigger electron with associated particles in different p_T slices. The distribution is characterized by two peaks: The near- and away-side. Where the near-side peak is a measure of the angular distribution of particles correlated with the trigger in the same jet, and the away-side peak is the correlation of the trigger to recoil jet particles. Three trigger electron transverse momentum intervals were studied to measure how the jet p_T and the relative abundance of charm vs beauty jets affect the jet-medium interactions. Additionally, this measurement was performed in two centrality classes for the purpose of determining how the size and temperature of the QGP medium affects the measurement. Multiple observables can be obtained from the distribution. If present, the distribution peaks can be characterized by distribution functions to extract the peak width. The associated particle yield can be obtained by integrating the distribution peaks.

The results of this analysis was compared to a previously published measurement of the same analysis performed in pp and p—Pb collisions with the ALICE detector in the same center of mass energy ($\sqrt{s} = 5.02$ TeV) [135]. The measurement in pp and p—Pb collisions presents a baseline comparison for the Pb—Pb analysis, given that the pp measurement represents the jet fragmentation in vacuum. Deviations in the p—Pb measurement compared to pp would be indicative of cold-nuclear matter effects, which must be considered when interpreting the Pb—Pb measurement. The yield and width observables in pp and p—Pb exhibit a similar value between the

two collision systems for all $p_T^{\text{trig.}}$ and $p_T^{\text{assoc.}}$ intervals measured. The similarity of the observable values between pp and p—Pb indicates that cold-nuclear matter effects are not observable in the p_T ranges used in this analysis.

For both the central and semicentral Pb—Pb centrality classes, some features of the correlation distributions differed in comparison to pp collisions. This indicates the presence of medium-induced modification of the jet. The Pb—Pb near-side widths were close in value to pp within uncertainty, suggesting that the angular distribution of associated particles in the near-side did not significantly differ between the two collision systems. However, this measurement is dominated by events where one of the heavy-quarks from the initial hard scattering is produced close to the surface of the QGP. If the heavy quark experiences little interaction with the QGP, the shape of the near-side peak may not be significantly modified. The observables of high- $p_T^{\text{trig.}}$ (7 – 16 GeV/c) and low- $p_T^{\text{trig.}}$ (4 – 7 GeV/c) intervals were compared in the most-central Pb—Pb collisions, which analyzes trigger particles originating from high- to low- p_T jets. At these p_T intervals, the higher $p_T^{\text{trig.}}$ range should originate from $\sim 65\%$ beauty, where the lower $p_T^{\text{trig.}}$ should originate from $\sim 40\%$ beauty. The measured width values of these $p_T^{\text{trig.}}$ intervals were consistent within uncertainty, although the central value of the 4 – 7 GeV/c was consistently greater in all $p_T^{\text{assoc.}}$ intervals.

The correlation peak yields in Pb—Pb were compared directly to the peak yields obtained in pp by means of their ratio, or per-trigger nuclear modification factor (I_{AA}). The I_{AA} is sensitive to changes in the heavy-quark fragmentation function, and so provides a quantitative measure of the QGP's effect of the jet fragmentation. The near-side I_{AA} of the most-central Pb—Pb collisions (in 4 – 12 GeV/c) appeared to show an enhancement of 1.27σ in the lowest $p_T^{\text{assoc.}}$ interval, indicating some modification due to the medium in this range. Whereas the away-side I_{AA} shows a slight enhancement at low- $p_T^{\text{assoc.}}$ and a suppression at high- $p_T^{\text{assoc.}}$. The semicentral near-side I_{AA} appeared consistent with one, whereas the away-side I_{AA} displayed an overall suppression. The differences between the I_{AA} of the two centrality classes indicate that the size of the medium has an effect on the fragmentation. Such that a QGP with the size, temperature, and energy density resulting from the most-central collisions noticeably affects the fragmentation function to produce more low- p_T hadrons in Pb—Pb compared to pp (for both the near- and away-side jets). This in tandem with possible medium excitation results in an enhancement of the low- p_T region of the I_{AA} . In contrast, the semicentral near-side I_{AA} suggests that the QGP formed

did not significantly affect the fragmentation of the near-side due its smaller size, or any signatures of medium excitation were not significant enough to measure experimentally in this analysis. The I_{AA} for the correlations in the split $p_T^{\text{trig.}}$ intervals were compared, where they exhibited a similar distribution pattern for both the near- and away-side. This similarity, especially for the near-side I_{AA} , suggests that the QGP generated in the most-central collisions modifies the phase space of the jet similarly for jets of different energies. However, the $7 - 16$ GeV/ c measurement displays a greater enhancement in low- $p_T^{\text{assoc.}}$ in the away-side I_{AA} . One would expect that the higher $p_T^{\text{trig.}}$ results in more particles correlated in $p_T^{\text{assoc.}}$ compared to the lower $p_T^{\text{trig.}}$, which is true. However, this effect would be true for both the Pb-Pb and pp collision systems, and would be effectively canceled out in the I_{AA} . It could be that the mechanism which produces the enhancement at low- $p_T^{\text{assoc.}}$ either has a greater effect in the jet phase space explored with a high- p_T trigger, or the jets in the energies which are selected when correlating with a high- p_T trigger experience a greater enhancement mechanism.

When comparing the heavy-flavor I_{AA} to the light-flavor I_{AA} of different species, the data points are consistent between the two measurements for both the near- and away-side. Given that heavy quarks experience less collisional energy loss and are expected to experience less radiative energy loss in the medium (due to their higher mass), one would expect a difference in the level of suppression observed on the away-side between heavy and light flavor. This suggests that the fragmentation of this phase space of the jet experiences similar modification by the QGP, independent of the initiating jet parton's mass (and possibly independent of whether the initiating parton is a quark or gluon). Although a suitable model was not available for the heavy-flavor measurement, inferences can still be drawn from the AMPT comparison for the light-flavor I_{AA} . AMPT predicts a suppression of the high- $p_T^{\text{assoc.}}$ section of the near-side I_{AA} , which is not shared by the data. It could be that the AMPT model is correlating trigger particles that originate from partons produced both deep within and near the surface of the QGP. Whereas in reality, the near-side peak is dominated by jets which are produced near the surface, where they experience less modification of the QGP compared to the recoil jet. Therefore, AMPT is predicting a larger path-length-dependent energy loss of the originating parton, resulting in this inconsistency with data for the near-side I_{AA} at high- $p_T^{\text{assoc.}}$. AMPT describes the suppression at high- $p_T^{\text{assoc.}}$ of the away-side I_{AA} and qualitatively describes an

enhancement at low- $p_T^{\text{assoc.}}$, although the prediction does not describe the magnitude of the enhancement in the lowest $p_T^{\text{assoc.}}$ interval. Given that the away-side I_{AA} shows a greater enhancement than the near-side, it could be that the away-side experiences the same mechanism which causes the near-side enhancement and experiences an increased number of associated particles in low- $p_T^{\text{assoc.}}$ due to the parton energy loss producing more low- p_T associated particles or from the result of medium excitation, or a combination of both effects.

The same away-side I_{AA} pattern in the light and heavy-flavor measurements is observed for Z-boson-triggered correlations. Measurements by ATLAS of the away-side I_{AA} of Z-bosons correlated with charged particles exhibits a suppression at high $p_T^{\text{assoc.}}$ and approach one or greater than one (depending on the p_T^Z) at low $p_T^{\text{assoc.}}$. The I_{AA} for both $60 < p_T^Z$ and $30 < p_T^Z < 60$ GeV/c are similarly-valued to the heavy and light flavor I_{AA} in every common $p_T^{\text{assoc.}}$ region. The models compared to the ATLAS measurement incorporate either a “wake” effect or at the very least some extent of medium “recoiling”. Before this will be discussed further, the most glaring difference must be addressed: The trigger particles (electroweak boson vs hadron) and the $p_T^{\text{trig.}}$ selected for the ATLAS measurement. One must consider that the p_T of the Z boson reflects the initial energy of the parton prior to experiencing energy loss [195], [196], whereas the hadrons and by extension the electron from HF hadron decays, will only carry a fraction of the initiating parton’s momentum. Therefore, a Z boson with a relatively higher- p_T is a better comparison than one with the same $p_T^{\text{trig.}}$ as the other measurements. That aside, the results in this thesis when viewed with the light-flavor and Z-boson I_{AA} results suggest a similar mechanism occurring in all measurements. The models support the overall theory that the energy transferred to the medium from the jet has generated some form of medium excitation, which manifests as an increase in the number of soft hadrons at freeze-out in the direction of the jet. This would be measured as an enhancement in the low- $p_T^{\text{assoc.}}$ range of the I_{AA} . Therefore, the behavior of the low- $p_T^{\text{assoc.}}$ region of the I_{AA} suggests a medium response, rather than the altered fragmentation of the jet. This is distinct from the theory that the energy loss experienced by the parton shower alters the fragmentation such that there is a larger proportion of low- p_T hadrons *within* the jet. Given that the models shown support the theory of medium excitation, the first interpretation is a compelling narrative to support. However, the change in fragmentation and medium excitation are not mutually exclusive phenomena, so both effects could be

contributing to the results of the electron I_{AA} . One must also consider that the results of the I_{AA} measurements have not been compared to all possible models. In particular, having a JETSCAPE or EPOS comparison would be imperative before claiming that medium excitation is the sole cause of these results. These models both incorporate hydrodynamic behavior of the medium, and the modularity of JETSCAPE can be exploited to incorporate the medium response from jets. The suppression observed at high- $p_T^{\text{assoc.}}$ describes a lower abundance of hadrons correlated with the trigger in Pb–Pb compared to pp. The suppression is indicative of the fragmentation being modified due to parton energy loss. So why this suppression is similar in magnitude for light-flavor, heavy-flavor, and the Z boson correlations is unclear. As stated earlier, perhaps this phase space of the jet experiences similar modification by the QGP, independent of the trigger species. One more question emerges: If there is medium excitation, does this take the form of a mach cone, followed by a diffusion wake? The CMS correlation measurement is the only experimental evidence suggesting the presence of a diffusion wake. This is supported by the model comparisons, but this observation applies for very high $p_T^{\text{trig.}}$ Z bosons. If there are such structures formed in the QGP due to the jet, perhaps this effect is observable only from medium interactions with very high energy jets.

6.2 Future outlook

The data from this measurement was obtained in 2018 during the Run 2 operation of the LHC. The ALICE detector has since undergone several major upgrades during the Long Shutdown 2 period. There are two primary objectives of these upgrades: to record Pb–Pb collision data with a 50 kHz interaction, which would increase the minimum-bias data sample by nearly two orders of magnitude, and to increase the vertexing capabilities for high-precision measurement of rare probes at low p_T [197]. For Run 3 and beyond, the ALICE experiment has entirely overhauled online data processing to support continuous readout rather than triggered-event recording. In the first two years of data recording for Run 3, ALICE has achieved an integrated luminosity of 1.5 nb^{-1} in Pb–Pb collisions. The greatest limiting factor of the measurement in this thesis is the statistics, i.e. the number of events studied. Although this measurement relies on the analysis of tens of millions of events, a future mea-

surement using Run 3 data would make use of hundreds of millions, or potentially billions of events. Just one order of magnitude more events would significantly reduce the statistical error and fluctuations of the correlation distribution, which could make characterizing the entire distribution more feasible.

With the greater statistics available in Run 3, other heavy-flavor correlation measurements can be performed. These would include D meson correlations in Pb–Pb, which can be used to obtain a D-meson I_{AA} measurement. This would be useful to compare to the light-flavor I_{AA} so that there is a more even comparison by looking at only hadron triggers. Additionally, electrons (from heavy flavor) correlated with associated electrons from heavy flavor could also be measured (perhaps selecting for both like-sign and unlike-sign correlations). This would provide insight into how both the near-side jet and recoil jet evolve in relation to each other due to the medium. If there are enough statistics to create a $D\bar{D}$ measurement, the heavy-flavor jet fragmentation can be explored with the heavy-flavor hadron.

Bibliography

- [1] Y. Okada, “Higgs Particle: The Origin of Mass,” *J. Phys. Soc. Jap.*, vol. 76, p. 111 011, 2007. DOI: 10.1143/JPSJ.76.111011. arXiv: 0708.2016 [hep-ph] (cit. on p. 25).
- [2] F. Englert and R. Brout, “Broken Symmetry and the Mass of Gauge Vector Mesons,” *Phys. Rev. Lett.*, vol. 13, J. C. Taylor, Ed., pp. 321–323, 1964. DOI: 10.1103/PhysRevLett.13.321 (cit. on p. 25).
- [3] P. W. Higgs, “Broken Symmetries and the Masses of Gauge Bosons,” *Phys. Rev. Lett.*, vol. 13, J. C. Taylor, Ed., pp. 508–509, 1964. DOI: 10.1103/PhysRevLett.13.508 (cit. on p. 25).
- [4] G. Aad *et al.*, “Observation of a new particle in the search for the Standard Model Higgs boson with the ATLAS detector at the LHC,” *Phys. Lett. B*, vol. 716, pp. 1–29, 2012. DOI: 10.1016/j.physletb.2012.08.020. arXiv: 1207.7214 [hep-ex] (cit. on p. 25).
- [5] S. Chatrchyan *et al.*, “Observation of a New Boson at a Mass of 125 GeV with the CMS Experiment at the LHC,” *Phys. Lett. B*, vol. 716, pp. 30–61, 2012. DOI: 10.1016/j.physletb.2012.08.021. arXiv: 1207.7235 [hep-ex] (cit. on p. 25).
- [6] K. Riesselmann, *The standard model of particle physics*, Jul. 2016. [Online]. Available: <https://www.symmetrymagazine.org/article/july-2015/standard-model> (cit. on p. 26).
- [7] R. Aliberti *et al.*, “The anomalous magnetic moment of the muon in the Standard Model: an update,” *Phys. Rept.*, vol. 1143, pp. 1–158, 2025. DOI: 10.1016/j.physrep.2025.08.002. arXiv: 2505.21476 [hep-ph] (cit. on p. 26).
- [8] V. Khachatryan *et al.*, “Observation of the rare $B_s^0 \rightarrow \mu^+ \mu^-$ decay from the combined analysis of CMS and LHCb data,” *Nature*, vol. 522, pp. 68–72, 2015. DOI: 10.1038/nature14474. arXiv: 1411.4413 [hep-ex] (cit. on p. 26).

- [9] L. Canetti, M. Drewes, and M. Shaposhnikov, “Matter and Antimatter in the Universe,” *New J. Phys.*, vol. 14, p. 095 012, 2012. DOI: 10.1088/1367-2630/14/9/095012. arXiv: 1204.4186 [hep-ph] (cit. on p. 26).
- [10] Y. Huang, S. Jin, and P. Zhang, “Discovery of a glueball-like particle X(2370) at BESIII,” *Int. J. Mod. Phys. A*, vol. 40, no. 19, p. 2530 007, 2025. DOI: 10.1142/S0217751X25300078. arXiv: 2503.13286 [hep-ex] (cit. on p. 28).
- [11] S. Navas *et al.*, “Review of particle physics,” *Phys. Rev. D*, vol. 110, no. 3, p. 030 001, 2024. DOI: 10.1103/PhysRevD.110.030001 (cit. on pp. 28, 43, 92).
- [12] S. Bethke, “World Summary of α_s (2012),” *Nucl. Phys. B Proc. Suppl.*, vol. 234, S. Narison, Ed., pp. 229–234, 2013. DOI: 10.1016/j.nuclphysbps.2012.12.020. arXiv: 1210.0325 [hep-ex] (cit. on p. 28).
- [13] D. J. Gross and F. Wilczek, “Asymptotically free gauge theories. i,” *Phys. Rev. D*, vol. 8, pp. 3633–3652, 10 Nov. 1973. DOI: 10.1103/PhysRevD.8.3633. [Online]. Available: <https://link.aps.org/doi/10.1103/PhysRevD.8.3633> (cit. on p. 29).
- [14] H. D. Politzer, “Asymptotic Freedom: An Approach to Strong Interactions,” *Phys. Rept.*, vol. 14, pp. 129–180, 1974. DOI: 10.1016/0370-1573(74)90014-3 (cit. on p. 29).
- [15] S. Acharya *et al.*, “The ALICE experiment: a journey through QCD,” *Eur. Phys. J. C*, vol. 84, no. 8, p. 813, 2024. DOI: 10.1140/epjc/s10052-024-12935-y. arXiv: 2211.04384 [nucl-ex] (cit. on pp. 29, 32–34, 53).
- [16] A. Bazavov *et al.*, “Chiral crossover in qcd at zero and non-zero chemical potentials,” *Physics Letters B*, vol. 795, pp. 15–21, 2019, ISSN: 0370-2693. DOI: <https://doi.org/10.1016/j.physletb.2019.05.013>. [Online]. Available: <https://www.sciencedirect.com/science/article/pii/S0370269319303223> (cit. on p. 29).
- [17] F. Karsch *et al.*, “Flavor and quark mass dependence of qcd thermodynamics,” *Nuclear Physics B - Proceedings Supplements*, vol. 94, no. 1, pp. 411–414, 2001, Proceedings of the XVIIIth International Symposium on Lattice Field Theory, ISSN: 0920-5632. DOI: [https://doi.org/10.1016/S0920-5632\(01\)00988-4](https://doi.org/10.1016/S0920-5632(01)00988-4).

- [Online]. Available: <https://www.sciencedirect.com/science/article/pii/S0920563201009884> (cit. on pp. 29, 30).
- [18] E. V. Shuryak, “Quantum chromodynamics and the theory of superdense matter,” *Physics Reports*, vol. 61, no. 2, pp. 71–158, 1980, ISSN: 0370-1573. DOI: [https://doi.org/10.1016/0370-1573\(80\)90105-2](https://doi.org/10.1016/0370-1573(80)90105-2). [Online]. Available: <https://www.sciencedirect.com/science/article/pii/0370157380901052> (cit. on p. 29).
- [19] W. Florkowski, “The realistic qcd equation of state in relativistic heavy-ion collisions and the early universe,” *Nuclear Physics A*, vol. 853, no. 1, pp. 173–188, 2011, ISSN: 0375-9474. DOI: <https://doi.org/10.1016/j.nuclphysa.2011.01.024>. [Online]. Available: <https://www.sciencedirect.com/science/article/pii/S0375947411000443> (cit. on pp. 29, 31).
- [20] T. Fischer *et al.*, “Quark deconfinement as a supernova explosion engine for massive blue supergiant stars,” *Nature Astron.*, vol. 2, no. 12, pp. 980–986, 2018. DOI: 10.1038/s41550-018-0583-0. arXiv: 1712.08788 [astro-ph.HE] (cit. on p. 29).
- [21] L. Apolinário, Y.-J. Lee, and M. Winn, “Heavy quarks and jets as probes of the QGP,” *Prog. Part. Nucl. Phys.*, vol. 127, p. 103990, 2022. DOI: 10.1016/j.ppnp.2022.103990. arXiv: 2203.16352 [hep-ph] (cit. on pp. 29, 31, 38, 42).
- [22] T. Niida and Y. Miake, “Signatures of QGP at RHIC and the LHC,” *AAPPS Bull.*, vol. 31, no. 1, p. 12, 2021. DOI: 10.1007/s43673-021-00014-3. arXiv: 2104.11406 [nucl-ex] (cit. on p. 30).
- [23] D. J. Schwarz and M. Stuke, “Lepton asymmetry and the cosmic QCD transition,” *JCAP*, vol. 11, p. 025, 2009, [Erratum: JCAP 10, E01 (2010)]. DOI: 10.1088/1475-7516/2009/11/025. arXiv: 0906.3434 [hep-ph] (cit. on pp. 30, 31).
- [24] M. Stephanov, “QCD critical point: Recent developments,” *EPJ Web Conf.*, vol. 314, p. 00042, 2024. DOI: 10.1051/epjconf/202431400042. arXiv: 2410.02861 [nucl-th] (cit. on p. 30).

- [25] U. W. Heinz, “The Strongly coupled quark-gluon plasma created at RHIC,” *J. Phys. A*, vol. 42, D. Neilson and G. Senatore, Eds., p. 214003, 2009. DOI: 10.1088/1751-8113/42/21/214003. arXiv: 0810.5529 [nucl-th] (cit. on p. 31).
- [26] S. Chen, L. Yan, and S. Shi, “Quantum thermalization of Quark-Gluon Plasma,” Nov. 2024. arXiv: 2412.00662 [hep-ph] (cit. on p. 31).
- [27] E. Shuryak, “Why does the quark gluon plasma at RHIC behave as a nearly ideal fluid?” *Prog. Part. Nucl. Phys.*, vol. 53, A. Faessler, Ed., pp. 273–303, 2004. DOI: 10.1016/j.ppnp.2004.02.025. arXiv: hep-ph/0312227 (cit. on p. 31).
- [28] S. S. Gubser, S. S. Pufu, F. D. Rocha, and A. Yarom, “Energy loss in a strongly coupled thermal medium and the gauge-string duality,” in *Quark-gluon plasma 4*, R. C. Hwa and X.-N. Wang, Eds. 2010, pp. 1–59. DOI: 10.1142/9789814293297_0001. arXiv: 0902.4041 [hep-th] (cit. on pp. 31, 38).
- [29] H. Niemi *et al.*, “Influence of shear viscosity of quark-gluon plasma on elliptic flow in ultrarelativistic heavy-ion collisions,” *Phys. Rev. Lett.*, vol. 106, p. 212302, 21 May 2011. DOI: 10.1103/PhysRevLett.106.212302. [Online]. Available: <https://link.aps.org/doi/10.1103/PhysRevLett.106.212302> (cit. on p. 31).
- [30] M. Bluhm and T. Schäfer, “From cold Fermi fluids to the hot QGP,” *Acta Phys. Polon. Supp.*, vol. 10, p. 481, 2017. DOI: 10.5506/APhysPolBSupp.10.481. arXiv: 1705.08710 [cond-mat.quant-gas] (cit. on p. 31).
- [31] J. Thomas, “Is an ultra-cold strongly interacting fermi gas a perfect fluid?” *Nuclear Physics A*, vol. 830, no. 1, pp. 665c–672c, 2009, Quark Matter 2009, ISSN: 0375-9474. DOI: <https://doi.org/10.1016/j.nuclphysa.2009.09.055>. [Online]. Available: <https://www.sciencedirect.com/science/article/pii/S0375947409006472> (cit. on p. 31).
- [32] S. M. J. Sanches, D. A. Fogaça, and F. S. Navarra, “The time evolution of the quark gluon plasma in the early universe,” *Journal of Physics. Conference Series (Online)*, vol. 630, no. 1, [10 p.] Jul. 2015, ISSN: 1742-6596. DOI: 10.1088/1742-6596/630/1/012028 (cit. on p. 31).

- [33] T. Kalaydzhyan and E. Shuryak, “Gravity waves generated by sounds from big bang phase transitions,” *Phys. Rev. D*, vol. 91, no. 8, p. 083502, 2015. DOI: 10.1103/PhysRevD.91.083502. arXiv: 1412.5147 [hep-ph] (cit. on p. 31).
- [34] V. R. C. Mourão Roque and G. Lugones, “Unveiling the cosmological QCD phase transition through the eLISA/NGO detector,” *Phys. Rev. D*, vol. 87, no. 8, p. 083516, 2013. DOI: 10.1103/PhysRevD.87.083516. arXiv: 1303.6978 [astro-ph.CO] (cit. on p. 31).
- [35] J. W. Harris, “Introduction to hard scattering processes and recent results from hard probes at rhic and lhc,” *Journal of Physics: Conference Series*, vol. 630, no. 1, p. 012052, Jul. 2015. DOI: 10.1088/1742-6596/630/1/012052. [Online]. Available: <https://dx.doi.org/10.1088/1742-6596/630/1/012052> (cit. on pp. 32, 169).
- [36] D. E. Soper, “Parton distribution functions,” *Nucl. Phys. B Proc. Suppl.*, vol. 53, C. Bernard, M. Golterman, M. Ogilvie, and J. Potvin, Eds., pp. 69–80, 1997. DOI: 10.1016/S0920-5632(96)00600-7. arXiv: hep-lat/9609018 (cit. on p. 32).
- [37] U. W. Heinz, “Concepts of heavy ion physics,” in *2nd CERN-CLAF School of High Energy Physics*, Jul. 2004, pp. 165–238. arXiv: hep-ph/0407360 (cit. on pp. 32, 33).
- [38] T. Kalaydzhyan and E. Shuryak, “Collective flow in high-multiplicity proton-proton collisions,” *Phys. Rev. C*, vol. 91, p. 054913, 5 May 2015. DOI: 10.1103/PhysRevC.91.054913. [Online]. Available: <https://link.aps.org/doi/10.1103/PhysRevC.91.054913> (cit. on p. 32).
- [39] S. Chatrchyan *et al.*, “Observation of Long-Range Near-Side Angular Correlations in Proton-Lead Collisions at the LHC,” *Phys. Lett. B*, vol. 718, pp. 795–814, 2013. DOI: 10.1016/j.physletb.2012.11.025. arXiv: 1210.5482 [nucl-ex] (cit. on p. 32).
- [40] J. Adam *et al.*, “Enhanced production of multi-strange hadrons in high-multiplicity proton-proton collisions,” *Nature Phys.*, vol. 13, pp. 535–539, 2017. DOI: 10.1038/nphys4111. arXiv: 1606.07424 [nucl-ex] (cit. on p. 32).

- [41] S. Pucillo, “Recent results on strangeness enhancement in small collision systems with ALICE,” in *13th International Conference on New Frontiers in Physics*, Apr. 2025. arXiv: 2504.02527 [nucl-ex] (cit. on p. 32).
- [42] e. a. Abdulameer N., “Disentangling centrality bias and final-state effects in the production of high- p_T neutral pions using direct photon in d +au collisions at $\sqrt{s_{NN}}=200$ gev,” *Physical Review Letters*, vol. 134, no. 2, Jan. 2025. DOI: 10.1103/physrevlett.134.022302 (cit. on p. 32).
- [43] W. Busza, K. Rajagopal, and W. van der Schee, “Heavy Ion Collisions: The Big Picture, and the Big Questions,” *Ann. Rev. Nucl. Part. Sci.*, vol. 68, pp. 339–376, 2018. DOI: 10.1146/annurev-nucl-101917-020852. arXiv: 1802.04801 [hep-ph] (cit. on p. 33).
- [44] T. Hirano and Y. Nara, “Hydrodynamic afterburner for the color glass condensate and the parton energy loss,” *Nucl. Phys. A*, vol. 743, pp. 305–328, 2004. DOI: 10.1016/j.nuclphysa.2004.08.003. arXiv: nucl-th/0404039 (cit. on p. 34).
- [45] F.-M. Liu and S.-X. Liu, “Quark-gluon plasma formation time and direct photons from heavy ion collisions,” *Phys. Rev. C*, vol. 89, no. 3, p. 034906, 2014. DOI: 10.1103/PhysRevC.89.034906. arXiv: 1212.6587 [nucl-th] (cit. on p. 34).
- [46] A. Toia, “Participants and spectators at the heavy-ion fireball,” *CERN Courier*, vol. 53, no. 4, pp. 31–34, 2013. [Online]. Available: <https://cds.cern.ch/record/1734942> (cit. on p. 37).
- [47] M. L. Miller, K. Reygers, S. J. Sanders, and P. Steinberg, “Glauber modeling in high energy nuclear collisions,” *Ann. Rev. Nucl. Part. Sci.*, vol. 57, pp. 205–243, 2007. DOI: 10.1146/annurev.nucl.57.090506.123020. arXiv: nucl-ex/0701025 (cit. on pp. 37, 75).
- [48] S. Acharya *et al.*, “Centrality determination in heavy ion collisions,” Tech. Rep. ALICE-PUBLIC-2018-011, Aug. 2018. [Online]. Available: <https://cds.cern.ch/record/2636623> (cit. on pp. 37, 81, 82).

- [49] B. Abelev *et al.*, “Centrality determination of Pb-Pb collisions at $\sqrt{s_{NN}} = 2.76$ TeV with ALICE,” *Phys. Rev. C*, vol. 88, no. 4, p. 044 909, 2013. DOI: 10.1103/PhysRevC.88.044909. arXiv: 1301.4361 [nucl-ex] (cit. on pp. 38, 75, 81).
- [50] S. S. Gubser, S. S. Pufu, and A. Yarom, “Sonic booms and diffusion wakes generated by a heavy quark in thermal AdS/CFT,” *Phys. Rev. Lett.*, vol. 100, p. 012 301, 2008. DOI: 10.1103/PhysRevLett.100.012301. arXiv: 0706.4307 [hep-th] (cit. on pp. 38, 39, 169, 183).
- [51] Y. Tachibana, N.-B. Chang, and G.-Y. Qin, “Full jet in quark-gluon plasma with hydrodynamic medium response,” *Phys. Rev. C*, vol. 95, no. 4, p. 044 909, 2017. DOI: 10.1103/PhysRevC.95.044909. arXiv: 1701.07951 [nucl-th] (cit. on pp. 39, 169, 183).
- [52] S. Cao and G.-Y. Qin, “Medium Response and Jet–Hadron Correlations in Relativistic Heavy-Ion Collisions,” *Ann. Rev. Nucl. Part. Sci.*, vol. 73, pp. 205–229, 2023. DOI: 10.1146/annurev-nucl-112822-031317. arXiv: 2211.16821 [nucl-th] (cit. on p. 39).
- [53] Z. Yang *et al.*, “3D Structure of Jet-Induced Diffusion Wake in an Expanding Quark-Gluon Plasma,” *Phys. Rev. Lett.*, vol. 130, no. 5, p. 052 301, 2023. DOI: 10.1103/PhysRevLett.130.052301. arXiv: 2203.03683 [hep-ph] (cit. on p. 39).
- [54] A. Luo *et al.*, “Jet shape and redistribution of the lost energy from jets in Pb + Pb collisions at the LHC in a multiphase transport model,” *Eur. Phys. J. C*, vol. 82, no. 2, p. 156, 2022. DOI: 10.1140/epjc/s10052-022-10110-9. arXiv: 2107.11751 [hep-ph] (cit. on p. 39).
- [55] B. Betz *et al.*, “Universal flow-driven conical emission in ultrarelativistic heavy-ion collisions,” *Phys. Rev. Lett.*, vol. 105, p. 222 301, 22 Nov. 2010. DOI: 10.1103/PhysRevLett.105.222301. [Online]. Available: <https://link.aps.org/doi/10.1103/PhysRevLett.105.222301> (cit. on p. 39).
- [56] M. Arslanodok *et al.*, “Hot QCD White Paper,” Mar. 2023. arXiv: 2303.17254 [nucl-ex] (cit. on pp. 39, 52).

- [57] A. Ali and G. Kramer, “Jets and QCD: A Historical Review of the Discovery of the Quark and Gluon Jets and its Impact on QCD,” *Eur. Phys. J. H*, vol. 36, pp. 245–326, 2011. DOI: 10.1140/epjh/e2011-10047-1. arXiv: 1012.2288 [hep-ph] (cit. on p. 39).
- [58] Y. L. Dokshitzer, V. A. Khoze, A. H. Mueller, and S. I. Troian, *Basics of perturbative QCD*. 1991 (cit. on p. 40).
- [59] J. Viinikainen, “Jet transverse fragmentation momentum from h–h correlations in pp and p–Pb collisions,” *Nucl. Part. Phys. Proc.*, vol. 289-290, G.-Y. Qin *et al.*, Eds., pp. 293–296, 2017. DOI: 10.1016/j.nuclphysbps.2017.05.067. arXiv: 1612.05475 [hep-ex] (cit. on pp. 40, 154).
- [60] G. Rauco, “Distinguishing quark and gluon jets at the LHC,” in *Parton radiation and fragmentation from LHC to FCC-ee*, Feb. 2017, pp. 73–78 (cit. on p. 40).
- [61] W. Liu, C. M. Ko, and B. W. Zhang, “Jet conversions in a quark-gluon plasma,” *Phys. Rev. C*, vol. 75, p. 051 901, 2007. DOI: 10.1103/PhysRevC.75.051901. arXiv: nucl-th/0607047 (cit. on pp. 40, 183).
- [62] J. Collins and T. C. Rogers, “Definition of fragmentation functions and the violation of sum rules,” *Phys. Rev. D*, vol. 109, no. 1, p. 016 006, 2024. DOI: 10.1103/PhysRevD.109.016006. arXiv: 2309.03346 [hep-ph] (cit. on pp. 40, 154).
- [63] E. M. Metodiev, *The fractal lives of jets*, Apr. 2020. [Online]. Available: <https://www.ericmetodiev.com/post/jetformation/> (cit. on p. 40).
- [64] D.-J. Yang and H.-n. Li, “Charm fragmentation functions in the Nambu–Jona-Lasinio model,” *Phys. Rev. D*, vol. 102, no. 3, p. 036 023, 2020. DOI: 10.1103/PhysRevD.102.036023. arXiv: 2007.05678 [hep-ph] (cit. on p. 41).
- [65] X.-N. Wang, “What hard probes tell us about the quark–gluon plasma: Theory,” *Nucl. Phys. A*, vol. 932, W. Horowitz *et al.*, Eds., pp. 1–8, 2014. DOI: 10.1016/j.nuclphysa.2014.09.065. arXiv: 1404.2327 [nucl-th] (cit. on pp. 41, 56).
- [66] M. Cacciari, G. P. Salam, and G. Soyez, “The anti- k_t jet clustering algorithm,” *JHEP*, vol. 04, p. 063, 2008. DOI: 10.1088/1126-6708/2008/04/063. arXiv: 0802.1189 [hep-ph] (cit. on p. 41).

- [67] P. T. Komiske, I. Moulton, J. Thaler, and H. X. Zhu, “Analyzing N-Point Energy Correlators inside Jets with CMS Open Data,” *Phys. Rev. Lett.*, vol. 130, no. 5, p. 051 901, 2023. DOI: 10.1103/PhysRevLett.130.051901. arXiv: 2201.07800 [hep-ph] (cit. on p. 41).
- [68] M. Aaboud *et al.*, “Measurement of jet fragmentation in Pb+Pb and *pp* collisions at $\sqrt{s_{NN}} = 5.02$ TeV with the ATLAS detector,” *Phys. Rev. C*, vol. 98, no. 2, p. 024 908, 2018. DOI: 10.1103/PhysRevC.98.024908. arXiv: 1805.05424 [nucl-ex] (cit. on p. 41).
- [69] C. Adler *et al.*, “Disappearance of back-to-back high p_T hadron correlations in central Au+Au collisions at $\sqrt{s_{NN}} = 200$ -GeV,” *Phys. Rev. Lett.*, vol. 90, p. 082 302, 2003. DOI: 10.1103/PhysRevLett.90.082302. arXiv: nucl-ex/0210033 (cit. on p. 41).
- [70] S. Acharya *et al.*, “Jet-like correlations with respect to K_S^0 and Λ ($\bar{\Lambda}$) in *pp* and Pb–Pb collisions at $\sqrt{s_{NN}} = 5.02$ TeV,” *Eur. Phys. J. C*, vol. 83, no. 6, p. 497, 2023. DOI: 10.1140/epjc/s10052-023-11614-8. arXiv: 2211.01197 [nucl-ex] (cit. on pp. 41, 61, 106, 113, 130, 181–185).
- [71] J. Adam *et al.*, “Jet-like correlations with neutral pion triggers in *pp* and central Pb–Pb collisions at $\sqrt{s_{NN}} = 2.76$ TeV,” *Phys. Lett. B*, vol. 763, pp. 238–250, 2016. DOI: 10.1016/j.physletb.2016.10.048. arXiv: 1608.07201 [nucl-ex] (cit. on pp. 41, 49, 61–63, 181, 183, 184).
- [72] K. Aamodt *et al.*, “Particle-yield modification in jet-like azimuthal di-hadron correlations in Pb–Pb collisions at $\sqrt{s_{NN}} = 2.76$ TeV,” *Phys. Rev. Lett.*, vol. 108, p. 092 301, 2012. DOI: 10.1103/PhysRevLett.108.092301. arXiv: 1110.0121 [nucl-ex] (cit. on pp. 41, 169, 181, 183, 184).
- [73] A. M. Sirunyan *et al.*, “Study of jet quenching with isolated-photon+jet correlations in PbPb and *pp* collisions at $\sqrt{s_{NN}} = 5.02$ TeV,” *Phys. Lett. B*, vol. 785, pp. 14–39, 2018. DOI: 10.1016/j.physletb.2018.07.061. arXiv: 1711.09738 [nucl-ex] (cit. on p. 41).
- [74] F. Prino and R. Rapp, “Open Heavy Flavor in QCD Matter and in Nuclear Collisions,” *J. Phys. G*, vol. 43, no. 9, p. 093 002, 2016. DOI: 10.1088/0954-3899/43/9/093002. arXiv: 1603.00529 [nucl-ex] (cit. on pp. 42, 54, 65).

- [75] F. Scardina *et al.*, “Estimating the charm quark diffusion coefficient and thermalization time from D meson spectra at energies available at the BNL Relativistic Heavy Ion Collider and the CERN Large Hadron Collider,” *Phys. Rev. C*, vol. 96, no. 4, p. 044 905, 2017. DOI: 10.1103/PhysRevC.96.044905. arXiv: 1707.05452 [nucl-th] (cit. on p. 42).
- [76] S. Acharya *et al.*, “Prompt D^0 , D^+ , and D^{*+} production in Pb–Pb collisions at $\sqrt{s_{\text{NN}}} = 5.02$ TeV,” *JHEP*, vol. 01, p. 174, 2022. DOI: 10.1007/JHEP01(2022)174. arXiv: 2110.09420 [nucl-ex] (cit. on pp. 42, 57, 59).
- [77] S. Acharya *et al.*, “Direct observation of the dead-cone effect in quantum chromodynamics,” *Nature*, vol. 605, no. 7910, pp. 440–446, 2022, [Erratum: *Nature* 607, E22 (2022)]. DOI: 10.1038/s41586-022-04572-w. arXiv: 2106.05713 [nucl-ex] (cit. on p. 42).
- [78] S. Kluth, W. Ochs, and R. Perez Ramos, “The dead cone effect in heavy quark jets observed in momentum space and its QCD explanation,” Dec. 2023. arXiv: 2312.17697 [hep-ph] (cit. on p. 43).
- [79] R. Sharma, I. Vitev, and B.-W. Zhang, “Light-cone wave function approach to open heavy flavor dynamics in QCD matter,” *Phys. Rev. C*, vol. 80, p. 054 902, 2009. DOI: 10.1103/PhysRevC.80.054902. arXiv: 0904.0032 [hep-ph] (cit. on p. 43).
- [80] G. Gustafson, “Event generators for heavy-ion physics, recent developments,” English, in *PoS LHCP 2018*, ser. Proceedings of Science, Sissa Medialab srl, 2018. DOI: 10.22323/1.321.0215 (cit. on pp. 43, 46, 48).
- [81] B. Andersson, G. Gustafson, and B. Soderberg, “A General Model for Jet Fragmentation,” *Z. Phys. C*, vol. 20, p. 317, 1983. DOI: 10.1007/BF01407824 (cit. on p. 44).
- [82] A. Kupco, “Cluster hadronization in HERWIG 5.9,” in *Workshop on Monte Carlo Generators for HERA Physics (Plenary Starting Meeting)*, Apr. 1998, pp. 292–300. arXiv: hep-ph/9906412 (cit. on p. 44).
- [83] T. Sjostrand, S. Mrenna, and P. Z. Skands, “PYTHIA 6.4 Physics and Manual,” *JHEP*, vol. 05, p. 026, 2006. DOI: 10.1088/1126-6708/2006/05/026. arXiv: hep-ph/0603175 (cit. on pp. 44, 45, 95).

- [84] X.-N. Wang and M. Gyulassy, “HIJING: A Monte Carlo model for multiple jet production in p p, p A and A A collisions,” *Phys. Rev. D*, vol. 44, pp. 3501–3516, 1991. DOI: 10.1103/PhysRevD.44.3501 (cit. on pp. 44, 45, 95, 184).
- [85] S. Porteboeuf, T. Pierog, and K. Werner, “Producing Hard Processes Regarding the Complete Event: The EPOS Event Generator,” in *45th Rencontres de Moriond on QCD and High Energy Interactions*, Gioi Publishers, 2010, pp. 135–140. arXiv: 1006.2967 [hep-ph] (cit. on pp. 44, 46).
- [86] C. Bierlich *et al.*, “A comprehensive guide to the physics and usage of PYTHIA 8.3,” *SciPost Phys. Codeb.*, vol. 2022, p. 8, 2022. DOI: 10.21468/SciPostPhysCodeb.8. arXiv: 2203.11601 [hep-ph] (cit. on p. 45).
- [87] G. Gustafson, “Event generators for heavy-ion physics, recent developments,” Sep. 2018, p. 215. DOI: 10.22323/1.321.0215 (cit. on p. 45).
- [88] M. Gyulassy and X.-N. Wang, “HIJING 1.0: A Monte Carlo program for parton and particle production in high-energy hadronic and nuclear collisions,” *Comput. Phys. Commun.*, vol. 83, p. 307, 1994. DOI: 10.1016/0010-4655(94)90057-4. arXiv: nucl-th/9502021 (cit. on pp. 45, 46).
- [89] L. Pang, Q. Wang, and X.-N. Wang, “Relics of minijets amid anisotropic flows in high-energy heavy-ion collisions,” *Phys. Rev. C*, vol. 89, p. 064910, 6 Jun. 2014. DOI: 10.1103/PhysRevC.89.064910. [Online]. Available: <https://link.aps.org/doi/10.1103/PhysRevC.89.064910> (cit. on p. 46).
- [90] A. H. Rezaeian and Z. Lu, “Cronin effect for protons and pions in high-energy pA collisions,” *Nucl. Phys. A*, vol. 826, pp. 198–210, 2009. DOI: 10.1016/j.nuclphysa.2009.05.073. arXiv: 0810.4942 [hep-ph] (cit. on p. 46).
- [91] G. Papp *et al.*, “First Results with HIJING++ on High-energy Heavy Ion Collisions,” in *12th International Workshop on High-pT Physics in the RHIC/LHC Era*, May 2018. arXiv: 1805.02635 [hep-ph] (cit. on p. 46).
- [92] M. Gyulassy, P. Levai, and I. Vitev, “Jet tomography of Au+Au reactions including multigluon fluctuations,” *Phys. Lett. B*, vol. 538, pp. 282–288, 2002. DOI: 10.1016/S0370-2693(02)01990-1. arXiv: nucl-th/0112071 (cit. on p. 46).

- [93] Z. Wolff and D. Molnar, “Self-consistent Cooper-Frye freeze-out of a viscous fluid to particles,” *J. Phys. Conf. Ser.*, vol. 535, p. 012020, 2014. DOI: 10.1088/1742-6596/535/1/012020. arXiv: 1407.6413 [nucl-th] (cit. on p. 46).
- [94] T. Pierog *et al.*, “EPOS LHC: Test of collective hadronization with data measured at the CERN Large Hadron Collider,” *Phys. Rev. C*, vol. 92, no. 3, p. 034906, 2015. DOI: 10.1103/PhysRevC.92.034906. arXiv: 1306.0121 [hep-ph] (cit. on p. 46).
- [95] J. H. Putschke *et al.*, “The JETSCAPE framework,” Mar. 2019. arXiv: 1903.07706 [nucl-th] (cit. on p. 47).
- [96] C. Sirimanna *et al.*, “Hard-photon-triggered jets in p-p and A-A collisions,” *Phys. Rev. C*, vol. 111, no. 6, p. 064911, 2025. DOI: 10.1103/yyr5-zp16. arXiv: 2412.19738 [hep-ph] (cit. on pp. 47, 48).
- [97] B. E. Aboona *et al.*, “Measurement of In-Medium Jet Modification Using Direct Photon+Jet and π^0 +Jet Correlations in p+p and Central Au+Au Collisions at sNN=200 GeV,” *Phys. Rev. Lett.*, vol. 134, no. 23, p. 232301, 2025. DOI: 10.1103/PhysRevLett.134.232301. arXiv: 2309.00156 [nucl-ex] (cit. on pp. 47, 48).
- [98] Z.-W. Lin *et al.*, “A Multi-phase transport model for relativistic heavy ion collisions,” *Phys. Rev. C*, vol. 72, p. 064901, 2005. DOI: 10.1103/PhysRevC.72.064901. arXiv: nucl-th/0411110 (cit. on pp. 48, 184).
- [99] L.-Y. Zhang *et al.*, “Two-particle angular correlations in heavy ion collisions from a multiphase transport model,” *Phys. Rev. C*, vol. 99, no. 5, p. 054904, 2019. DOI: 10.1103/PhysRevC.99.054904. arXiv: 1904.08603 [nucl-th] (cit. on p. 48).
- [100] B. Zhang, “ZPC 1.0.1: A Parton cascade for ultrarelativistic heavy ion collisions,” *Comput. Phys. Commun.*, vol. 109, pp. 193–206, 1998. DOI: 10.1016/S0010-4655(98)00010-1. arXiv: nucl-th/9709009 (cit. on p. 48).
- [101] V. Greco and C. M. Ko, “Hadronization via coalescence,” *Acta Phys. Hung. A*, vol. 24, W. Bauer *et al.*, Eds., pp. 235–240, 2005. DOI: 10.1556/APH.24.2005.1-4.32. arXiv: nucl-th/0405040 (cit. on pp. 48, 58).

- [102] X. Ke-Feng *et al.*, “Properties of dihadron correlations for p+p collisions at $\sqrt{s_{NN}} = 200$ gev,” *Chinese Physics Letters*, vol. 26, p. 062 503, Jun. 2009. DOI: 10.1088/0256-307X/26/6/062503 (cit. on p. 49).
- [103] E. L. Bratkovskaya *et al.*, “PHSD - a microscopic transport approach for strongly interacting systems,” Aug. 2019. arXiv: 1908.00451 [nucl-th] (cit. on p. 49).
- [104] W. Cassing, “From Kadanoff-Baym dynamics to off-shell parton transport,” *Eur. Phys. J. ST*, vol. 168, R. Alkofer, H. Gies, and B.-J. Schaefer, Eds., pp. 3–87, 2009. DOI: 10.1140/epjst/e2009-00959-x. arXiv: 0808.0715 [nucl-th] (cit. on p. 49).
- [105] W. Ehehalt and W. Cassing, “Relativistic transport approach for nucleus-nucleus collisions based on a NJL Lagrangian,” Jul. 1995. arXiv: hep-ph/9507274 (cit. on p. 49).
- [106] W. Cassing and E. L. Bratkovskaya, “Parton transport and hadronization from the dynamical quasiparticle point of view,” *Phys. Rev. C*, vol. 78, p. 034 919, 2008. DOI: 10.1103/PhysRevC.78.034919. arXiv: 0808.0022 [hep-ph] (cit. on p. 49).
- [107] R. Kunnawalkam Elayavalli and K. C. Zapp, “Simulating V+jet processes in heavy ion collisions with JEWEL,” *Eur. Phys. J. C*, vol. 76, no. 12, p. 695, 2016. DOI: 10.1140/epjc/s10052-016-4534-6. arXiv: 1608.03099 [hep-ph] (cit. on p. 50).
- [108] R. Kunnawalkam Elayavalli and K. C. Zapp, “Medium response in JEWEL and its impact on jet shape observables in heavy ion collisions,” *JHEP*, vol. 07, p. 141, 2017. DOI: 10.1007/JHEP07(2017)141. arXiv: 1707.01539 [hep-ph] (cit. on p. 50).
- [109] M. He, R. J. Fries, and R. Rapp, “Heavy Flavor at the Large Hadron Collider in a Strong Coupling Approach,” *Phys. Lett. B*, vol. 735, pp. 445–450, 2014. DOI: 10.1016/j.physletb.2014.05.050. arXiv: 1401.3817 [nucl-th] (cit. on p. 50).

- [110] S. Li, C. Wang, R. Wan, and J. Liao, “Probing the transport properties of Quark-Gluon Plasma via heavy-flavor Boltzmann and Langevin dynamics,” *Phys. Rev. C*, vol. 99, no. 5, p. 054909, 2019. DOI: 10.1103/PhysRevC.99.054909. arXiv: 1901.04600 [hep-ph] (cit. on p. 50).
- [111] S. Li and J. Liao, “Data-driven extraction of heavy quark diffusion in quark-gluon plasma,” *Eur. Phys. J. C*, vol. 80, no. 7, p. 671, 2020. DOI: 10.1140/epjc/s10052-020-8243-9. arXiv: 1912.08965 [hep-ph] (cit. on p. 50).
- [112] I. Karpenko, P. Huovinen, and M. Bleicher, “A 3+1 dimensional viscous hydrodynamic code for relativistic heavy ion collisions,” *Comput. Phys. Commun.*, vol. 185, pp. 3016–3027, 2014. DOI: 10.1016/j.cpc.2014.07.010. arXiv: 1312.4160 [nucl-th] (cit. on p. 51).
- [113] K. Redlich and A. Tounsi, “Strangeness enhancement in heavy ion collisions,” in *36th Rencontres de Moriond on QCD and Hadronic Interactions*, 2001, pp. 309–312. arXiv: hep-ph/0105201 (cit. on p. 51).
- [114] e. a. Agakishiev G., “Strangeness enhancement in cu-cu and au-au collisions at $\sqrt{s_{NN}} = 200$ GeV,” *Phys. Rev. Lett.*, vol. 108, p. 072301, 7 Feb. 2012. DOI: 10.1103/PhysRevLett.108.072301. [Online]. Available: <https://link.aps.org/doi/10.1103/PhysRevLett.108.072301> (cit. on pp. 51, 52).
- [115] S. Acharya *et al.*, “Transverse-momentum and event-shape dependence of D-meson flow harmonics in Pb–Pb collisions at $\sqrt{s_{NN}} = 5.02$ TeV,” *Phys. Lett. B*, vol. 813, p. 136054, 2021. DOI: 10.1016/j.physletb.2020.136054. arXiv: 2005.11131 [nucl-ex] (cit. on p. 53).
- [116] S. Acharya *et al.*, “ J/ψ elliptic and triangular flow in Pb–Pb collisions at $\sqrt{s_{NN}} = 5.02$ TeV,” *JHEP*, vol. 10, p. 141, 2020. DOI: 10.1007/JHEP10(2020)141. arXiv: 2005.14518 [nucl-ex] (cit. on p. 53).
- [117] S. Acharya *et al.*, “Anisotropic flow of identified particles in Pb–Pb collisions at $\sqrt{s_{NN}} = 5.02$ TeV,” *JHEP*, vol. 09, p. 006, 2018. DOI: 10.1007/JHEP09(2018)006. arXiv: 1805.04390 [nucl-ex] (cit. on p. 53).
- [118] C. Beattie, “Study of Path-length-dependent Energy Loss of Jets in p –Pb and Pb–Pb Collisions with ALICE,” *Acta Phys. Polon. Supp.*, vol. 16, no. 1, 1–A58, 2023. DOI: 10.5506/APhysPolBSupp.16.1-A58. arXiv: 2210.02937 [nucl-ex] (cit. on p. 54).

- [119] C.-Y. Wong, “Heavy quarkonia in quark-gluon plasma,” *Phys. Rev. C*, vol. 72, p. 034 906, 3 Sep. 2005. DOI: 10.1103/PhysRevC.72.034906. [Online]. Available: <https://link.aps.org/doi/10.1103/PhysRevC.72.034906> (cit. on p. 54).
- [120] S. Acharya *et al.*, “Measurements of inclusive J/ψ production at midrapidity and forward rapidity in Pb–Pb collisions at $\sqrt{s_{\text{NN}}} = 5.02$ TeV,” *Phys. Lett. B*, vol. 849, p. 138 451, 2024. DOI: 10.1016/j.physletb.2024.138451. arXiv: 2303.13361 [nucl-ex] (cit. on pp. 54, 55).
- [121] A. M. Sirunyan *et al.*, “Measurement of nuclear modification factors of $\Upsilon(1S)$, $\Upsilon(2S)$, and $\Upsilon(3S)$ mesons in PbPb collisions at $\sqrt{s_{\text{NN}}} = 5.02$ TeV,” *Phys. Lett. B*, vol. 790, pp. 270–293, 2019. DOI: 10.1016/j.physletb.2019.01.006. arXiv: 1805.09215 [hep-ex] (cit. on pp. 55, 56).
- [122] A. Mocsy and P. Petreczky, “Color screening melts quarkonium,” *Phys. Rev. Lett.*, vol. 99, p. 211 602, 2007. DOI: 10.1103/PhysRevLett.99.211602. arXiv: 0706.2183 [hep-ph] (cit. on p. 56).
- [123] J. Peng *et al.*, “Unraveling the collisional energy loss of a heavy quark in a quark-gluon plasma,” *Phys. Rev. D*, vol. 109, p. 096 028, 9 May 2024. DOI: 10.1103/PhysRevD.109.096028. [Online]. Available: <https://link.aps.org/doi/10.1103/PhysRevD.109.096028> (cit. on p. 56).
- [124] S. Acharya *et al.*, “Charm production and fragmentation fractions at midrapidity in pp collisions at $\sqrt{s} = 13$ TeV,” *JHEP*, vol. 12, p. 086, 2023. DOI: 10.1007/JHEP12(2023)086. arXiv: 2308.04877 [hep-ex] (cit. on p. 56).
- [125] N. N. Ajitanand *et al.*, “Decomposition of harmonic and jet contributions to particle-pair correlations at ultra-relativistic energies,” *Phys. Rev. C*, vol. 72, p. 011 902, 2005. DOI: 10.1103/PhysRevC.72.011902. arXiv: nucl-ex/0501025 (cit. on pp. 56, 169).
- [126] A. M. Sirunyan *et al.*, “Nuclear modification factor of D^0 mesons in PbPb collisions at $\sqrt{s_{\text{NN}}} = 5.02$ TeV,” *Phys. Lett. B*, vol. 782, pp. 474–496, 2018. DOI: 10.1016/j.physletb.2018.05.074. arXiv: 1708.04962 [nucl-ex] (cit. on pp. 56, 57).

- [127] A. M. Sirunyan *et al.*, “Measurement of prompt and nonprompt charmonium suppression in PbPb collisions at 5.02 TeV,” *Eur. Phys. J. C*, vol. 78, no. 6, p. 509, 2018, [Erratum: *Eur.Phys.J.C* 83, 145 (2023)]. DOI: 10.1140/epjc/s10052-018-5950-6. arXiv: 1712.08959 [nucl-ex] (cit. on p. 57).
- [128] A. M. Sirunyan *et al.*, “The production of isolated photons in PbPb and pp collisions at $\sqrt{s_{NN}} = 5.02$ TeV,” *JHEP*, vol. 07, p. 116, 2020. DOI: 10.1007/JHEP07(2020)116. arXiv: 2003.12797 [hep-ex] (cit. on p. 57).
- [129] V. Khachatryan *et al.*, “Charged-particle nuclear modification factors in PbPb and pPb collisions at $\sqrt{s_{NN}} = 5.02$ TeV,” *JHEP*, vol. 04, p. 039, 2017. DOI: 10.1007/JHEP04(2017)039. arXiv: 1611.01664 [nucl-ex] (cit. on p. 57).
- [130] e. a. Sirunyan A. M., “Measurement of the B^\pm meson nuclear modification factor in pb-pb collisions at $\sqrt{s_{NN}} = 5.02$ TeV,” *Phys. Rev. Lett.*, vol. 119, p. 152301, 15 Oct. 2017. DOI: 10.1103/PhysRevLett.119.152301. [Online]. Available: <https://link.aps.org/doi/10.1103/PhysRevLett.119.152301> (cit. on p. 57).
- [131] S. Acharya *et al.*, “Measurement of beauty production via non-prompt D^0 mesons in Pb–Pb collisions at $\sqrt{s_{NN}} = 5.02$ TeV,” *JHEP*, vol. 12, p. 126, 2022. DOI: 10.1007/JHEP12(2022)126. arXiv: 2202.00815 [nucl-ex] (cit. on pp. 57–59).
- [132] J. Adams *et al.*, “Direct observation of dijets in central Au+Au collisions at $\sqrt{s_{NN}} = 200$ -GeV,” *Phys. Rev. Lett.*, vol. 97, p. 162301, 2006. DOI: 10.1103/PhysRevLett.97.162301. arXiv: nucl-ex/0604018 (cit. on p. 59).
- [133] A. Ohlson, “Ridges in p–A (and pp) collisions,” in *3rd Large Hadron Collider Physics Conference*, Gatchina: Kurchatov Institute, 2016, pp. 489–493. arXiv: 1901.00747 [nucl-ex] (cit. on p. 61).
- [134] B. Abelev *et al.*, “Long-range angular correlations on the near and away side in p–Pb collisions at $\sqrt{s_{NN}} = 5.02$ TeV,” *Phys. Lett. B*, vol. 719, pp. 29–41, 2013. DOI: 10.1016/j.physletb.2013.01.012. arXiv: 1212.2001 [nucl-ex] (cit. on p. 61).

- [135] S. Acharya *et al.*, “Azimuthal correlations of heavy-flavor hadron decay electrons with charged particles in pp and p–Pb collisions at $\sqrt{s_{\text{NN}}} = 5.02$ TeV,” *Eur. Phys. J. C*, vol. 83, no. 8, p. 741, 2023. DOI: 10.1140/epjc/s10052-023-11835-x. arXiv: 2303.00591 [nucl-ex] (cit. on pp. 64, 106, 110, 120, 154–157, 177, 178, 189).
- [136] O. Bruning, H. Burkhardt, and S. Myers, “The Large Hadron Collider,” *Prog. Part. Nucl. Phys.*, vol. 67, pp. 705–734, 2012. DOI: 10.1016/j.pnpnp.2012.03.001 (cit. on p. 66).
- [137] “LHC Design Report Vol.1: The LHC Main Ring,” O. S. Bruning *et al.*, Eds., Jun. 2004. DOI: 10.5170/CERN-2004-003-V-1 (cit. on p. 66).
- [138] “LHC Design Report. 3. The LHC injector chain,” M. Benedikt *et al.*, Eds., Dec. 2004. DOI: 10.5170/CERN-2004-003-V-3 (cit. on p. 66).
- [139] C. W. Fabjan *et al.*, “ALICE: Physics Performance Report,” *J. Phys. G*, vol. 32, B. Alessandro *et al.*, Eds., pp. 1295–2040, 2006. DOI: 10.1088/0954-3899/32/10/001 (cit. on pp. 67, 68, 75).
- [140] B. B. Abelev *et al.*, “Performance of the ALICE Experiment at the CERN LHC,” *Int. J. Mod. Phys. A*, vol. 29, p. 1430044, 2014. DOI: 10.1142/S0217751X14300440. arXiv: 1402.4476 [nucl-ex] (cit. on p. 68).
- [141] “ALICE: from LS1 to readiness for Run 2,” *CERN Courier*, vol. 55, no. 4, pp. 35–40, 2015. [Online]. Available: <https://cds.cern.ch/record/2231993> (cit. on p. 69).
- [142] A. Khatun, “UPC physics with ALICE in Run 3,” *Phys. Proc. UPC*, vol. 1, p. 22, 2024. DOI: 10.17161/5b46x852. arXiv: 2405.19069 [hep-ex] (cit. on p. 69).
- [143] G. Dellacasa *et al.*, “ALICE technical design report of the inner tracking system (ITS),” Jun. 1999 (cit. on p. 69).
- [144] D. Colella, “ALICE ITS: the Run 1 to Run 2 transition and recent operational experience,” *PoS*, vol. VERTEX2015, p. 003, 2015. DOI: 10.22323/1.254.0003. [Online]. Available: <https://cds.cern.ch/record/2159190> (cit. on p. 70).

- [145] E. Botta, “ALICE ITS: Operational Experience, Performance and Lessons Learned,” *PoS*, vol. Vertex2019, p. 002, 2020. DOI: 10.22323/1.373.0002. [Online]. Available: <https://cds.cern.ch/record/2747953> (cit. on pp. 70, 71).
- [146] A. Rossi, “Alice Alignment, Tracking and Physics Performance Results,” *PoS*, vol. VERTEX2010, p. 017, 2010. DOI: 10.22323/1.113.0017. arXiv: 1101.3491 [physics.ins-det] (cit. on p. 71).
- [147] J. Alme *et al.*, “The ALICE TPC, a large 3-dimensional tracking device with fast readout for ultra-high multiplicity events,” *Nucl. Instrum. Meth. A*, vol. 622, pp. 316–367, 2010. DOI: 10.1016/j.nima.2010.04.042. arXiv: 1001.1950 [physics.ins-det] (cit. on pp. 71, 72, 82).
- [148] H. Bethe, “Theory of the Passage of Fast Corpuscular Rays Through Matter,” *Annalen Phys.*, vol. 5, pp. 325–400, 1930. DOI: 10.1002/andp.19303970303 (cit. on p. 71).
- [149] C. Lippmann, “Performance of the alice time projection chamber,” *Physics Procedia*, vol. 37, pp. 434–441, 2012, Proceedings of the 2nd International Conference on Technology and Instrumentation in Particle Physics (TIPP 2011), ISSN: 1875-3892. DOI: <https://doi.org/10.1016/j.phpro.2012.02.390>. [Online]. Available: <https://www.sciencedirect.com/science/article/pii/S187538921201721X> (cit. on p. 71).
- [150] P. Cortese *et al.*, “ALICE electromagnetic calorimeter technical design report,” Sep. 2008 (cit. on pp. 73, 74).
- [151] S. Acharya *et al.*, “Performance of the ALICE Electromagnetic Calorimeter,” *JINST*, vol. 18, no. 08, P08007, 2023. DOI: 10.1088/1748-0221/18/08/P08007. arXiv: 2209.04216 [physics.ins-det] (cit. on pp. 73, 74, 83, 86).
- [152] E. Abbas *et al.*, “Performance of the ALICE VZERO system,” *JINST*, vol. 8, P10016, 2013. DOI: 10.1088/1748-0221/8/10/P10016. arXiv: 1306.3130 [nucl-ex] (cit. on pp. 75, 80).
- [153] M. Zimmermann, “The ALICE analysis train system,” *J. Phys. Conf. Ser.*, vol. 608, no. 1, L. Fiala, M. Lokajicek, and N. Tumova, Eds., p. 012019, 2015. DOI: 10.1088/1742-6596/608/1/012019. arXiv: 1502.06381 [hep-ex] (cit. on pp. 76, 77).

- [154] “LHC computing Grid. Technical design report,” I. Bird *et al.*, Eds., Jun. 2005 (cit. on p. 76).
- [155] B. B. Abelev *et al.*, “Beauty production in pp collisions at $\sqrt{s} = 2.76$ TeV measured via semi-electronic decays,” *Phys. Lett. B*, vol. 738, pp. 97–108, 2014. DOI: 10.1016/j.physletb.2014.09.026. arXiv: 1405.4144 [nucl-ex] (cit. on pp. 79, 172).
- [156] W. Herr and B. Muratori, “Concept of luminosity,” 2006. DOI: 10.5170/CERN-2006-002.361. [Online]. Available: <https://cds.cern.ch/record/941318> (cit. on p. 81).
- [157] I. Belikov, “Event reconstruction and particle identification in the ALICE experiment at the LHC,” *EPJ Web Conf.*, vol. 70, p. 00029, 2014 (cit. on p. 82).
- [158] S. Acharya *et al.*, “The ALICE definition of primary particles,” Tech. Rep. ALICE-PUBLIC-2017-005, Jun. 2017. [Online]. Available: <https://cds.cern.ch/record/2270008> (cit. on p. 83).
- [159] S. Oh, A. Morsch, C. Loizides, and T. Schuster, “Correction methods for finite-acceptance effects in two-particle correlation analyses,” *Eur. Phys. J. Plus*, vol. 131, no. 8, p. 278, 2016. DOI: 10.1140/epjp/i2016-16278-0. arXiv: 1604.05332 [nucl-th] (cit. on p. 89).
- [160] J. H. Hubbell, “Electron-positron pair production by photons. an historical overview,” *Radiation Physics and Chemistry*, vol. 75, Jan. 2006. DOI: <https://doi.org/10.1016/j.radphyschem.2005.10.008> (cit. on p. 92).
- [161] K. Aamodt, “pi0 and eta reconstruction from photon conversions in ALICE for first p-p collisions at the LHC,” *J. Phys. Conf. Ser.*, vol. 270, M. Bleicher *et al.*, Eds., p. 012035, 2011. DOI: 10.1088/1742-6596/270/1/012035 (cit. on p. 92).
- [162] M. C. Danisch, “Direct Photon Production and HBT Correlations in Pb–Pb Collisions at $\sqrt{s_{NN}} = 5.02$ TeV with the ALICE Experiment,” *Acta Phys. Pol. B Proc. Suppl.*, vol. 16, no. 1, p. 122, 2023. DOI: 10.5506/APhysPolBSupp.16.1-A122. [Online]. Available: <https://cds.cern.ch/record/2869512> (cit. on p. 92).

- [163] R. H. Dalitz, “On an alternative decay process for the neutral η -meson,” *Proceedings of the Physical Society. Section A*, vol. 64, no. 7, pp. 667–669, Jul. 1951. DOI: 10.1088/0370-1298/64/7/115. [Online]. Available: <https://dx.doi.org/10.1088/0370-1298/64/7/115> (cit. on p. 92).
- [164] B. I. Abelev *et al.*, “Transverse momentum and centrality dependence of high- p_T non-photon electron suppression in Au+Au collisions at $\sqrt{s_{NN}} = 200$ GeV,” *Phys. Rev. Lett.*, vol. 98, p. 192 301, 2007, [Erratum: *Phys. Rev. Lett.* 106, 159902 (2011)]. DOI: 10.1103/PhysRevLett.98.192301. arXiv: nucl-ex/0607012 (cit. on pp. 93, 94).
- [165] R. Brun *et al.*, *GEANT: detector description and simulation tool; March 1994* (CERN Program Library). Geneva: CERN, 1993, Long Writeup W5013. [Online]. Available: <http://cds.cern.ch/record/1073159> (cit. on p. 95).
- [166] G. Aad *et al.*, “Measurement of azimuthal anisotropy of muons from charm and bottom hadrons in Pb+Pb collisions at $s_{NN}=5.02$ TeV with the ATLAS detector,” *Phys. Lett. B*, vol. 807, p. 135 595, 2020. DOI: 10.1016/j.physletb.2020.135595. arXiv: 2003.03565 [nucl-ex] (cit. on pp. 101, 129).
- [167] G. Aad *et al.*, “Measurement of the nuclear modification factor for muons from charm and bottom hadrons in Pb+Pb collisions at 5.02 TeV with the ATLAS detector,” *Phys. Lett. B*, vol. 829, p. 137 077, 2022. DOI: 10.1016/j.physletb.2022.137077. arXiv: 2109.00411 [nucl-ex] (cit. on p. 101).
- [168] S. Acharya *et al.*, “Energy dependence and fluctuations of anisotropic flow in Pb–Pb collisions at $\sqrt{s_{NN}} = 5.02$ and 2.76 TeV,” *JHEP*, vol. 07, p. 103, 2018. DOI: 10.1007/JHEP07(2018)103. arXiv: 1804.02944 [nucl-ex] (cit. on pp. 101, 129).
- [169] S. Acharya *et al.*, “Transverse momentum spectra and nuclear modification factors of charged particles in pp, p–Pb and Pb–Pb collisions at the LHC,” *JHEP*, vol. 11, p. 013, 2018. DOI: 10.1007/JHEP11(2018)013. arXiv: 1802.09145 [nucl-ex] (cit. on p. 101).
- [170] S. Acharya *et al.*, “Investigating charm production and fragmentation via azimuthal correlations of prompt D mesons with charged particles in pp collisions at $\sqrt{s} = 13$ TeV,” *Eur. Phys. J. C*, vol. 82, no. 4, p. 335, 2022. DOI:

- 10.1140/epjc/s10052-022-10267-3. arXiv: 2110.10043 [nucl-ex] (cit. on pp. 106, 110, 130).
- [171] L. Lista, *Statistical methods for data analysis in particle physics*. Springer, 2017 (cit. on p. 107).
 - [172] S. Acharya *et al.*, “Azimuthal correlations of prompt D mesons with charged particles in pp and p–Pb collisions at $\sqrt{s_{NN}} = 5.02$ TeV,” *Eur. Phys. J. C*, vol. 80, no. 10, p. 979, 2020. DOI: 10.1140/epjc/s10052-020-8118-0. arXiv: 1910.14403 [nucl-ex] (cit. on pp. 107, 108, 110).
 - [173] S. Nadarajah, “A generalized normal distribution,” *Journal of Applied Statistics*, vol. 32, no. 7, pp. 685–694, 2005. DOI: 10.1080/02664760500079464. eprint: <https://doi.org/10.1080/02664760500079464>. [Online]. Available: <https://doi.org/10.1080/02664760500079464> (cit. on p. 108).
 - [174] F. Wang and A. E. Gelfand, “Directional data analysis under the general projected normal distribution,” *Statistical methodology*, vol. 10, no. 1, pp. 113–127, 2013 (cit. on p. 109).
 - [175] J. Adam *et al.*, “Measurement of azimuthal correlations of D mesons and charged particles in pp collisions at $\sqrt{s} = 7$ TeV and p–Pb collisions at $\sqrt{s_{NN}} = 5.02$ TeV,” *Eur. Phys. J. C*, vol. 77, no. 4, p. 245, 2017. DOI: 10.1140/epjc/s10052-017-4779-8. arXiv: 1605.06963 [nucl-ex] (cit. on p. 110).
 - [176] S. Acharya *et al.*, “Studying charm hadronisation into baryons with azimuthal correlations of Λ_c^+ with charged particles in pp collisions at $s=13$ TeV,” *Phys. Lett. B*, vol. 868, p. 139681, 2025. DOI: 10.1016/j.physletb.2025.139681. arXiv: 2411.10104 [hep-ex] (cit. on p. 110).
 - [177] T. A. Trainor, “Zero yield at minimum (zyam) method and v_2 : Underestimating jet yields from dihadron azimuth correlations,” *Phys. Rev. C*, vol. 81, p. 014905, 1 Jan. 2010. DOI: 10.1103/PhysRevC.81.014905. [Online]. Available: <https://link.aps.org/doi/10.1103/PhysRevC.81.014905> (cit. on p. 113).
 - [178] P. Sinervo, “Definition and Treatment of Systematic Uncertainties in High Energy Physics and Astrophysics,” *eConf*, vol. C030908, L. Lyons, R. P. Mount, and R. Reitmeyer, Eds., TUAT004, 2003 (cit. on p. 116).

- [179] B. Andersson, G. Gustafson, G. Ingelman, and T. Sjöstrand, “Parton fragmentation and string dynamics,” *Physics Reports*, vol. 97, no. 2, pp. 31–145, 1983, ISSN: 0370-1573. DOI: [https://doi.org/10.1016/0370-1573\(83\)90080-7](https://doi.org/10.1016/0370-1573(83)90080-7). [Online]. Available: <https://www.sciencedirect.com/science/article/pii/0370157383900807> (cit. on p. 154).
- [180] I. J. Abualrob *et al.*, “Medium-induced modification of azimuthal correlations of electrons from heavy-flavor hadron decays with charged particles in Pb-Pb collisions at $\sqrt{s_{NN}} = 5.02$ TeV,” Jul. 2025. arXiv: 2507.13197 [nucl-ex] (cit. on pp. 159, 160, 162, 163, 168, 169, 171, 179, 180).
- [181] E. Norrbin and T. Sjostrand, “Production and hadronization of heavy quarks,” *Eur. Phys. J. C*, vol. 17, pp. 137–161, 2000. DOI: 10.1007/s100520000460. arXiv: hep-ph/0005110 (cit. on p. 164).
- [182] I. Vitev, “Large angle hadron correlations from medium-induced gluon radiation,” *J. Phys. Conf. Ser.*, vol. 27, G. Roland and T. Trainor, Eds., pp. 11–21, 2005. DOI: 10.1088/1742-6596/27/1/002. arXiv: hep-ph/0506281 (cit. on p. 164).
- [183] e. a. L. Adamczyk, “Jet-like correlations with direct-photon and neutral-pion triggers at $s_{NN}=200$ gev,” *Physics Letters B*, vol. 760, pp. 689–696, 2016, ISSN: 0370-2693. DOI: <https://doi.org/10.1016/j.physletb.2016.07.046>. [Online]. Available: <https://www.sciencedirect.com/science/article/pii/S0370269316303872> (cit. on p. 166).
- [184] e. a. Adamczyk L., “Experimental studies of di-jets in au + au collisions using angular correlations with respect to back-to-back leading hadrons,” *Phys. Rev. C*, vol. 87, p. 044903, 4 Apr. 2013. DOI: 10.1103/PhysRevC.87.044903. [Online]. Available: <https://link.aps.org/doi/10.1103/PhysRevC.87.044903> (cit. on p. 166).
- [185] G. J. Feldman and R. D. Cousins, “A Unified approach to the classical statistical analysis of small signals,” *Phys. Rev. D*, vol. 57, pp. 3873–3889, 1998. DOI: 10.1103/PhysRevD.57.3873. arXiv: physics/9711021 (cit. on p. 168).
- [186] X.-N. Wang and M. Gyulassy, “Gluon shadowing and jet quenching in $A + A$ collisions at $\sqrt{s} = 200A$ gev,” *en, Phys. Rev. Lett.*, vol. 68, no. 10, pp. 1480–1483, Mar. 1992 (cit. on p. 169).

- [187] Z. Yang *et al.*, “Search for the Elusive Jet-Induced Diffusion Wake in Z/γ -Jets with 2D Jet Tomography in High-Energy Heavy-Ion Collisions,” *Phys. Rev. Lett.*, vol. 127, no. 8, p. 082301, 2021. DOI: 10.1103/PhysRevLett.127.082301. arXiv: 2101.05422 [hep-ph] (cit. on p. 169).
- [188] P. M. Chesler and K. Rajagopal, “On the Evolution of Jet Energy and Opening Angle in Strongly Coupled Plasma,” *JHEP*, vol. 05, p. 098, 2016. DOI: 10.1007/JHEP05(2016)098. arXiv: 1511.07567 [hep-th] (cit. on p. 183).
- [189] J. G. Milhano and K. C. Zapp, “Origins of the di-jet asymmetry in heavy ion collisions,” *Eur. Phys. J. C*, vol. 76, no. 5, p. 288, 2016. DOI: 10.1140/epjc/s10052-016-4130-9. arXiv: 1512.08107 [hep-ph] (cit. on p. 183).
- [190] G.-L. Ma and X.-N. Wang, “Comparative study of hadron- and γ -triggered azimuthal correlations in relativistic heavy-ion collisions,” in *Acta Phys. Pol. B*, vol. 43, no. 4, p. 697, 2012 (cit. on p. 186).
- [191] G. Aad *et al.*, “Medium-Induced Modification of Z -Tagged Charged Particle Yields in $Pb + Pb$ Collisions at 5.02 TeV with the ATLAS Detector,” *Phys. Rev. Lett.*, vol. 126, no. 7, p. 072301, 2021. DOI: 10.1103/PhysRevLett.126.072301. arXiv: 2008.09811 [nucl-ex] (cit. on p. 186).
- [192] V. Chekhovsky *et al.*, “Evidence of medium response to hard probes using correlations of Z bosons with hadrons in heavy ion collisions,” Jul. 2025. arXiv: 2507.09307 [nucl-ex] (cit. on pp. 186–188).
- [193] L. Adamczyk *et al.*, “Jet-like Correlations with Direct-Photon and Neutral-Pion Triggers at $\sqrt{s_{NN}} = 200$ GeV,” *Phys. Lett. B*, vol. 760, pp. 689–696, 2016. DOI: 10.1016/j.physletb.2016.07.046. arXiv: 1604.01117 [nucl-ex] (cit. on pp. 186, 187).
- [194] e. a. Adare A., “Medium modification of jet fragmentation in Au+Au collisions at $\sqrt{s_{NN}}=200$ GeV measured in direct photon-hadron correlations,” *Phys. Rev. Lett.*, vol. 111, p. 032301, 3 Jul. 2013. DOI: 10.1103/PhysRevLett.111.032301. [Online]. Available: <https://link.aps.org/doi/10.1103/PhysRevLett.111.032301> (cit. on pp. 186, 187).

- [195] Z.-B. Kang, I. Vitev, and H. Xing, “Vector-boson-tagged jet production in heavy ion collisions at energies available at the CERN Large Hadron Collider,” *Phys. Rev. C*, vol. 96, no. 1, p. 014912, 2017. DOI: 10.1103/PhysRevC.96.014912. arXiv: 1702.07276 [hep-ph] (cit. on p. 192).
- [196] W. Dai, I. Vitev, and B.-W. Zhang, “Momentum imbalance of isolated photon-tagged jet production at RHIC and LHC,” *Phys. Rev. Lett.*, vol. 110, no. 14, p. 142001, 2013. DOI: 10.1103/PhysRevLett.110.142001. arXiv: 1207.5177 [hep-ph] (cit. on p. 192).
- [197] F. Reidt, “Upgrade of the ALICE ITS detector,” *Nucl. Instrum. Meth. A*, vol. 1032, p. 166632, 2022. DOI: 10.1016/j.nima.2022.166632. arXiv: 2111.08301 [physics.ins-det] (cit. on p. 193).